EPFL

Mixing processes and their ecological implications: From vertical to lateral variability in stratified lakes

Présentée le 17 septembre 2020

à la Faculté de l'environnement naturel, architectural et construit
Laboratoire de physique des systèmes aquatiques - Chaire Margaretha Kamprad
Programme doctoral en génie civil et environnement

pour l'obtention du grade de Docteur ès Sciences

par

Oscar Rodrigo SEPÚLVEDA STEINER

Acceptée sur proposition du jury

Prof. T. I. Battin, président du jury
Prof. A. J. Wüest, Dr D. Bouffard, directeurs de thèse
Prof. A. Lorke, rapporteur
Prof. I. Fer, rapporteur
Prof. M. Holzner, rapporteur

École
polytechnique
fédérale
de Lausanne

2020

Πάντα ῥεῖ
(everything flows)

<small>HERACLITUS</small>

A mis padres Elizabeth y Jaime
Gracias por tanto, perdón por tan poco

Acknowledgements

Acknowledgements

Abstract

The physical environment of natural waters influences biogeochemical processes to generate specific ecological niches, promoting biophysical interactions. Bacteria and phytoplankton communities can form spatial structures, such as layers and patches. The physical characteristics of these structures in lakes, particularly their vertical and horizontal variability are the focus of this PhD thesis.

Using temperature microstructure measurements, we aim to characterize turbulent mixing within biological formations and their surroundings in lakes. We start in Lake Cadagno, where unusual bio-convectively-driven mixing takes place. Then we move to Lake Zurich where a thin layer of cyanobacteria persists throughout the stratified season. Finally, we study the thermocline of Lake Geneva, a large and more energetic system, where basin-scale processes are expected to induce lateral variability of algae. While the first two interactions concern vertical structures, we use an autonomous underwater glider, equipped with a turbulence package, to explore lateral variability in this large lake.

Bioconvection observed in Lake Cadagno offered a unique environment to analyze the role of microorganism in shaping the water column they inhabit. Within the stratified water column, a highly concentrated layer of heavy, motile and photoautotrophic sulfur bacteria *Chromatium okenii* migrates upward to form a subsurface convective mixed layer. Field measurements revealed that the mixed layer persists throughout the diel cycle, maintaining a virtually unchanged structure. Direct estimates of turbulent diffusion indicate that without active convective turbulence, the mixed layer would be smoothed in ≈2.5 hours. As this time-scale is much shorter than a night and in principle *C. okenii* need light, the nighttime mixed layer is not expected. Using intensive and high-resolution measurements throughout two diel cycles, we provide proof that bioconvection occurs also at night and is responsible for the mixed layer persistence.

The second interaction was the thin layer of cyanobacteria *Planktothrix rubescens* forming every spring in the thermocline of Lake Zurich. In this zone, our measurements revealed only tiny overturns, resulting in negligible vertical exchange. This strong stratification inhibits mixing and provides a remarkably stable environment for the *P. rubescens* thin layer, explaining its persistence.

Finally, in Lake Geneva, we first concentrated efforts in the validation of glider-based turbulence estimations, possibly the first of their kind in a large-lake. Although weak turbulence and strong stratification hinder the applicability of state of the art procedures, we demonstrate that our measurements capture the expected variance and spectral shape. We explore the data from repeated transects to assess lateral variability of chlorophyll-a patches.

Abstract

This thesis documents in an exemplary way how vertical turbulent processes interact with bacteria and phytoplankton layers in lakes. Regarding lateral variability, the results presented are a first step for future in-situ studies of phytoplankton patches affected by turbulence and transport processes.

Keywords

Résumé

L'environnement physique des eaux naturelles influence des processus biogéochimiques pour générer des niches écologiques spécifiques, qui favorisent des interactions biophysiques. Les communautés de bactéries et de phytoplancton peuvent former des structures spatiales comme des couches et des nappes. Les caractéristiques physiques de ces structures dans les lacs, en particulier leur variabilité verticale et horizontale, constitue le cœur de recherche de cette thèse.

A l'aide de mesures de microstructures de températures, notre objectif est de caractériser le mélange turbulent au niveau des formations biologiques et leur milieu environnant dans les lacs. Nous commençons au lac Cadagno, dans lequel un inhabituel mélange induit par bioconvection prend place. Ensuite, nous continuons avec le lac de Zurich où une fine couche de cyanobactéries persiste au fil de la saison stratifiée. Enfin, nous étudions la thermocline du lac Léman, un système large et plus énergétique, où des processus à l'échelle du bassin sont attendus pour induire une variation latérale des algues. Alors que les deux premières interactions concernent des structures verticales, nous utilisons un planeur sous-marin autonome, équipé d'un système de mesure de turbulence, pour explorer la variabilité latérale dans ce grand lac.

La bioconvection observée au lac Cadagno a offert un environnement unique pour analyser le rôle des microorganismes dans la modification de la colonne d'eau dans laquelle ils habitent. Dans la colonne d'eau stratifiée, une couche hautement concentrée en *Chromatium okenii*, une bactérie sulfureuse lourde, motile et photo-autotrophe, migre vers le haut pour former une couche mélangée par convection sous la surface. Les mesures de terrain ont révélé que cette couche persiste pendant le cycle nycthéméral maintenant une structure pratiquement inchangée. Les estimations directes de diffusion turbulente indiquent qu'en l'absence d'une turbulence convective active, la couche mélangée s'estomperait en ≈2.5 heures. Comme cette échelle de temps est plus courte qu'une nuit et qu'en principe *C. okenii* a besoin de lumière, la couche mélangée ne devrait pas être observée la nuit. A l'aide de mesures intensives et à haute-résolution pendant deux cycles nycthéméraux, nous avons la preuve que la bioconvection prend place également pendant la nuit et qu'elle est responsable de la persistance de la couche mélangée.

La deuxième interaction était la fine couche de cyanobactéries *Planktothrix rubescens* formant chaque printemps dans la thermocline du lac de Zurich. Dans cette zone, nos mesures ont révélé seulement de petits renversements, résultant en un échange vertical négligeable. Cette forte stratification inhibe le mélange et offre un environnement remarquablement stable pour la fine couche de *P. rubescens*, et expliquant la persistance de celle-ci.

Enfin, dans le lac Léman, nous avons d'abord concentré nos efforts dans la validation des estimations de turbulence obtenues par le planeur sous-marin, qui sont à notre connaissance les premières obtenues dans un grand lac. Bien qu'une faible turbulence et une forte stratification gêne la mise en œuvre des procédures

de pointe, nous démontrons que nos mesures capturent la variance et la distribution spectrale attendue. Nous explorons les données de transects répétés pour évaluer la variabilité latérale des nappes de chlorophylle-a.

Cette thèse documente d'une façon exemplaire comment les processus turbulent verticaux interagissent avec les couches de bactéries et de phytoplanctons dans les lacs. Concernant la variabilité latérale, les résultats présentés constitue une première étape pour les futures études in-situ des nappes de phytoplancton affectées par la turbulence et les processus de transport.

Mots-clés

Turbulence dans des écoulements stratifiés, microstructures de température, bioconvection, couches mélangées, fines couches, inhibition du mélange, variabilité latérale, planeur sous-marin autonome

Contents

Contents

1 Introduction

1.1 Motivation

In aquatic systems, biogeochemical processes are strongly tied to the geophysical environment. This interaction prevails across the entire hydrosphere, from rivers (Peterson, 2001; Raymond et al., 2016), to lakes (MacIntyre, 1998; Adrian et al., 2009), to estuaries (Monbet, 1992; Cadier et al., 2017) and to the ocean (McGillicuddy et al., 2003; Sarmiento et al., 2004). From a deterministic viewpoint, the development of an ecosystem can be described as an unsteady interplay between transport, reactive processes, and any other sinks and sources. Yet, a challenge is that these interactions span many temporal and spatial scales. The ultimate goal of this work is to contribute to the knowledge of ecosystem functioning in lakes at small scales, where microorganisms and their resources are affected in similar ways by the physical surrounding (Stocker, 2012; Sengupta et al., 2017).

Water bodies are characterized by vertical and horizontal gradients in their properties. Lake research has traditionally adopted a vertical representation because water properties such as density, temperature and light are all strongly vertically structured. At first order, vertical characterization appears sufficient. The seasonal phytoplankton growth as well as the sequential development of species are usually described as a response of nutrients and water properties in the different density layers (Talling, 1966; Legendre, 1981). According to the iconic but today-debated example of the phytoplankton paradox (Hutchinson, 1961), the various phytoplankton species observed in lakes are adapted to the different physical niches (level of light, turbulence, temperature etc.). However, the physical characteristics of such niches are not comprehensively defined. Specifically, the vertical and horizontal structures of tracers and matter and ad-hoc characterization of turbulent mixing remains to be investigated with in-situ observations.

This research gap can be addressed today with either conventional vertical microstructure profilers or similar turbulence instruments mounted on autonomous underwater gliders, enabling coverage from vertical to lateral variability of turbulence characteristics. In this thesis, we investigate interactions between turbulence and biological formations at different length- and time-scales, from vertical to horizontal dimensions, in three lakes of different hydrodynamic complexity. While we evaluated vertical examples of these interactions in detail, our research on their lateral variability is exploratory.

1.2 Mixing processes and ecological implications

1.2.1 Stratification and mixing in lakes

In lakes, the vertical profile of potential density is a function of temperature and salinity and occasionally of particles and gases. It defines the stratification and stability of the water column. This spatial structure affects both vertical and horizontal processes.

The generation of mixing in a stratified lake requires an external input of energy, such as wind or cooling (Wüest and Lorke, 2003). The former transfers energy to the water body through surface shearing, generating large-scale dynamics (e.g. internal waves; Mortimer 1952) that provide turbulent kinetic energy (TKE). Then TKE cascades to smaller scales, generating shear-induced turbulence until it dissipates by friction mostly at the boundaries (Imberger, 1998). In the case of cooling, the temperature changes alter the density structure of the surface layer, leading to unstable density profiles, which drives convection. There is a variety of different convective processes that can take place in lakes due to their diverse meteorological, geochemical and morphological conditions (Bouffard and Wüest, 2019). The convective plumes triggered by convection also inject TKE into the water body. Both shear-induced turbulence and convection are the main processes driving mixing in the water column of stratified lakes.

The different mixing effects generated by convection and diffusion can locally occur simultaneously. In the case of convectively-driven mixed layers (Huppert and Turner, 1972; Tedford et al., 2014) these two processes have opposing effects, with diffusion smoothing those homogeneous layers. A better understanding of the interaction of convection and turbulent diffusion can help elucidate the role of background turbulence in the maintenance of convective mixed layers.

To describe mixing, it is necessary to characterize stratification and turbulence parameters, e.g. the rate of TKE dissipation (ε). Small-scale measurements, such as temperature microstructure, allow us to estimate ε. For vertical mixing processes, including convective mixed layers, this key quantity can be estimated using standard vertical microstructure profilers. The specific methods we employed to obtain ε from temperature microstructure measurements are detailed below (section 1.3).

In large lakes, the combined effect of wind and earth rotation affects internal motions leading to complex basin-scale dynamics (Csanady, 1975). Processes such as upwelling events (Schladow et al., 2004; Roberts, 2019), gyres (Ishikawa et al., 2002; Shimizu et al., 2007) and basin-scale rotational internal waves (Antenucci et al., 2000; Appt et al., 2004; Bouffard et al., 2012), drive stirring and spatial variability of water constituents. Direct numerical simulations have demonstrated that these mechanisms distribute TKE in a broad range of scales, and can generate heterogeneous turbulent properties in the water body (Ulloa et al., 2015). Recent advances in underwater vehicle technology have allowed unprecedented in-situ characterization of the spatial variability of turbulence in ocean environments (e.g. Schultze et al., 2017; Fisher et al., 2018). Although there have been efforts using manned submersibles (Thorpe et al., 1999; Fer et al., 2002), the spatial response of turbulence and mixing due to large-scale processes in lakes remains overlooked. In this thesis, we measured temperature microstructure in a combined vertical to horizontal fashion using an autonomous underwater glider equipped with a microstructure profiler (Peterson and Fer, 2014). This technique was developed for oceans, which are a much more energetic system than lakes. Validating glider-based turbulence measurement in a lake environment (weak to moderate turbulence) comprises one of the main efforts of this work.

1.2.2 Biophysical interactions

In aquatic systems, stratification and mixing processes as well as spatial variability determine access to resources for plankton. Given the conditions imposed by the physical environment phytoplankton communities often form spatial structures such as patches (Abraham, 1998; Ng et al., 2011; Lévy et al., 2018), and thin layers (Durham and Stocker, 2012). Zooplankton grazing on phytoplankton follow these formations and turbulence enhance the encounter rates (Rothschild and Osborn, 1988; Visser and Kiørboe, 2006). Understanding the biophysical interactions that occur in such plankton structures is important because these are aquatic ecosystem hot-spots for primary production, nutrient cycling and foraging (Prairie et al., 2012). Once formed, these structures continue to interact with their physical environment. One classical example is the increase in primary production within phytoplankton patches due to increased nutrient availability driven by hydrodynamic processes (Weiss et al., 1991; Oschlies and Garçon, 1998; Dufois et al., 2016). At the microscale, turbulence can exert an effect on phytoplankton growth and community composition (Margalef, 1997).

Although more unusual and less studied, biological activity can also influence and force physical processes in aquatic ecosystems. At large scales, spatial structures of phytoplankton can affect water characteristics. This can modify the water light absorption (Lorenzen, 1972; Schanz, 1985) and lead to differential heating (Sathyendranath et al., 1991; Strutton and Chavez, 2004). At small scales, biogenic turbulence is expected to drive water and mass fluxes (Kunze et al., 2006). The topic is mostly investigated by laboratory experiments (Noss and Lorke, 2014; Houghton et al., 2018) and in-situ examples of plankton-induced turbulence are available only for the case of zooplankton (Simoncelli et al., 2018). However, the capacity of swimming microorganisms to effectively generate (biogenic) mixing has not been conclusively observed in-situ (Kunze, 2019).

Bioconvection (Bees, 2020) is a process, where dense and motile organisms migrating upward change the local density of their fluid environment, make it density-unstable and thus drive mixing. A recent study by Sommer et al. (2017) demonstrated that a layer of bacterial plankton can induce bioconvection in a stratified lake. Up to now, this example is the sole well-documented and consistent observation of biogenic mixing in natural waters.

How nutrient-limited environments can host rich plankton diversity (e.g. the phytoplankton paradox) remains an open question. Turbulence is expected to play a major role by favoring certain species (Barton et al., 2014). The above-described biophysical interactions are sustained by a specific stratification and turbulence (thin layers and patches) or they actively generate such interaction (bioconvection). To advance the field, it is required to disentangle stratification and turbulence effects on plankton structures from ecological interactions. A possible strategy is to study structures dominated by a single species. In this thesis, we first study the persistence of two distinct and well-defined vertical structures dominated by a single species: (i) a bacterial layer generating bioconvection and (ii) a thin layer of cyanobacteria (Posch et al., 2012). Finally, we move to a larger system, exhibiting large-scale horizontal motions and a more complex phytoplankton diversity (Anneville et al., 2002). This will potentially allow us to explore the effect of spatial variability of water properties and turbulence on phytoplankton patches.

1.3 Turbulence estimations using temperature microstructure

The research performed in this thesis shares the methodology – turbulence estimations using temperature microstructure – which is applied to data obtained from different acquisition platforms. Therefore, key concepts are included for completeness, as method explanations are kept short in each research chapter.

The nature of turbulent flows can be summarized with the following statement (Thorpe, 2007):

"Stirring + diffusion = mixing"

In a thermally stratified flow, turbulence creates thermal micro-fronts at small scales through stirring. Diffusion balances that process by homogenizing fluid properties (Osborn and Cox, 1972). Both processes combined, stirring and diffusion, generate irreversible mixing of the originally different water parcels (Thorpe, 2007).

There are two types of microstructure measurements used for estimating turbulent parameters: direct velocity-based measurements (i.e. shear; Osborn and Crawford, 1980; Lueck et al., 2002) and indirect scalar-based measurements (temperature; Lueck et al., 1977; Oakey, 1982). The valuable information of the acquired data is contained in the spectral domain of these microstructure measurements. The Taylor frozen-flow hypothesis allows to convert spectra from frequency (f) to wavenumber (k) domain and thereby make measurements performed at different speeds comparable. When conducting in-situ measurements, the speed of free falling devices (U) is considered as the mean flow and the wavenumber spectra $\Psi(k) = U\Psi(f)$, where $k = fU^{-1}$.

We focus on temperature microstructure, because it was found better-suited for weak turbulence environments, such as the interior of lakes (Kocsis et al., 1999). The technique to estimate turbulent quantities, from temperature microstructure, relies on the concept of the Batchelor (1959) length (ℓ_B). Defined as the length-scale at which stirring and diffusion balances, preventing micro-fronts generated by strain became infinitely sharp, it is represented as:

$$\ell_B = \left(\frac{\nu D_T^2}{\varepsilon} \right)^{\frac{1}{4}}$$

(1.1)

where ν is the viscosity, D_T is the molecular thermal diffusivity and ε is the rate of TKE dissipation per unit of mass. Consequently, the Batchelor wavenumber, k_B, is defined as:

$$k_B = \frac{1}{2\pi} \left(\frac{\varepsilon}{\nu D_T^2} \right)^{\frac{1}{4}}$$

(1.2)

In a turbulent flow, the temperature gradient spectra $S(k)$ can be represented by the Batchelor (1959) theoretical form, which accounts for its high-wavenumber end, given by:

$$S_B(k) = \left(\frac{q}{2} \right)^{\frac{1}{2}} \chi_\theta k_B^{-1} D_T^{-1} f(\alpha) \quad [°\text{C}^2\,\text{m}^{-2}\,\text{cpm}^{-1}]$$

(1.3)

where $f(\alpha)$ is the universal spectral shape (Oakey, 1982):

$$f(\alpha) = \alpha \left(e^{-\frac{\alpha^2}{2}} - \alpha \int_\alpha^\infty e^{-\frac{x^2}{2}}\,dx \right); \quad \alpha = k k_B^{-1} \sqrt{2q}$$

(1.4)

with $q \approx 3.4$ to 4.1 as universal constant. The quantity χ_θ corresponds to the rate of smoothing of the thermal variance by diffusion of heat. Assuming that at those small scales the temperature gradient field is isotropic, χ_θ is given by:

$$\chi_\theta = 6D_T \int_o^\infty S(k)\,dk = 6D_T \overline{\left(\frac{\partial T'}{\partial z} \right)^2}$$

(1.5)

The estimation of χ_θ and ε can be accomplished by adjusting $S(k)$ to $S_B(k)$ (e.g. Ruddick et al., 2000). Temperature microstructure measurements involve using small-diameter glass-coated fast thermistors (FP07 – General Electric, USA). At the high frequencies at which they are sampled for turbulence studies (greater than 100 Hz for in-situ applications), these sensors yield inherent noise with characteristic spectra. Taking

this into account, χ_θ, can be estimated directly using Eq. 1.5 after subtracting the instrument noise spectra ($S_n(k)$) by:

$$\chi_\theta = 6D_T \int_l^u (S_{obs} - S_n)\, dk \tag{1.6}$$

where l and u are the lower and upper cutoff limits, respectively, of the resolved spectra. Figures 1.1a,b show examples of the sensibility of the theoretical spectra, $S_B(k)$, to ε and χ_θ. This is accompanied by an example of Batchelor fitting through maximum likelihood method (Ruddick et al., 2000) for a section of a measured microstructure profile (Figure 1.1c).
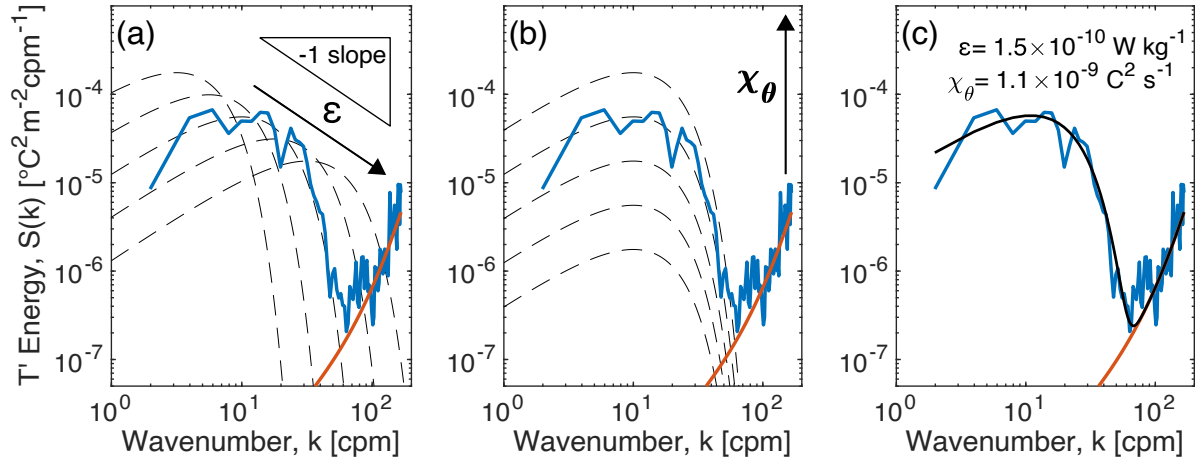
Figure 1.1 – Batchelor spectra fitting. (a) Theoretical temperature gradient spectra for $\varepsilon = 10^{-11} - 10^{-6}$ [W kg^{-1}], with $\chi_\theta = 10^{-10}$ [°C^2 s^{-1}] (dashed lines), (b) Theoretical temperature gradient spectra for $\chi_\theta = 10^{-11} - 10^{-9}$ [C^2 s^{-1}], with $\varepsilon = 10^{-9}$ [W kg^{-1}] (dashed lines). (c) Temperature gradient spectra (blue line) and its respective noise spectra (red line) of a ~1.2 m thick mixed layer, measured in Lake Cadagno on 19 August 2016 using a Rockland Scientific VMP-500 microstructure profiler (data also shown in (a) and (b)). The black line in (c) is the fitted Bachelor spectra obtained through the maximum likelihood method (Ruddick et al., 2000).

1.4 Research overview and objectives

The main objective of this thesis is to characterize at fine scales the variability of turbulent mixing, and relate these properties to plankton distribution in three lakes of different size and distinct stratification, using temperature microstructure as a main tool.

This thesis was conducted as a part of an interdisciplinary SNF-Sinergia project between Robotics, Aquatic Physics and Phytoplankton Ecology – "A Flexible Underwater Distributed Robotic System for High-Resolution Sensing of Aquatic Ecosystems". The project baseline was the innovative implementation of an Autonomous Underwater Vehicle (AUV) – Hydromea Vertex (Schill et al., 2018). Equipped with a water quality payload and a fast thermistor, the vehicle is intended to provide detailed mapping of lateral variability of gradients and patches. Increasing level of hydrodynamic complexity was part of the project design, thus allowing the evaluation of continuous navigational and robotic improvements throughout the project. Although the AUV did not work as expected and turbulence estimations were not achieved, field campaigns followed the initial plan of the project.

The research starts in Lake Cadagno, a quiet system with an unusual highly-concentrated bacterial layer, and then we move to Lower Lake Zurich where a thin layer of cyanobacteria persists for the whole stratified season.

Finally, we study Lake Geneva, a more energetic system where basin-scale processes induce lateral variability.

The following sections cover a brief review of the literature and present the scientific questions for each sub-topic.

1.4.1   Bioconvection in natural waters

The first research subject concerns the convective mixing generated by upward swimming of heavy bacteria in the alpine Lake Cadagno (surface area of 0.26 km^2 and maximal depth of 21 m). Due to subaquatic inflows (Del Don et al., 2001), this lake remains permanently stratified, a phenomenon known as meromixis (Boehrer and Schultze, 2008). In the sulfide-rich and oxygen depleted deep layer (bottom 10 m) of this lake, anaerobic phototrophic and motile bacteria – *Chromatium okenii* – finds ideal living conditions for their main metabolic process of anoxygenic photosynthesis (Schanz et al., 1998).

This biophysical interaction leads to subsurface convectively-driven mixed layers (Sommer et al., 2017), which are smoothed by turbulent diffusion in the adjacent stratified water. To characterize the interplay between convection and turbulent diffusion, and the smoothing time-scale, we studied the shape of mixed layers and compared them to turbulent characteristics obtained from microstructure analysis.

Then, we focused on understanding intriguing measurements of mixed layers during night. Current knowledge strongly suggests that bioconvection in Lake Cadagno is caused by light-driven photosynthesis. However, the smoothing of omnipresent turbulent diffusion would then erode the mixed layers when convection is inactive during nights. Therefore, we sought to elucidate whether bioconvection can maintain the mixed layers during nighttime, purely based on physical measurements.

1.4.2   Seasonal persistence of a cyanobacterial thin layer

The second topic examines the vertical distribution of the cyanobacteria *Planktothrix rubescens* (Codd et al., 2005) that has been encountered in several perialpine lakes (Cuypers et al., 2011; Stöckli, 2012; Garneau et al., 2013). This species is adapted to low light irradiances, is capable of cell-buoyancy-control to modify its vertical location and forms high-concentrated layers in the thermocline (Walsby, 2001). The current frequent observation of cyanobacterial blooms in temperate lakes has been attributed to favorable conditions given by (i) increased temperatures due to climate change (Paerl and Paul, 2012) and (ii) the decrease of phosphorus due to reoligotrophication (Posch et al., 2012).

Here we study the layer of *P. rubescens* forming in Lower Lake Zurich (Posch et al., 2012; Garneau et al., 2013) a perialpine lake that usually mixes completely only once per year (Schmid and Köster, 2016). To elucidate the role of turbulent mixing in the maintenance of the *P. rubescens* layer, we performed the first water column turbulence characterization of this lake. Ultimately, we use these measurements to explore whether *P. rubescens* take advantage of stratification to persist throughout the stratified season (May-October).

1.4.3   Large-scale lateral variability of small-scale structures: Effects on phytoplankton patches.

The third subject aims to study the effects of lateral variability induced by large scale dynamics on algae heterogeneity. We performed this study in Lake Geneva, the largest natural freshwater body of western Europe. This lake is qualified as warm-monomictic with complete winter mixing rarely occurring (Schwefel et al., 2016).

Hosting a complex phytoplankton diversity (Anneville et al., 2002), the actual chlorophyll-a concentration has a typical maximum in the range of 1 to 20 μg L^{-1} (Nouchi et al., 2018). Because of its size (582 km^2 of surface), earth rotation affect the baroclinic response of the lake, inducing basin-scale internal waves (Bouffard and Lemmin, 2013) and gyres (Baracchini et al., 2020). The stirring resulting from this processes is expected to induce mixing hot-spots and to actively modify the spatial distribution of algae, forming patches. We explore the connection between lateral variability of physical properties, namely turbulence, and the distribution of chlorophyll-a in Lake Geneva using an underwater glider equipped with a turbulence package.

1.5 Dissertation roadmap

The core of this dissertation comprises four self-contained research chapters (2 to 5). I played the main role in the design of the field studies and performed the measurements of almost the entire data-set presented in this dissertation. Under the guidance of my supervisors, I conducted the analyses and drafted all parts myself, except for Chapter 4. The formal analysis and writing of Chapter 4 was performed by Bieito Fernández-Castro. However, I led the design of the research and contributed to all stages of fieldwork and data analysis. The thesis is structured as follows:

- **Chapter 2** *Convection-diffusion competition within mixed layers of stratified natural waters* – We characterize the effect of background turbulence on convectively-driven mixed layers for the case of bioconvection in Lake Cadagno. Combining bulk and microstructure analyses, we propose a Péclet number type scaling that relates mixed layer shapes to the opposing effects of convection and turbulent diffusion. Furthermore, we show that applying such a scaling yields turbulence estimates in good agreement with other cases of mixed layer-forming convection in natural waters.

- **Chapter 3** *Persistence of bioconvection-induced mixed layers in a stratified lake* – We examine the temporal diel development of bioconvection in Lake Cadagno. This process is characterized in-situ by traditional and microstructure measurements revealing intriguingly persistent mixed layers during nighttime within the bacteria-populated waters. Based on physical analyses of our measurements we examine whether nocturnal bacterial migration activity sustains this observed stratification feature.

- **Chapter 4** *Inhibited vertical mixing and seasonal persistence of a cyanobacterial thin layer in a stratified lake* – In this chapter, we examine the persistence of the *Planktothrix rubescens* thin layer that forms in the thermocline of Lake Zurich every stratified season. With a series of small-scale turbulence measurements, we show that this unusual persistence is explained by extremely weak turbulence. We also provide strong evidence that the breakdown of the *P. rubescens* layer is driven by nighttime convective deepening of the surface mixed-layer as the lake cools in fall.

- **Chapter 5** *Towards the assessment of lateral variability in lakes: Turbulent mixing from an underwater glider in Lake Geneva* – We study a large and more energetic system, where basin-scale processes induce lateral variability, promoting the formation of more complex algae patches. To accomplish this, we use an underwater glider equipped with a turbulence package. The main effort of this chapter focused on the interpretation and validation of challenging microstructure data obtained with the novel glider platform. We explore spatio-temporal heterogeneity in the distribution of algae using fluorescence measurements collected during a set of repeated cross-shore and along-shore transects.

- **Chapter 6** *Conclusions and Outlook* – provides a summary containing the main findings of the previous chapters and offers an outlook on possible future research based on open questions emanating from this dissertation.

2 Convection-diffusion competition within mixed layers of stratified natural waters

Oscar Sepúlveda Steiner[1]**, Damien Bouffard**[2]**, and Alfred Wüest**[1,2]

[1]Physics of Aquatic Systems Laboratory, Margaretha Kamprad Chair, Institute of Environmental Engineering, École Polytechnique Fédérale de Lausanne, Lausanne, Switzerland.

[2]Department of Surface Waters – Research and Management, Eawag, Swiss Federal Institute of Aquatic Science and Technology, Kastanienbaum, Switzerland.

Abstract

In stratified natural waters, convective processes tend to form nearly homogeneous mixed layers. However, shear-driven turbulence generated by large-scale background flow often rapidly smooths them through mixing with the stratified surroundings. Here we studied the effect of background turbulence on convectively-driven mixed layers for the case of bioconvection in Lake Cadagno, Switzerland. Along with microstructure measurements, a diffusive-shape model for the mixed layers allowed us to define (i) mixed layer thickness and (ii) diffusive transition length. Further microstructure analysis was performed allowing estimation of convective turbulence in the mixed layer and shear driven turbulence quantified by eddy diffusion in their surroundings. Based upon these results we propose a Péclet number scaling that relates mixed layer shape to the opposing effects of convection and diffusion. We further validate this quantitative approach by applying it to two other distinct convective systems representative of double-diffusive convection and radiatively driven under-ice convection.

Plain language summary

In natural waters with density stratification, convection and diffusion are generated by different mechanisms and induce different mixing effects. Convection is driven by local instabilities in the density profile, whereas enhanced diffusion is due to turbulence generated by large-scale circulation. These processes can occur simultaneously in the case of convectively driven mixed layers, which are smoothed by turbulent diffusion. Mixed layers can also be created by a specific bio-physical interaction: bioconvection. A community of motile and heavy bacteria that accumulate at a specific depth in Lake Cadagno, Switzerland, drive bioconvection and are able to create homogeneous layers of up to 1 m thickness. Using a combination of high-resolution temperature measurements along with a mixed layer model, we propose an empirical relation between this layer shape and the different mixing effects from convection and diffusion. We also relate mixed layer shape to turbulence estimates for other types of convection in natural waters.

2.1 Introduction

Convective turbulence and eddy diffusion are key concepts for quantifying mixing in natural waters. Both processes often occur simultaneously; however, separating their contribution to mixing in stratified systems remains a challenge. Interactions of these processes can augment or limit mixing. Shear-induced bottom boundary convection (Lorke et al., 2005; Moum et al., 2004) provides an example of positive feedback. In this case, large-scale currents interact with a sloping bathymetry to generate shear instabilities which drive convection and mix bottom layers. The limiting effect occurs, for example, in the classic case of cooling-induced surface convection (Imberger, 1985; Shay and Gregg, 1986). This interaction consists of a surface mixed layer formed during nighttime cooling which has to overcome smoothing effects of wind-driven entrainment and can be characterized by the Monin-Obukhov length (Lombardo and Gregg, 1989; Tedford et al., 2014). In the present study, we focus on the limiting effect and refer to it as competition.

In lakes, where background turbulence is weaker than that observed in the ocean (Wüest et al., 2000), a variety of convective processes can develop within different, stably stratified sections of the water column (Bouffard and Wüest, 2019). These can induce formation of almost homogeneous mixed layers (hereafter referred to as MLs). Typical examples include double-diffusive convection (Huppert and Turner, 1972; Sommer et al., 2013a), radiatively driven under-ice convection (Bouffard et al., 2016; Kirillin et al., 2012; Yang et al., 2017), thermobaric convection (Crawford and Collier, 1997; Schmid et al., 2008) and bioconvection (Sommer et al., 2017). Yet, large-scale flows of surrounding stratified waters generate shear-induced turbulence (Bouffard et al., 2012; Saggio and Imberger, 2001) usually quantified by eddy diffusion, which can smooth out those MLs (Figure S2.1 in the Supporting Information). A better understanding of convection and turbulent diffusion interaction can help elucidate the role of background turbulence in the maintenance of convective MLs.

We investigated bioconvective MLs to this end. Bioconvection is a process in which dense and motile organisms change the density of their fluid environment triggering hydrodynamic instabilities. Initially observed in laboratory experiments, this phenomenon was recently detected in natural waters by Sommer et al. (2017) who describe a high concentration of dense and motile bacteria inducing formation of MLs in Lake Cadagno, Switzerland (Figure 2.1). The bioconvective MLs of Lake Cadagno are an exemplary case for studying convection-diffusion competition because wind-induced shearing is weak in the interior (Figure S2.2). This enables the bacteria to develop well-defined and persistent MLs (Figures 2.1b and S2.2a, respectively).

In this paper, we analyzed vertical profiles of bacteria-induced convective MLs from six field campaigns conducted on Lake Cadagno. The analysis used microstructure measurements of the water column complemented with a diffusive-shape model that characterizes the effect of background turbulence on the MLs. This
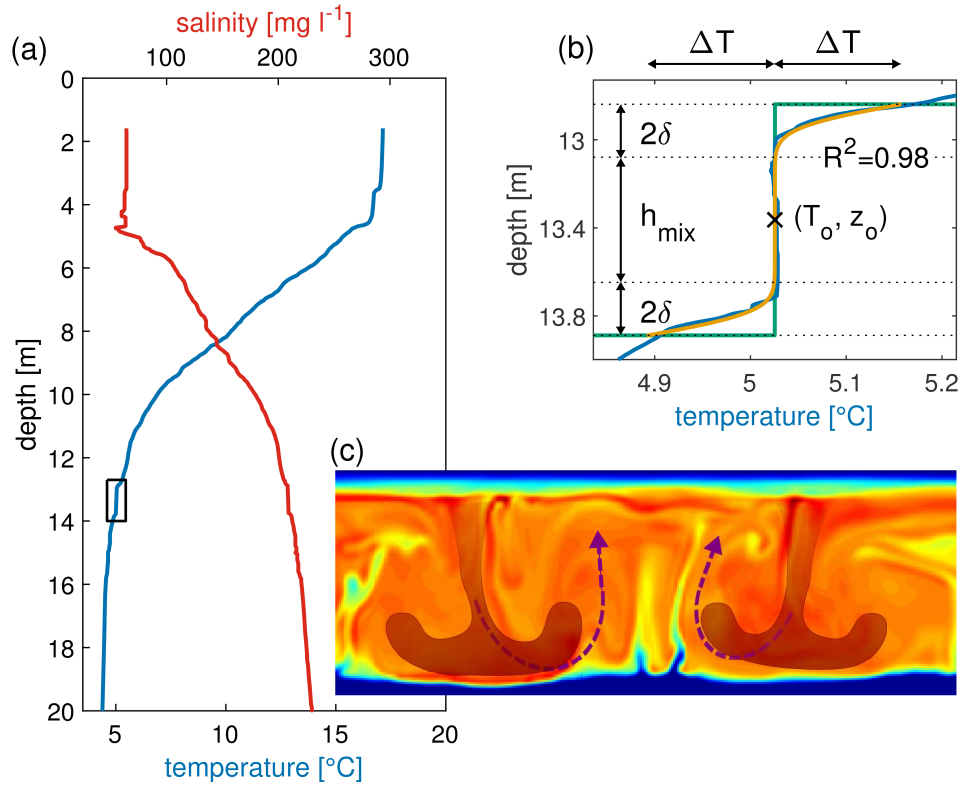
Figure 2.1 – Water column profile and ML structure of Lake Cadagno. (a) Temperature (blue) and salinity (red) profiles measured on 12 July 2017 at 15:30. (b) Enlargement of the black box region in (a) showing the ML temperature profile (blue) with its respective fitting of the ML model (orange), initial step-like ML (green) and the definition of h_{mix} and δ interpreted in this study. R^2 is the coefficient of determination indicating goodness of fit. (c) Snapshot of bacteria-driven convective plumes that generate MLs in Lake Cadagno. Color map corresponds to relative bacteria concentration [-] resulting from Direct Numerical Simulations (DNS; courtesy of George Constantinescu and Tobias Sommer).

approach allows us to relate ML profile shapes to eddy diffusion acting against convective mixing by using a Péclet number scaling. These findings can be generalized by applying the scaling to MLs resulting from double-diffusive and under-ice convection in natural water environments.

2.2 Measurements and methods

2.2.1 Study site and field campaigns

This study was conducted on the alpine meromictic Lake Cadagno (46° 33' 3.13" N, 8° 42' 41.51" E, 1920 m asl, max. depth of 21 m and surface area of 0.26 km^2). Lake Cadagno is permanently stratified exhibiting an oxygen-rich upper layer (top 10 m) and an anoxic and sulfide-rich deep-water layer (deepest 10 m). During summer, the phototrophic, heavy and motile bacteria Chromatium okenii find ideal conditions for their metabolism at the oxic-anoxic transition zone (Schanz et al., 1998), where they accumulate at high concentrations. The oxycline limits their vertical extent, as anoxic conditions are necessary to perform anoxygenic photosynthesis, their main metabolic process. Upward migration of these heavy bacteria (density ~1150 kg m^{-3}) leads to an upward density flux, which in turn causes density instability of the fluid and initiation of convective mixing.

11

This process forms MLs of temperature and salinity (Figure 2.1).

To resolve the vertical shape and estimate turbulent parameters for the MLs, we measured temperature and conductivity at high resolution with a VMP-500 (Rockland Scientific International, Canada) free-falling vertical microstructure profiler. The profiler is equipped with two fast FP07 thermistors and two fast SBE-7 conductivity microsensors mounted at the nose of the instrument sampling at frequencies of 512 Hz. The sinking speed of the profiler was set between 0.10 - 0.20 m s^{-1}. Sommer et al. (2013b) provides detailed description of the VMP-500 and its sensors. Continuous measurements (from 8 to 48 h duration with intervals of 20 to 30 min between profiles) were performed during the summers of 2016, 2017 and 2018 (Table 2.1).

Table 2.1 – Characteristics of observed convective MLs in Lake Cadagno for each of the six field campaigns.

Parameter	Units	July 2016[a]	August 2016	July 2017	August 2017a	August 2017b	August 2018
Thickness of mixed layer (h_{mix})[b]	m	0.83 ± 0.28 (26)	0.75 ± 0.35 (38)	0.67 ± 0.30 (63)	0.66 ± 0.34 (85)	0.37 ± 0.11 (24)	0.50 ± 0.22 (136)
Diffusive length (δ)[b]	m	0.09 ± 0.05 (26)	0.06 ± 0.04 (38)	0.17 ± 0.11 (63)	0.15 ± 0.09 (85)	0.14 ± 0.05 (24)	0.18 ± 0.09 (136)
Background stability (N_B^2)[b]	10^{-5} s^{-2}	10.1 ± 1.8 (26)	11.6 ± 1.9 (38)	16.2 ± 4.0 (63)	11.5 ± 2.6 (85)	12.3 ± 2.5 (24)	7.9 ± 1.5 (136)
Mixed layer dissipation rate (ε_{ML})[c]	10^{-10} W kg^{-1}	4.5 ⟨1.9⟩ (26)	4.1 ⟨1.2⟩ (38)	14.5 ⟨3.9⟩ (61)	10.6 ⟨2.7⟩ (85)	3.1 ⟨1.9⟩ (24)	4.3 ⟨2.7⟩ (130)
Background dissipation rate (ε_B)[c]	10^{-10} W kg^{-1}	5.7 ⟨1.1⟩ (26)	29.6 ⟨3.1⟩ (38)	34.1 ⟨3.0⟩ (63)	24.9 ⟨2.0⟩ (85)	8.6 ⟨1.0⟩ (24)	17.5 ⟨2.2⟩ (136)
Background diffusivity (K_B)[c]	10^{-6} m^2 s^{-1}	1.0 ⟨0.8⟩ (26)	3.4 ⟨2.1⟩ (38)	3.4 ⟨2.5⟩ (63)	3.4 ⟨1.6⟩ (85)	1.2 ⟨0.7⟩ (24)	2.8 ⟨1.3⟩ (136)
Convective plume velocity (w_*)[b]	10^{-3} m s^{-1}	0.49 ± 0.40 (26)	0.48 ± 0.25 (38)	0.55 ± 0.59 (61)	0.56 ± 0.50 (85)	0.33 ± 0.25 (24)	0.37 ± 0.25 (130)

[a]Data from this field campaign was also presented in Sommer et al. (2017). Although the analysis is similar, the results are independent and according to the methods presented herein.

[b]Results are reported as arithmetic mean ± standard deviation and the number of samples in parentheses.

[c]Statistics of the rate of dissipation and diffusivity are reported following Baker and Gibson (1987) given by the mle-mean for a lognormal distribution accompanied by its intermittency factor (σ_{mle}^2) inside pointy brackets and the number of samples in parentheses.

2.2.2 Diffusive-shape mixed layer model

A model was developed to interpret measured ML temperature profiles. The specific objectives of the model were to (i) properly define ML thickness (h_{mix}) and (ii) define the extent of the upper and lower ML boundaries affected by the vertical diffusivity which generates a smooth transition to background stratification (2δ in Figure 2.1b). The mixed layer model (Φ_T) is derived from the 1D vertical diffusion equation given a step function (i.e. fully convective ML) with height h and temperature T_o as initial conditions (green line in Figure 2.1b). The equation is subject to Dirichlet boundary conditions at the top (T_{top}) and bottom (T_{bottom}) of the domain. An analytical solution can be derived by applying the superposition method to recover the boundary conditions. In this paper, we focus on symmetric MLs, whereas the non-symmetric case is presented in Text S2.1 and Figure S2.3 (Supporting Information). Given a symmetric temperature step function ($\Delta T = T_o - T_{bottom} = -T_o + T_{top}$) and limited time-scales (with respect to the diffusive time-scale), the solution is expressed as:

$$\Phi_T = \Delta T \left[\operatorname{erf}\left(\frac{\frac{h}{2} - (z - z_o)}{\delta} \right) - \operatorname{erf}\left(\frac{\frac{h}{2} + (z - z_o)}{\delta} \right) \right] + T_o \qquad (2.1)$$

where z is positive downwards and x_o is the center of the ML position, $\delta = \sqrt{4K\tau}$ is the diffusive length with K expressing diffusivity and τ the diffusive time-scale ($\tau = \delta^2/4K$). Consequently, τ is the elapsed time since complete homogenization of the ML (step-like function) and the measured temperature profile. The ML thickness h_{mix} is then given by:

$$h_{mix} = h - 4\delta \qquad (2.2)$$

Fitting the measured profiles to Φ_T provides information about the background diffusivity affecting the ML shape at the time of measurement. Lower δ values relate to high convective activity relative to diffusivity whereas higher δ values suggests weak convection relative to background turbulence.

Finally, including a ML slope (G_T) improves the goodness of fit for cases exhibiting enhanced turbulence within h_{mix}. For well-defined MLs, G_T reaches values close to zero, without affecting the procedure. The final ML model reads:

$$\Phi_T = \Delta T \left[\mathrm{erf}\left(\frac{\frac{h}{2} - (z - z_o)}{\delta} \right) - \mathrm{erf}\left(\frac{\frac{h}{2} + (z - z_o)}{\delta} \right) \right] + T_o - G_T(z - z_o) \qquad (2.3)$$

2.2.3 Data analysis

Physicochemical characteristics and water column stability – Temperature and conductivity microstructure values were adjusted against CTD data obtained from Sea-Bird SBE-3F and SBE-4C sensors (sampled at 64 Hz) installed on the VMP-500. We use the water ionic composition of Lake Cadagno (Uhde, 1992) to calculate salinity and density from the CTD-adjusted corrected temperature and conductivity microstructure profiles. This density estimate corresponds to the density of water without bacteria. Finally, $N^2 = \frac{g}{\rho_o} \frac{\partial \rho}{\partial z}$ accounts for the stability of the water column, where $g = 9.81$ m s^{-2} and $\rho_o = 1000$ kg m^{-3}. N^2 is obtained in vertical segments of interest by linear fitting of the density $\rho(z)$ profiles over those segments.

Mixed layer model fitting – A bounded nonlinear method was used to fit the CTD-adjusted temperature microstructure profiles and obtain the ML model (Φ_T) parameters. This approach allows h_{mix} and δ estimates characterizing the convective ML and diffusive region, respectively, for each profile collected on the six field campaigns (Table 2.1). Further details on initial values and boundary conditions for the fitting method are provided in Table S2.1. After fitting, only Φ_T with a $R^2 > 0.75$ and a ML thickness $h_{mix} > 0.2$ m were considered for further analysis.

Dissipation rate estimates – We used temperature microstructure profiles to estimate rates of turbulent kinetic energy dissipation ε (W kg^{-1}) by adjusting the theoretical Batchelor (1959) spectrum to measured spectra of temperature gradients. This procedure used the maximum likelihood spectral fitting method (Ruddick et al., 2000) complemented with the Steinbuck et al. (2009) correction to calculate the smoothing rate of temperature variance χ_θ (^{o}C^2 s^{-1}).

Dissipation in the ML (ε_{ML}) was estimated by applying the method to the microstructure segment defined by h_{mix} resulting from Φ_T curve fitting. The section was divided into three sub-segments with 50% overlap. Temperature gradient spectra of these segments were calculated, averaged and then treated with the Batchelor fitting to estimate (ε_{ML}). Background dissipation (ε_B) was estimated in a similar way from segments of 1.5 m above and below h_{mix}, which were also divided into three sub-segments with 50% overlap. A sensitivity analysis justifying the choice of 1.5 m segment lengths is presented in Figure S2.4.

Buoyancy flux and convective quantities – Buoyancy flux (J_b) represents a key parameter for characterizing convective MLs. To estimate J_b, we use bioconvection DNS results reported by Sommer et al. (2017). These showed that for a constant upward bacterial migration speed and background stratification, the modeled ML reached a steady-state with a ratio between dissipated (ε) and bacteria-produced (R) energies of $\varepsilon/R = 0.45$. These parameters give a bioconvective mixing efficiency of $\eta_{bC} = 0.55$. In this study, the buoyancy flux in the ML is then calculated as:

$$J_b^{ML} = \eta_{bC}\varepsilon_{ML} \tag{2.4}$$

Subsequently, the vertical convective velocity (w_*) can be characterized by:

$$w_* = (J_b^{ML}\hbar)^{1/3} \tag{2.5}$$

where $\hbar$ is a convective length scale. In this study we considered two independent estimates of $\hbar$: (i) $\hbar = h_{mix}$ obtained from the ML model fitting and (ii) $\hbar \approx L_T$ with L_T defined as the Thorpe scale of overturns (Thorpe, 1977) within h_{mix}. L_T is calculated using temperature microstructure data only (Dillon, 1982). The purpose of the second estimate is to further validate results obtained using bulk estimations (i.e. the ML model) by means of instantaneous microstructure properties.

Mixing and transport – The influence of diapycnal mixing on the ML background (B) is accounted for by turbulent diffusivity following the Osborn (1980) model:

$$K_B = \Gamma\frac{\varepsilon_B}{N_B^2} \tag{2.6}$$

where ε_B is the background dissipation rate and N_B^2 is the background stability. N_B^2 is obtained from linear fitting over 1.5 m long segments above and below the ML. Here we use a diapycnal mixing coefficient of $\Gamma = 0.15$, which is well-suited for small to medium size lakes (Wüest et al., 2000).

Given the two transport processes involved in our ML analysis, the following Péclet number:

$$Pe = \frac{w_*\hbar}{K_B} \tag{2.7}$$

can be defined to compare the intensity of convection in the ML with background turbulent diffusion. Finally, to characterize the background energy regime, we use the buoyancy Reynolds number (Gibson, 1980):

$$Re_b = \frac{\varepsilon_B}{\nu N_B^2} \tag{2.8}$$

with $\nu = 1.5 \times 10^{-6}$ m^2 s^{-1} (water temperature ~5 ^{o}C; Figure 2.1). Re_b defines three energy regimes (Ivey et al., 2008): molecular ($Re_b < 7$), transitional ($7 < Re_b < 100$) and turbulent ($Re_b > 100$).

2.3 Results

2.3.1 Mixed layer model fitting

We acquired 336 VMP-500 profiles during six field campaigns (Table 2.1). Each profile reports duplicates of microstructure measurements (two FP07 sensors) for a total of 672 temperature profiles. Of these, 372 profiles (55.4%) passed the Φ_T fitting test with $R^2 > 0.75$ and $h_{mix} > 0.2$ m and 39% (145 profiles) were measured during nighttime. Field campaigns thus detected numerous well-defined MLs and revealed their persistent presence during the entire day-night cycle.

Figure 2.2a summarizes ML model fitting results. Arithmetic means were 0.15 ± 0.09 m for δ and 0.61 ± 0.30 m for h_{mix}. Table 2.1 lists details of δ and h_{mix} for each of the six field campaigns. The July 2017 and August 2017a field campaigns were representative of the average values obtained for the entire dataset.

2.3.2 Turbulent quantities

Distributions of ML (ε_{ML}) and background (ε_B) dissipation rates (Figure 2.2b) appear lognormal. However, both are negatively skewed, presenting extreme values for $\varepsilon > 10^{-8}$ W kg^{-1}. Moreover, the kurtosis of the log-data is larger than the expected value of 3 (4.8 and 4.3 for ε_{ML} and ε_B, respectively). To reduce the weight of extreme values, the maximum likelihood estimator (mle) of a lognormal distribution was used to estimate means accompanied by their respective intermittency factor $\langle \sigma_{mle}^2 \rangle$ (Baker and Gibson, 1987). This approach gives an ε_{ML} mle-mean of 6.7×10^{-10} W kg^{-1} $\langle 2.7 \rangle$ and an ε_B mle-mean of 2.0×10^{-9} W kg^{-1} $\langle 2.3 \rangle$, indicating a generally weak turbulent regime with slightly more energetic turbulence outside the MLs.

The background diffusivity (K_B) distribution (not shown) also appears log-normal (log-data kurtosis of 5.0), with a resulting mle-mean of 2.8×10^{-6} m^2 s^{-1} $\langle 1.6 \rangle$. This value is in good agreement with the vertical diffusivity $K_{W94} = 1.6 \times 10^{-6}$ m^2 s^{-1}, which resulted from a tracer release experiment at the same depth in Lake Cadagno (Wüest, 1994).

Analysis of Thorpe scales of overturns showed an arithmetic mean of 0.14 ± 0.13 m. Moreover when compared to h_{mix} (Figure 2.2c), the data follows a linear trend $L_T = 0.29 h_{mix} - 0.02$ ($R^2 = 0.46$; slope 95% confidence interval of ± 0.03). This result depicts a relation close to $h_{mix} \cong 3 L_T$, which has also been reported for MLs formed by triple-diffusion convection (Sánchez and Roget, 2007). For further analysis we thus consider $\hbar = 3 L_T$. Considering fully-developed MLs from bioconvection DNS (Sommer et al. (2017); Figure 2.1c), and applying the ML model fitting along the whole lateral domain (>500 profiles) yields $L_T = 0.20 \pm 0.01$ m and $L_T h_{mix}^{-1} = 0.43 \pm 0.02$.

2.3.3 Convection-diffusion competition

A twofold comparison of the δh_{mix}^{-1} ratio versus the Péclet number (Pe; Figure 2.2d-f) depicts opposing effects of convection and diffusion. High Pe values and low δh_{mix}^{-1} values generally indicate that background diffusivity does not significantly influence convective MLs. Low Pe values and δh_{mix}^{-1} values on the other hand denote MLs subject to the smoothing effect of background diffusivity.

The dataset also reveals more specific aspects of the interaction between convection and diffusion. Considering $\hbar = h_{mix}$, cases in which convection occurred almost without the influence of background diffusivity were characterized by $Pe > 10^3$ (Figure 2.2d). Moreover, all these cases occur in a background molecular regime and with a δh_{mix}^{-1} ratio less than 0.50. Diffusivity-influenced MLs (i.e. $\delta h_{mix}^{-1} > 0.50$) were encountered throughout
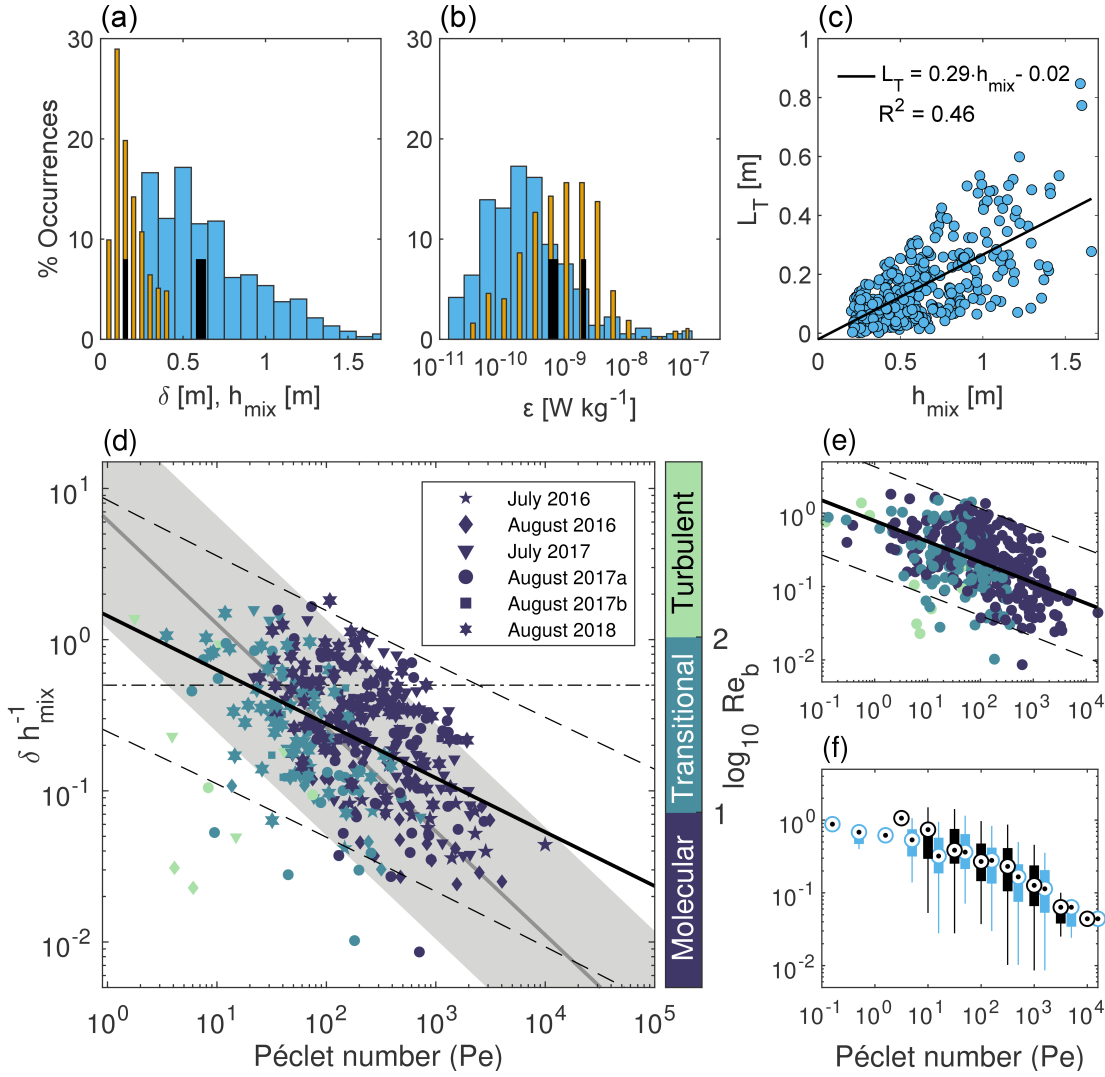
Figure 2.2 – Distribution of ML model fitting and microstructure analysis results accompanied with a comparison of convection and diffusion. (a) Histograms of mixed layer thickness (h_{mix}; blue) and diffusive length (δ; orange). Thick and thin black bars represent arithmetic means for h_{mix} and δ, respectively. (b) Histogram of dissipation rates of turbulent kinetic energy in the MLs (ε_{ML}; blue) and background (ε_B; orange). Thick and thin black bars represent mle-means for ε_{ML} and ε_B, respectively. (c) Comparison of h_{mix} with Thorpe scales (L_T) within the MLs, black line represent best linear fit. (d) Geometrical ratio δh_{mix}^{-1} for convective MLs as a function of h_{mix}-based Péclet number (Pe). The blue to green color bar represents the three different background energy regimes defined by Re_b. For simplicity, we use $Re_b = 10$ as the limit between the molecular and transitional regime. The thick black line is the best fit for molecular and transitional regimes only (thin dashed lines, 95% confidence interval). Gray line and shade represent best fit and 95% confidence interval, respectively, when considering a constant diffusivity (K_{W94}) for the Pe calculation. The horizontal dot-dashed line indicates $h_{mix}^{-1} = 0.5$. (e) Analogous to (d) for L_T-based Pe with $\hbar = 3L_T$. The thick black line and the thin dashed lines represent the best fit and its 95% confidence interval, respectively. (f) Boxplot of h_{mix}^{-1} versus Pe for (d) in black and (e) in light blue. Dotted white circles represent median estimate of δh_{mix}^{-1} for half-decade bins of Pe. Vertical bars and lines represent the 25th and 25th percentiles.

the six campaigns and represent 23% of the dataset. These have Pe values ranging from $10^1 - 10^3$. The majority of profiles that meet the Φ_T fitting criteria develop in molecular-to-transitional energy regimes ($Re_b < 100$). Although 10 profiles show MLs with a turbulent background, these profiles represent only 3% of the dataset. In cases representing molecular and transitional regimes only, the data follow a power-law (black line, Figure 2.2d):

$$\delta h_{mix}^{-1} = Pe^{-0.36} \tag{2.9}$$

that relates the interplay of convection and diffusion to the ML shape. The results from Figure 2.2d show a relatively large degree of scatter within a 95% confidence interval and indicate an uncertainty up to $O(1)$ for Pe. For constant diffusivity (e.g. 1.6×10^{-6} m^2 s^{-1}; Wüest (1994)), the data points are well aligned with a power-law $\delta h_{mix}^{-1} = 6.0 Pe^{-0.68}$ (gray line, Figure 2.2d) and show a smaller spread (gray area, Figure 2.2d). The large scatter when considering varying diffusivities in Figure 2.2d, reflects the intrinsic variability (intermittency) of instantaneous microstructure-based turbulent estimates (Figure 2.2b).

An axis-independent analysis can be performed by using a L_T-based Péclet number (Pe_{L_T}) with $\hbar = 3 L_T$ (Figure 2.2e). This yields a power-law $\delta h_{mix}^{-1} = 0.78 Pe_{L_T}^{-0.28}$, similar to Eq. 2.9. Resemblance of both results is more evident from a boxplot comparison (Figure 2.2f), particularly for Pe in the range of $10^1 - 10^3$.

2.4   Discussion

This study investigated the dynamics of bioconvective MLs in Lake Cadagno, over a period of six field campaigns. The average h_{mix} was 0.61 ± 0.30 m associated with a mean convective-time-scale of $\tau_* \approx 23$ min (where $\tau_* = (h_{mix}^2 / J_b)^{1/3}$). To quantify the interplay between convection and diffusion, we compare the rate of ML smoothing with the convective velocity. Given a background diffusivity of $K_{W94} = 1.6 \times 10^{-6}$ m^2 s^{-1} (in agreement with our average result), the time scale required to smooth out a 1.2 m ($\overline{h} = \overline{h_{mix}} + 4\overline{\delta}$) inactive ML is only 2.5 hrs (i.e. when $h_{mix} = \delta$, hence $\tau = h^2/100K$; Figure S2.1c). This yields a ML smoothing rate of $u_K \approx 0.13$ mm s^{-1}. In comparison, the estimated average convective plume velocity w_* is 0.46 ± 0.37 mm s^{-1}. Observed conditions of $w_* > u_K$ explain the maintenance of the convective ML. Moreover, it demonstrates that convection generated by bacteria should be quasi-continuous or else diffusion would smooth out the MLs within ~2.5 hrs. This implies that, although present photoautotrophic bacteria rely on sunlight, they need to remain actively moving also during nights, which last much longer than 2.5 hrs. Although less intense during night, dissipation is still not negligible ($\varepsilon_{ML}^{night} = 4.0 \times 10^{-10}$ W kg^{-1} ⟨2.8⟩; $\varepsilon_{ML}^{night}/\varepsilon_{ML}^{day} \approx 0.5$), which supports a quasi-continuous bacterial swimming activity.

Whether measured MLs exhibit instantaneous active convection cannot be assessed with the Φ_T shape model. To maintain a homogeneous ML, convective mixing has to overcome the smoothing effects of background diffusivity, i.e. $J_b^{ML} \geq J_b^B$. Using microstructure measurements, we further estimated the background buoyancy flux as $J = KN_B^2$. A χ_θ-based buoyancy flux (Monismith et al., 2018) yields the following condition:

$$J_b^{ML} = \eta_{bC} \varepsilon_{ML} \geq \frac{\chi_\theta}{2 \left(\frac{\partial T}{\partial T} \right)^2} N_B^2 = J_b^B \tag{2.10}$$

where the background χ_θ is obtained from the Batchelor fitting procedure (together with ε_B) and $\frac{\partial T}{\partial z}$ is the background temperature gradient. J_b^B is presented in Figure 2.3a as a function of ε_{ML} and compared with the relation $J_b^{ML} = 0.55 \varepsilon_{ML}$ (black line; Eq. 2.4). This comparison shows that 49% of the observed MLs do not fulfill the activity condition imposed by Eq. (2.10). The relation used may be representative of active MLs only, yet
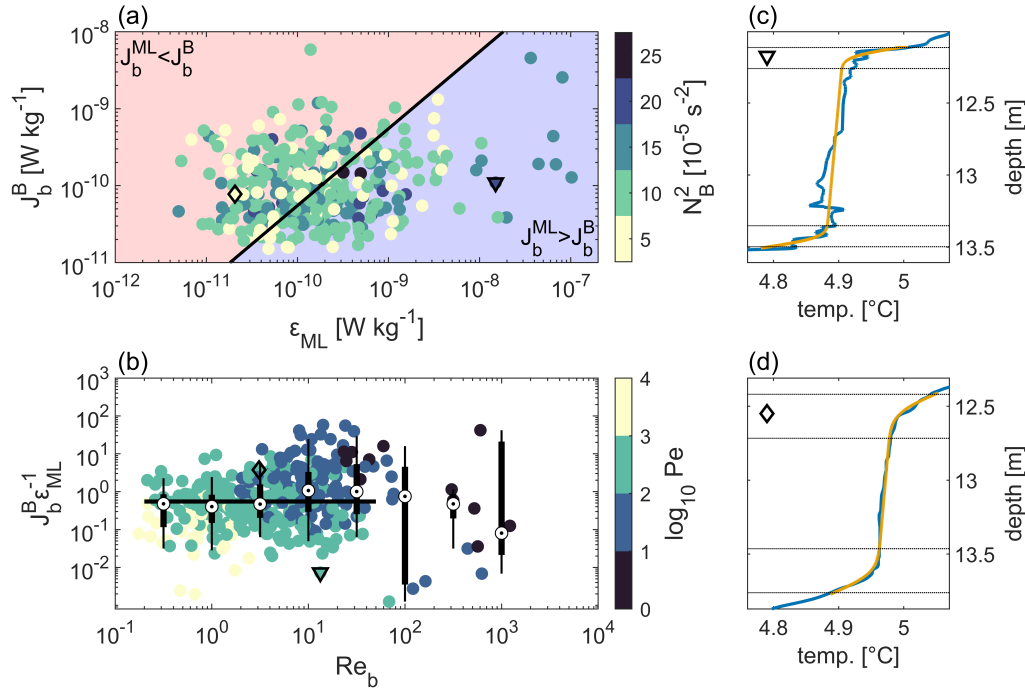
Figure 2.3 – Activity condition for buoyancy fluxes. (a) χ_θ-based background buoyancy flux as a function of ε_{ML}, color-coded according to background stability N_B^2. The thick black line represents the relation $J_b^B = 0.55\varepsilon_{ML}$. (b) $J_b^B\varepsilon_{ML}^{-1}$ as a function of background Re_b, with a Péclet number (Pe) color bar. Dotted white circles represent the median of buoyancy fluxes for half-decade Re_b bins. Black vertical bars and lines represent 75% and 95% confidence intervals for each bin, respectively. The black horizontal line denotes the convective mixing efficiency $\eta_{bC} = 0.55$ used in this study. (c) and (d) Examples of measured MLs (blue) accompanied by its respective Φ_T fitting (yellow). Segments between dotted lines, represent 2δ. These examples are noted in (a) and (b) by the symbols $\triangledown$ and $\diamond$, respectively.

an average mixing efficiency of 0.55 for the range $Re_b < 10$ (Figure 2.3b) represents a realistic approximation. Figures 2.3c and 2.3d show examples that respectively fulfill or violate condition (2.10), depicting different MLs for relatively similar J_b^B conditions. Sharp MLs (Figure 2.3c) could be due to active convection, whereas smooth MLs (Figure 2.3d) to decaying convective turbulence. Therefore, we suggest that cases not fulfilling Eq. 2.10 could be related to reduced bacterial migration.

Convective-diffusive systems and their specific mixing efficiency remain poorly investigated at field-scale in natural waters. Although this study focuses on in-situ characterization of biologically driven MLs, findings presented in Figure 2.3 could also constrain hydrodynamic parameters for modelling (bio)convection.

We characterized the competition between convection and turbulent diffusion using two different approximations. The first consists of estimating bulk ML properties by fitting temperature profiles to a diffusive-shape model. The second is dynamic and microstructure measurements are used to estimate instantaneous dissipations and buoyancy fluxes in the ML and its surroundings. In general, convection dominates; however, the measurements present a non-negligible variability (Figures 2.2d-f and 2.3). This can be explained by an irregular injection of energy to the system (internal waves weakly energized by wind forcing; Figure S2.2), non-constant bacterial migration and the intermittent nature of turbulence. Altogether, the results suggest that dynamic characteristics can be estimated from ML shape properties (and vice versa; Eq. 2.9).

To generalize our results, we investigated whether turbulent estimates can be obtained from varying macroscopic parameters (i.e. δh_{mix}^{-1}) of other systems exhibiting convectively-driven MLs. Using data from double-diffusive staircases in Lake Kivu (Sommer et al., 2013a) and analyzing a microstructure profile with the ML model Φ_T (Eq. 2.3; Figure S2.5) gives $\overline{\delta h_{mix}^{-1}} = 0.08$ (Sommer et al. (2013a) reported $\overline{h_T} = \overline{2\delta} = 0.09$ m, $\overline{H_T} = \overline{h_{mix}} = 0.70$ m to give a $\overline{\delta h_{mix}^{-1}} = 0.07$). Applying equation (2.9) yields $Pe = 3.4 \times 10^3$ and thus $J_b^{Pe} = 3.1 \times 10^{-10}$ W kg^{-1}. Recently, Sommer et al. (2019) reported an average dissipation within the MLs of Lake Kivu of 1.5×10^{-10} W kg^{-1}. The same study considers a mixing efficiency of 0.8 and thus a $J_b = 1.9 \times 10^{-10}$ W kg^{-1}, which is in good agreement with J_b^{Pe}.

We also analyzed data from under-ice convection in Lake Onega (Bouffard et al., 2016, 2019). Mooring measurements during radiative daytime hours in March 2016 (Figure S2.6) indicate a ML with an average $\overline{\delta h_{mix}^{-1}} = 0.08$ ($\overline{\delta} = 0.66$ m and $\overline{h_{mix}} = 8.3$ m). This combines with equation (2.9) to give $Pe = 3.5 \times 10^3$. A known buoyancy flux for under-ice convection, determined from the radiative forcing (Ulloa et al., 2018) allows us to estimate diffusivity using the scaling described here. The average $J_b = 3.6 \times 10^{-10}$ W kg^{-1} (Figure S2.6a; $w_* = 1.4$ mm s^{-1}) thus gives a bulk diffusivity of $K_B^{Pe} = 3.4 \times 10^{-6}$ m^2 s^{-1}. This value coincides with an independent microstructure profiler-based estimate of 1.4×10^{-6} m^2 s^{-1} (measured the same day, Figure S2.6b, c).

Bulk turbulent parameters estimated using the proposed methods show good agreement with independent observations of double-diffusion in Lake Kivu and under-ice convection in Lake Onega. Moreover, the non-symmetric ML model showed good potential for analyzing surface convective MLs in Lake Geneva (Figure S3). Therefore, a data-based Péclet number scaling of convection-diffusion competition could be considered to estimate bulk turbulent parameters of other convective processes, such as cooling-induced surface convection (Shay and Gregg, 1986; Tedford et al., 2014) and thermobaric convection (Crawford and Collier, 1997; Schmid et al., 2008).

2.5 Conclusions

In this study, we focused on the competition between convection and turbulent diffusion in stratified natural waters. The bioconvection observed during six field campaigns in the strongly stratified Lake Cadagno (Switzerland) offers an ideal environment for this analysis with the following conclusions:

1. Dense and heavy motile photoautotrophic bacteria are able to convectively homogenize a meter-scale layer against the omnipresent effect of shear-induced eddy diffusion as typical in stratified lakes. The presented analysis allows comparing the competing effects of convection and turbulent diffusion and thereby allows drawing conclusions on biological activities purely based on physical profile information.

2. Bioconvective mixed layers (MLs), which consistently form in the interior of the strongly stratified water body, were analyzed using a diffusive-shape ML model. This approach allowed us to estimate ML thickness (h_{mix}) as well as the extent of the transition to background stratification influenced by (turbulent) diffusive processes (δ) and thereby to characterize the competition between convection and (turbulent) diffusion.

3. The combined ML shape (h_{mix} and δ) and Péclet number scaling yield bulk estimates of the ML buoyancy flux and background diffusivity. The generalization of this scheme showed good agreement with double-diffusive and under-ice radiatively driven convection in other aquatic systems.

Acknowledgments

Data

Field measurements used in this research are available online:
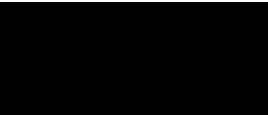https://doi.org/10.5281/zenodo.3507638

References

Baker, M. A. and Gibson, C. H. (1987). Sampling turbulence in the stratified ocean: Statistical consequences of strong intermittency. *Journal of Physical Oceanography*, 17(10):1817–1836. doi:10.1175/1520-0485(1987)017<1817:STITSO>2.0.CO;2.

Batchelor, G. K. (1959). Small-scale variation of convected quantities like temperature in turbulent fluid Part 1. General discussion and the case of small conductivity. *Journal of Fluid Mechanics*, 5(1):113–133. doi:10.1017/S002211205900009X.

Bouffard, D., Boegman, L., and Rao, Y. R. (2012). Poincaré wave–induced mixing in a large lake. *Limnology and Oceanography*, 57(4):1201–1216. doi:10.4319/lo.2012.57.4.1201.

Bouffard, D. and Wüest, A. (2019). Convection in lakes. *Annual Review of Fluid Mechanics*, 51(1):189–215. doi:10.1146/annurev-fluid-010518-040506.

Bouffard, D., Zdorovennov, R. E., Zdorovennova, G. E., Pasche, N., Wüest, A., and Terzhevik, A. Y. (2016). Ice-covered Lake Onega: effects of radiation on convection and internal waves. *Hydrobiologia*, 780(1):21–36. doi:10.1007/s10750-016-2915-3.

Bouffard, D., Zdorovennova, G., Bogdanov, S., Efremova, T., Lavanchy, S., Palshin, N., Terzhevik, A., Vinnå, L. R., Volkov, S., Wüest, A., Zdorovennov, R., and Ulloa, H. N. (2019). Under-ice convection dynamics in a boreal lake. *Inland Waters*, 9(2):142–161. doi:10.1080/20442041.2018.1533356.

Crawford, G. B. and Collier, R. W. (1997). Observations of a deep-mixing event in Crater Lake, Oregon. *Limnology and Oceanography*, 42(2):299–306. doi:10.4319/lo.1997.42.2.0299.

Dillon, T. M. (1982). Vertical overturns: A comparison of Thorpe and Ozmidov length scales. *Journal of Geophysical Research*, 87(C12):9601–9613. doi:10.1029/JC087iC12p09601.

Gibson, C. H. (1980). Fossil temperature, salinity, and vorticity turbulence in the ocean. In J. C. Nihoul, editor, *Marine Turbulence Proceedings of the 11th International Liege Colloquium on Ocean Hydrodynamics, Elsevier Oceanography Series,* pages Vol. 28, pp. 221–257, New York NY. Elsevier/North-Holland Inc.

Huppert, H. E. and Turner, J. S. (1972). Double-diffusive convection and its implications for the temperature and salinity structure of the ocean and Lake Vanda. *Journal of Physical Oceanography*, 2(4):456–461. doi:10.1175/1520-0485(1972)002<0456:DDCAII>2.0.CO;2.

Imberger, J. (1985). The diurnal mixed layer. *Limnology and Oceanography*, 30(4):737–770. doi:10.4319/lo.1985.30.4.0737.

Ivey, G., Winters, K., and Koseff, J. (2008). Density Stratification, Turbulence, but How Much Mixing? *Annual Review of Fluid Mechanics*, 40(1):169–184. doi:10.1146/annurev.fluid.39.050905.110314.

Kirillin, G., Leppäranta, M., Terzhevik, A., Granin, N., Bernhardt, J., Engelhardt, C., Efremova, T., Golosov, S., Palshin, N., Sherstyankin, P, Zdorovennova, G., and Zdorovennov, R. (2012). Physics of seasonally ice-covered lakes: a review. *Aquatic Sciences*, 74(4):659–682. doi:10.1007/s00027-012-0279-y.

Lombardo, C. P. and Gregg, M. C. (1989). Similarity scaling of viscous and thermal dissipation in a convecting surface boundary layer. *Journal of Geophysical Research*, 94(C5):6273–6284. doi:10.1029/JC094iC05p06273.

Lorke, A., Peeters, F., and Wüest, A. (2005). Shear-induced convective mixing in bottom boundary layers on slopes. *Limnology and Oceanography*, 50(5):1612–1619. doi:10.4319/lo.2005.50.5.1612.

Monismith, S. G., Koseff, J. R., and White, B. L. (2018). Mixing efficiency in the presence of stratification: When is it constant? *Geophysical Research Letters*, 45(11):5627–5634. doi:10.1029/2018GL077229.

Moum, J. N., Perlin, A., Klymak, J. M., Levine, M. D., Boyd, T., and Kosro, P. M. (2004). Convectively driven mixing in the bottom boundary layer. *Journal of Physical Oceanography*, 34(10):2189–2202. doi:10.1175/1520-0485(2004)034<2189:CDMITB>2.0.CO;2.

Osborn, T. R. (1980). Estimates of the local rate of vertical diffusion from dissipation measurements. *Journal of Physical Oceanography*, 10(1):83–89. doi:10.1175/1520-0485(1980)010<0083:EOTLRO>2.0.CO;2.

Ruddick, B., Anis, A., and Thompson, K. (2000). Maximum likelihood spectral fitting: The batchelor spectrum. *Journal of Atmospheric and Oceanic Technology*, 17(11):1541–1555. doi:10.1175/1520-0426(2000)017<1541:MLSFTB>2.0.CO;2.

Saggio, A. and Imberger, J. (2001). Mixing and turbulent fluxes in the metalimnion of a stratified lake. *Limnology and Oceanography*, 46(2):392–409. doi:10.4319/lo.2001.46.2.0392.

Sánchez, X. and Roget, E. (2007). Microstructure measurements and heat flux calculations of a triple-diffusive process in a lake within the diffusive layer convection regime. *Journal of Geophysical Research*, 112(C2):C02012. doi:10.1029/2006JC003750.

Schanz, F., Fischer-Romero, C., and Bachofen, R. (1998). Photosynthetic production and photoadaptation of phototrophic sulfur bacteria in Lake Cadagno (Switzerland). *Limnology and Oceanography*, 43(6):1262–1269. doi:10.4319/lo.1998.43.6.1262.

Schmid, M., Budnev, N. M., Granin, N. G., Sturm, M., Schurter, M., and Wüest, A. (2008). Lake Baikal deepwater renewal mystery solved. *Geophysical Research Letters*, 35(9):L09605. doi:10.1029/2008GL033223.

Shay, T. J. and Gregg, M. C. (1986). Convectively driven turbulent mixing in the upper ocean. *Journal of Physical Oceanography*, 16(11):1777–1798. doi:10.1175/1520-0485(1986)016<1777:CDTMIT>2.0.CO;2.

References

Sommer, T., Carpenter, J. R., Schmid, M., Lueck, R. G., Schurter, M., and Wüest, A. (2013a). Interface structure and flux laws in a natural double-diffusive layering. *Journal of Geophysical Research: Oceans*, 118(11):6092–6106. doi:10.1002/2013JC009166.

Sommer, T., Carpenter, J. R., Schmid, M., Lueck, R. G., and Wüest, A. (2013b). Revisiting microstructure sensor responses with implications for double-diffusive fluxes. *Journal of Atmospheric and Oceanic Technology*, 30(8):1907–1923. doi:10.1175/JTECH-D-12-00272.1.

Sommer, T., Danza, F., Berg, J., Sengupta, A., Constantinescu, G., Tokyay, T., Bürgmann, H., Dressler, Y., Sepúlveda Steiner, O., Schubert, C. J., Tonolla, M., and Wüest, A. (2017). Bacteria-induced mixing in natural waters. *Geophysical Research Letters*, 44(18):9424–9432. doi:10.1002/2017GL074868.

Sommer, T., Schmid, M., and Wüest, A. (2019). The role of double diffusion for the heat and salt balance in Lake Kivu. *Limnology and Oceanography*, 64(2):650–660. doi:10.1002/lno.11066.

Steinbuck, J. V., Stacey, M. T., and Monismith, S. G. (2009). An Evaluation of χT estimation techniques: Implications for Batchelor fitting and ϵ. *Journal of Atmospheric and Oceanic Technology*, 26(8):1652–1662. doi:10.1175/2009JTECHO611.1.

Tedford, E. W., MacIntyre, S., Miller, S. D., and Czikowsky, M. J. (2014). Similarity scaling of turbulence in a temperate lake during fall cooling. *Journal of Geophysical Research: Oceans*, 119(8):4689–4713. doi:10.1002/2014JC010135.

Thorpe, S. A. (1977). Turbulence and mixing in a Scottish Loch. *Philosophical Transactions of the Royal Society A: Mathematical, Physical and Engineering Sciences*, 286(1334):125–181. doi:10.1098/rsta.1977.0112.

Uhde, M. (1992). Mischungsprozesse im Hypolimnion des meromiktischen lago Cadagno: Eine Untersuchung mit Hilfe natürlicher und künstlicher Tracer. Master Thesis, University of Freiburg, Germany.

Ulloa, H. N., Wüest, A., and Bouffard, D. (2018). Mechanical energy budget and mixing efficiency for a radiatively heated ice-covered waterbody. *Journal of Fluid Mechanics*, 852:R1. doi:10.1017/jfm.2018.587.

Wüest, A. (1994). Interactions in lakes: Biology as source of dominant physical forces. *Limnologica*, 24(2):93–104.

Wüest, A., Piepke, G., and Van Senden, D. C. (2000). Turbulent kinetic energy balance as a tool for estimating vertical diffusivity in wind-forced stratified waters. *Limnology and Oceanograhy*, 45(6):1388–1400. doi:10.4319/lo.2000.45.6.1388.

Yang, B., Young, J., Brown, L., and Wells, M. (2017). High-frequency observations of temperature and dissolved oxygen reveal under-ice convection in a large lake. *Geophysical Research Letters*, 44(24):12,218–12,226. doi:10.1002/2017GL075373.

Supporting information for Chapter 2
Convection-diffusion competition within mixed layers of stratified natural waters

Oscar Sepúlveda Steiner[1], Damien Bouffard[2], and Alfred Wüest[1,2]

[1]Physics of Aquatic Systems Laboratory, Margaretha Kamprad Chair, Institute of Environmental Engineering, École Polytechnique Fédérale de Lausanne, Lausanne, Switzerland.

[2]Department of Surface Waters – Research and Management, Eawag, Swiss Federal Institute of Aquatic Science and Technology, Kastanienbaum, Switzerland.

Text S2.1

A non-symmetric mixed layer model (Φ'_T) is derived from the 1D vertical diffusion equation given a step function (i.e. fully convective ML) with height h and temperature T_o as initial conditions. For non-symmetric Dirichlet boundary conditions such as:

$$T_1 = T_{up} \tag{S2.1}$$

$$T_2 = T_{down} \tag{S2.2}$$

with a vertical domain $z_1 \leq z \leq z_2$, some assumptions can lead to deduct a solution. Assuming that vertical diffusivity (K) changes in the vertical domain, following:

$$K(z) = \begin{cases} K_1 & z_1 \leq z < z_o \\ K_2 & z_0 \leq z \leq z_2 \end{cases} \tag{S2.3}$$

with $z_o \in [z_1, z_2]$ and considering the regions of the domain affected by K_1 and K_2 relative to z_o, the length of their respective portions of the initial ML h_1 and h_2, can be identified ($h = h_1 + h_2$). Following this and applying the superposition method, a pseudo-analytical solution that recovers the boundary conditions is given by:

$$\Phi'_T(z) = (T_1 - T_o)\left[1 - \mathrm{erf}\left(\frac{h_1 + (z - z_o)}{\delta_1}\right)\right] + (T_2 - T_o)\left[1 - \mathrm{erf}\left(\frac{h_2 - (z - z_o)}{\delta_2}\right)\right] + T_o \tag{S2.4}$$

with δ_1 and δ_2 the diffusive lengths associated to each border of the domain. It must be noted that taking Φ'_T, imposing symmetric boundary conditions, constant K and a profile with negative temperature gradient, yields:

$$\Phi_T = \Delta T\left[\mathrm{erf}\left(\frac{\frac{h}{2} - (z - z_o)}{\delta}\right) - \mathrm{erf}\left(\frac{\frac{h}{2} + (z - z_o)}{\delta}\right)\right] + T_o \tag{S2.5}$$

where $\Delta T = -T_o + T_1 = T_o - T_2$ and $\delta = \delta_1 = \delta_2$, as Eq. 2.1 in the main text. Then, the general (non-symmetric) ratio of ML geometric characteristics reads:

$$\frac{\delta'}{h_{mix}} = \frac{\left(\frac{2\delta_1 2\delta_2}{2\delta_1 + 2\delta_2}\right)}{h_{mix}} \tag{S2.6}$$

If $\delta = \delta_1 = \delta_2$, we recover the symmetric ratio relation:

$$\frac{\delta'}{h_{mix}} = \frac{\left(\frac{2\delta 2\delta}{2\delta + 2\delta}\right)}{h_{mix}} = \frac{\delta}{h_{mix}} \tag{S2.7}$$

For comparison, a numerical solution for this problem was implemented (Figure S2.3a). Results of Φ'_T obtained using the same conditions are presented in Figure S2.3b. Furthermore, a real example of an upward microstructure profile recently measured in Lake Geneva, exhibiting a surface cooling-driven convective mixed layer with its respective Φ'_T fitting, is shown in Figure S2.3d.
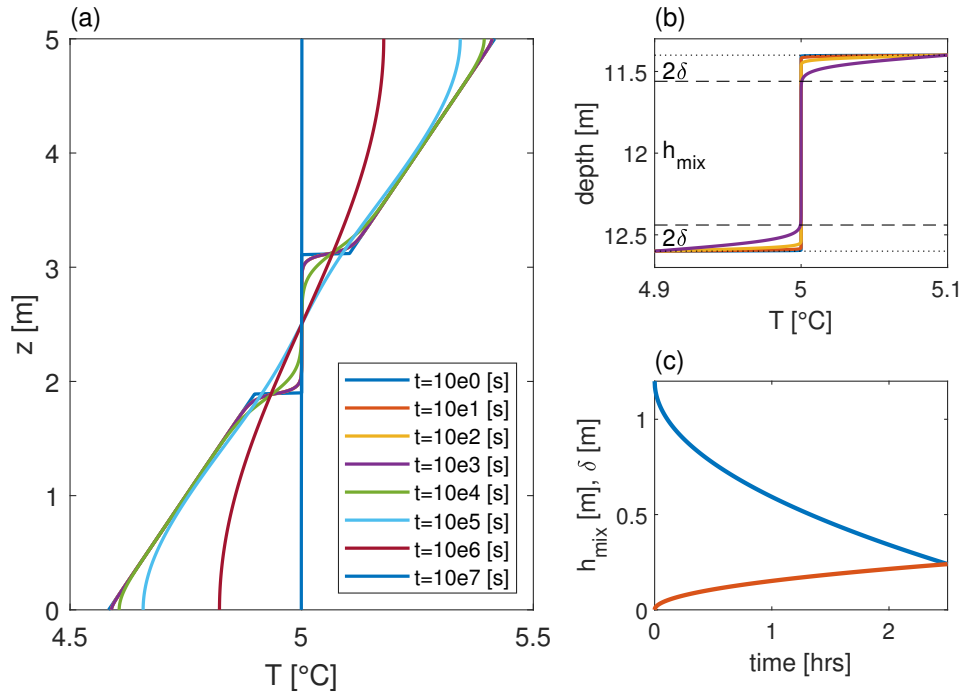
Figure S2.1 – Effect of vertical diffusivity on the mixed layer (ML) and the adjacent water columns. (a) Effect of diffusivity on a stratified water column with an inactive ML (between 2 and 3 m depth) as a function of time. Diffusive effects smoothen the ML. This result corresponds to a numerical solution of the 1D vertical diffusion equation using no-flux (Neumann) boundary conditions. (b) Diffusive-shape ML model as used in this research, valid for short time-scales only. The pseudo-analytical solution is obtained applying the superposition method to the 1D vertical diffusion equation with an initial step-like function and Dirichlet boundary condition. The legend in (a) is also valid for (b). (c) Temporal evolution of the ML with h_{mix} (blue line) and δ (red line) according to the diffusive-shape ML model. All calculations consider an initial mixed layer of 1.2 m thickness and a diffusivity $K_{W94} = 1.6 \times 10^{-6}$ m^2 s^{-1}, obtained from a tracer experiment in Lake Cadagno (Wüest, 1994). Segments defined by horizontal dashed and dotted lines in (b) represent the results of the ML model in terms of h_{mix} and diffusive length-scales (δ) for $t = 15$ min.
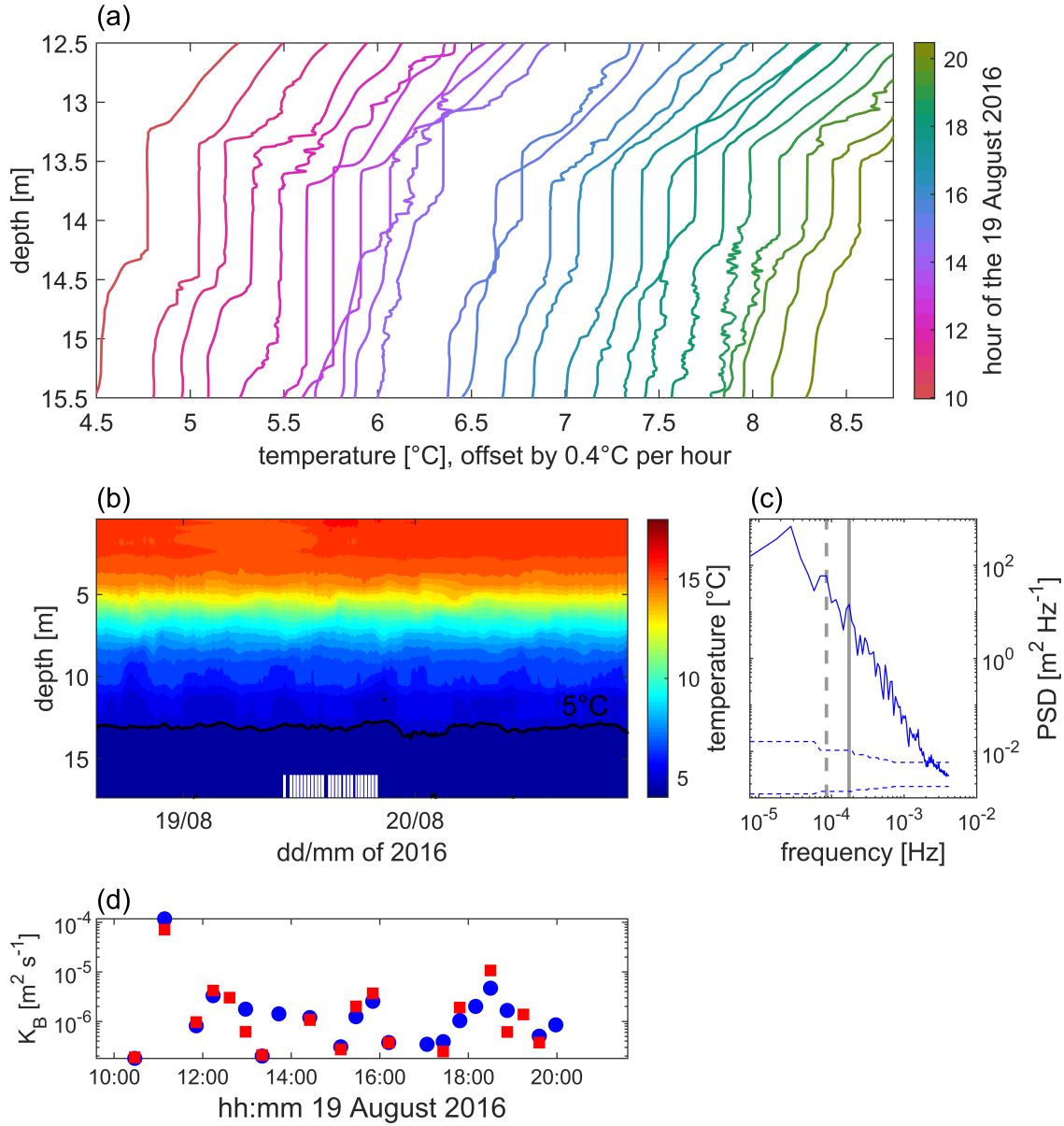
Figure S2.2 – Long lasting mixed layers in Lake Cadagno and hydrodynamic background characteristics. (a) Waterfall plot of 25 temperature microstructure profiles performed with a VMP-500 (Rockland Scientific International, Canada), measured on 19 August 2016. (b) Temperature profile time series measured with a RBRconcerto[3] Tx thermistor string in the middle of the lake. White vertical lines indicate the measuring time of VMP profiles shown in (a). 5 ^oC isothermal is highlighted in black. (c) Power spectral density (PSD) of the 5 ^oC isothermal (blue line). Internal waves corresponding to 3.3 and 1.6 hrs period are highlighted by gray lines (dashed and continues, respectively). Dashed blue lines represent the confidence interval (d) Time evolution of background diffusivity (K_B) during the measurements (i.e. adjacent to the mixed layers). Estimates are obtained from the VMP measurements following the methods exposed in the main text and using the (Osborn, 1980) diapycnal diffusivity model. Blue dots and red squares represent estimates using fast thermistors 1 and 2, respectively.
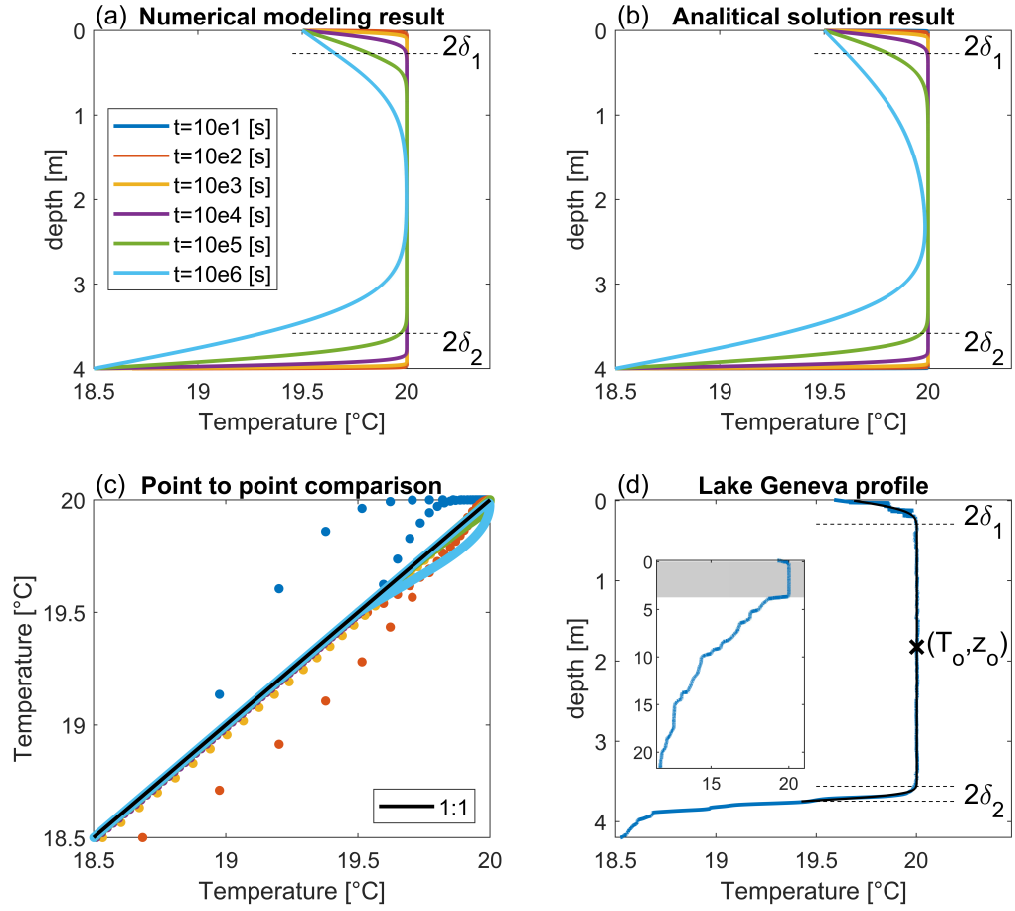
Figure S2.3 – Non-symmetric mixed layer model. (a) Numerical solution considering an initial mixed layer $h = 4$ m and boundary conditions $T_1 = 19.5\ ^oC$, $T_2 = 18.5\ ^oC$, with $K_1 = 5.0 \times 10^{-6}$ m^2 s^{-1} and $K_2 = 1.6 \times 10^{-6}$ m^2 s^{-1}. (b) Analytical solution for the same parameters as in (a). (c) Point to point comparison of numerical and analytical solutions. For time scales relevant to the analysis (minutes to several hours), the analytical and numerical models are in excellent agreement. (d) Upward microstructure profile measured in Lake Geneva on 14 July 2019 at 03:00 am with a Rockland Scientific MicroCTD. The profile exhibits a surface cooling-induced convective mixed layer. The fitting of $\Phi'_T(z)$ yields $h_{mix} = 3.3$ m, $\delta_1 = 0.15$ m and $\delta_2 = 0.09$ m.
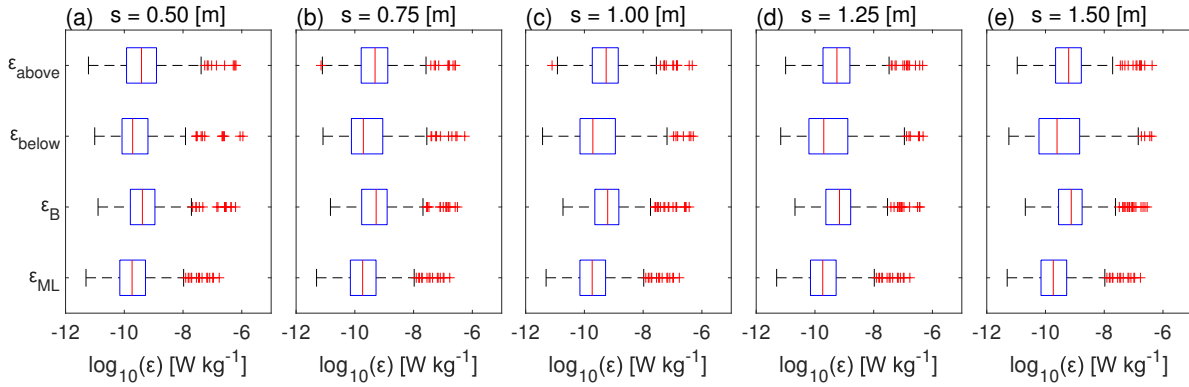
Figure S2.4 – Sensitivity analysis of segments considered for background dissipation estimates ε_B, also compared to estimations above (ε_{above}) and below (ε_{below}) the ML. (a)-(e) Boxplots showing the median (central red mark), 25th and 75th percentile (left and right box edges, respectively), ~ 99 % coverage (whiskers) and outliers (red crosses) for segments $s = 0.50$, 0.75, 1.00, 1.25 and 1.50 m, respectively. For comparison, ε_{ML} (lowest row) is presented in each panel (same distribution).
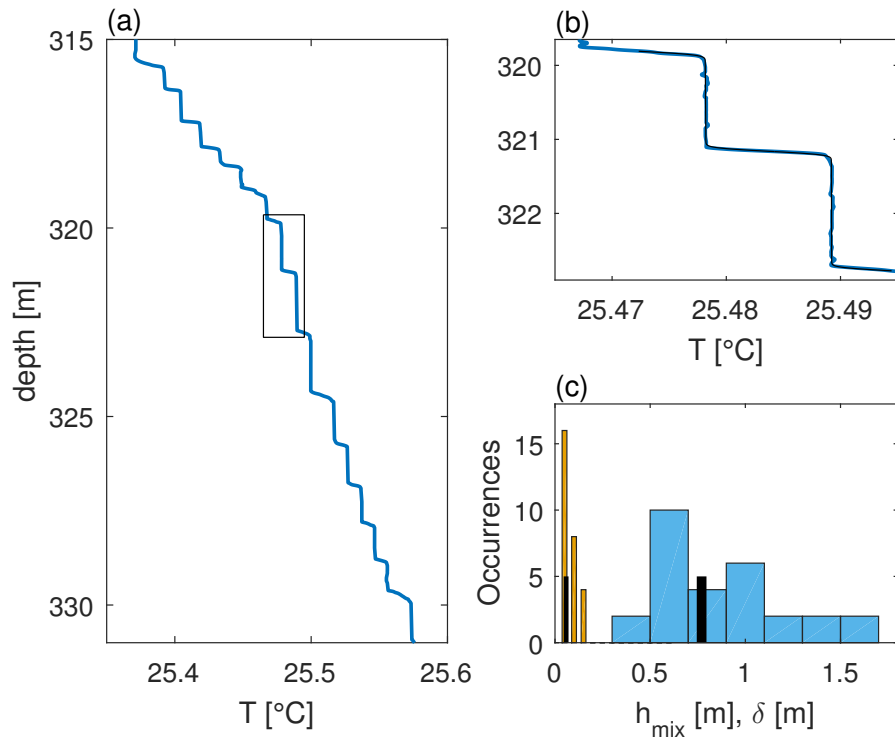
Figure S2.5 – Analysis of a double-diffusive staircase from Lake Kivu (Sommer et al., 2013). (a) Temperature profile (blue line) from 315 to 330 m depth measured with the VMP-500 on 30 April 2010 at 11:57 (UTC + 2). (b) Zoom of the black box in (a), showing the results from the diffusive-shape ML model (black line) for two MLs. For this case, δ is estimated assuming molecular diffusion. (c) Histograms of the 14 mixed layers detected (28 measurements, as the VMP-500 reports duplicate profiles). ML thickness (h_{mix}; light blue) and the diffusive length (δ; orange). The arithmetic averages are 0.77 ± 0.33 m for h_{mix} (thick black bar) and 0.058 ± 0.032 m for δ (thin black bar). Each profile passed the Φ_T model test with an average $R^2 = 0.96$.
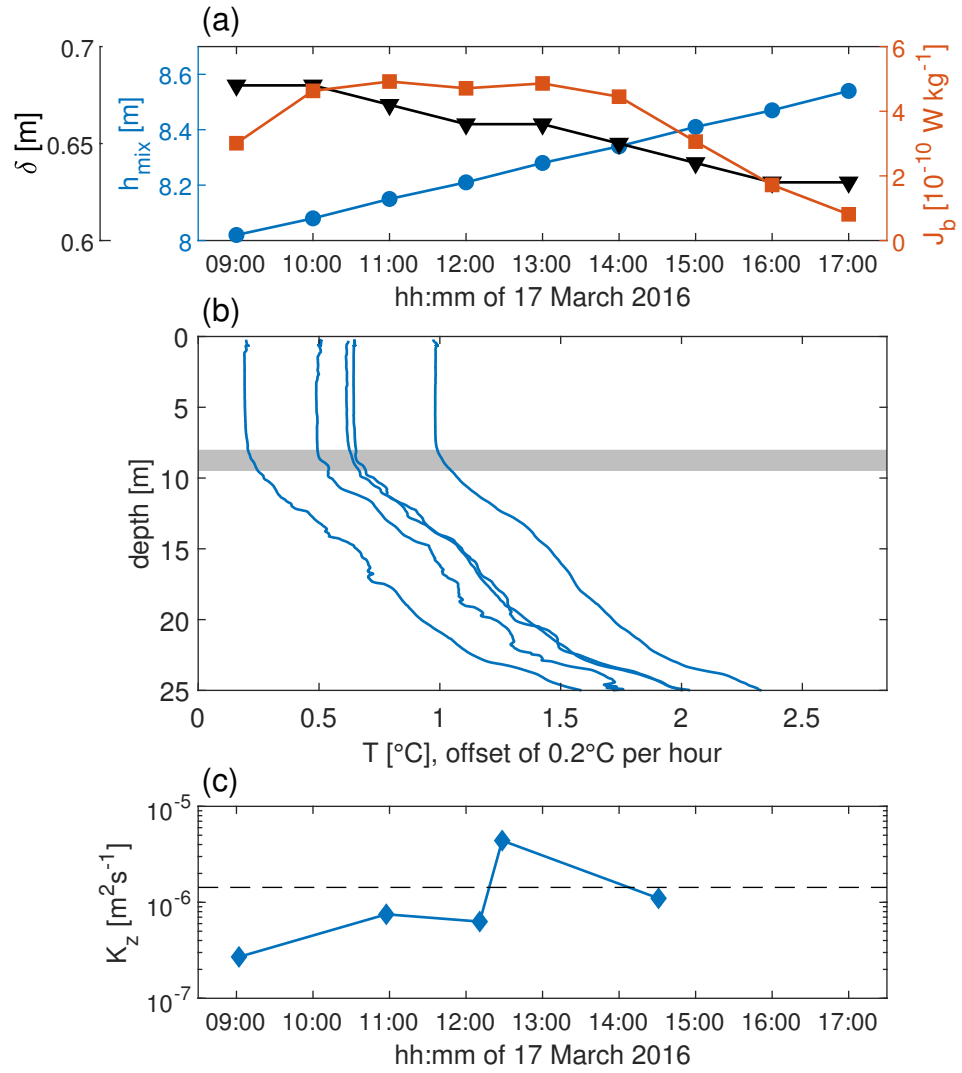
Figure S2.6 – Analysis of under-ice mixed layers caused by radiatively-driven convection in Lake Onega (Bouffard et al., 2019). (a) Time series from the moored instruments for the diffusive length δ (considering below the ML only; black triangles), mixed layer thickness h_{mix} (blue circles) and buoyancy flux J_b within the ML (red squares) measured during radiative daytime on 17 March 2016. The mean values for δ, h_{mix} and J_b where 0.66 m, 8.3 m and 3.6×10^{-10} W kg^{-1}, respectively. J_b is obtained following Eq. (5) from Bouffard et al. (2019). (b) Temperature profiles measured with SCAMP (PME, USA) microstructure profiler, between 9:00 and 14:00 on 17 March 2016. (c) Diffusivity estimations obtained following the Osborn-Cox method using 0.5 m bins. Gray area in (b) indicates the portion considered for depth-averaged K_z below the MLs. Dashed black line indicates the averaged diffusivity $K_z = 1.4 \times 10^{-6}$ m^2 s^{-1}.

Table S2.1 – Fitting bounds for each parameter of the diffusive-shape ML model Φ_T. The subscript *be* stand for below the ML, *ab* stands for above the ML and *ei* stands for eye-inspection analysis.

	ΔT [^{o}C]	δ [m]	z_o [m]	T_o [^{o}C]	h [m]	G_T [^{o}C m^{-1}]
lower bound	0	0	z_{ab}^{ei}	T_{be}^{ei}	0	0
upper bound	$1.5\left(T_{be}^{ei} - T_{ab}^{ei}\right)$	0.4	z_{be}^{ei}	T_{ab}^{ei}	$1.1\left(z_{be}^{ei} - z_{ab}^{ei}\right)$	2×10^{-2}

References

Bouffard, D., Zdorovennova, G., Bogdanov, S., Efremova, T., Lavanchy, S., Palshin, N., Terzhevik, A., Vinnå, L. R., Volkov, S., Wüest, A., Zdorovennov, R., and Ulloa, H. N. (2019). Under-ice convection dynamics in a boreal lake. *Inland Waters*, 9(2):142–161. doi:10.1080/20442041.2018.1533356.

Osborn, T. R. (1980). Estimates of the local rate of vertical diffusion from dissipation measurements. *Journal of Physical Oceanography*, 10(1):83–89. doi:10.1175/1520-0485(1980)010<0083:EOTLRO>2.0.CO;2.

Sommer, T., Carpenter, J. R., Schmid, M., Lueck, R. G., Schurter, M., and Wüest, A. (2013). Interface structure and flux laws in a natural double-diffusive layering. *Journal of Geophysical Research: Oceans*, 118(11):6092–6106. doi:10.1002/2013JC009166.

Wüest, A. (1994). Interactions in lakes: Biology as source of dominant physical forces. *Limnologica*, 24(2):93–104.

3 Persistence of bioconvection-induced mixed layers in a stratified lake

Oscar Sepúlveda Steiner[1]**, Damien Bouffard**[2]**, and Alfred Wüest**[1,2]

[1]Physics of Aquatic Systems Laboratory, Margaretha Kamprad Chair, Institute of Environmental Engineering, École Polytechnique Fédérale de Lausanne, Lausanne, Switzerland.

[2]Department of Surface Waters – Research and Management, Eawag, Swiss Federal Institute of Aquatic Science and Technology, Kastanienbaum, Switzerland.

Abstract

In situ observations of biophysical interactions in natural waters typically focus on physical mechanisms influencing biological activity. Yet, biological activity can also drive physical processes in aquatic environments. A community of photoautotrophic, motile and heavy bacteria – *Chromatium okenii*, which requires light, sulfide and anoxic conditions to perform anoxygenic photosynthesis, accumulates below the chemocline of the meromictic Lake Cadagno (Switzerland). Upward vertical migration drives bioconvection, which modifies the physical environment of the bacteria-populated water to create homogeneous mixed layers of up to 1 m thickness. Continuous convection-diffusion competition between the mixed layer and diapycnal diffusivity from the adjacent stratified surroundings smoothens their sharp boundaries. The well-understood daytime vertical migration is bounded by the upper part of the anoxic layer. However, nocturnal activity is unclear. Careful study of the changes in physical properties within the bacterial layer can help advance ecological understanding of daily activity cycles. An intensive 48-hour survey was conducted in August 2018 using standard and microstructure profilers, as well as a moored high-resolution current meter coupled with temperature and turbidity sensors deployed across the mixed layer depth. This survey detected persistent mixed layers also during nighttime hours. Using a mixed layer profile shape model, vertical velocity measurements and turbulent dissipation estimates, we conclude that photoautotrophic bacteria continue their vertical migration at night. This nocturnal activity thereby drives "dark bioconvection" and maintains the mixed bacterial layer in Lake Cadagno throughout the diel cycle.

3.1   Introduction

The long-standing description of natural waters assumes that the physical environment influences biogeo-chemical processes to generate specific ecological niches. Hydrodynamically-driven enhancement of primary production (Weiss et al., 1991; Oschlies and Garçon, 1998; Dufois et al., 2016) and formation of plankton spatial structures (Abraham, 1998; Ng et al., 2011; Lévy et al., 2018), such as thin layers (Steinbuck et al., 2009a; Durham and Stocker, 2012), are typical examples of physical mechanisms that drive biological processes.

However, biological activity can also influence and drive physical processes in aquatic systems. Examples of biophysical interactions affecting water characteristics at large spatial scales include planktonic modification of light absorption (Lorenzen, 1972; Schanz, 1985), which can lead to differential heating (Sathyendranath et al., 1991; Strutton and Chavez, 2004), and biogenic stratification (Weimer and Lee, 1973; Culver, 1977; Viaroli et al., 2018). At smaller scales, biologically-induced turbulence (Kunze et al., 2006; Lorke and Probsta, 2010; Simoncelli et al., 2018) is expected to drive water transport and mass exchange. The specific capacity of plankton to drive mixing has been demonstrated by laboratory experiments (Noss and Lorke, 2014; Houghton et al., 2018). However, it still lacks conclusive *in situ* observations (Kunze, 2019).

Bioconvection represents an intriguing example of bio-induced physical forcing (Hill and Pedley, 2005; Bees, 2020). This phenomenon describes heavy and motile organisms driving hydrodynamic changes in their immediate aquatic surroundings. This biophysical interaction has been extensively documented in laboratory settings using unicellular microorganisms (Bees and Hill, 1997; Jánosi et al., 1998; Bearon and Grünbaum, 2006). A recent study by Sommer et al. (2017) demonstrated that it also occurs in stratified natural waters.

Such biological phenomena leave specific, yet subtle physical traces in the aquatic environment. If those traces are sufficiently prominent, we attain the possibility to observe and investigate the original biological process by following its physical effects. This study documents bacteria-driven bioconvection in a lake by connecting several physical effects caused by motile, photoautotrophic sulfur *Chromatium okenii* communities. Lake Cadagno, a small alpine and meromictic lake in the Swiss Alps, provides an ideal natural laboratory. It hosts abundant photoautotrophic bacteria that create homogeneous mixed layers (MLs; Figure 3.1). The goal of this study is to infer bacterial migration activity based on the bio-induced convective mixing characteristics of the water layer they inhabit. Specifically, using physical measurements, we sought to elucidate whether these bacteria remain active at night (Sepúlveda Steiner et al., 2019). This study should motivate the use of physical observations to infer biological processes. It can specifically serve as model for studies seeking to detect ecological phenomena at low to moderate *in situ* energetics, which are measurable in lakes.

3.2   Bioconvection in Lake Cadagno

3.2.1   Study site

The study site, Lake Cadagno (Figure 3.2; 46°33'3.13"N, 8°42'41.51"E) is located in the Swiss Alps at 1920 m asl. This small alpine lake has a maximum depth of 21 m and a surface area of 0.26 km^2. Deep, ion-rich, subaquatic inflows (Del Don et al., 2001) lead to permanent stratification and qualify Lake Cadagno as a crenogenically meromictic lake (Boehrer and Schultze, 2008). The stratified water column exhibits a chemocline separating the oxygen-rich upper layer (top ~10 m) from the anoxic and sulfide-rich deep-water (deepest ~10 m).
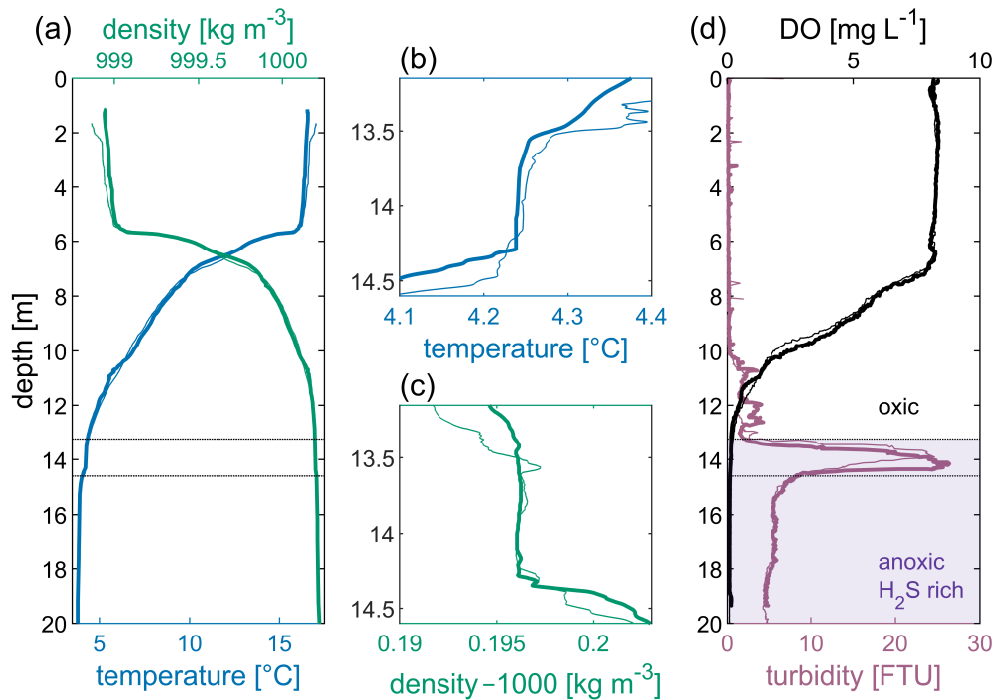
Figure 3.1 – Comparison of day-night profiles. Night profile: 15 Aug 2018 21:00 (thin lines), and day profile: 16 Aug 2018 13:00 (thick lines). (a) Profile of water density (green) and temperature (blue; measured with a VMP-500 microstructure profiler). (b, c) Enlargement of profiles between dotted black lines in (a) that exhibit the mixed layer (ML). (d) Profile of turbidity (purple) and dissolved oxygen (DO; black) measured with a Sea & Sun CTD profiler. Dotted black lines, as in (a), show the turbidity peak associated with bacteria at the depth of the ML as highlighted in (b) and (c).

3.2.2 Bioconvection in natural environments

Bioconvection induced by unicellular organisms develops when the density of motile cells exceeds that of ambient water and their local concentration reaches critical levels for determining the density of the water column they populate. These conditions create unstable density gradients. In order to sustainably maintain a consistent generation of convective plumes, cells must accumulate in a confined layer and perform net upward motion. Conditions limiting vertical migration of cells above the layer of accumulation are also necessary for its confinement (Sommer et al., 2017).

The photoautotrophic sulfur bacteria *C. okenii*, inhabits mainly below the chemocline of Lake Cadagno. These microorganisms are denser than water ($\rho_B \approx 1150$ kg m^{-3}) and capable of upward motility. Hydrological, morphological and geochemical characteristics of Lake Cadagno are favorable to meet those conditions described above for bioconvection. Particularly, the chemocline characteristics of Lake Cadagno contribute to the development of this process. During summer, *C. okenii* find ideal conditions of sunlight and H$_2$S below the chemocline (Schanz et al., 1998), where they can grow and accumulate at high concentrations (10^5 - 10^6 cells mL^{-1} = 10^{11} - 10^{12} cells m^{-3}) in the oxic-anoxic transition layer (Danza et al., 2017; Sommer et al., 2017). The vertical distribution of the layer they inhabit is well correlated (R^2 = 0.96) with turbidity measurements (Figure S3.1 in the Supporting Information). This correlation allows for accurate constraints of the bacteria vertical location. Above the chemocline, the presence of oxygen (Figure 3.1d) limits their vertical migration, since anoxygenic photosynthesis requires anoxic conditions (Tonolla et al., 1999; Danza et al., 2017).
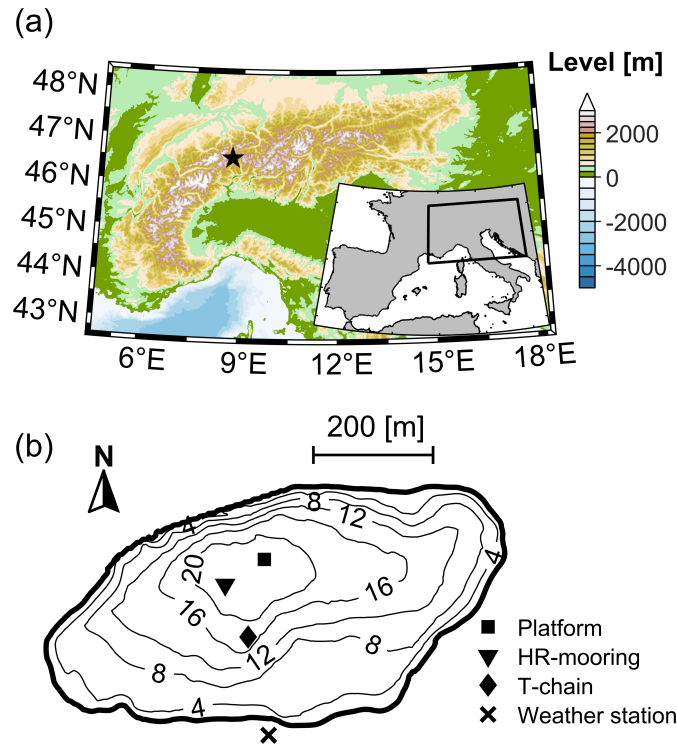
Figure 3.2 – Study site location. (a) Map of the European Alps. The star denotes the location of Lake Cadagno. (b) Lake Cadagno bathymetry (depth isolines in m) with location of the platform (profiles), moorings and weather station.

The upward migration of *C. okenii* towards the chemocline generates unstable density profiles of the water-bacteria mixture. This initiates convective mixing that generates a ML. Once established, convection allows the bacterial community to access sunlight from above and sulfide from below (Figure 3.1d). The formation mechanism of MLs, starting with a stratified water column early in the season, is depicted in Figure 3.3. Development of such MLs has been previously described using direct numerical simulations (DNS; Sommer et al., 2017). Once the ML is formed, continuous convection-diffusion competition (Sepúlveda Steiner et al., 2019) between the ML and its adjacent stratified waters above and below determines their vertical structure (Figure 3.3c).

Up to this point, bioconvection in Lake Cadagno has been attributed to upward migration of *C. okenii* seeking light below the chemocline in order to optimize anoxygenic photosynthesis. This process explains the presence of a ML during daytime hours. Nevertheless, Sepúlveda Steiner et al. (2019) describe MLs that also occur at night. Three distinct hypotheses might explain the persistence of such a "dark ML". First, background hydrodynamic processes in the lake may create or sustain it. Second, the decay timescale of the diurnal bioconvection may exceed the duration of nighttime conditions. Third, active upward migration of bacteria may occur in the absence of light.

In this paper, we analyzed the persistent development of a bioconvective ML in Lake Cadagno during daytime and nighttime hours using an intensive 48-hour field campaign. Specifically, we used (i) vertical microstructure profiles to evaluate the competing effects of bacteria-induced convection and turbulent diffusion adjacent to the bacterial layer and (ii) temperature and velocity at different spatial and temporal scales to explain maintenance and persistence of the ML below the chemocline of Lake Cadagno throughout the diel cycle.
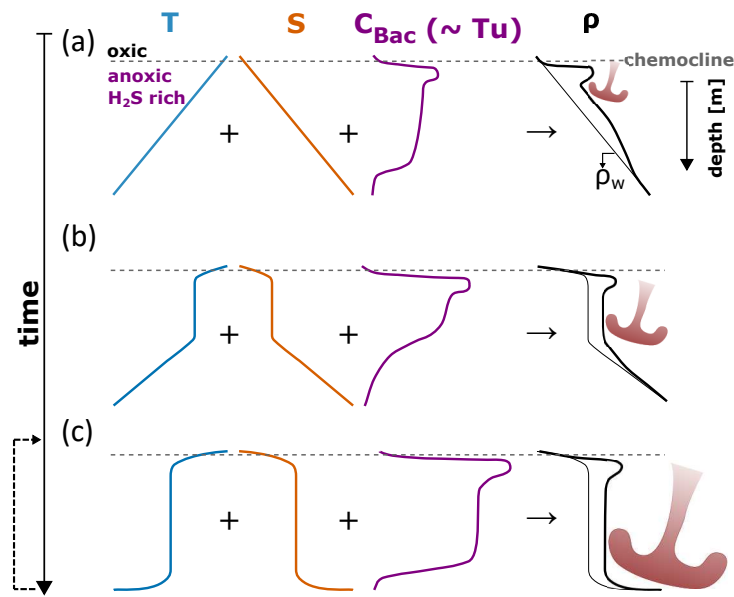
Figure 3.3 – Bioconvective mixed layer (ML) formational stages: (a) initial, (b) intermediate and (c) fully developed ML. Presence of high bacterial concentration C_{Bac} (m^{-3}) well-correlated with turbidity (Tu), increases the density of the water-bacteria mixture, exceeding the water density (ρ_w; function of temperature and salinity). The water density plus the bacterial density contribution (water-bacteria mixture) is represented as $\rho_w + \rho_o \xi C_{Bac}$, with ξ (m^3) representing the *C. okenii* density coefficient and ρ_o the reference density. Upward migrating bacteria accumulate at the oxic-anoxic interface and thereby cause unstable density profiles, which drive convective plumes (red mushroom-shaped feature).

3.3 Methods

3.3.1 Field measurements

The persistence of the bioconvective-induced ML in Lake Cadagno was investigated during an intensive 48-hour survey in August 2018. To characterize the ML, microstructure and CTD profile measurements were conducted from a platform situated in the open waters. In addition, an array of thermistors (T-chain) and a moored high-resolution (HR) current meter coupled with temperature sensors were installed at the ML depth (HR-mooring). Locations of the sampling platform and moorings are detailed in Figure 3.2. Hydrodynamic measurements were complemented with meteorological observations obtained from a weather station (Vaisala instruments with a CR-6 Campbell Scientific data logger) installed on the south shore of the lake (Figure 3.2). Weather conditions during the field campaign were warm with mild winds not exceeding 5 m s^{-1}. However, the observed ML was weaker compared to previous years (Sommer et al., 2017; Sepúlveda Steiner et al., 2019).

Microstructure and CTD profiles: To resolve the ML and estimate turbulent parameters in the water column, we measured temperature and conductivity at high vertical resolution using a free-falling Vertical Microstructure Profiler VMP-500 (Rockland Scientific International, Canada). The profiler is equipped with two fast FP07 thermistors and two fast SBE-7 conductivity microsensors mounted at the nose of the instrument and sampling at 512 Hz. Sommer et al. (2013) provides detailed description of the VMP-500 and its sensors. Profiles were measured at a sinking speed of 0.10 - 0.20 m s^{-1} every 20 min during the 48-hour survey period. These measurements were complemented with CTD profiles performed every hour using a Sea & Sun 75M CTD sampling at 8 Hz. In addition to the common CTD sensors, this profiler was equipped with pH, chlorophyll-a, dissolved oxygen and turbidity sensors.

Table 3.1 – Details for sensors deployed on T-chain and HR-mooring (Figure 3.1).

Station	Instrument	Accuracy	Time response [s]	Sampling frequency [Hz]	Depths [m]
T-chain	RBR*solo* T	± 0.002° C	~1	0.1	0.25, 0.5
	RBR TR-150	± 0.002° C	~1	0.1	0.75, 1.0
	RBRconcerto[3] Tx	± 0.005° C	~30	0.2	0.25, 0.5, 0.75, 1,0, 1.25, 1.5, 2.0, 2.5, 3.0 4.9, 5.0, 6.0, 7.0, 8.0, 9.0, 10.0, 11.0, 12.0, 13.0, 14.0, 14.5 15.0, 16.0 17.0 [mab]
HR-mooring	Nortek Aquadopp HR profiler (2 MHz)	± 1% of measured values ± 5 mm s^{-1}	–	0.5	Installation: 14.5 Measurements: 11.9 to 14.0 m; 0.02 m bins
	RBR*solo* T	± 0.002° C	~1	2	12.0, 12.7, 12.9, 13.1, 13.8
	RBR*solo* Tu/Seapoint Turbidity sensor	–	0.1	0.1	12.0*, 12.9, 13.8
	PME MiniDOT	± 0.3 mg L^{-1}	30	0.02	12.0, 12.9, 13.8

mab: meters above the bottom
*sensor did not record

T-chain: A mooring equipped with an array of thermistors was installed close to the center of the lake (Figure 3.2) to evaluate the temporal evolution of water column stratification. Table 3.1 lists thermistors characteristics and deployment depths.

HR-mooring: Hydrodynamic fluctuations in and around the ML were monitored with a high resolution mooring deployed below the chemocline (~12 m depth). This equipment included a Nortek Aquadopp HR profiler (2 MHz) that faced upwards and measured current velocities (between 11.9 to 14.0 m depth; 0.02 m bins) at 0.5 Hz. The mooring devices also measured temperature, turbidity and dissolved oxygen using sensors installed at different depths above the Aquadopp. Table 3.1 lists detailed settings, sensitivities and other information for sensors. Turbidity is used as a proxy to identify the location of the bacterial layer (e.g. Egli et al., 2004). Although we successfully collected data within the bacterial layer, inaccurate observations of the lake bottom depth caused the mooring to be deployed 0.6 m higher than intended. HR-mooring measurements below the bacterial layer are therefore not available.

3.3.2 Convection-diffusion competition

We used the symmetric diffusive-shape model (Φ_T) of Sepúlveda Steiner et al. (2019) to interpret convection-diffusion competition within the measured ML temperature profiles. The model is as follows:

$$\Phi_T = \Delta T \left[\text{erf}\left(\frac{\frac{h}{2} - (z - z_o)}{\delta} \right) - \text{erf}\left(\frac{\frac{h}{2} + (z - z_o)}{\delta} \right) \right] + T_o - G_T(z - z_o) \tag{3.1}$$

where z is the depth coordinate (positive downwards) and z_o represents the center of the ML. The model assumes an initial step-function of height h (m), temperature T_o, and symmetric step ΔT. The diffusive length $\delta = \sqrt{4K\tau}$ (m) defines the extent of the ML boundaries affected by the vertical background diffusivity K (m^2 s^{-1}), which generates a smooth transition to background stratification over a diffusive timescale $\tau = \delta^2/4K$ (s).

The term G_T describes slope of the ML. The ML thickness h_{mix} is then given by:

$$h_{mix} = h - 4\delta \tag{3.2}$$

Lower δ values relate to sharp transitions from ML to ambient lake water and therefore to strong convective ML activity relative to turbulent background diffusivity. Higher δ values indicate weak convection relative to background turbulent diffusion.

A bounded nonlinear fitting method was used to estimate ML model (Φ_T) parameters from temperature microstructure profiles. After fitting, only Φ_T with a coefficient of determination $R^2 > 0.75$ and a ML thickness $h_{mix} > 0.2$ m were considered for further analysis. Initial values and boundary conditions were the same as those provided in Sepúlveda Steiner et al. (2019). An equivalent procedure for analysis of the turbidity profile is given in the Supporting Information (Text S3.1 and Figure S3.2).

3.3.3 Data analysis

Density calculations: For this particular study, accurate estimates for water density (ρ_w) is required. We calculated ρ_w following Wüest et al. (1996) and using the ionic water composition of Lake Cadagno. Expressed as a function of temperature (T) and conductivity (κ_{20}), ρ_w can be represented as:

$$\rho_w(T, \kappa_{20}) = \rho'_w(T) + \gamma \kappa_{20} \tag{3.3}$$

where $\rho'_w(T) = 999.84 + 6.55 \times 10^{-2}T - 8.56 \times 10^{-3}T^2 + 5.94 \times 10^{-5}T^3$ is the T-dependent water density, $\gamma = 0.69 \times 10^{-3}$ kg m^{-3} (μS cm^{-1})$^{-1}$ is Lake Cadagno's specific conductivity to density factor (Uhde, 1992) and κ_{20} (μS cm^{-1}) is conductivity normalized to 20° C. The term $\rho_w(T, \kappa_{20})$ represents the density of water only, without bacteria. The water-bacteria mixture density can be represented as:

$$\rho = \rho_w + \rho_o \xi C_{Bac} \tag{3.4}$$

where C_{Bac} is the bacterial concentration (m^{-3}), $\xi = 3.7 \times 10^{-17}$ m^3 is the *C. okenii* density coefficient (Sommer et al., 2017) and $\rho_o = 1000$ kg m^{-3} is the reference density. A temperature-salinity diagram (Figure S3.3), which constrains bacterial ML location, was used to estimate water density based on temperature only given HR-mooring data ($\rho_w = -0.03T + 1000.3$; for $3.8 \leq T \leq 4.5$).

Turbulent quantities and diffusivity: Temperature microstructure profiles were used to estimate rates of turbulent kinetic energy dissipation, ε, the Thorpe (1977) scale of overturn and turbulent diffusivities. These were estimated both for the water column and within the ML and adjacent waters (ML background).

Turbulent dissipation estimates, ε (W kg^{-1}), were obtained by adjusting the Batchelor (1959) spectrum to the measured spectra of temperature gradient fluctuations. This procedure used a maximum likelihood spectral fitting method (Ruddick et al., 2000) and a correction by Steinbuck et al. (2009b) to calculate the smoothing rate of temperature variance, χ_θ (°C^2 s^{-1}). Dissipation estimates obtained from poorly resolved spectra and those which did not comply with Bachelor fitting, were discarded according to likelihood and mean absolute deviation criteria proposed by Ruddick et al. (2000). Following Sepúlveda Steiner et al. (2019), turbulent dissipation estimates in the ML (ε_{ML}) were obtained using the microstructure segment defined by h_{mix} that results from Φ_T-fitting. Background estimates, (ε_B), were derived from segments 1.5 m above and below h_{mix}.

Mixing is quantified twofold following diapycnal diffusivity models given in Osborn (1980) and Osborn and Cox (1972). The former model uses dissipation estimates by applying:

$$K_\rho = \Gamma \frac{\varepsilon}{N^2} \qquad (3.5)$$

where $N^2 = g\rho_o^{-1}\partial\rho_w/\partial z$ (s^{-2}) is the water column stability, $g = 9.81$ m s^{-2} and z is the depth coordinate (positive downwards). The density gradient, $\partial\rho_w/\partial z$, is obtained through linear fitting of ρ_w in the vertical segment of interest. Here we use a diapycnal mixing coefficient of $\Gamma = 0.15$, which is well-suited for small- to medium-sized stratified lakes (Wüest et al., 2000). This method works well when ε complies with spectral fitting criteria. Diffusivity estimates from the ML background (hereafter K_B) are obtained using this method. The Osborn and Cox (1972) model instead uses χ_θ as follows:

$$K_{OC} = \frac{\chi_\theta}{2\left(\frac{\partial T}{\partial z}\right)^2} \qquad (3.6)$$

This provides diffusivity estimates for the whole water column since χ_θ can be directly estimated by integrating the temperature microstructure spectra.

Turbulent quantities and diffusivity often exhibit lognormal character. Statistical analyses therefore used a maximum likelihood estimator (mle) for a lognormal distribution (Baker and Gibson, 1987). This reduced the influence of extreme values and provided ad-hoc estimates of statistical variability through the intermittency factor $\langle\sigma^2_{mle}\rangle$.

Buoyancy flux and convective velocity: The buoyancy flux within the ML, a key parameter for characterizing convection, was calculated following Sepúlveda Steiner et al. (2019) as:

$$J_b^{ML} = 0.55\varepsilon \qquad (3.7)$$

where ε_{ML} is the ML dissipation. The vertical convective velocity (w_*) can then be characterized by Deardorff (1970) as:

$$w_* = (J_b^{ML} h_{mix})^{1/3} \qquad (3.8)$$

where h_{mix} is the ML thickness. Finally, the convective timescale is given by $\tau_* = (h_{mix}/J_b^{ML})^{1/3}$.

Flow stability: The gradient Richardson number Ri_g (Turner, 1973) was used to account for flow stability. This dimensionless number is defined as:

$$Ri_g = \frac{N^2}{S^2} \qquad (3.9)$$

where $S^2 = (\partial u/\partial z)^2 + (\partial v/\partial z)^2$ is the square of the shear with u and v representing horizontal velocities. For shear flows wherein $Ri_g > Ri_g^c = 0.25$, buoyancy suppresses vertical dislocations to maintain stable hydrodynamic conditions. For $Ri_g < Ri_g^c$, stratified shear flow can initiate shear instabilities and enhance vertical mixing (Ivey et al., 2008). Time series for Ri_g were obtained from the Aquadopp HR profiler data averaged over 5 minutes and vertically smoothed using a running mean among four vertical bins.

3.4 Results

3.4.1 Water column structure

This study sought to determine whether hydrodynamic factors create or sustain MLs as observed in Lake Cadagno. In summer, the Lake Cadagno water column consists of three distinct hydrodynamic zones (Figures 3.1, 3.4a and S3.4). A 5 m thick surface layer (yellow zone in Figure 3.4a), an extremely stable interior (5 to 12 m depth; orange to purple) and a weakly stratified deep layer (dark purple). In the interior, the T-chain measurements (Figure 3.4a) indicated a temperature gradient of $1.4 \pm 0.1\,°C\,m^{-1}$ and the CTD profile recorded a strong median stability of $N^2 \approx 1.1 \times 10^{-3}\ s^{-2}$ This suggests that the strongly stratified interior isolates the bacterial layer at 12 m depth from the surface layer. This surface layer is not considered further. The weakly-stratified deep waters below the bacterial layer exhibited a temperature gradient of $0.08 \pm 0.03\,°C\,m^{-1}$ with a low stability of $N^2 \approx 3.8 \times 10^{-5}\ s^{-2}$.
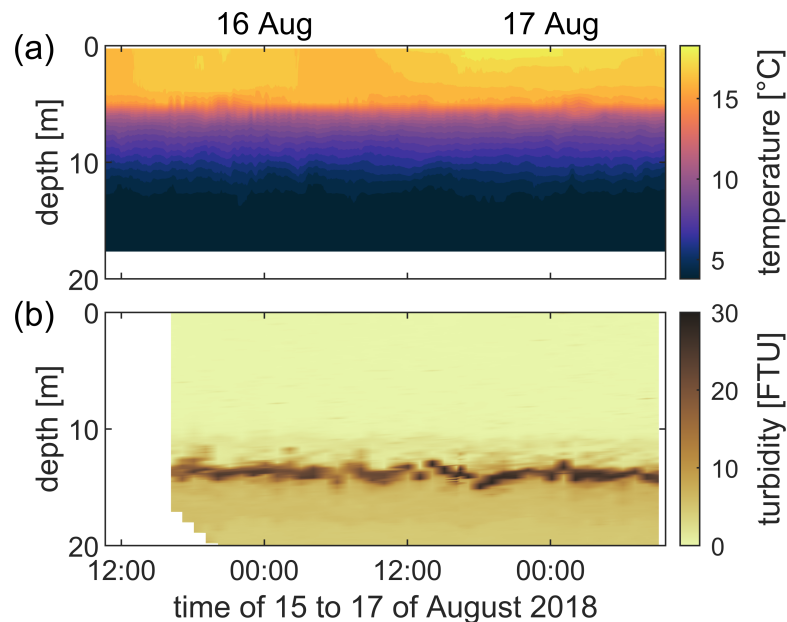

Figure 3.4 – Water column conditions during the field campaign. (a) Temperature profiles continuously measured by the T-chain mooring. (b) Turbidity profiles measured with the Sea & Sun CTD.

The strong stratification suppressed overturns and vertical mixing in the interior. The Thorpe scale (Figure S3.4c) fell below the cm scale indicating an extremely well sorted thermocline without small-scale overturns. Consequently, diapycnal diffusivity (Figure S3.4d) was close to molecular, with a mle-mean of $4.1 \times 10^{-7}\ m^2\,s^{-1}$ $\langle 0.8 \rangle$. By contrast, the water column showed enhanced mixing below 12 m depth. The average Thorpe scale was $L_T = 0.14 \pm 0.13$ m and diffusivity gave a mle-mean of $3.5 \times 10^{-5}\ m^2\,s^{-1}$ $\langle 4.9 \rangle$ with strong intermittency.

The bacterial layer occurred below the oxic-anoxic interface and was tracked using turbidity profiles (Figures 3.1 and S3.1). Time series of turbidity profiles (Figure 3.4b) revealed a consistent peak in turbidity at ~14 m depth. We observed that the position and thickness (expansion / contraction) of the turbidity layer oscillated throughout the field campaign coupled with isothermal movements, which exhibited periodicities of 4.0, 1.7 and 0.6 hr (Figure S3.5a).

3.4.2   Mixed layer characteristics and evolution

During the August 2018 field campaign, we collected 142 temperature microstructure profiles using duplicated sampling (284 total). Figure 3.5a provides an example of the temporal evolution of a typical ML temperature profile as collected on 15 August 2018. This is accompanied by a mid-day profile subjected to fitting to the ML-shape model (Φ_T; Figure 3.5b). From the total of 284 samples, 136 met the Φ_T-fitting procedure criteria. These allowed for direct deduction of h_{mix} and δ, represented as arithmetic means of 0.50 ± 0.22 m and 0.18 ± 0.09 m, respectively. Time series results of Φ_T (Figure 3.5c) show mixed layer position (z_o) and h_{mix} throughout the 48-hour sampling. These parameters present considerable variability following the baroclinic displacements of isotherms (see above).
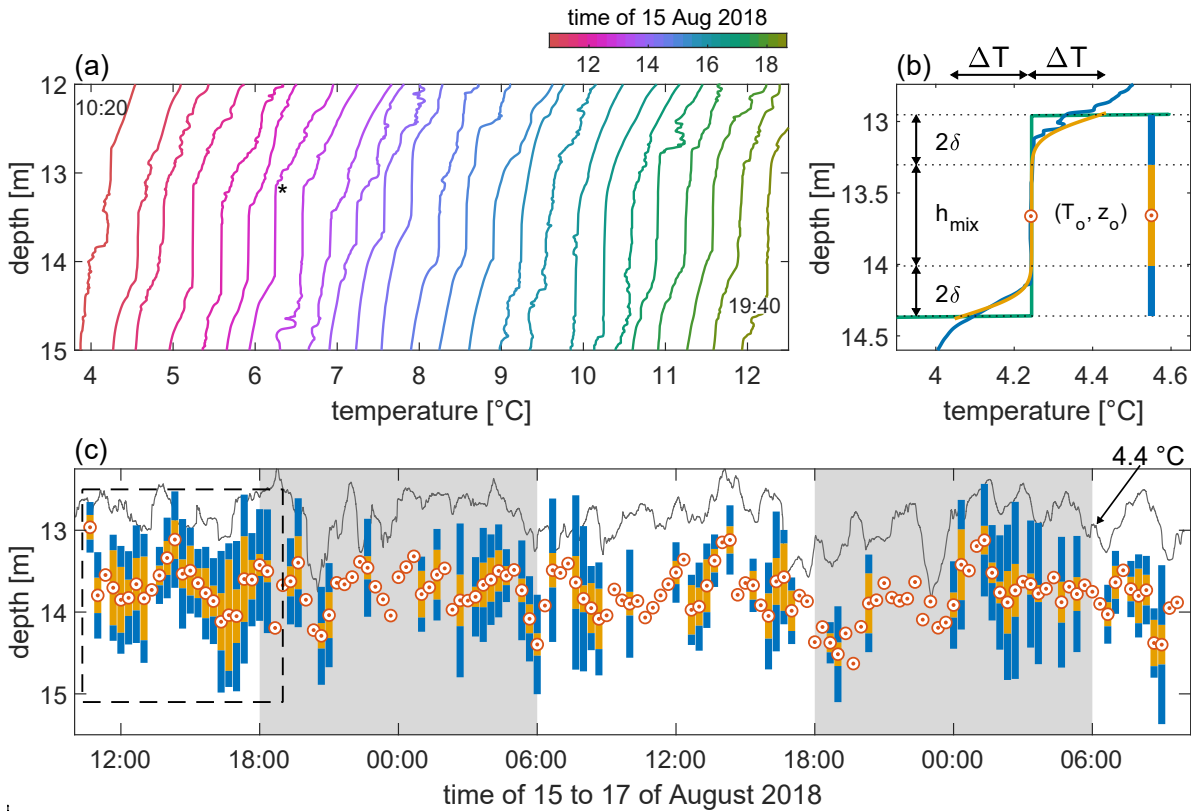

Figure 3.5 – Time series of measured mixed layer (ML) profiles and ML-shape model (Φ_T) analysis. (a) Waterfall plot of measured MLs during 15 August 2018. An offset of 1° C per hour was applied to separate the profiles. (b) Example of the ML-shape model showing a temperature profile (blue; *-marked profile in (a); $R^2 = 0.97$) with its respective fitting (orange), initial step-like ML (green) and the definition of h_{mix} and δ following Sepúlveda Steiner et al. (2019). (c) Time-series of Φ_T results. Blue and orange bars represent h_{mix} and 2δ as defined in (b). Only profiles that meet the Φ_T-fitting criteria are considered. Bars represent averages of Φ_T results from the two fast thermistors mounted on the VMP. Profiles with only one sample meeting the criteria are also displayed. For reference, z_o (orange dotted circles) of discarded profiles are included. Gray areas represent the nighttime periods for the 48-hour measurement interval. The gray line depicts the 4.4° C isotherm obtained from the HR-mooring. The dashed box corresponds to the measurements displayed in (a).

Mixed layers were observed during both daytime and nighttime hours. Table 3.2 and Figures 3.6a,b show a statistical comparison of ML characteristics between these two periods. While h_{mix} was 13% larger during

daytime, δ was 19% larger during nighttime. This finding indicates more vigorous convection during daytime coupled with more effective diffusion-driven smoothing (enhanced δ) at night (Sepúlveda Steiner et al., 2019). Analysis of variability in the vertical profiles performed by stretching/compressing the MLs to a normalized scale (Figures 3.7a,b), however, showed only subtle shape differences between daytime and nighttime. Consistent with these results, ML stability estimates (N^2_{ML}; Table 3.2) showed only minor variation. This suggests that the differences between daytime and nighttime estimates are not significant.

Table 3.2 – Characteristics of the observed convective ML in Lake Cadagno during August 2018. Results are shown separately for daytime and nighttime periods.

Parameter measured	Units	All	Daytime	Nighttime
Thickness of mixed layer (h_{mix})†	m	0.50 ± 0.22	0.53 ± 0.24	0.46 ± 0.18
Diffusive boundary length-scale (δ)†	m	0.18 ± 0.09	0.17 ± 0.09	0.21 ± 0.08
Mixed layer stability (N^2_{ML})†	10^{-5} s^{-2}	0.54 ± 1.38	0.56 ± 1.59	0.52 ± 1.01
Background stability (N^2_B)†	10^{-5} s^{-2}	7.9 ± 1.5	7.9 ± 1.6	7.8 ± 1.4
Dissipation rate in the mixed layer (ε_{ML})‡	10^{-10} W kg^{-1}	$4.3 \langle 2.7 \rangle$	$6.9 \langle 2.7 \rangle$	$1.4 \langle 1.9 \rangle$
Convective plume velocity (w_*)†	mm s^{-1}	0.37 ± 0.25	0.43 ± 0.27	0.27 ± 0.17
Convective timescale (τ_*)†	min	30 ± 19	27 ± 20	35 ± 17
Background diffusivity (K_B)‡	10^{-6} m^2 s^{-1}	$2.8 \langle 1.3 \rangle$	$3.4 \langle 1.5 \rangle$	$2.1 \langle 1.1 \rangle$

†Results are reported as arithmetic mean ± standard deviation.
‡ Statistics of the rate of dissipation and diffusivity are reported following Baker and Gibson (1987) given by mle-mean for log-normal distribution and intermittency factor (σ^2_{mle}) inside $\langle \rangle$ brackets.

Microstructure data within the MLs and their adjacent regions were analyzed according to the methods presented above (Figure 3.6). Here we focus on distributions of dissipation rates (ε_{ML}) in the ML, convective velocity scale (w_*) and background diffusivity (K_B). The histograms in Figure 3.6 also distinguish daytime and nighttime values. Table 3.2 summarizes the statistics from this analysis and highlights the overall low energy level in the ML (mle-mean $\varepsilon_{ML} = 4.3 \times 10^{-10}$ W kg^{-1} $\langle 2.7 \rangle$). In general, daytime profiles exhibited enhanced convection compared to that observed in nighttime profiles. Difference factors between these periods were 4.9 and 1.6 for ε_{ML} and w_*, respectively. Regions of the water column adjacent to the ML consistently showed an average diffusivity of $K_B = 2.8 \times 10^{-6}$ $\langle 1.3 \rangle$ m^2 s^{-1}, or one order of magnitude higher than molecular diffusion. This value agrees with the diapycnal diffusivity estimate of $K_{W94} = 1.6 \times 10^{-6}$ m^2 s^{-1} reported from a tracer release experiment at the same depth in Lake Cadagno (Wüest, 1994). Diffusivity was more intense during the daytime evident from a factor 1.6 difference between daytime and nighttime measurements (Table 3.2).
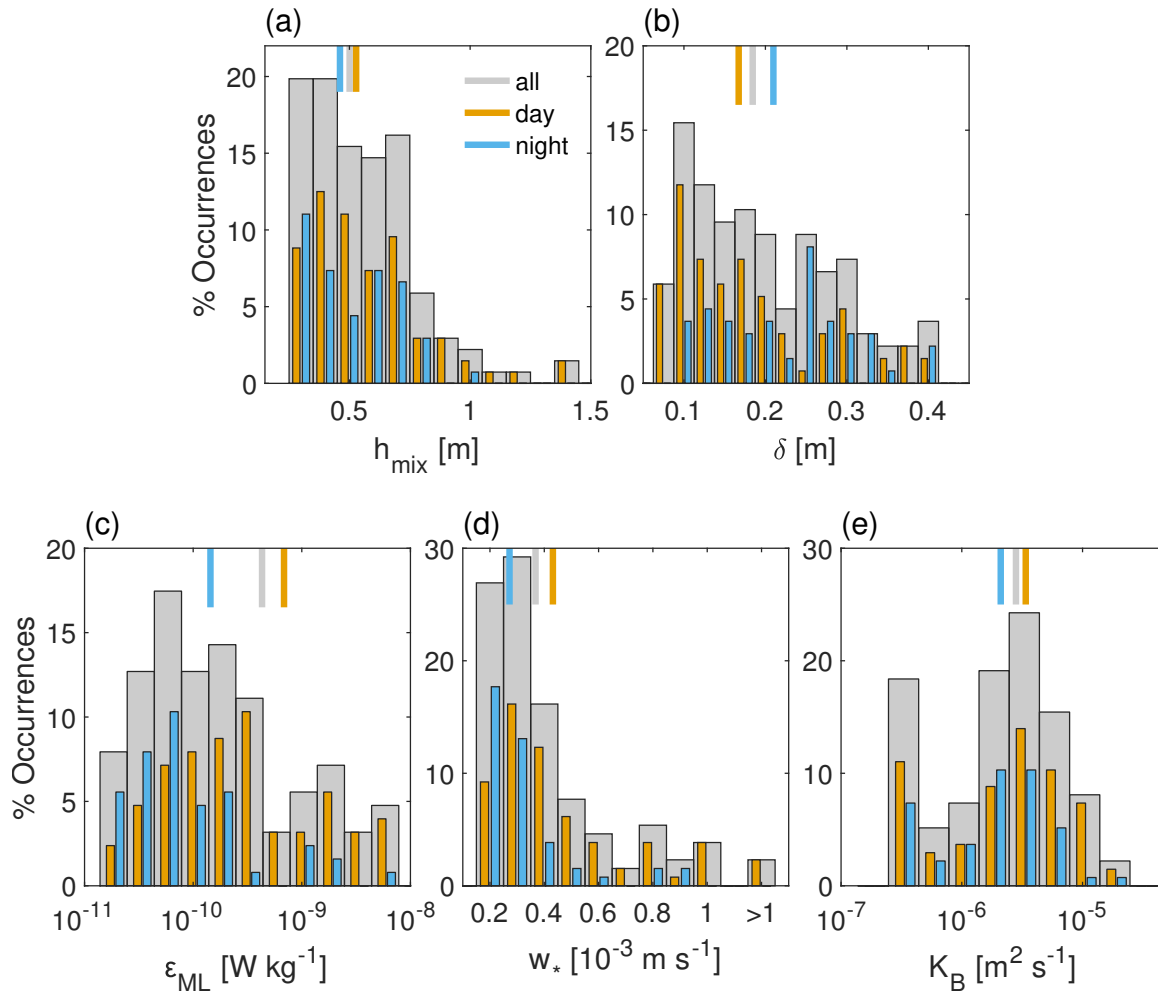
Figure 3.6 – Statistical distribution of mixed layer (ML) characteristics. (a) ML thickness h_{mix} , (b) diffusive length scale δ related to ML boundaries, (c) dissipation ε_{ML} in the mixed layer, (d) convective velocity scale w_* within the ML, and (e) background diapycnal diffusivity K_B (gray bars) following (Osborn, 1980). Histograms are also presented for separate daytime (orange bars) and nighttime (blue bars) periods. Vertical bars at the top of each panel correspond to the arithmetic mean in (a), (b) and (d) and to the mle-mean (Baker and Gibson, 1987) in (c) and (e).

3.4.3 Day-night comparison of turbidity profiles

Additional analysis of turbidity profiles was used to investigate physical signatures of bioconvection (Figures 3.7c,d). Measured turbidity profiles (43 total) are separated for daytime and nighttime periods (25 and 18 profiles, respectively). The bacterial layer appears as a consistent peak (>10 FTU) at around 14 m depth (ranging from 13 to 15 m) with a maximum not exceeding 30 FTU. The upper boundary of the layer appears as a slightly sharper transition than its lower boundary. This feature represents the oxic-anoxic transition since dissolved oxygen prevent further vertical migration of the bacteria. This constraint may generate the sharper upper boundary transition. The more gradual lower transition likely arises from higher turbulent diffusion (Figure S4d) that mixes the deep water and because bacteria can also sink beyond the ML zone. Vertical displacements affect the turbidity peak position (Figure 3.4b), however Figures 3.7c,d show that these remained in a more stable position during nighttime hours.
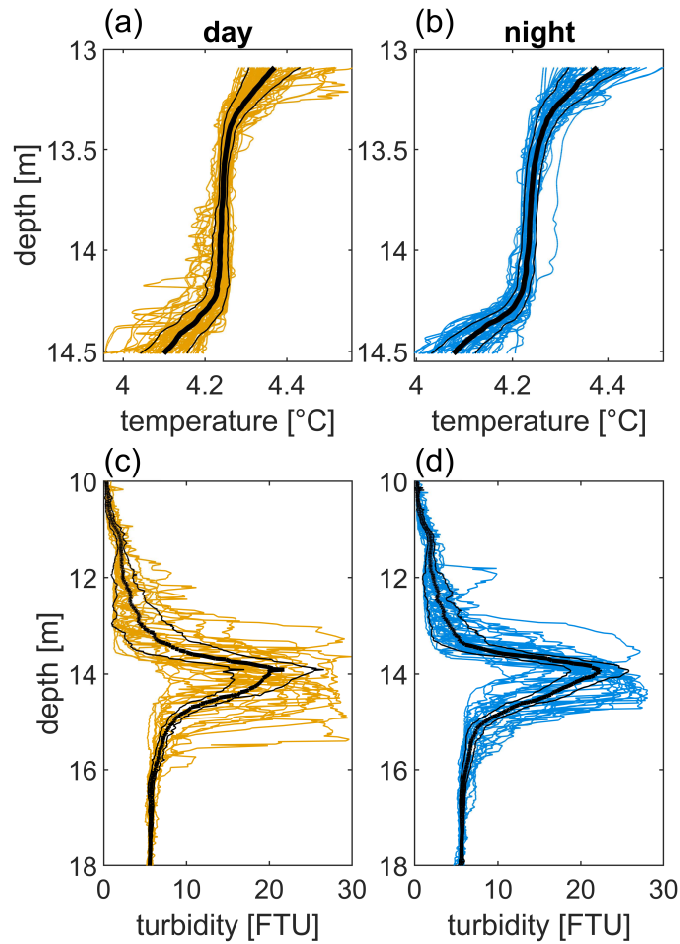
Figure 3.7 – Comparison of mixed layers and turbidity profiles measured during daytime and nighttime hours. (a, b) Stretched/compressed MLs separated for daytime and nighttime hours, respectively. Only profiles that meet the Φ_T-fitting criteria are considered. An offset of 0.3° C is applied to the nighttime profiles. The thick black line and the thin black lines represent arithmetic mean and standard deviation, respectively. (c, d) Measured turbidity profiles accompanied by their isopycnal-averaged profile (black thick line). Thin black lines represent the standard deviation of the isopycnal-averaged profile.

Isopycnal-averaged profiles (Figures 3.7c,d; thick black lines) enable the analysis of turbidity peaks without the influence of vertical displacements in the density field. This analysis reveals subtle differences between daytime and nighttime turbidity profiles and offers no indication of bacteria sinking at night. Additionally, a turbidity shape model (Tu-model; Text S3.1 and Figure S3.2) was used to evaluate turbidity profiles. Although this analysis resulted in smaller h_{mix} estimates compared to those generated by the ML-shape model (explanation in Text S3.1), the resulting daytime and nighttime parameters also do not show significant differences (Table S3.1). Taken together, these analyses suggest a net energy input to maintain turbidity peak characteristics. We interpret this input to represent bacterial upward migration in the water column.

3.4.4 HR-mooring measurements

Fluctuations in velocity measured by the HR-mooring equipment provide further confirmation of bacteria-induced convection. Detailed time series of wind, dissolved oxygen and currents are presented in Figure S3.6. Here, we focus on turbidity, vertical velocities and estimates of the gradient Richardson number Ri_g (Figure 3.8).

Measured vertical velocities ranged between -1.5 and +1.5 mm s^{-1} (Figure 3.8b; positive upwards). Continuous changes of the sign of velocity values (from red to blue and vice versa) below the 4.4° C isoline indicate convective activity. Spectral analysis of vertical velocity (Figure S3.5b) also detected a marked oscillation with periods of 25 to 30 min. This period agrees with the estimated convective timescale values, τ_* (Eq. 3.8), of 30 ± 19 min (Table 3.2).
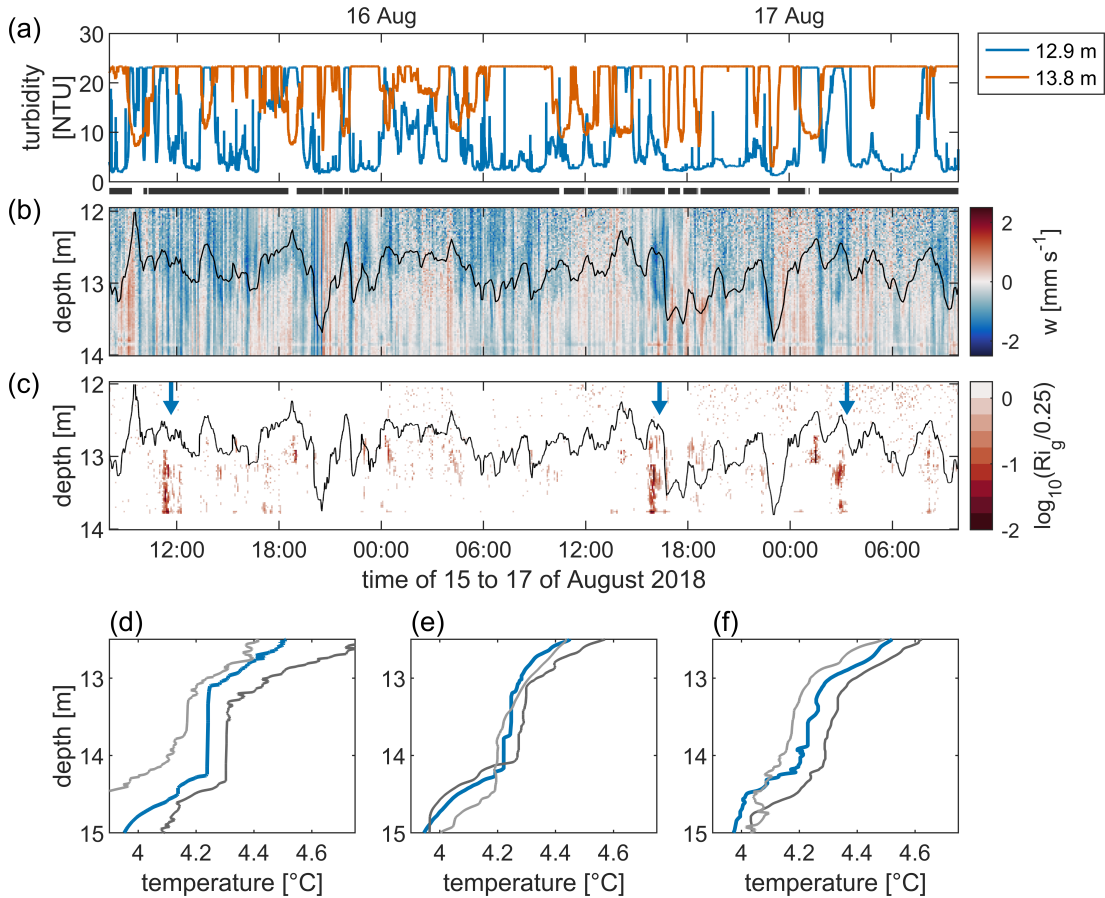

Figure 3.8 – HR-mooring observations and gradient Richardson number (Ri_g) estimates. (a) Turbidity. (b) Vertical velocity component (w), measured with the Aquadopp HR profiler. Thick black line between panels (a) and (b) corresponds to measurement of turbidity at 13.8 m exceeding 10 NTU (i.e. measurement performed within the bacterial layer). (c) Gradient Richardson number (Ri_g) normalized by the critical value 0.25. Continuous black line in (b) and (c) depicts the 4.4° C isotherms. (d, e and f) Examples of temperature microstructure profiles for the ML and adjacent regions during periods of $Ri_g \leq Ri_g^c \approx 0.25$. Thick blue lines correspond to profiles performed at intervals indicated by blue arrows in (c), same order. Profiles performed 20 minutes before (light gray; -0.05° C offset) and after (dark gray; +0.05° C offset) the $Ri_g \leq Ri_g^c$ events are provided to account for discrepancies between profiles and HR measurements. HR measurements were performed at ~50 m distance from the profiling platform.

Turbidity sensors mounted on the HR mooring provided estimates of ML position that were subsequently used to analyze convective velocity fluctuations. Turbidity time series (Figure 3.8a) show strong variability (coefficient of variation of 0.87 for the central sensor) indicating fluctuations in the vertical position of the bacterial ML. This result agrees with the T-chain and profiling results. The turbidity sensor installed at 13.8 m depth was configured in auto-range mode. Unfortunately, the sensor sampled only within the 0 to 25 FTU range and failed to record values above (Figure 3.8a). The data were still adequate for identifying periods when the bacterial ML appeared at ~13.8 m depth with turbidities exceeding 10 FTU (Figures 3.7a,b).

A statistical analysis of measured vertical velocities was performed to further validate microstructure-based estimates (w_*; see Figure 3.6d). To select vertical velocity data, which were reliably within the ML, we discarded data above the 4.4° C isotherm and beneath the lowermost turbidity sensor (13.8 m depth) for turbidities below 10 FTU (thick black line between Figures 3.8a,b).
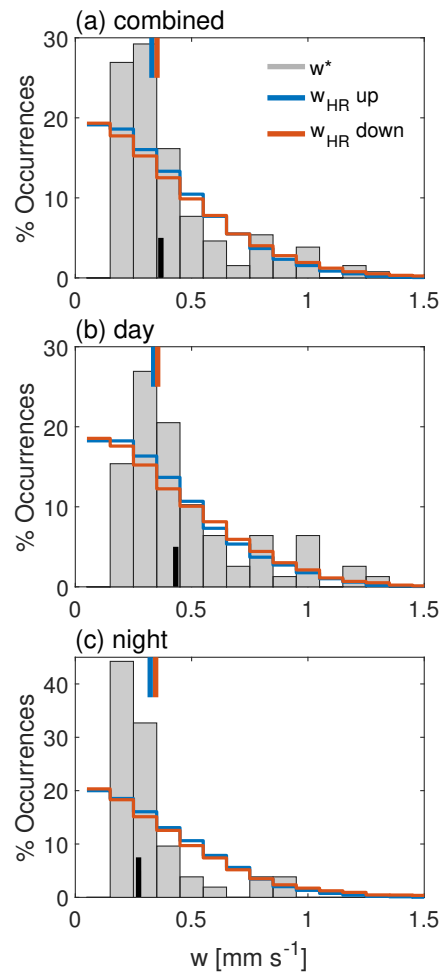

Figure 3.9 – Comparison of depth-averaged vertical velocity (w) distributions within the ML with convective plume velocity. (a) Whole dataset (combined). (b, c) Daytime and nighttime sub-datasets, respectively. Gray bars corresponds to the ε-based convective plume velocity (w_*; Deardorff 1970), whereas blue and red lines were obtained from the Aquadopp HR-mooring separated for upward and downward components, respectively. In each panel, the vertical bars correspond to arithmetic means following the same color-code with the exception of w_*, which is shown in black for better visibility.

Figure 3.9a shows distributions of depth-averaged vertical velocity. This analysis was performed by detrending the depth-averaged velocity time-series and separating them into upward and downward components This process gave results strongly resembling half-normal distributions with arithmetic averages of 0.33 ± 0.25 mm s^{-1} and 0.35 ± 0.28 mm s^{-1} for upward and downward components, respectively. Downward plumes exhibited slightly higher velocities, whereas upward plumes were more frequent (6%), particularly in the range 0.15 – 0.55 mm s^{-1}. This directional asymmetry balances the mass flux budget (Jonas et al., 2003). Moreover, average velocities showed good agreement with microstructure-based estimates of w_* (0.37 ± 0.25 mm s^{-1}). This represents further evidence of the convective nature of the ML observed in Lake Cadagno.

The same analysis is performed separately for daytime and nighttime periods (Figures 3.9b,c). These periods show similar upward and downwards averages and asymmetric directional features. The distributions do not show considerable difference between daytime and nighttime values. Although w_* varies by 59% between daytime and nighttime hours, the HR current measurements shows only minor differences (< 5%).

The Aquadopp HR current profiler recorded lateral current magnitudes of up to 10 mm s^{-1} (Figures S3.6e,f). This information was used to account for flow stability by estimating Ri_g. The magnitudes of Ri_g show that shear is not capable of generating instabilities above the bacterial ML (Figure 3.8c). However, values of $Ri_g < 0.25$ appeared primarily within the bacterial ML (below 4.4° C isotherm). This indicates an interplay between enhanced shear and weakening of stratification as triggered by convection.

3.5 Discussion

The study focused on detecting a bioconvective ML in Lake Cadagno over a 48-hour period. It provides physical evidence of ML persistence throughout the daily cycle likely driven by bacterial activity.

Day-night cycle persistency – The bacteria layer remained mixed over the entire observation period regardless of light conditions (Figures 3.5 and 3.7a,b). Small-scale analysis detected a noticeable decrease in turbulent dissipation at night ($\varepsilon_{ML}^{night}/\varepsilon_{ML}^{day} \approx 0.2$) indicating a decrease in convection. However, ML characteristics did not change significantly as demonstrated by $h_{mix} \approx 0.50 \pm 0.22$ m, a parameter that differs by only 15% between daytime and nighttime observation periods. The diffusive boundary transition of $\delta \approx 0.18 \pm 0.09$ m, as driven by adjacent diapycnal diffusivity ($K_B = 2.8 \times 10^{-6}$ ⟨1.3⟩ m^2 s^{-1}), differed by ~19% between daytime and nighttime periods. Turbidity peak shape (Figures 3.7c,d) and convective scale velocities (Figure 3.9) also indicate that ML characteristics remained virtually unchanged through the day-night cycle.

Dissipation decay – To further elucidate whether bacteria actively migrate upward at nights, we analyzed the temporal evolution of turbulent dissipation in the ML (ε_{ML}; Figure 3.10a). We compared the observed decay in convective activity to the e-folding decay (Caldwell et al., 1997) expected to result from a sudden cessation of convective activity triggered by a drop in phototrophic activity. In our case, the e-folding decay is characterized by the convective timescale $\overline{\tau_*} = 30 \pm 19$ min (Table 3.2). This implies a 95% reduction of ε_{ML} (Figure 3.10a) over a ~1.5 hr period ($3\tau_*$). However, the measured dissipation exhibited much slower decay than the e-folding predictions. Although the measured dissipation declines during nighttime, time series indicate a continuation of the bacteria-induced convection at night to maintain the ML.

Mixed layer thickness decay – Similarly, the temporal evolution of h_{mix} also records nighttime bacterial activity. A completely inactive ML would smooth out unhindered due to the action of eddy diffusivity in the adjacent water column. Figure 3.10b shows this scenario assuming a ML-model for two different levels of constant diffusivity (measured and molecular). Field estimates of diffusivity suggest smoothing of the ML takes about 25 min. Molecular diffusion suggest it could take 10 and 7 hrs for each of the two monitored nighttime

periods. Comparison of measured h_{mix} with ML-model predictions also suggests that ML maintenance during nighttime hours requires active, upward bacterial migration to maintain the layer.

The role of stratification – Stratification plays a key role in ML maintenance. The lake interior (Figure S3.4a) exhibits a strong stratification. Thorpe scales of overturn are extremely low (< 1 cm; Figure S3.4c) and diffusivities approach molecular rates (4.1×10^{-7} m^2 s^{-1} $\langle 0.8 \rangle$; Figure S3.4d). Strong stratification counteracts background turbulence and its smoothing effects. The importance of this interplay becomes most evident when analyzing bacterial accumulation at the top of the ML (e.g. Figure 3.3). A series of turbidity profiles measured in July 2017 (Figure S3.7a) provide a compelling example of this feature. Using a numerical scheme to account for 1D vertical diffusion (Figure S3.7b), we show that the background diffusivity would smooth out the turbidity profiles and disrupt the ML in absence of active upward migration of bacteria. By comparison, a more energetic environment ($K_{ocean} \sim 10^{-5}$ m^2 s^{-1}; Figure S3.7b) would more rapidly vanish the bacterial layer due to strong background smoothing. Therefore, the mild background diffusivities in Lake Cadagno, which result from a resistance to diapycnal mixing imposed by the strong stratification, enable bacterial accumulation that in turn drives convection. Analysis of ML shapes having achieved critical gradient Richardson number ($Ri_g^c \approx 0.25$) criterion supports this interpretation (Figures 3.8d,e,f). In these cases, buoyancy can no longer suppress vertical dislocations. Diffusivity and shear turbulence then influence the ML to induce enhanced smoothing and/or adjacent sheared layers.
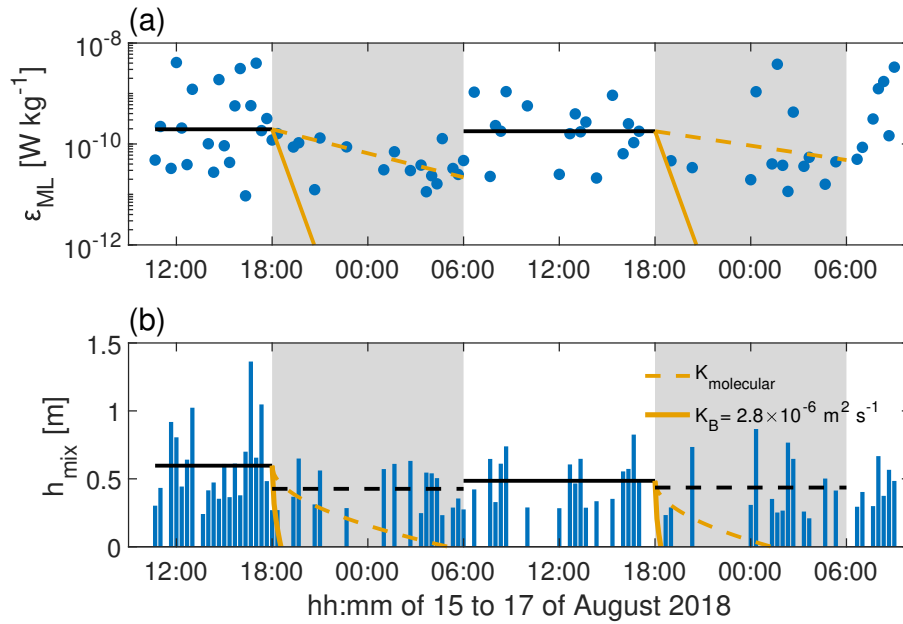

Figure 3.10 – Temporal evolution of ML convective turbulence. (a) ML dissipation rate ε_{ML} (blue dots). Gray areas correspond to nighttime periods. The orange line corresponds to the e-folding decay (Caldwell et al., 1997) following $\varepsilon(t) = \varepsilon_* \exp(-t/\tau^*)$, with ε_* the daytime median value (black lines) and τ^* the convective timescale (~30 min). Dashed orange line represent fits of the e-folding decay for the same ε_* and adjusting for τ^*. This procedure yields $\tau_1^* = 5.5$ hrs and $\tau_2^* = 9.1$ hrs for each nighttime period. (b) ML thickness h_{mix} (blue bars). Daytime and nighttime averages are depicted by black lines and black dashed lines, respectively. The orange lines represent the evolution of h_{mix} during nighttime hours assuming a completely inactive ML, i.e. diffusivity smoothing out the ML without opposition (no convection). Following the ML-shape model (Φ_T), this situation can be accounted for by $h_{mix}(t) = h_{mix}^* - 4\delta$, with h_{mix}^* as the daytime average value and $\delta = \sqrt{4Kt}$. Data displayed (blue dots and bars) were obtained by averaging the resulting estimates from the profile as sampled by the two fast thermistors mounted on the VMP. Only sampled profiles that meet the Φ_T criteria were considered (profiles with only one sample meeting the criteria were also considered).

Dark bioconvection – To perform upward migration and drive bioconvection during nighttime, *C. okenii* requires an energy source different than anoxygenic photosynthesis. Recently, Berg et al. (2019) reported on *C. okenii*'s ability to perform aerobic sulfide respiration, independent of light, in the presence of nano-scale oxygen concentrations. Luedin et al. (2019) provided genetic evidence for dark chemolithotrophic oxidation of sulfur compounds by *C. okenii*. These metabolic pathways along with the presence of intracellular sulfur globules and energy storage molecules such as polyhydroxybutyrate (PHB; Luedin et al., 2019) or glycogen (Berg et al., 2019) in *C. okenii*, indicate the existence of a nighttime energy source crucial for bacterial motility. Chemotaxis, negative for oxygen and positive towards H_2S, is well described in *C. okenii* and provides a credible orientation mechanism for bacterial accumulation below the chemocline (Luedin et al., 2019) and subsequent generation of bioconvection despite the absence of light. Bioconvection may in turn improve the opportunities for microorganisms to access the trace amounts of oxygen needed to maintain a dark energy metabolism. Further research is needed to better characterize *C. okenii*'s range of metabolic processes and orientation behavior involved in the observed dark bacterial activity. The physical analysis presented in this paper does not resolve metabolic processes, but highlights several constraints regarding upward migration during nighttime hours.

Mixed layer formation timescale – Solely phototactic migration would imply that the ML forms every morning after sunrise. This would be due to the omnipresent effect of shear-induced eddy diffusion that smooths out the ML during nighttime (Figure 3.10; Sepúlveda Steiner et al., 2019). If convective plumes within the ML represent a favorable environment for *C. okenii*, the timescale of their formation is critical given the ~12 hrs maximum duration of sunlight. To estimate this, it is necessary to analyze the energetics of ML formation (Figure 3.3). Given a constant initial density gradient ($\rho_w(z) \sim \rho_o N_B^2 g^{-1} z$), the potential energy required to mix a h_{mix}-thick water column below the chemocline can be represented as:

$$PE = \int_{-\frac{h_{mix}}{2}}^{\frac{h_{mix}}{2}} \rho_w(z) g z \ dz = \int_{-\frac{h_{mix}}{2}}^{\frac{h_{mix}}{2}} \rho_o N_B^2 z^2 \ dz = \frac{1}{12} \rho N_B^2 h_{mix}^3 \qquad (3.10)$$

where PE is in $J\,m^{-2}$ and the origin lies at the center of the resulting ML. Furthermore, the energy flux generated by upward bacterial migration can be expressed as $E_f = J_{net} \rho_o h_{mix}$ ($W\,m^{-2}$) with J_{net} as the net buoyancy flux for ML expansion. This can be modeled as $J_{net} = J_b^{ML} - J_b^B$, i.e. the difference between ML and background buoyancy fluxes, with $J_b^B = K_B N_B^2$. Finally, $\tau_{h_{mix}} = PE/E_f$ represents the timescale for generating a ML of thickness h_{mix}. Average values reported in Table 3.2 for daytime hours yield $PE = 8.2 \times 10^{-4}$ $J\,m^{-2}$ and a $\tau_{h_{mix}} = 4$ hr timescale to form a 0.5 m thick ML. For the average conditions throughout the field campaign, the formation timescale of a 0.5 m thick ML increases to $\tau_{h_{mix}} = 30$ hr. A 0.3 m thick ML requires a formation timescale of 11 hr, a result that is in good agreement with the DNS results of Sommer et al. (2017). These results indicate that ML formation can take up a major fraction of one day if not the duration of several days. Given that the background smoothing effect remains active, our analysis suggests that the continuation of bioconvection at night represents a more energy-efficient strategy than forming the ML on a daily basis.

Vertical velocity scales relevant for C. okenii – During nighttime, *C. okenii* (density $\rho_B \approx 1150$ $kg\,m^{-3}$) would immediately sink if they stopped migrating upwards. Their sinking speed can be approximated as the Stokes sedimentation of a particle with ellipsoidal shape (Guazzelli and Morris, 2011). Assuming sinking parallel to the main axis and rod-shaped dimensions as reported by (Imhoff, 2015), sinking speeds range from 0.01 to 0.02 mm s^{-1} (Text S3.2 and Figure S3.8). For context, their upward migration speed is of the same order of magnitude (0.03 ± 0.01 mm s^{-1}; Sommer et al., 2017). On the other hand, our measurements suggest a convective plume scale of 30 ± 19 mm s^{-1} (Table 3.2). This indicates that the convective plumes are a vertical

transport mechanism two orders of magnitude more efficient than individual cell migration. This suggests that the generation of bioconvection during nighttime, although reduced and non-constant, offsets the sinking rate of the bacterial community.

Critical bacterial concentration to trigger bioconvection – The stability ($N^2 = g\rho_o^{-1}\partial\rho/\partial z$) of the water-bacteria mixture in the ML can be analyzed to determine the minimal density contribution by bacteria for convective plumes to occur. Combining an unstable density profile given by $N^2 < 0$ with the water-bacteria mixture density ($\rho = \rho_w + \rho_o\xi C_{Bac}$) and discretizing (forward finite difference) for the ML thickness, yields the following condition for bacterial concentration difference over the entire ML:

$$-\Delta C_{Bac} > \frac{h_{mix}}{g\xi} N^2_{ML} \tag{3.11}$$

(positive downwards) which leads to unstable density conditions. Results presented in Table 3.2 give a $\Delta C_{Bac} = 7.5 \times 10^9$ m^{-3}. Average bacterial concentration in the ML $C_{Bac}^{ML} = 1.3 \times 10^{11}$ m^{-3} (Figure S3.1) yields a difference of only 6% between the upper layer concentration and C_{Bac}^{ML} necessary to induce convective plumes. Furthermore, considering data presented here and in Sommer et al. (2017) we find that $\Delta C_{Bac} \sim 10\%$ of C_{Bac}^{ML}, which translates into a 1 to 2 FTU difference in turbidity (see Figure S3.1b for turbidity as a function of C_{Bac}). Such a difference in bacterial concentration is even more evident for the profiles collected in July 2017 (Figure S3.7a), which show a peak maxima exceeding C_{Bac}^{ML} by ~5 FTU. Altogether, the present analysis suggests that high concentration of *C. okenii* generate favorable conditions for bioconvective plumes in Lake Cadagno.
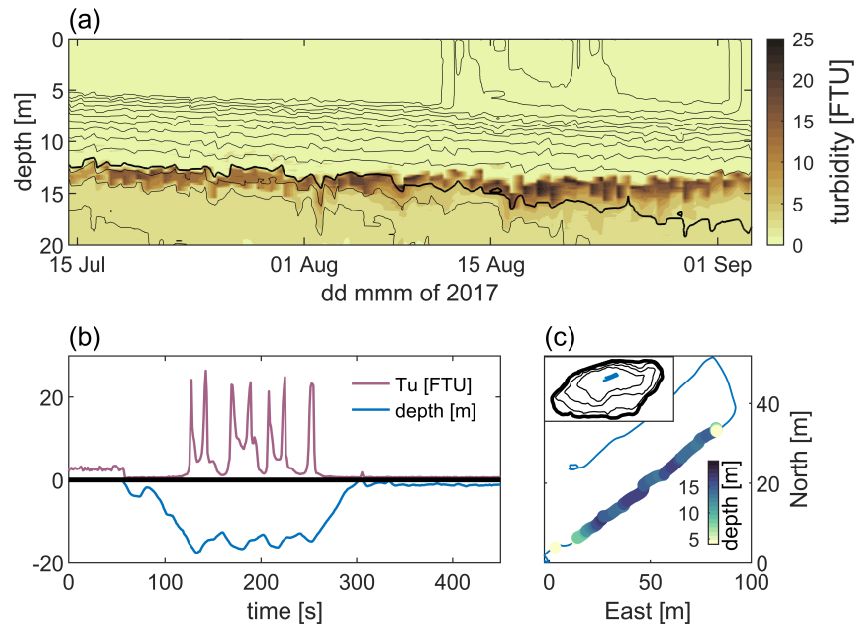

Figure 3.11 – Seasonal and spatial persistence of the bacterial layer. (a) Time series of turbidity profile during summer 2017, as measured by the Sea & Sun 75M CTD. Thick black line corresponds to 5° C isothermal. Thin black lines above the thick black line represent isothermals from 15° to 6° C with 1° C decrement. Lines below correspond to 4.75°, 4.50° and 4.25° C isothermals. (b) Vertex AUV transect performed on the afternoon of 16 August 2017. The Y-axis is shared between turbidity (Tu [FTU]; positive) and depth (in m; negative; same scale). (c) Plan view of the AUV trajectory with distances measured from the sampling platform and depth color-code for positions below 4 m depth. Inset in (c) shows the AUV transect plan view within the lake. Thin black lines depict 5, 10 and 15 m depth bathymetric isolines.

Seasonal and spatial persistency – The process of bioconvection has been detected in Lake Cadagno during summer months (Sommer et al., 2017; Sepúlveda Steiner et al., 2019). The present work details the temporal evolution of a bacteria-induced ML maintained throughout a diel cycle and links records of this bacterial ML to turbidity. The question arises as to whether these measurements represent a transient, episodic or a systematic process. A bi-daily CTD profile monitoring performed during the summer of 2017 provides evidence of seasonal persistency (Figure 3.11a). These measurements reveal a turbid layer located at ~12 to ~15 m depth and persisting throughout the entire density-stratified summer period. Furthermore, turbidity transects (Figures 3.11b,c) performed in 2017 with an AUV (Hydromea-Vertex; Schill et al., 2018; Quraishi et al., 2018) documented spatial persistence of the bacterial layer along several tens of meters. Further research is needed to unravel the seasonal and spatial variability of the bioconvective ML. However, preliminary analyses presented in Figure 3.11 provide compelling evidence that bioconvection occurs (i) throughout the summertime and (ii) consistently below the chemocline throughout the entire lake basin.

Bioconvection appears as a biophysical interaction capable of generating mixing and actively shaping the thermal structure of a lake. Specifically, in Lake Cadagno, bioconvection expands the habitat of *C. okenii*, exposing the bacterial community to light and entraining H_2S from below. This suggests active participation in the creation of their ecological niche. We show here that the expanded habitat of these photoautotrophic bacteria – the ML, does not form every day at dawn but rather persists throughout nighttime hours (Figures 3.1 and 3.5). Although reduced in comparison to daytime, our analysis shows that the bacteria remain active during nighttime hours (Figures 3.9 and 3.10). Further research can help resolve physiological / metabolic reasons for this behavior. We provide several physical hypotheses concerning the advantages of a continuous vertical migration and resultant bioconvection.

3.6   Conclusions

In this study, we focused on the persistence of a mixed layer induced by bioconvection over the daily cycle in a natural lake system. Analyses from an intensive 48-hour campaign, investigating the *C. okenii* bacterial layer in the alpine and meromictic Lake Cadagno (Switzerland) offer the following conclusions:

1. Measurements analysis allowed comparison of the competing effects of convection and turbulent diffusion. Physical profile information gave clear evidence of the role of biological activity in water column dynamics.

2. Our observations demonstrate that although the level of homogeneity of the bioconvective mixed layer (ML) varies over time, it persists throughout the diel cycle. This persistence also applies on seasonal (during the density-stratified summer period) and spatial (below the chemocline over the lateral extent of the whole lake) scales.

3. Despite strong stratification during summer in Lake Cadagno, there is considerable diapycnal mixing adjacent to the bioconvective ML to erode their shape. The development of profile shapes over the daily cycle suggests that bacterial migration occurs during nighttime hours. Without upward migration, the bio-convectively induced ML would vanish over the duration of one night.

With this study, we examine the possibility of drawing conclusions on biological phenomena, purely based on *in situ* physical observational methods. Small to medium size lakes are ideal environments for further exploration of this encouraging development. They are characterized by low to moderate energetics which can be accurately sensed with modern small-scale instrumentation.

Acknowledgments

References

Abraham, E. R. (1998). The generation of plankton patchiness by turbulent stirring. *Nature*, 391(6667):577–580. doi:10.1038/35361.

Baker, M. A. and Gibson, C. H. (1987). Sampling turbulence in the stratified ocean: Statistical consequences of strong intermittency. *Journal of Physical Oceanography*, 17(10):1817–1836. doi:10.1175/1520-0485(1987)017<1817:STITSO>2.0.CO;2.

Batchelor, G. K. (1959). Small-scale variation of convected quantities like temperature in turbulent fluid Part 1. General discussion and the case of small conductivity. *Journal of Fluid Mechanics*, 5(1):113–133. doi:10.1017/S002211205900009X.

Bearon, R. N. and Grünbaum, D. (2006). Bioconvection in a stratified environment: Experiments and theory. *Physics of Fluids*, 18(12):127102. doi:10.1063/1.2402490.

Bees, M. A. (2020). Advances in bioconvection. *Annual Review of Fluid Mechanics*, 52(1):449–476. doi:10.1146/annurev-fluid-010518-040558.

Bees, M. A. and Hill, N. A. (1997). Wavelengths of bioconvection patterns. *Journal of Experimental Biology*, 200(10):1515–1526.

Berg, J. S., Pjevac, P., Sommer, T., Buckner, C. R., Philippi, M., Hach, P. F., Liebeke, M., Holtappels, M., Danza, F., Tonolla, M., Sengupta, A., Schubert, C. J., Milucka, J., and Kuypers, M. M. (2019). Dark aerobic sulfide oxidation by anoxygenic phototrophs in anoxic waters. *Environmental Microbiology*, 21(5):1611–1626. doi:10.1111/1462-2920.14543.

Boehrer, B. and Schultze, M. (2008). Stratification of lakes. *Reviews of Geophysics*, 46(2):RG2005. doi:10.1029/2006RG000210.
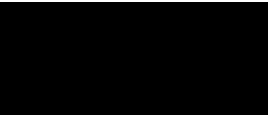
References

Caldwell, D. R., Lien, R.-C., Moum, J. N., and Gregg, M. C. (1997). Turbulence decay and restratification in the equatorial ocean surface layer following nighttime convection. *Journal of Physical Oceanography*, 27(6):1120–1132. doi:10.1175/1520-0485(1997)027<1120:TDARIT>2.0.CO;2.

Culver, D. A. (1977). Biogenic meromixis and stability in a soft-water lake. *Limnology and Oceanography*, 22(4):667–686. doi:10.4319/lo.1977.22.4.0667.

Danza, F., Storelli, N., Roman, S., Lüdin, S., and Tonolla, M. (2017). Dynamic cellular complexity of anoxygenic phototrophic sulfur bacteria in the chemocline of meromictic Lake Cadagno. *PLoS ONE*, 12(12):e0189510. doi:10.1371/journal.pone.0189510.

Deardorff, J. W. (1970). Convective velocity and temperature scales for the unstable planetary boundary layer and for Rayleigh convection. *Journal of the Atmospheric Sciences*, 27(8):1211–1213. doi:10.1175/1520-0469(1970)027<1211:CVATSF>2.0.CO;2.

Del Don, C., Hanselmann, K. W., Peduzzi, R., and Bachofen, R. (2001). The meromictic alpine Lake Cadagno: Orographical and biogeochemical description. *Aquatic Sciences*, 63(1):70–90. doi:10.1007/PL00001345.

Dufois, F., Hardman-Mountford, N. J., Greenwood, J., Richardson, A. J., Feng, M., and Matear, R. J. (2016). Anticyclonic eddies are more productive than cyclonic eddies in subtropical gyres because of winter mixing. *Science Advances*, 2(5):e1600282. doi:10.1126/sciadv.1600282.

Durham, W. M. and Stocker, R. (2012). Thin phytoplankton layers: Characteristics, mechanisms, and consequences. *Annual Review of Marine Science*, 4(1):177–207. doi:10.1146/annurev-marine-120710-100957.

Egli, K., Wiggli, M., Fritz, M., Klug, J., Gerss, J., and Bachofen, R. (2004). Spatial and temporal dynamics of a plume of phototrophic microorganisms in a meromictic alpine lake using turbidity as a measure of cell density. *Aquatic Microbial Ecology*, 35(2):105–113. doi:10.3354/ame035105.

Guazzelli, E. and Morris, J. F. (2011). *A Physical Introduction to Suspension Dynamics*. Cambridge University Press, Cambridge.

Hill, N. A. and Pedley, T. J. (2005). Bioconvection. *Fluid Dynamics Research*, 37(1-2):1–20. doi:10.1016/j.fluiddyn.2005.03.002.

Houghton, I. A., Koseff, J. R., Monismith, S. G., and Dabiri, J. O. (2018). Vertically migrating swimmers generate aggregation-scale eddies in a stratified column. *Nature*, 556(7702):497–500. doi:10.1038/s41586-018-0044-z.

Imhoff, J. F. (2015). Chromatium. In *Bergey's Manual of Systematics of Archaea and Bacteria*, pages 1–8. John Wiley & Sons, Ltd, Chichester, UK.

Ivey, G., Winters, K., and Koseff, J. (2008). Density stratification, turbulence, but how much mixing? *Annual Review of Fluid Mechanics*, 40(1):169–184. doi:10.1146/annurev.fluid.39.050905.110314.

Jánosi, I. M., Kessler, J. O., and Horváth, V. K. (1998). Onset of bioconvection in suspensions of Bacillus subtilis. *Physical Review E*, 58(4):4793–4800. doi:10.1103/PhysRevE.58.4793.

Jonas, T., Stips, A., Eugster, W., and Wüest, A. (2003). Observations of a quasi shear-free lacustrine convective boundary layer: Stratification and its implications on turbulence. *Journal of Geophysical Research*, 108(C10):3328. doi:10.1029/2002JC001440.

Kunze, E. (2019). Biologically generated mixing in the ocean. *Annual Review of Marine Science*, 11(1):215–226. doi:10.1146/annurev-marine-010318-095047.

Kunze, E., Dower, J. F., Beveridge, I., Dewey, R., and Bartlett, K. P. (2006). Observations of biologically generated turbulence in a coastal inlet. *Science.*, 313(5794):1768–1770. doi:10.1126/science.1129378.

Lévy, M., Franks, P. J. S., and Smith, K. S. (2018). The role of submesoscale currents in structuring marine ecosystems. *Nature Communications*, 9(1):4758. doi:10.1038/s41467-018-07059-3.

Lorenzen, C. J. (1972). Extinction of light in the ocean by phytoplankton. *ICES Journal of Marine Science*, 34(2):262–267. doi:10.1093/icesjms/34.2.262.

Lorke, A. and Probsta, W. N. (2010). In situ measurements of turbulence in fish shoals. *Limnology and Oceanography*, 55(1):354–364. doi:10.4319/lo.2010.55.1.0354.

Luedin, S. M., Liechti, N., Cox, R. P., Danza, F., Frigaard, N.-U., Posth, N. R., Pothier, J. F., Roman, S., Storelli, N., Wittwer, M., and Tonolla, M. (2019). Draft genome sequence of Chromatium okenii isolated from the stratified alpine Lake Cadagno. *Scientific Reports*, 9(1):1936. doi:10.1038/s41598-018-38202-1.

Ng, S. M. Y., Antenucci, J. P., Hipsey, M. R., Tibor, G., and Zohary, T. (2011). Physical controls on the spatial evolution of a dinoflagellate bloom in a large lake. *Limnology and Oceanography*, 56(6):2265–2281. doi:10.4319/lo.2011.56.6.2265.

Noss, C. and Lorke, A. (2014). Direct observation of biomixing by vertically migrating zooplankton. *Limnology and Oceanography*, 59(3):724–732. doi:10.4319/lo.2014.59.3.0724.

Osborn, T. R. (1980). Estimates of the local rate of vertical diffusion from dissipation measurements. *Journal of Physical Oceanography*, 10(1):83–89. doi:10.1175/1520-0485(1980)010<0083:EOTLRO>2.0.CO;2.

Osborn, T. R. and Cox, C. S. (1972). Oceanic fine structure. *Geophysical Fluid Dynamics*, 3(1):321–345. doi:10.1080/03091927208236085.

Oschlies, A. and Garçon, V. (1998). Eddy-induced enhancement of primary production in a model of the North Atlantic Ocean. *Nature*, 394(6690):266–269. doi:10.1038/28373.

Quraishi, A., Bahr, A., Schill, F., and Martinoli, A. (2018). Autonomous feature tracing and adaptive sampling in real-world underwater environments. In *2018 IEEE International Conference on Robotics and Automation (ICRA)*, pages 5699–5704. IEEE.

Ruddick, B., Anis, A., and Thompson, K. (2000). Maximum likelihood spectral fitting: The Batchelor spectrum. *Journal of Atmospheric and Oceanic Technology*, 17(11):1541–1555. doi:10.1175/1520-0426(2000)017<1541:MLSFTB>2.0.CO;2.

Sathyendranath, S., Gouveia, A. D., Shetye, S. R., Ravindran, P., and Platt, T. (1991). Biological control of surface temperature in the Arabian Sea. *Nature*, 349(6304):54–56. doi:10.1038/349054a0.

Schanz, F. (1985). Vertical light attenuation and phytoplankton development in Lake Zürich. *Limnology and Oceanography*, 30(2):299–310. doi:10.4319/lo.1985.30.2.0299.

Schanz, F., Fischer-Romero, C., and Bachofen, R. (1998). Photosynthetic production and photoadaptation of phototrophic sulfur bacteria in Lake Cadagno (Switzerland). *Limnology and Oceanography*, 43(6):1262–1269. doi:10.4319/lo.1998.43.6.1262.

Schill, F., Bahr, A., and Martinoli, A. (2018). Vertex: A new distributed underwater robotic platform for environmental monitoring. In Groß, R., Kolling, A., Berman, S., Frazzoli, E., Martinoli, A., Matsuno, F., and Melvin, G., editors, *Distributed Autonomous Robotic Systems. Springer Proceedings in Advanced Robotics, vol 6*, pages 679–693. Springer, Cham.

References

Sepúlveda Steiner, O., Bouffard, D., and Wüest, A. (2019). Convection-diffusion competition within mixed layers of stratified natural waters. *Geophysical Research Letters*, 46(22):13199–13208. doi:10.1029/2019GL085361.

Simoncelli, S., Thackeray, S. J., and Wain, D. J. (2018). On biogenic turbulence production and mixing from vertically migrating zooplankton in lakes. *Aquatic Sciences*, 80(4):35. doi:10.1007/s00027-018-0586-z.

Sommer, T., Carpenter, J. R., Schmid, M., Lueck, R. G., and Wüest, A. (2013). Revisiting microstructure sensor responses with implications for double-diffusive fluxes. *Journal of Atmospheric and Oceanic Technology*, 30(8):1907–1923. doi:10.1175/JTECH-D-12-00272.1.

Sommer, T., Danza, F., Berg, J., Sengupta, A., Constantinescu, G., Tokyay, T., Bürgmann, H., Dressler, Y., Sepúlveda Steiner, O., Schubert, C. J., Tonolla, M., and Wüest, A. (2017). Bacteria-induced mixing in natural waters. *Geophysical Research Letters*, 44(18):9424–9432. doi:10.1002/2017GL074868.

Steinbuck, J. V., Stacey, M. T., McManus, M. A., Cheriton, O. M., and Ryan, J. P. (2009a). Observations of turbulent mixing in a phytoplankton thin layer: Implications for formation, maintenance, and breakdown. *Limnology and Oceanography*, 54(4):1353–1368. doi:10.4319/lo.2009.54.4.1353.

Steinbuck, J. V., Stacey, M. T., and Monismith, S. G. (2009b). An Evaluation of χT estimation techniques: Implications for Batchelor fitting and ϵ. *Journal of Atmospheric and Oceanic Technology*, 26(8):1652–1662. doi:10.1175/2009JTECHO611.1.

Strutton, P. G. and Chavez, F. P. (2004). Biological heating in the equatorial Pacific: Observed variability and potential for real-time calculation. *Journal of Climate*, 17(5):1097–1109. doi:10.1175/1520-0442(2004)017<1097:BHITEP>2.0.CO;2.

Thorpe, S. A. (1977). Turbulence and mixing in a Scottish Loch. *Philosophical Transactions of the Royal Society A: Mathematical, Physical and Engineering Sciences*, 286(1334):125–181. doi:10.1098/rsta.1977.0112.

Tonolla, M., Demarta, A., Peduzzi, R., and Hahn, D. (1999). In situ analysis of phototrophic sulfur bacteria in the chemocline of meromictic Lake Cadagno (Switzerland). *Applied and Environmental Microbiology*, 65(3):1325–1330.

Turner, J. S. (1973). *Buoyancy effects in fluids*. Cambridge University Press.

Uhde, M. (1992). Mischungsprozesse im Hypolimnion des meromiktischen Lago Cadagno: Eine Untersuchung mit Hilfe natürlicher und künstlicher Tracer. Master Thesis, University of Freiburg, Germany.

Viaroli, P., Azzoni, R., Bartoli, M., Iacumin, P., Longhi, D., Mosello, R., Rogora, M., Rossetti, G., Salmaso, N., and Nizzoli, D. (2018). Persistence of meromixis and its effects on redox conditions and trophic status in Lake Idro (Southern Alps, Italy). *Hydrobiologia*, 824(1):51–69. doi:10.1007/s10750-018-3767-9.

Weimer, W. C. and Lee, F. F. (1973). Some considerations of the chemical limnology of meromictic Lake Mary. *Limnology and Oceanography*, 18(3):414–425. doi:10.4319/lo.1973.18.3.0414.

Weiss, R. F., Carmack Carmack, E. C., and Koropalov, V. M. (1991). Deep-water renewal and biological production in Lake Baikal. *Nature*, 349(6311):665–669. doi:10.1038/349665a0.

Wüest, A. (1994). Interactions in lakes: Biology as source of dominant physical forces. *Limnologica*, 24(2):93–104.

Wüest, A., Piepke, G., and Halfman, J. (1996). Combined effects of dissolved solids and temperature on the density stratification of Lake Malawi (East Africa). In Johnson, T. C. and Odada, E. O., editors, *The Limnology, Climatology and Paleoclimatology of the East African Lakes,* pages 183–202. Gordon and Breach Scientific Publishers, New York.

Wüest, A., Piepke, G., and Van Senden, D. C. (2000). Turbulent kinetic energy balance as a tool for estimating vertical diffusivity in wind-forced stratified waters. *Limnology and Oceanograhy,* 45(6):1388–1400. doi:10.4319/lo.2000.45.6.1388.

Supporting information for Chapter 3
Persistence of bioconvection-induced mixed layers in a stratified lake

Oscar Sepúlveda Steiner[1]**, Damien Bouffard**[2]**, and Alfred Wüest**[1,2]

[1]Physics of Aquatic Systems Laboratory, Margaretha Kamprad Chair, Institute of Environmental Engineering, École Polytechnique Fédérale de Lausanne, Lausanne, Switzerland.

[2]Department of Surface Waters – Research and Management, Eawag, Swiss Federal Institute of Aquatic Science and Technology, Kastanienbaum, Switzerland.
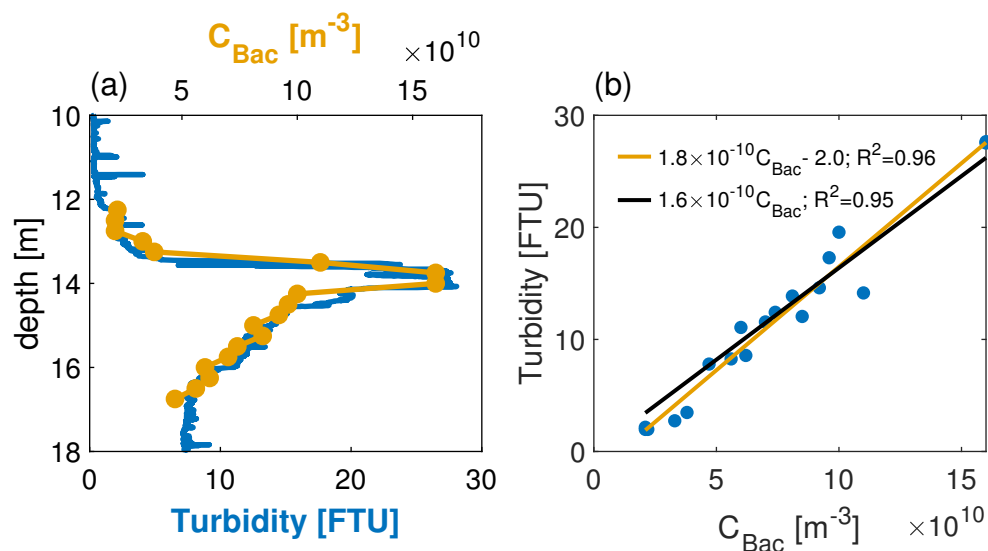
Figure S3.1 – (a) Turbidity profile (blue) measured with Sea & Sun CTD profiler accompanied by *C. okenii* concentration (C_{Bac}; orange) profile, measured during the afternoon of 29 August 2018 (Courtesy of Nicola Storelli and Mauro Tonolla). Concentrations were obtained by flow-cytometry analysis of water samples collected at the indicated depths. The reader is referred to Danza et al. (2017) for details in the treatment and preparation of samples and analysis. (b) Turbidity versus *C. okenii* concentrations (blue dots). The orange and black lines correspond to linear regression of the presented data, with the black line being forced to intersect with zero.

Text S3.1

Turbidity (Tu) profile information can also be used to interpret convection-diffusion competition from measured turbidity profiles containing a peak. The model is similar to the mixed layer (ML)-shape model developed by Sepúlveda Steiner et al. (2019). It aims to define the extent of upper and lower bounds of a turbidity peak affected by vertical turbulent diffusivity. The model is derived from the 1D vertical diffusion equation given a hat function (i.e. fully convective ML; see Figure S2b – red line) of thickness h and peak Tu_p as initial condition. Considering a Dirichlet boundary condition representing a residual turbidity Tu_{res} (above and below the peak) and applying the superposition method, a pseudo-analytical solution that recovers the boundary conditions is given by:

$$Tu(z) = \frac{Tu_p}{2}\left[1 + \text{erf}\left(\frac{\frac{h}{2} + (z - z_o)}{\delta}\right)\right] + \frac{Tu_p}{2}\left[1 + \text{erf}\left(\frac{\frac{h}{2} - (z - z_o)}{\delta}\right)\right] - Tu_p + Tu_{res} \qquad \text{(S3.1)}$$

where z is positive downward, z_o is the center of the Tu peak, and $\delta = \sqrt{4K\tau}$ is the diffusive length with vertical diffusivity K and diffusive timescale τ. By defining parameters in Eq. S3.1 as positive, it is straightforward to verify that this function satisfies the 1D diffusion equation. Fitting this function to measured data provides the required information (δ).

The measured profiles presented a different background turbidity above and below the peak (e.g. Figure 3.1 in the main text and Figure S3.1). Despite the usage of Dirichlet boundary conditions to deduct Eq. S3.1, the same expression can be extended to also account for these turbidity differences outside the peak zone (also expanding the domain for evaluation). By adding to Eq. S3.1 a diffusive step-like function (SF) with an increment imposed at the position z_o, a profile with different turbidity above and below the peak can be achieved. The modified function reads:

$$Tu(z) = \frac{Tu_p}{2}\left[1 + \text{erf}\left(\frac{\frac{h}{2} + (z - z_o)}{\delta}\right)\right] + \frac{Tu_p}{2}\left[1 + \text{erf}\left(\frac{\frac{h}{2} - (z - z_o)}{\delta}\right)\right]$$
$$+ (Tu_b - Tu_{res})\left[1 + \text{erf}\left(\frac{-\frac{h}{2} + (z - z_o)}{\delta}\right)\right] - Tu_p + Tu_{res} \qquad \text{(S3.2)}$$

where $(Tu_b - Tu_{res})\left[1 + \text{erf}\left(\frac{-\frac{h}{2} + (z - z_o)}{\delta}\right)\right] = SF$ and Tu_b is the turbidity below the peak. This modified function also satisfies the 1D diffusion equation. Finally, after the background correction, the turbidity at the peak is given by:

$$Tu_{peak} = Tu_+ Tu_{res} \qquad \text{(S3.3)}$$

Information from the profiles is extracted by fitting turbidity data to the Tu-model, similarly to the ML-shape model. In this case, the fitting procedure consists on minimizing the least squares between the Tu-model and measured profiles. Additionally, to ensure a minimal (and positive) value of $h_{mix} = h - 4\delta$, the optimization has to satisfy the additional constrain:

$$h - 4\delta \geq 0.15m \qquad \text{(S3.4)}$$

An evaluation of this method, accompanied with a comparison of the ML-shape model, is presented in Figure S3.2. Each measured turbidity profile was analyzed with this procedure. The results of the estimated parameters are presented in Table S3.1 grouped by daytime and nighttime periods.

The h_{mix} estimates from the Tu-model are clearly smaller than those obtained with the ML-shape model (Table 3.2; main text). Since turbidity distribution responds to bacteria concentration (Figure S3.1), additional processes such as bacterial migration, sinking and mortality may explain the resulting difference between models. Further research is needed to couple the ML-shape and Tu models. However, all the estimated parameters and particularly δ , show minor differences between daytime and nighttime periods, which is consistent with the rest of the small-scale analysis.
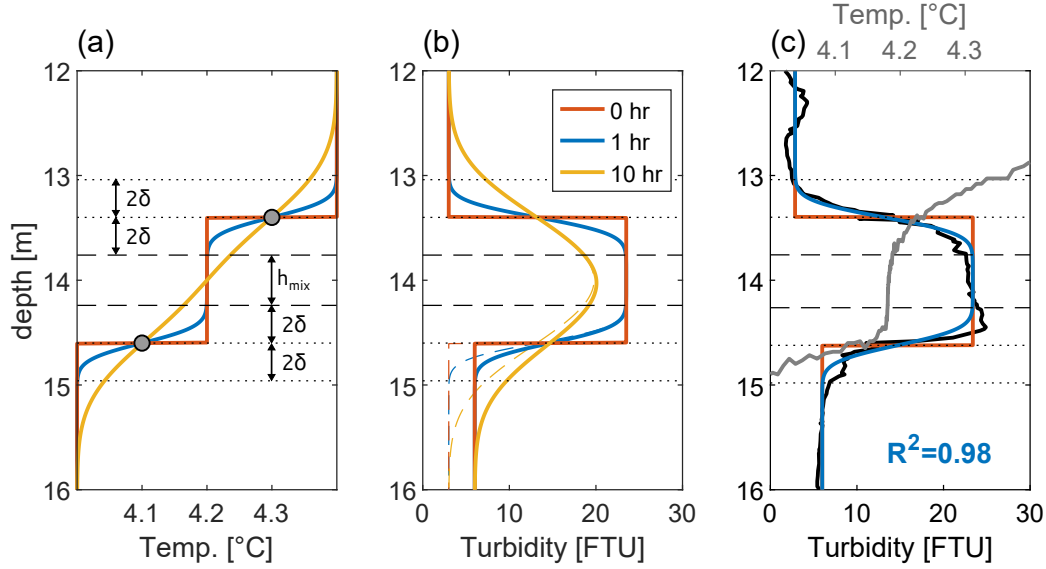

Figure S3.2 – Comparison of the ML-shape model (Φ_T) with the Turbidity (Tu) model. (a) ML-shape model for temperature. (b) Tu-model (Eq. S3.2). Calculations in (a) and (b) were performed with $K = 2.8 \times 10^{-6}$ m^2 s^{-1} ($\delta = \sqrt{4Kt}$) and share the same legend (approximated times in hr). The parameter $h_{mix} = h - 4\delta$ is the mixed layer thickness. Gray dots in (a) represent the vertical range for which the ML-shape model is considered valid (Sepúlveda Steiner et al. 2019). Colored dashed lines in (b) correspond to the symmetric version (Eq. S3.1) of the Tu-model. (c) Example of the Tu-model performance against a measured (16 Aug 2018 4am) turbidity profile (black) with its respective fitting (blue) and the deducted initial condition (red). Temperature profile shown for comparison in gray. Vertical spikes in the temperature profile are due to hand lowering of the CTD profiler.

Table S3.1 – Parameters estimated with the Tu-model.

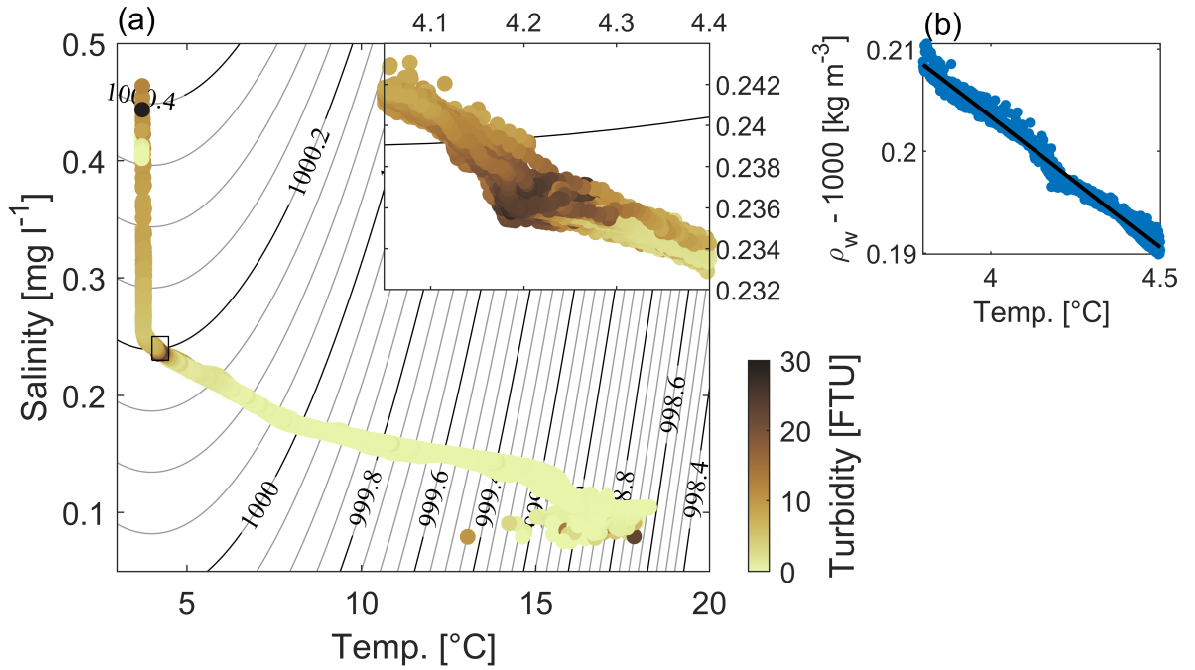| Parameter	Units	All	Daytime	Nighttime
z_o	[m]	14.1 ± 0.3	14.1 ± 0.4	14.1 ± 0.2
h	[m]	1.1 ± 0.2	1.1 ± 0.3	1.1 ± 0.2
δ	[m]	0.22 ± 0.05	0.22 ± 0.05	0.23 ± 0.05
Tu_{peak}	[FTU]	22.0 ± 3.5	22.2 ± 3.6	21.8 ± 3.4
Tu_b	[FTU]	6.5 ± 0.7	6.4 ± 0.6	6.7 ± 0.7
T_{res}	[FTU]	3.1 ± 1.2	3.1 ± 1.4	3.1 ± 1.0
h_{mix}	[m]	0.23 ± 0.16	0.26 ± 0.19	0.20 ± 0.12
R^2	[-]	0.94	0.93	0.94

Figure S3.3 – (a) Temperature-salinity (T-S) diagram color-coded for turbidity. The data was collected with a Sea & Sun CTD profiler. Water density (ρ_w) values (gray and black lines) are obtained following the methods described in the main text and using the specific ion water composition of Lake Cadagno. Inset corresponds to an enlargement (black square in (a)) of the turbid zone, characteristic of the bacterial layer. (b) Water density compared to temperature in the turbid layer (blue dots). Black line corresponds to a resulting data fit $\rho_w = -0.03\,T + 1000.3$ ($R^2 = 0.99$); for $3.8 \leq T \leq 4.5$.
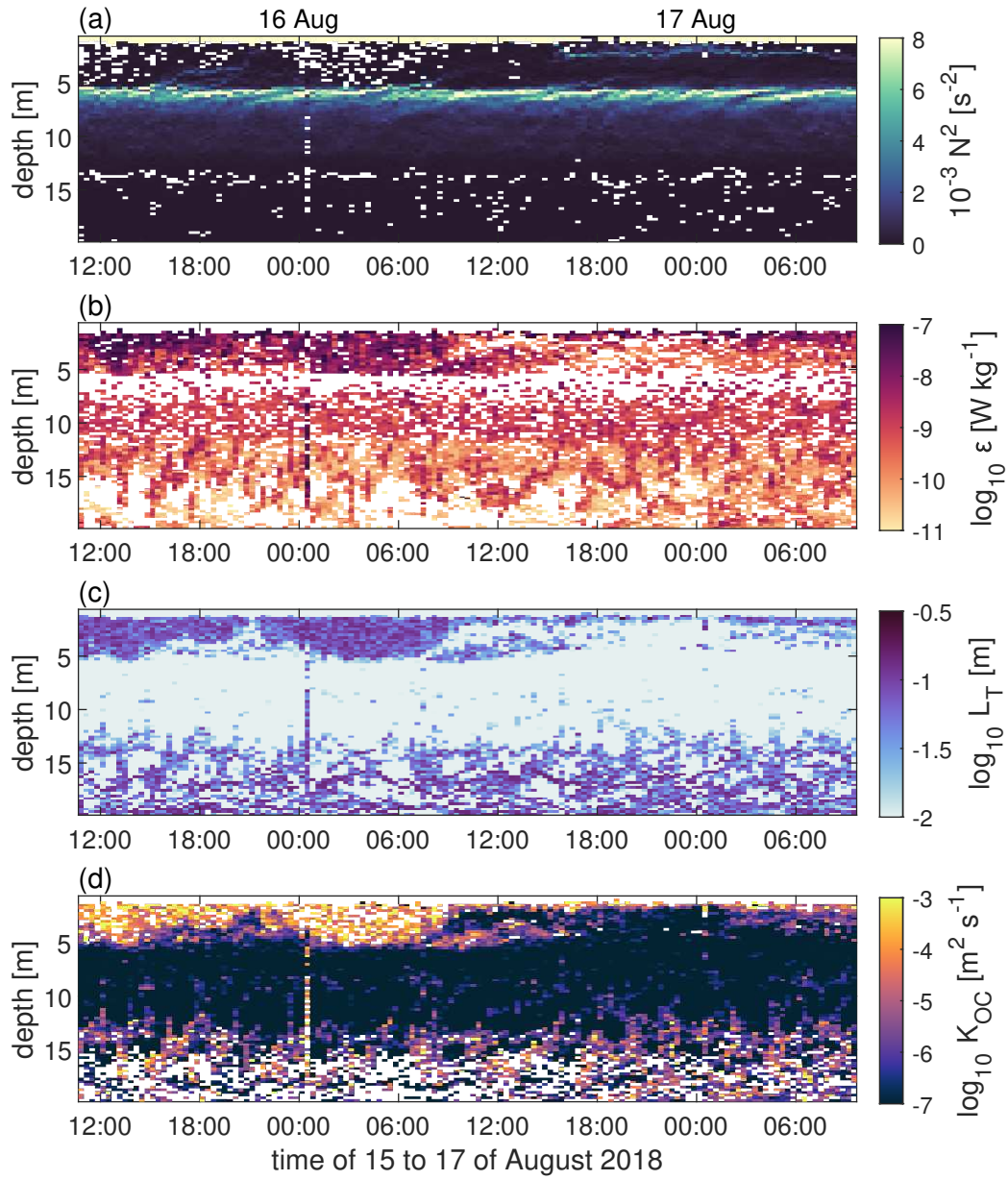
Figure S3.4 – Time evolution of microstructure-based stability and turbulent quantities. (a) Stability (N^2). (b) rate of turbulent kinetic energy dissipation (ε). (c) Thorpe scale of overturns (L_T). (d) Diffusivity following the Osborn and Cox (1972) model (K_{OC}). Calculations were performed using 0.25 m vertical bins. White-colored bins correspond to unstable values of N^2 in (a), whereas in (b) and (d) they indicate badly resolved spectra and/or to rejected spectra according to the Batchelor fitting procedure.
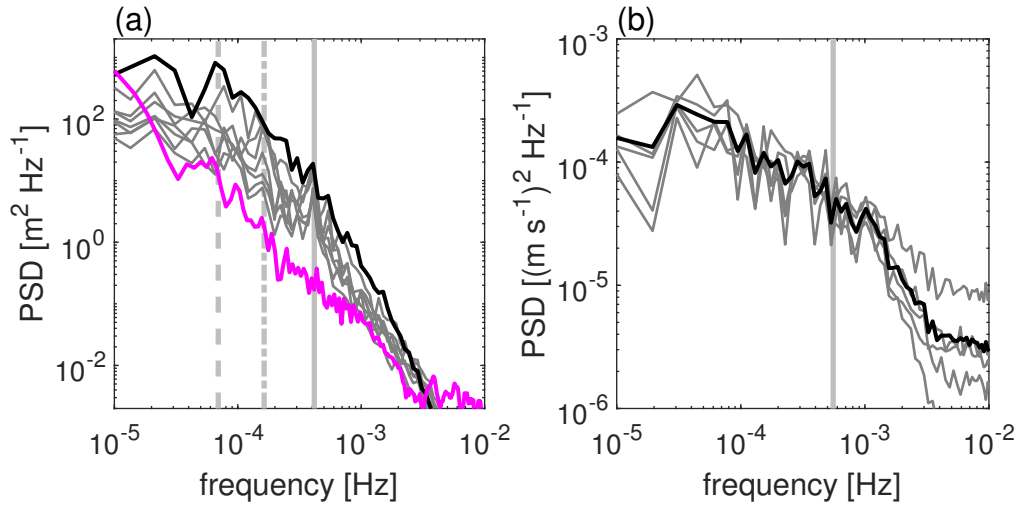
Figure S3.5 – Spectral analysis of time series. (a) Power spectral density (PSD) of isothermal depths corresponding to 5.5° – 9.5° C (gray lines) and 4.5° C (black line). Vertical light gray lines correspond to energized wave periods corresponding of 4.0, 1.7 and 0.6 hr. Additionally, the PSD of the turbidity sensor located at 12.9 m depth (HR-mooring) is shown in magenta (units: Hz^{-1}; normalized by its maximum value). This PSD also shows a 0.6 hr energized period suggesting that the turbidity layer location responds to vertical displacements induced by internal seiches. (b) Power spectral density of the vertical velocities measured with the Aquadopp current profiles (HR-mooring). Gray lines correspond to measurements performed at 13 to 14 m depth (with 0.25 m intervals) the average of these measurements is presented in black. The vertical light gray line correspond to the convective time scale deducted from microstructure measurement ($\tau_* \approx 30$ min).
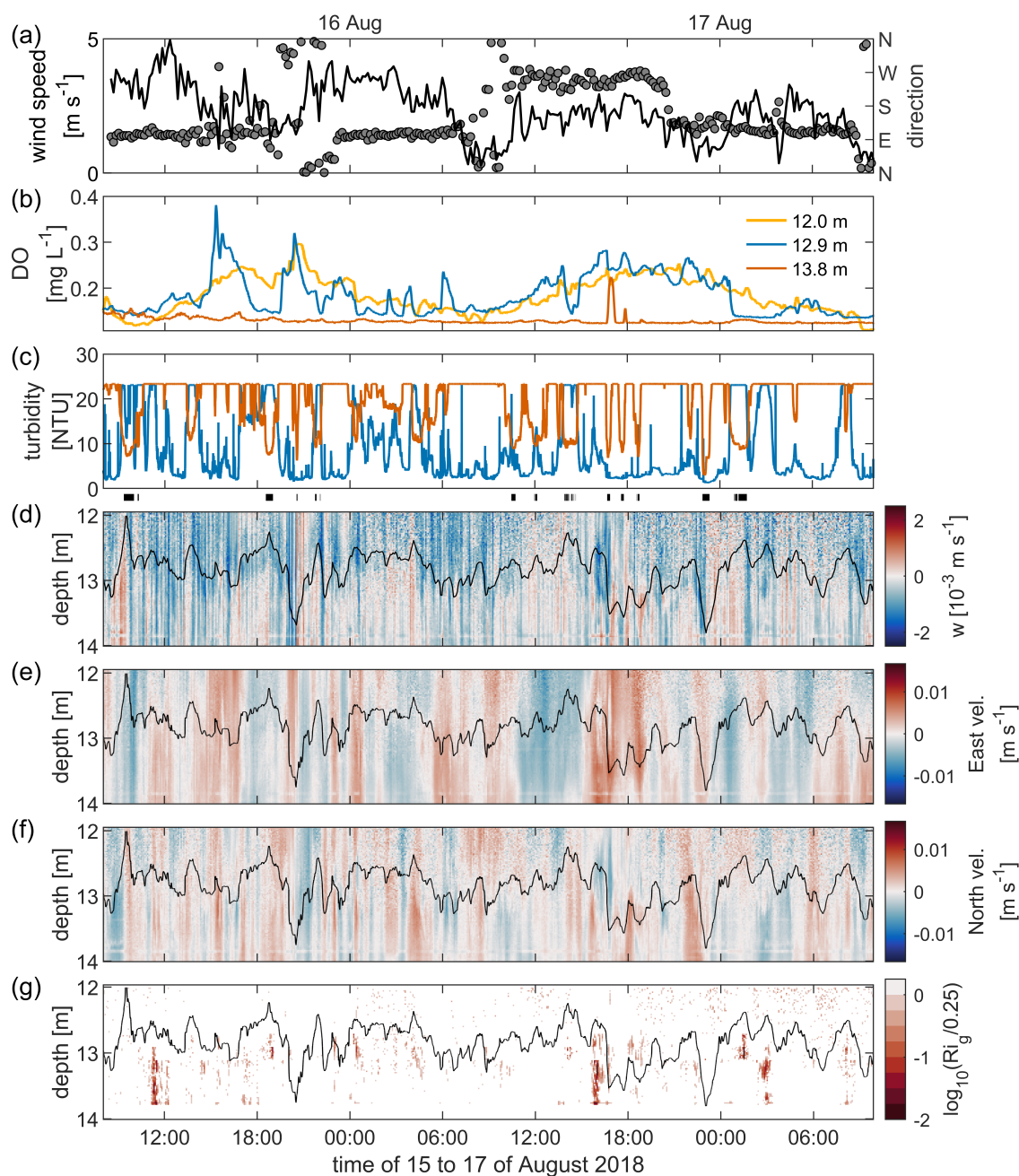
Figure S3.6 – HR-mooring results and gradient Richardson number (Ri_g) calculations. (a) Wind speed (black line) and direction (circles; directions relative to the North). (b) Dissolved oxygen (DO) at the three assessed depths. (c) Turbidity. Lines color-code is analog to (b). (d, e and f) vertical (w), eastward and northward velocity component, respectively, measured with the Aquadopp HR profiler. (g) gradient Richardson number calculation normalized by the critical value 0.25. Thick black line between panels (c) and (b) correspond to measurement of turbidity at 13.8 exceeding 10 NTU, i.e. measurement performed within the bacterial layer.
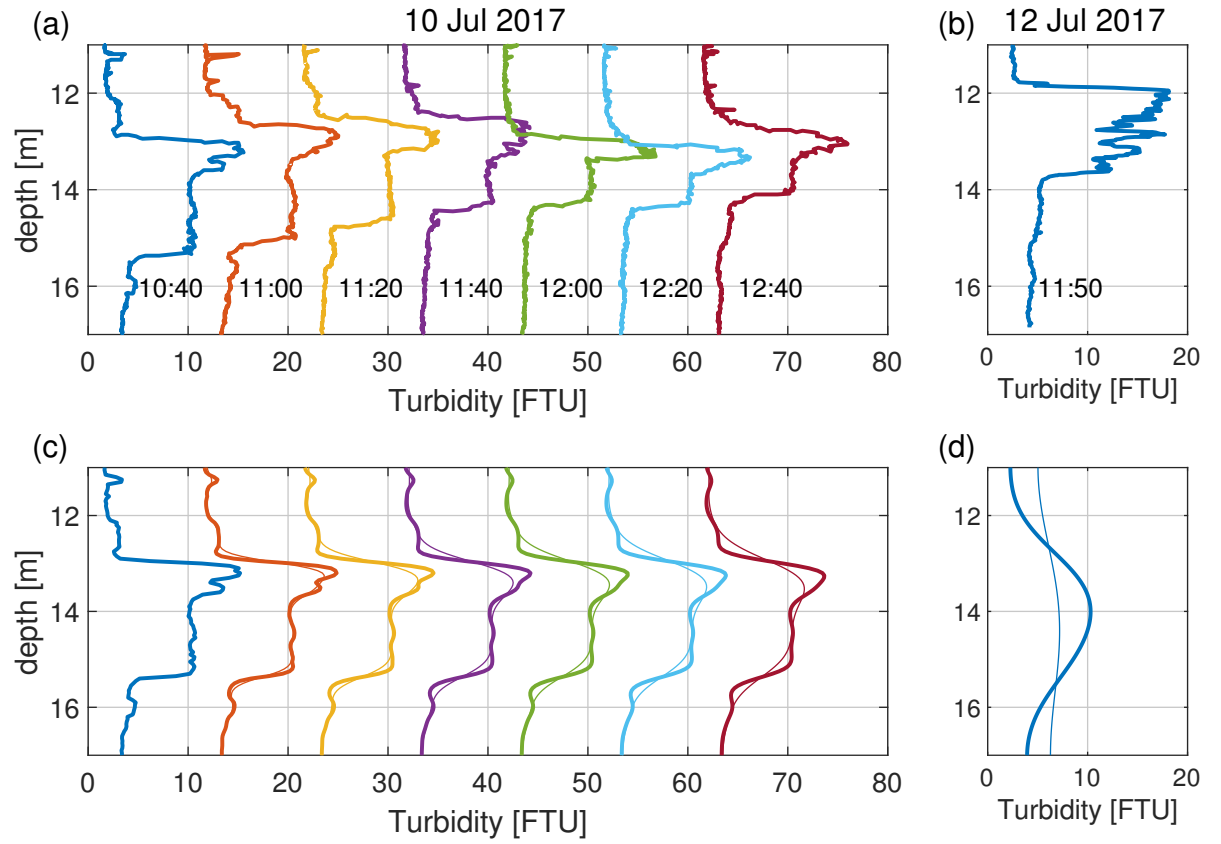
Figure S3.7 – (a) Waterfall plot of Turbidity profiles measured on the 12 Jul 2017. Profiles are presented with an offset of 10 FTU between each other. (b) Turbidity profile measured 48 hrs later. (c) Evaluation of the effect of background diffusivity on a turbidity profile considering an inactive layer (i.e. no changes due to bacteria swimming). Profiles are obtained by considering the initial profile in (a) subject to no-flux (Neumann) boundary conditions (at 11 and 17 m depth, respectively) and applying a numerical scheme to solve the 1D vertical diffusion equation for constant background diffusion. The time of each profile is analogous to (a). Thick lines correspond to $K_{W94} = 1.6 \times 10^{-6}$ m^2 s^{-1} and thin lines to $K_{Ocean} \approx 1.0 \times 10^{-5}$ m^2 s^{-1} (Waterhouse et al., 2014). (d) Same as (c) after an elapsed time of 48 hrs. Profiles measured in July 2017 exhibit peak concentrations 10 FTU lower than those measured in August 2018. This difference is explained by the timing within the season, where early July still corresponds to bacterial layer formation stage.

Text S3.2

An evaluation of the sinking speed of a single *Chromatium okenii* cell is performed following the concept of Stokes sedimentation. The shape of C. okenii has been reported as rod (Imhoff, 2015), which can be modelled as a long ellipsoid with $a_1 \gg a_2 = a_3$ (Figure S3.8a). Assuming this idealized geometry and considering sinking parallel to its long axis, an expression for the Stokes sedimentation speed is provided by following Guazzelli and Morris (2011):

$$U_s = \frac{1}{6} \frac{a_2^2}{\mu} \left[\ln\left(\frac{2a_1}{a_2}\right) \frac{1}{2} \right] (\rho_{Bac} - \rho_o) g \tag{S3.5}$$

where μ is the dynamic viscosity, $g = 9.81$ m s^{-2} is the gravitational acceleration and $(\rho_{Bac} - \rho_o) = 150$ kg m^{-3} (Sommer et al., 2017) is the density excess of bacteria compared to the ambient fluid. An evaluation of the Stokes sedimentation for different cell dimensions (reported in Imhoff, 2015) is detailed in Figure S3.8.
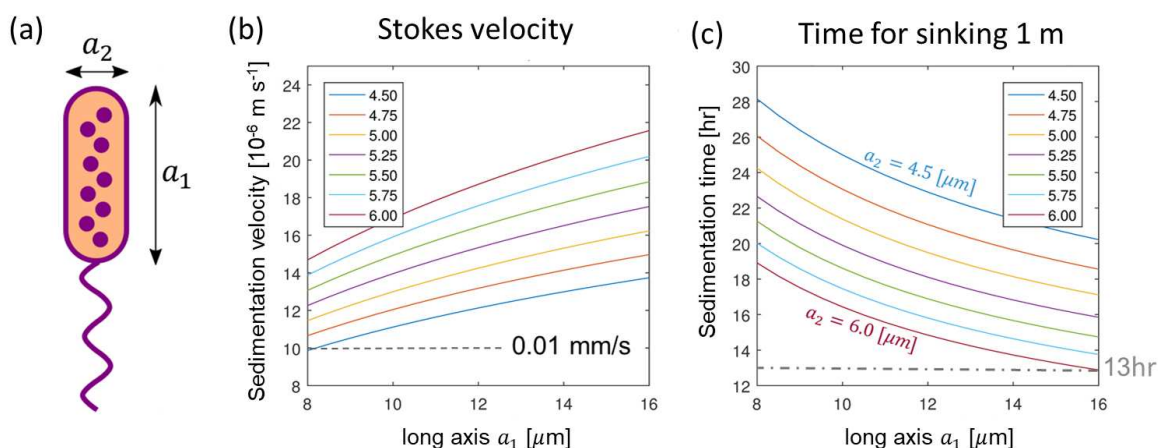

Figure S3.8 – Evaluation of the Stokes sedimentation for *C. okenii*. (a) rod shape schematic. (b) Sedimentation velocity as a function of the different lengths reported for the long (a_1) and secondary (a_2) axes. (c) Time for sinking 1 m as a function of the reported lengths for the long and secondary axes.

References

Danza, F., Storelli, N., Roman, S., Lüdin, S., and Tonolla, M. (2017). Dynamic cellular complexity of anoxygenic phototrophic sulfur bacteria in the chemocline of meromictic Lake Cadagno. *PLoS ONE*, 12(12):e0189510. doi:10.1371/journal.pone.0189510.

Guazzelli, E. and Morris, J. F. (2011). *A Physical Introduction to Suspension Dynamics*. Cambridge University Press, Cambridge.

Imhoff, J. F. (2015). Chromatium. In *Bergey's Manual of Systematics of Archaea and Bacteria*, pages 1–8. John Wiley & Sons, Ltd, Chichester, UK.

Osborn, T. R. and Cox, C. S. (1972). Oceanic fine structure. *Geophysical Fluid Dynamics*, 3(1):321–345. doi:10.1080/03091927208236085.

Sepúlveda Steiner, O., Bouffard, D., and Wüest, A. (2019). Convection-diffusion competition within mixed layers of stratified natural waters. *Geophysical Research Letters*, 46(22):13199–13208. doi:10.1029/2019GL085361.

Sommer, T., Danza, F., Berg, J., Sengupta, A., Constantinescu, G., Tokyay, T., Bürgmann, H., Dressler, Y., Sepúlveda Steiner, O., Schubert, C. J., Tonolla, M., and Wüest, A. (2017). Bacteria-induced mixing in natural waters. *Geophysical Research Letters*, 44(18):9424–9432. doi:10.1002/2017GL074868.

Waterhouse, A. F., MacKinnon, J. A., Nash, J. D., Alford, M. H., Kunze, E., Simmons, H. L., Polzin, K. L., St. Laurent, L. C., Sun, O. M., Pinkel, R., Talley, L. D., Whalen, C. B., Huussen, T. N., Carter, G. S., Fer, I., Waterman, S., Naveira Garabato, A. C., Sanford, T. B., and Lee, C. M. (2014). Global patterns of diapycnal mixing from measurements of the turbulent dissipation rate. *Journal of Physical Oceanography*, 44(7):1854–1872. doi:10.1175/JPO-D-13-0104.1.

4 Inhibited vertical mixing and the seasonal persistence of a cyanobacterial thin layer in a stratified lake

Bieito Fernández-Castro[1]**, Oscar Sepúlveda Steiner**[1]**, Deborah Knapp**[2]**, Thomas Posch**[2]**, Damien Bouffard**[3]**, and Alfred Wüest**[1,3]

[1]Physics of Aquatic Systems Laboratory, Margaretha Kamprad Chair, Institute of Environmental Engineering, École Polytechnique Fédérale de Lausanne, Lausanne, Switzerland.

[2]Limnological Station, Department of Plant and Microbial Biology, University of Zurich, Seestrasse 187, Kilchberg, Switzerland

[3]Department of Surface Waters – Research and Management, Eawag, Swiss Federal Institute of Aquatic Science and Technology, Kastanienbaum, Switzerland.

Abstract

Thin layers of plankton are ecologically relevant features of lakes and oceans. Due to their small size and high dynamism, the mechanisms controlling their formation and breakdown are poorly documented, but turbulent mixing is considered a key factor. Filamentous harmful cyanobacteria *Planktothrix rubescens* accumulate every stratified season (May–October) in an unusually persistent thin layer in the thermocline of Lake Zurich (Switzerland). With three surveys (April, July, October 2018), including microstructure profiles and high-resolution mooring measurements, we characterized the seasonal variations of turbulence in Lake Zurich in order to understand its role on the formation, persistence and decline of the *P. rubescens* layer. In July and October, the thin layer was associated with a strong thermocline where turbulent kinetic energy dissipation rates were relatively high ($\varepsilon \approx 10^{-8} - 10^{-7}$ W kg^{-1}), but vertical turbulent motions were suppressed, with overturns –described by the Thorpe scale– undetectable most of the time, and, when observed, smaller than the Ozmidov scale ($L_O \approx 1$ cm). As a consequence, mixing efficiency was very low ($\Gamma \approx 0.001$) and vertical diffusivity was hardly above molecular. This reduced wind-driven metalimnetic mixing explains the persistence of the thin layer, which starts to dissolve not before the mixed-layer deepens in late-summer/fall. With bi-weekly temperature profiles in 2018 and a nighttime microstructure sampling in September 2019, we showed that this deepening, and the layer breakdown, are driven by nighttime convection. These results highlight the ecological relevance of convective mixing in medium-sized stratified lakes exposed to light winds, where wind stirring has limited effect on vertical fluxes.

4.1 Introduction

Lakes, oceans and other water bodies become density-stratified during at least part of the annual cycle (Boehrer and Schultze, 2008; Simpson and Sharples, 2012). During the stratified period, the vertical distribution of density often presents a three layer structure, with a relatively warm surface mixed-layer (epilimnion) and a cooler, weakly stratified deep layer (hypolimnion), separated by variably sharp transition (metalimnion or thermocline). Density stratification limits the vertical exchange of mass, momentum, heat, dissolved and suspended matter, which is mainly driven by turbulent mixing (Imboden and Wüest, 1995; Wüest and Lorke, 2003). In stratified lakes, wind stress at the surface is considered the main energy source for interior mixing (Wüest et al., 2000; Stevens and Imberger, 1996). Wind forcing induces relative movement of the stratified layers, exciting internal modes of oscillation (Csanady, 1975) and high frequency propagating waves (Boegman et al., 2003), which can become unstable and generate turbulence (Lorke et al., 2005; Preusse et al., 2010).

The interplay between water column stability and turbulent mixing plays a prominent role in biogeochemical processes, shaping the aquatic ecosystem, and particularly phytoplankton growth (Spigel and Imberger, 1987; Huisman et al., 1999). The thermocline constitutes an ecological niche for certain planktonic species, frequently giving rise to the formation of sub-surface chlorophyll maxima, both in lakes and oceans (Abbott et al., 1984; Cullen, 2015; Leach et al., 2018). This niche results from water-column stability and from a trade-off between light and nutrient availability, which depends on turbulent fluxes from deeper layers (MacIntyre et al., 2006; Rippeth et al., 2009; Sharples et al., 2001). Thin plankton layers are an extremely narrow (typically < 5 m) and sharp variety of sub-surface chlorophyll maxima (Dekshenieks et al., 2001; Durham and Stocker, 2012). Due to their small vertical size, these structures have been historically under-sampled with standard techniques (Strickland, 1968). Recently, they are receiving growing attention by the scientific community owing to their relevant role as ecological hot-spots (Benoit-Bird et al., 2009), and because they often host harmful algal species (Nielsen et al., 1990; Broullón et al., 2020).

The filamentous harmful cyanobacterium *Planktothrix rubescens* has become the dominant phytoplanktonic species in Lake Zurich (Switzerland) over the last 40 years, coinciding with recovery from strong eutrophication after the 1970's (Posch et al., 2012). As Lake Zurich is a source of drinking water for up to 1 million people, this situation represents an obvious threat to human health. The success of *P. rubescens* is linked to ongoing changes in the nutrient, thermal and stratification/mixing regime of the lake (Yankova et al., 2016, 2017). Thanks to their adaptation to low light and their capacity to control their vertical position via buoyancy regulation with gas vesicles (Walsby and Schanz, 2002; Walsby, 2005), *P. rubescens* proliferate in a sub-surface thin layer that sets up in spring and persists during the whole stratified season (May-October; Posch et al., 2012). The thin layer is located in the thermocline, close or between the depths where the mean daily insolation supports neutral buoyancy and neutral growth, respectively (Walsby et al., 2004).

A few studies have so far reported microstructure measurements characterizing turbulence within and around thin plankton layers in the ocean, and showed that they are often associated with strong stratification and weak turbulent mixing (Sharples et al., 2001; Dekshenieks et al., 2001; McManus et al., 2003; Cheriton et al., 2009; Steinbuck et al., 2009; Shroyer et al., 2014). Although it might be transiently disturbed by internal wave motions (Cuypers et al., 2011), the persistence (~6 months) of the *P. rubescens* thin layer in Lake Zurich is extraordinary compared to its oceanic counterparts, which typically last only for hours or days (Durham and Stocker, 2012). A direct quantification and description of the characteristics of turbulence and mixing allowing for such unusual persistence are currently lacking. A better understanding of these processes is essential to anticipate the mid-term evolution of *P. rubescens* population as a result of changing climatic conditions (Livingstone, 2003; Schmid and Köster, 2016).

The goal of this study is to understand what mixing conditions allow for the extraordinary persistence of the *P. rubescens* thin layer, and what factors drive the seasonal variations that lead to the formation of the layer in spring, and its breakdown in fall. To do so, we quantified turbulent motions and mixing in the thermocline of Lake Zurich using microstructure profilers and high-resolution measurements of velocity and temperature fluctuations during four field campaigns in April, July and October 2018, and September 2019.

The manuscript is organized as follows: first, the methodology and the dataset are described. In the Results section, an overview on the seasonality of stratification conditions and *P. rubescens* population during year 2018 is presented, followed by a detailed description of the turbulence measurements. The Discussion section opens with an interpretation of the turbulence observations from a physical perspective. Secondly, their implications for the formation and maintenance of the *P. rubescens* thin layer are discussed. Finally, the processes driving the dissolution of the layer in fall are assessed before presenting the conclusions.
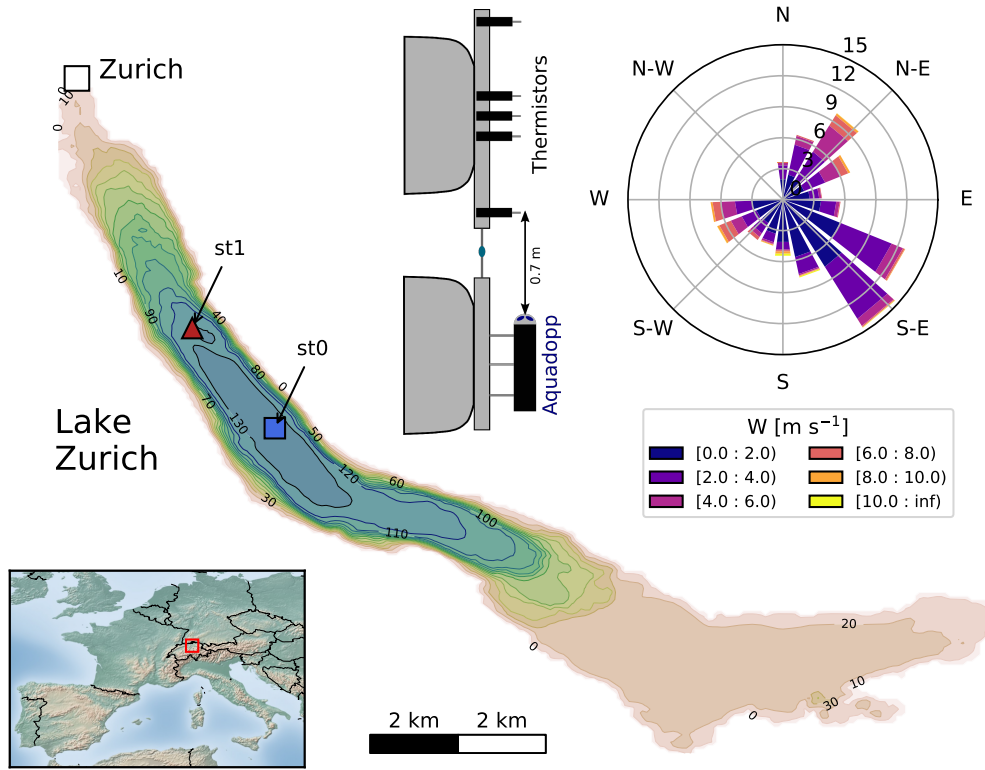

Figure 4.1 – Map of the sampling site at Lake Zurich. The blue square (st0) indicates the location of the long-term monitoring station, the microstructure sampling on September 2019 and the grid-point of the COSMO meteorological model where weather information was collected. The red triangle (st1) indicates the location of the microstructure and mooring samplings during year 2018. A schematic of the HR-mooring, and the wind-rose at st0 during year 2018 are also shown.

4.2 Methods

4.2.1 Study site and sampling overview

Lower Lake Zurich is a long (40 km), narrow (3.8 km), deep (max. depth 136 m), large (65 km^2) peri-alpine lake (Bossard et al., 2001). The seasonal thermal regime of Lake Zurich is typical for deep Central European lakes north of the Alps (Schmid and Köster, 2016). The lake is monomictic with one seasonal deep convective mixing of the water body, occasionally holomixis, in February-March, followed by a period of thermal stratification during summer. Lake Zurich is exposed to light winds mainly from the Northwest (mean $\pm$ SD of 2.6 ± 1.8 m s^{-1} for 2018), canalized along the main lake axis (Figure 4.1). The main mode of baroclinic response to wind forcing in stratified conditions is the first-longitudinal first-vertical seiche mode (~45 hours), with smaller contributions by the second and third longitudinal modes (Horn et al., 1986). The Rossby deformation radius, $Ro = c_f/f$, where f is the Coriolis frequency and c_f is the phase speed for the first vertical baroclinic mode, is larger than the lake's width ($Ro > 3$ km) between May and October, which is consistent with a restricted influence of Earth rotation in the low-frequency baroclinic response of the lake (Horn et al., 1986).

In order to investigate the seasonal variations in mixing conditions, three surveys were carried out on 24–26 April, 17–19 July and 2–4 October 2018 at station st1, located in the Lower Lake Zurich at a depth of 120 m, ~ 3 km from the deepest location (Figure 4.1). During these surveys, series of profiles with microstructure probes were performed (Table 4.1), and high-resolution current and temperature time-series were collected within the thermocline with a moored system (Table 4.2). In order to place this data in a broader seasonal context, we used hydrographic and biological data collected at the deepest point of the lake (st0, Figure 4.1) as part of a long-term monitoring program. Finally, an additional microstructure survey was carried out on 24–25 September 2019 to assess the role of nighttime convection for the seasonal breakdown of the *P. rubescens* layer.

Table 4.1 – Details on the instrument used and number of microstructure profiles collected during each survey. Local time is UTC+2 in all cases. Up and Down stand for free-rising and free-falling profiles, respectively.

Date	Location	Instrument	Time (UTC)	Number of profiles		
				Down	Up	Total
24 April 2018	st1	SCAMP	13:54–15:54	11		11
26 April 2018	st1	SCAMP	10:13–15:26	17		17
Total April				28		28
17 July 2018	st1	VMP	13:50	1		1
18 July 2018	st1	VMP	11:05–13:32	15		15
19 July 2018	st1	VMP	08:56–13:49	14		14
Total July				30		30
02 Oct 2018	st1	VMP	14:22–15:26	5		5
03 Oct 2018	st1	VMP	09:01–10:08	6		6
04 Oct 2018	st1	VMP	08:09–14:13	35		35
Total October				46		46
24–25 Sept 2019	st0	microCTD	14:28–10:28	31	22	53

4.2.2 Microstructure turbulence profiles

Microstructure profiles were collected with three different loose-tether microstructure profilers deployed at st1 (2018) and st0 (2019): a SCAMP (Self-Contained Autonomous Microstructure Profiler, Precision Measurement Engineering, PME) in April 2018, a VMP-500 (Vertical Microstructure Profiler, Rockland Scientific International,

RSI) in July and October 2018, and a microCTD (RSI) on September 2019 (Table 4.1).

The three instruments are equipped with two FP07 thermistors that measure temperature fluctuations with a resolution of 10^{-5} °C and a response time of $\tau \approx 10$ ms (Sommer et al., 2013). The FP07 were sampled at a frequency of 100 Hz (SCAMP) and 512 Hz (VMP and microCTD). Additionally, lower-resolution high-accuracy temperature-conductivity-depth (CTD) and fluorescence sensors were mounted on all three microstructure profilers, to measure the background properties. Lake water salinity and density (ρ) were calculated from the *in situ* temperature and conductivity measurements using lake-specific equations (Wüest et al., 1996). The buoyancy of the instruments was regulated to achieve a free-falling profiling speed of 10 to 20 cm s^{-1} (SCAMP and VMP) and 30 to 40 cm s^{-1} (microCTD). SCAMP and VMP were operated in free-falling mode, while the microCTD was operated alternatively in free-falling and free-rising mode, between the surface and roughly 30 m depth.

Table 4.2 – Details on HR-mooring deployment time, depth and sensors. The HR-mooring was deployed at st1 (Figure 4.1). Local time is UTC+2 in all cases.

Instrument	Accuracy	Time response [s]	Sampling frequency [Hz]	Depths [m]	
				18 July 2018 09:00–17:00 (UTC)	**4 October 2018** 08:00–16:00 (UTC)
Nortek Aquadopp HR profiler (2 MHz)	± 1% of measured values ≥ 0.005 m s^{-1}	–	1	Installation: 13.4 Measurements: 10.84 to 12.9 m; 0.02 m bins	Installation: 12.68 Measurements: 11.13 to 12.19 m; 0.02 m bins
RBRsolo T	± 0.002 °C	~1	2	10.9, 11.6, 11.8, 12.0, 12.7	10.2, 10.9, 11.1, 11.3, 12.0

The dissipation rate of thermal variance,

$$\chi = 6\kappa_T \langle \left(\frac{\partial T'}{\partial z}\right)^2 \rangle \qquad [\text{K}^2\ \text{s}^{-1}] \qquad (4.1)$$

where $\kappa_T = 1.4 \times 10^{-7}$ m^2 s^{-1} is the molecular diffusivity of heat, and the Batchelor wavenumber (k_B) were computed by fitting the power spectra of the vertical temperature gradient fluctuations to the Batchelor spectrum (Batchelor et al., 1959), using the maximum likelihood method (Ruddick et al., 2000). The rate of turbulent kinetic energy (TKE) dissipation (ε) was determined through the Batchelor wavenumber, $k_B = \frac{1}{2\pi}\left(\varepsilon \nu^{-1} \kappa_T^{-2}\right)^{1/4}$ [cpm].

Bad fits were discarded by using the misfit criteria proposed by Ruddick et al. (2000). For the estimation of ε it is also critical to consider the spatial resolution achieved with the thermistors, as this limitation might not necessarily manifest in the miss-fit parameters. Considering the falling speeds of the different instruments and the sensor time-response, the maximum k_B that can be resolved are ~ 670 cpm and ~ 280 cpm, for SCAMP/VMP and microCTD, respectively. Those values correspond to $\varepsilon \approx 6 \times 10^{-6}$ W kg^{-1} and $\approx 2 \times 10^{-7}$ W kg^{-1}, which are the maximum ε values that can be adequately resolved with the SCAMP/VMP and microCTD, respectively. Due to perturbations of the falling profiler by abrupt changes in ambient density or cable strumming, some unrealistically high values of the dissipation rates occurred when sampling with the VMP. Those spikes were removed. Seemingly, due to the difficulties to operate the microCTD in rising mode from a small ship under moderate winds, the lower parts of the profiles were often contaminated, and these values were also removed.

The vertical turbulent heat diffusivity was calculated using the Osborn and Cox (1972) model,

$$K_T = \frac{\chi}{2(\partial \overline{T}/\partial z)^2} \qquad [\text{m}^2 \text{ s}^{-1}] \tag{4.2}$$

Turbulent stirring transfers the variance contained in the large-scale gradients, such as of temperature, to the smaller scales, boosting the action of molecular diffusion, and increasing the rate of mixing. This effect was quantified with the Cox number, $C = K_T/\kappa_T$.

Mixing efficiency was calculated as the ratio of the potential energy increase by irreversible mixing (i.e. the buoyancy flux, $B = -K_\rho N^2$, where K_ρ is a turbulent mass diffusivity and N is the buoyancy frequency, $N^2 = -g/\rho \partial \rho/\partial z$) to energy dissipation: $\Gamma = -B/\varepsilon$. For mechanically driven turbulence, it is possible to assume that $K_T = K_\rho$ and the mixing efficiency was calculated as

$$\Gamma = \frac{\chi N^2}{2\varepsilon(\partial \overline{T}/\partial z)^2} \tag{4.3}$$

The vertical size of turbulent overturns was characterized with the Thorpe length-scale (L_T), calculated by comparing the measured temperature with an adiabatically resorted profile (Thorpe, 1977; Lorke and Wüest, 2002). Other relevant scales for turbulence are the Ozmidov ($L_O = (\varepsilon N^{-3})^{1/2}$) and the Kolmogorov length-scales ($L_K = (v^3 \varepsilon^{-1})^{1/4}$), at which inertial forces are in equilibrium with buoyancy and viscosity, respectively. Those length-scales represent the large and small-scale limits of the inertial sub-range of turbulence where inertia is dominant. The ratios of these length-scales, i.e. buoyancy Reynolds number ($Re_b = (L_O/L_K)^{4/3} = \varepsilon v^{-1} N^{-2}$) and the turbulent Froude number ($Fr_T = (L_O/L_T)^{2/3}$), are used to characterize the balance of forces and development of turbulence, and are related to the efficiency of mixing (Ivey and Imberger, 1991; Smyth et al., 2001; Shih et al., 2005; Ijichi and Hibiya, 2018).

4.2.3 High-resolution mooring

A high-resolution (HR) mooring (Figure 4.1) was deployed in the thermocline (∼12 m depth) at station st1, to characterize velocity and temperature fluctuations in and near the thin layer (Table 4.2). The mooring was composed of two fins. Five RBR temperature loggers were installed at different depths on the upper fin and sampled at 2 Hz. Current velocities were measured at 1 Hz using a Nortek Aquadopp HR profiler (2 MHz), installed in the lower fin facing upwards. The Aquadopp measured in 104 bins of 0.02 m size over a range of 2.06 m, covering the vertical extension of the temperature measurements. The HR-mooring was deployed for periods of several hours during several days in April, July and October 2018 close to st1 (Figure 4.1). Due to a number of issues, such as vibrations of the structure, the quality of the data was poor during some deployments. In this paper we analyzed two datasets in July and October that contained data of sufficient quality (Table 4.2).

The three-dimensional current velocities ($v_i = u, v, w$; for eastward, northward and upward currents) measured with the Aquadopp were decomposed into the mean ($\overline{v}_i$) and fluctuating turbulent (v_i') components, $v_i(z,t) = \overline{v}_i - v_i'$. The fluctuating term was calculated by band-pass filtering the measured velocities between twice the local buoyancy frequency (N) and a maximum frequency of 0.1 Hz. This maximum frequency was selected because, the velocity spectra were contaminated by instrumental white noise, mooring vibrations and surface waves at higher frequencies. After band-pass filtering, the vertical mean was subtracted from v_i'. The buoyancy frequency was calculated using the thermistors data as $N^2 = g\alpha \partial T/\partial z$, as stratification was dominated by temperature. Horizontal, vertical and overall turbulent velocity scales were calculated over 5-minutes intervals as $q_h = (\langle u'^2 \rangle + \langle v'^2 \rangle)^{1/2}$, $q_v = (\langle w'^2 \rangle)^{1/2}$ and $q = (\langle u'^2 \rangle + \langle v'^2 \rangle + \langle w'^2 \rangle)^{1/2}$, respectively.

Segments containing data with poor beam correlation ($< 50\%$) were excluded.

TKE dissipation rates (ε) were estimated using the large-eddy method (LEM) (Gargett, 1999). In this approximation, ε is proportional to the ratio between the TKE (q^2) in the energy-containing scales and an overturn time-scale ($\tau \sim l/q$, where l is the characteristic length of turbulent overturns), $\varepsilon \sim q^2/\tau \sim q^3/l$. Here we used $l \sim L_O$, and ε was calculated as:

$$\varepsilon = cq^2 N \tag{4.4}$$

where c is a constant $c \approx 1$ (Sanford, 1997).

In order to quantify the degree of anisotropy in the turbulent field, the anisotropy tensor (a_{ij}) was calculated:

$$a_{ij} = \frac{\langle v_i' v_j' \rangle}{\sum_k v_k' v_k'} - \frac{\delta_{ij}}{3} \tag{4.5}$$

where δ_{ij} is the Kronecker delta ($\delta_{ij} = 0$ except when $i = j$, for which $\delta_{ij} = 1$), and the second ($I_2 = \sum_{i,j} a_{ij} a_{ji}$) and third ($I_3 = \sum_{i,j,k} a_{ij} a_{ik} a_{jk}$) invariants of a_{ij} were used to place our measurements in the Lumley triangle (Lumley and Newman, 1977; Banerjee et al., 2007).

Fluoroprobe and CTD profiles

As part of a long-term monitoring program, bi-weekly profiles ($n = 25$) of temperature, and *P. rubescens* chlorophyll-*a* fluorescence (chl-*a*), among other variables, were measured near the deepest location of the lake at st0 (Figure 4.1) between 10 January and 12 December 2018 with a TS-16–12 fluoroprobe (bbe Moldaenke GmbH, Kronshagen, Germany). Additionally, during the convection-oriented sampling in September 2019, 11 fluoroprobe casts were performed between 14h00 (local time, UTC+2) on the 24th and 12h40 on the 25th. CTD profiles ($n = 15$) were also collected during the convection-oriented sampling at st0 with a SBE19plus V2 SEACAT profiler, between 16h05 on the 24th and 12h03 on the 25th of September 2019. The instrument also includes oxygen (SBE 43I) and optical sensors for measuring beam transmission and attenuation (WET Labs C-Star) and fluorescence (WET Labs ECO-AFL/FL).

4.2.4 Meteorological data

Hourly values of meteorological variables were obtained from the COSMO-1 (COnsortium of Small-scale MOdeling) weather model run by the Swiss Federal Office of Meteorology and Climatology (MeteoSwiss) over the Swiss territory with a horizontal resolution of 1.1 km. Data was extracted for the grid-bin closest to st0. Heat fluxes through the lake surface (including shortwave and longwave radiation, as well as latent and sensible fluxes) were calculated following the derivation of Fink et al. (2014). Hourly surface water temperatures required for this calculation were calculated from air temperatures with the *air2water* model (Piccolroaz et al., 2013; Toffolon et al., 2014).

4.2.5 Analysis of the basin-scale stability and mixing

Water column stability was quantified as minus the background potential energy, i.e. the amount of mechanical energy that would be required to remove the existing stratification and fully mix the water column:

$$Sc = -\frac{1}{A_0} \int_{z_{max}}^{0} g(\rho(z) - \overline{\rho})(z - z_c) A(z)\, dz \qquad [\text{J m}^{-2}] \tag{4.6}$$

where g is the gravitational acceleration, ρ is water density, $\overline{\rho}$ is the volume-averaged water density, $A(z)$ is the lake area at a depth z (where z is defined positive upwards and it is zero at the surface and negative below), $A_0 = A(0)$ is the surface area, z_{max} is the maximum depth of the lake and z_c is the depth of the center of volume of the lake. Lake bathymetry was available through the Swiss Federal Office of Topography (https://www.swisstopo.admin.ch/).

The temporal evolution of Sc in a water body is mainly determined by the balance between stabilizing heating and destabilizing cooling as well as wind stirring, when other sources and sinks of buoyancy are not relevant (Simpson and Sharples, 2012; Woolway et al., 2018). In order to disentangle the contribution of heat fluxes and wind forcing to changes in water column stability we modelled the evolution of Sc as

$$\frac{\partial Sc}{\partial t} = -|z_c| \underbrace{\frac{g\alpha}{c_p} H_{\text{net}}}_{B_0} - \delta \tau W_{10} \qquad [\text{W m}^{-2}] \tag{4.7}$$

where H_{net} is the net heat flux at the surface; c_p, the heat capacity of water; α, the thermal expansion coefficient; B_0, the surface buoyancy flux, and δ is an unknown basin-scale mixing efficiency relating the wind work rate 10 m above the surface ($P_{10} = \tau W_{10}$) with the actual decrease of stability due to wind stirring. Wind stress (τ) was calculated as $\tau = \rho_{air} C_{10} W_{10}^2$, where W_{10} is the wind speed 10 m above the lake surface, C_{10} is the wind drag coefficient, calculated according to Wüest and Lorke (2003), and ρ_{air} is the density of air. Observations of Sc were fit to Eq. 4.7 to determine δ, which was $\delta = 0.45\%$, in agreement with previous studies (Wüest et al., 2000; Ravens et al., 2000; Woolway et al., 2018).

In addition, the potential of wind stirring to overcome the restoring effect of stratification, disturb the metal-imnion and produce diapycnal mixing was quantified with the lake number, L_N (Imberger and Patterson, 1989; Robertson and Imberger, 1994). Basin-scale vertical heat diffusivity (K_T^{BS}) was calculated with the heat-budget method (Powell and Jassby, 1974; Li, 1973), by comparing consecutive bi-weekly temperature profiles and taking into account the penetrative shortwave radiation.

4.3 Results

4.3.1 Seasonal stratification and *P. rubescens* thin layer

The evolution of atmospheric forcing and lake temperature at the regular monitoring station (st0) of Lake Zurich during year 2018 is shown in Figure 4.2. From January to March, the lake was loosing heat to the atmosphere (Figure 4.2A), and the water column was initially weakly stratified with a surface temperature decreasing from 5.9 °C (bottom temperature was 4.8 °C) on the 10 January to a minimum of 4.5 °C on the 19 March (Figure 4.2B), indicating that deep mixing took place after a period of ~10 days of significant heat loss and week-long wind speed average of up to 5 m s^{-1}. The holomixis period was short, as solar heating started to dominate from early March, and a weak stratification of 2 °C difference, already developed at the next sampling day, on 4 April.

Surface water temperature was > 10 °C by mid-April and a shallow thermocline already formed. From then on, surface temperature and water column stratification progressively increased to a maximum of 26.5 °C observed on 8 August. The most intense warming took place before June, where nighttime heat loss to the atmosphere was weak. The nighttime cooling became stronger afterwards. During the warming period, weekly averaged winds varied between 2 and 4 m s^{-1}, but where mostly below 3 m s^{-1}, except for some days by the end of June. A strong thermocline, with a temperature gradient increasing from ~ 0.5 °C m^{-1} to ~ 3.0 °C m^{-1},
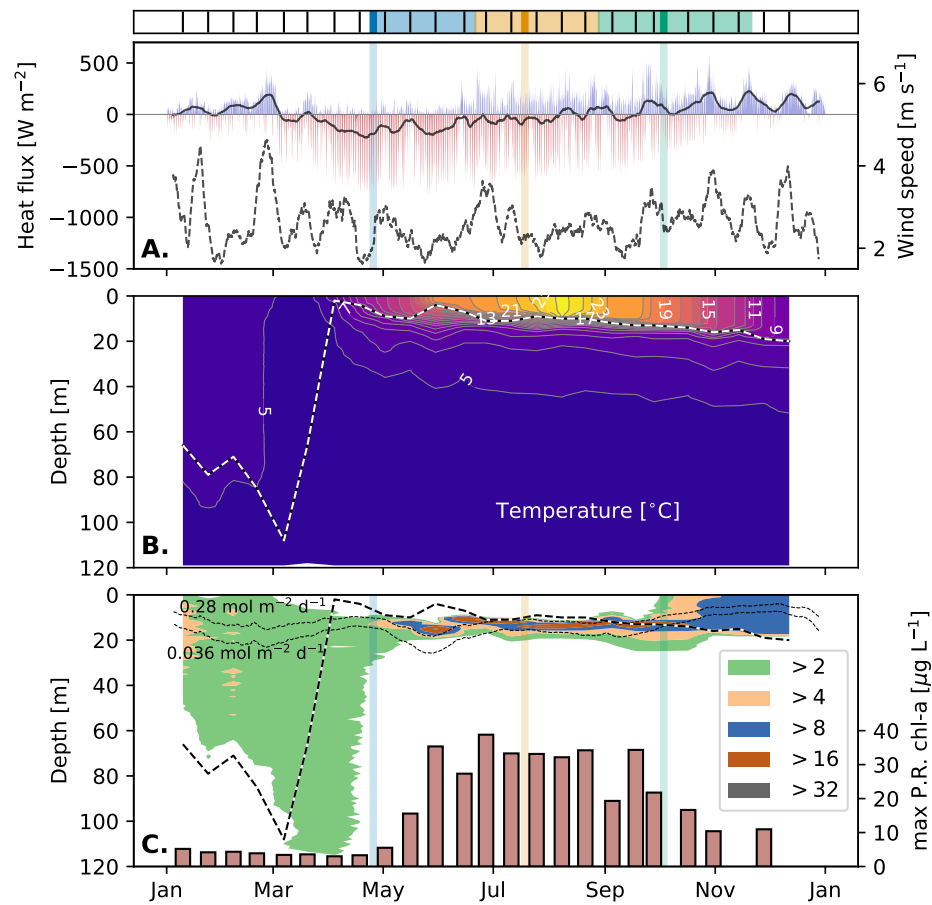
Figure 4.2 – Seasonal time-series of atmospheric and hydrographic conditions, and *P. rubescens* chl-*a* concentration in Lake Zurich during 2018. **A.** hourly (red-blue curves) net heat flux between the lake and the atmosphere (positive upwards) and 7-day mean wind speed (dashed) derived from the meteorological COSMO model; **B.** vertical distribution of water temperature; and **C.** vertical distribution of *P. rubescens* chl-*a* concentration (μg L^{-1}) (contours) and maximum concentration (bars). In panel **A.**, the black line represents a 7-day moving average of heat fluxes. In panel **B.** and **C.**, the dashed thick line represents the depth of thermocline (maximum temperature gradient). In panel **C.**, the dashed thin lines represent the daily PAR fluxes resulting in *P. rubescens* neutral buoyancy (0.28 mol photon m^{-2} d^{-1}) and zero net growth (0.36 mol photon m^{-2} d^{-1}). Above the upper panel, vertical lines represent the sampling dates and the color shading represents the different stages of the seasonal evolution of *P. rubescens* thin layer from growth and settling during spring (blue), maximum stable concentration in early-mid summer (orange) to decline in late-summer and fall (green). Turbulence-oriented surveys are highlighted with darker shading.

was located at 2 to 11 m depth, showing a slight deepening trend.

Net cooling prevailed from August on, with alternated periods of 20–30 days of stronger and weaker cooling (even slight net heating at the beginning of September) and wind speeds (~2 vs. 4 m s^{-1}). Surface temperature decreased steadily to 8 °C in mid-December. The thermocline also deepened steadily from 9 to 20 m depth, but the maximum thermal stratification remained strong (2 to 3 °C m^{-1}) until the end of September, and then progressively reduced as the surface mixed-layer (SML) with uniform temperature expanded into the deeper part of the thermocline, which was more weakly stratified.

Chapter 4. Inhibited vertical mixing and the seasonal persistence of a cyanobacterial thin layer in a stratified lake

Lake stability was weak ($Sc < 0.2$ kJ m^{-2}) during winter and minimum during holomixis on 19 March (Figure 4.3A), after which it increased progressively during the heating period to a maximum value of 13 kJ m^{-2} on 8 August. After the onset of net cooling, Sc decreased back to < 1 kJ m^{-2}. This reduction in Sc was only briefly interrupted during the net heating period in September. Lake number was mostly $L_N < 1$ over the winter period (Figure 4.3B), indicating that wind stirring could easily overcome the existing weak stratification and drive turbulent mixing. L_N was minimal during holomixis in mid-March and then increased. During April, L_N was generally < 10, and during May, only occasionally, indicating a progressive rarefaction of mixing events. Between June and October, wind stirring was strongly suppressed by stratification as L_N was always > 10. From October-November on, L_N showed a decreasing trend and was < 10 over short periods. Finally, in December L_N was again < 10 most of the time.

Consistently, mean basin-scale vertical heat diffusivity (K_T^{BS}), inferred from the heat budget method (Figure 4.3C), was larger in the meta- and hypolimnion during the spring period (blue line, $1 - 2 \times 10^{-5}$ m^2 s^{-1}) compared to the summer and fall periods (orange and green, $10^{-6} - 10^{-5}$ m^2 s^{-1}). Mixing was suppressed at the main thermocline at $\sim$12 m depth ($\sim$15 m) for summer (fall), with K_T^{BS} as low as $1 - 2 \times 10^{-6}$ m^2 s^{-1}.

The large values of L_N during summer suggest that the decrease of lake stability after the onset of cooling in August is mainly driven by destabilizing buoyancy flux, rather than wind stirring. This was further evaluated with the stability model (Eq. 4.7; Figure 4.3A). The model indicates that the seasonal trends in Sc are largely driven by the buoyancy flux (red shading, Figure 4.3A), and that Sc increases as long as heating dominates, and $B_0 < 0$. During the warming period, wind mixing (blue shading, Figure 4.3A) reduced lake stability by 13%, and its contribution to destabilization during cooling was of 24%.
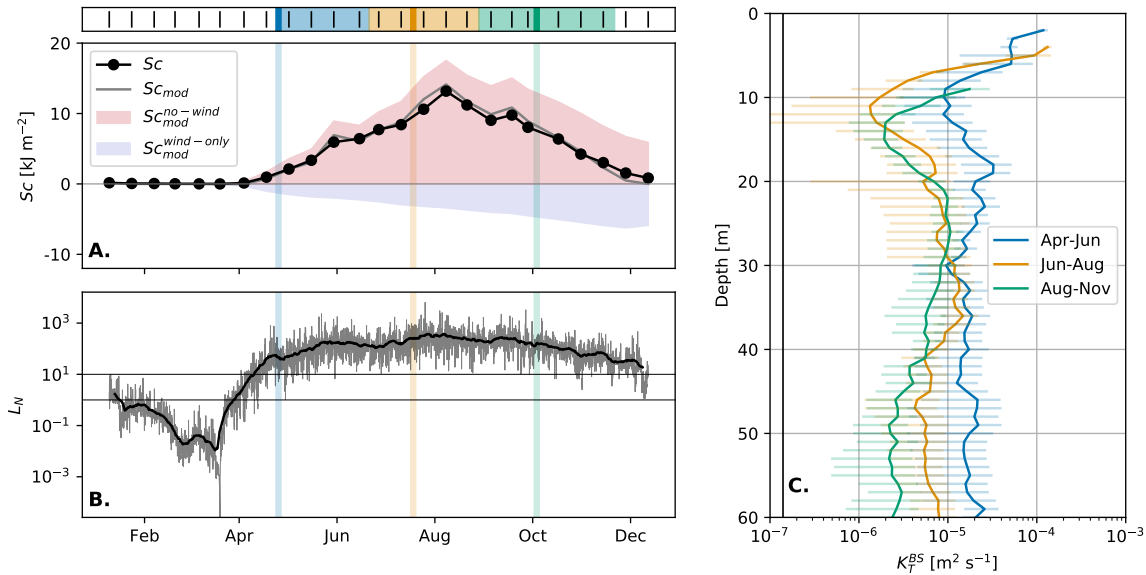

Figure 4.3 – Seasonal time-series of **A.** lake stability (Sc), **B.** hourly (gray) and weekly (black) lake number (L_N) in Lake Zurich during 2018. In panel **C.**, basin-scale vertical heat diffusivity (K_T^{BS}) calculated using the heat budget method for the spring (blue), mid-summer (orange) and late-summer/fall (green). Horizontal lines represent 95% confidence intervals. In panel **A.**, the evolution of Sc derived from the bulk model (Eq. 4.7) is also represented as a gray line, and the variations due to buoyancy flux only and wind only are represented by the red and blue shading, respectively.

P. rubescens was observed throughout the mixed-layer at relatively low chl-a concentrations (chl-$a < 4$ μg L^{-1}) during the mixing period, and it was spread over the full water column after holomixis (Figure 4.2C). From

May on, *P. rubescens* concentrated in a thin layer located within the main thermocline between $10 - 17$ m depth. The vertical position of *P. rubescens* is determined by the daily dose of photosynthetically available radiation (PAR; Walsby et al., 2004). This is clearly illustrated in our record, where the *P. rubescens* layer was located most of the time between the daily PAR isolines for which *P. rubescens* acquires neutral buoyancy (0.28 mol photon m^{-2} d^{-1}) and for which the net growth becomes zero (0.036 mol photon m^{-2} d^{-1}) (thin dashed lines in Figure 4.2C). The layer remained stable, with peak concentrations between 30 and 40 μg L^{-1}, until October, when the thermocline deepened and approached the depth of the layer. From mid-October, *P. rubescens* concentration in the SML began to increase but the peak persisted until the end of the month, when the thermocline crossed the depth of the daily PAR levels supporting neutral buoyancy and growth. After that, the *P. rubescens* population was located exclusively in the SML at moderate concentrations of ~10 μg L^{-1}.
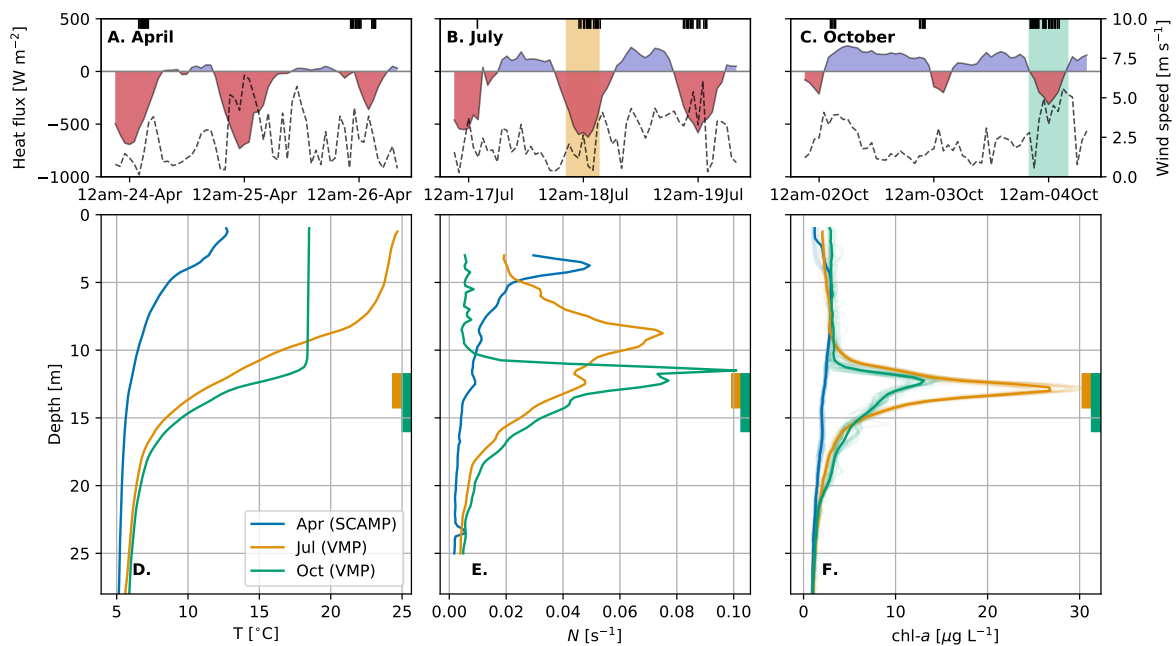
Figure 4.4 – Meteorological conditions (net heat flux, blue-red colors; wind speed, dashed black) derived from the COSMO model during the 3 microstructure and mooring samplings in 2018: **A.** 24–26 April 2018, **B.** 17–19 July 2018, and **C.** 2–4 October 2018. Mean profiles of **D.** temperature, **E.** buoyancy frequency and **F.** chl-*a* fluorescence derived from the microstructure profiles in st1 for April 2018 (blue, SCAMP profiler), July 2018 (orange, VMP profiler) and October 2018 (green, VMP profiler). In panels **A-C.**, microstructure profiles are indicated with black ticks, and the duration of mooring deployments is indicated with color filling. In panels **C-F.** the depth range of the *P. rubescens* thin layer (where chl-*a* > max(chl-*a*)/*e*) is indicated by filled rectangles for July (orange) and October (green). Individual profiles for chl-*a* are shown in panel **F.** as semi-transparent lines. Individual profiles were projected onto isothermal coordinates to remove the effect of internal wave motions.

Our turbulence sampling captured three key stages of the seasonal development of the *P. rubescens* layer. The first microstructure and HR-mooring survey was carried out between 24 and 26 April 2018 (blue, Figures 4.2, 4.3), shortly before the formation of the thin layer. The second was conducted between 17 and 19 July (orange), when the thin layer had been established for more than two months and water column stability was close to its maximum value. Finally, the third sampling took place between 2 and 4 October (green), when some *P. rubescens* chl-*a* was already observed in the SML but the chl-*a* peak remained sharp and well defined, although with reduced peak concentration. A detailed description of turbulence based on these

measurements is presented in the next two sections. The reader interested in the overall implications of turbulence for the dynamics of the *P. rubescens* layer may refer directly to the Discussion.

4.3.2 Microstructure measurements

Hydrography, chlorophyll and microstructure profiles

During the sampling in April, heating outpaced nighttime cooling and hourly wind speeds were maximal (6 m s^{-1}) on the 25$^{\text{th}}$, when no microstructure profiles were carried out, but otherwise remained < 4 m s^{-1} with a mean ($\pm$ SD) of 2.4 $\pm$ 1.7 m s^{-1} (Figure 4.4A). Thermal stratification was still weak, with a shallow thermocline, located above 5 m depth, and where $N_{max} \approx 0.05$ s^{-1}, at 3 m depth (Figure 4.4D,E). Chl-a measured with the SCAMP was low (< 5 μg L^{-1}) and the thin layer was not observed (Figure 4.4F). In July, nighttime cooling intensified but it was still weaker than daytime heating, and wind speeds were variable and averaged 2.4 $\pm$ 1.4 m s^{-1} (Figure 4.4B). The water column was thermally stratified from the surface ($N \approx 0.02$ s^{-1}), and a strong thermocline extended from 7 to 17 m depth, with maximum stratification ($N_{max} = 0.075$ s^{-1}) at 9 m depth (Figure 4.4D,E). A 2.5 m thick, vertically symmetric thin layer of chl-a (max. 30 μg L^{-1}) was centered at 13 m, 4 m below the stratification maximum (Figure 4.4F). In October, nighttime cooling was prominent and daytime heating was weak, however, most of the microstructure profiles were performed during daytime when heating prevailed. Winds were weak (2 m s^{-1}) for more than one entire day, but larger on 4$^{\text{th}}$ October (6 m s^{-1}, mean: 2.3 $\pm$ 1.3 m s^{-1}; Figure 4.4C). A well-mixed SML, not observed in the previous surveys, extended down to 10.5 m depth, and sat on top of an even sharper thermocline ($N_{max} \approx 0.1$ s^{-1} at 11.5 m depth, Fig 4.4D,E). A weaker chl-a maximum (13 μg L^{-1}) was observed at 12.25 m depth, in coincidence with maximum N, and the chl-a peak was broader (4.5 m), but strongly asymmetric, with a sharp upper boundary (Figure 4.4F).

In April, the dissipation ε was relatively high, $\sim 10^{-6}$ W kg^{-1}, in the upper 8 m. Below, it dropped sharply to very low values ($\leq 10^{-10}$ W kg^{-1}; Figure 4.5A). The dissipation rate of thermal variance (χ) also decreased with depth, from $\sim 10^{-4}$ K^2 s^{-1} in the upper 5 m to $\sim 10^{-9}$ K^2 s^{-1} below 10 m, with a slight increase between 20 and 25 m depth (Figure 4.5B). The Thorpe scale, L_T, describing the size of turbulent overturns, was 1–3 cm in the upper 10 m and, below that, it gradually increased with depth to up to 10 cm. In the lower layer, L_T was similar to the Ozmidov scale (L_O), but the latter was 10 times larger than L_T in the upper layer (Figure 4.5C). The buoyancy Reynolds number was $Re_b > 100$ in the upper layers, implying relatively energetic turbulence, and it was mostly $Re_b < 15$ below, until a depth of 20 m (Figure 4.5D). These small values are indicative of a buoyancy-controlled turbulence (Bouffard and Boegman, 2013) with dominance of non-turbulent fluxes (Ivey and Imberger, 1991; Shih et al., 2005). Consistently, turbulent heat diffusivity (K_T) was $\sim 10^{-5}$ m^2 s^{-1} in the upper 5 m, and dropped to molecular levels below 8 m, with slightly larger values below 20 m depth (Figure 4.5.R). Finally, mixing efficiency (Γ) was about one order of magnitude lower than the canonical value of 0.2 (Osborn, 1980; Oakey, 1982) for most of the water column, except the upper 5 m, where $\Gamma \approx 0.1$ (Figure 4.5F).

In July, ε was $\sim 10^{-7}$ W kg^{-1} in the upper 5 m –one order of magnitude smaller compared to April–, it showed a minimum of 10^{-8} W kg^{-1} between 5–10 m depth and then increased again in the thermocline range, to a local maximum exceeding 10^{-7} W kg^{-1} at about 13 m depth (Figure 4.5A). From the base of the main thermocline, ε decreased from 10^{-8} W kg^{-1} to 10^{-10} W kg^{-1} at 25 m depth, being overall much larger than in April for the same depth range. A similar vertical pattern was found for χ, although the sub-surface dissipation maximum was located shallower at 9–10 m depth, in coincidence with maximum N. The Thorpe scale, L_T, was of about 3 cm in the upper 5 m, but very small below ($L_T = 1$ mm to 1 cm. On the other hand, L_O was about one order of magnitude larger than L_T throughout the water column. Similarly, Re_b was > 100 in the upper 5 m, dropped sharply below this depth, being $Re_b < 10$ in the deeper layers, except at the ε local maximum in the

thermocline. Diffusivity $K_T \approx 10^{-5}$ m^2 s^{-1} in the shallow layers, like in April, but it dropped below molecular ($\sim 10^{-8}$ m^2 s^{-1}) at the thermocline. Finally, Γ was very low everywhere, and minimal (10^{-4}) at the ε maximum at ~ 13 m depth.
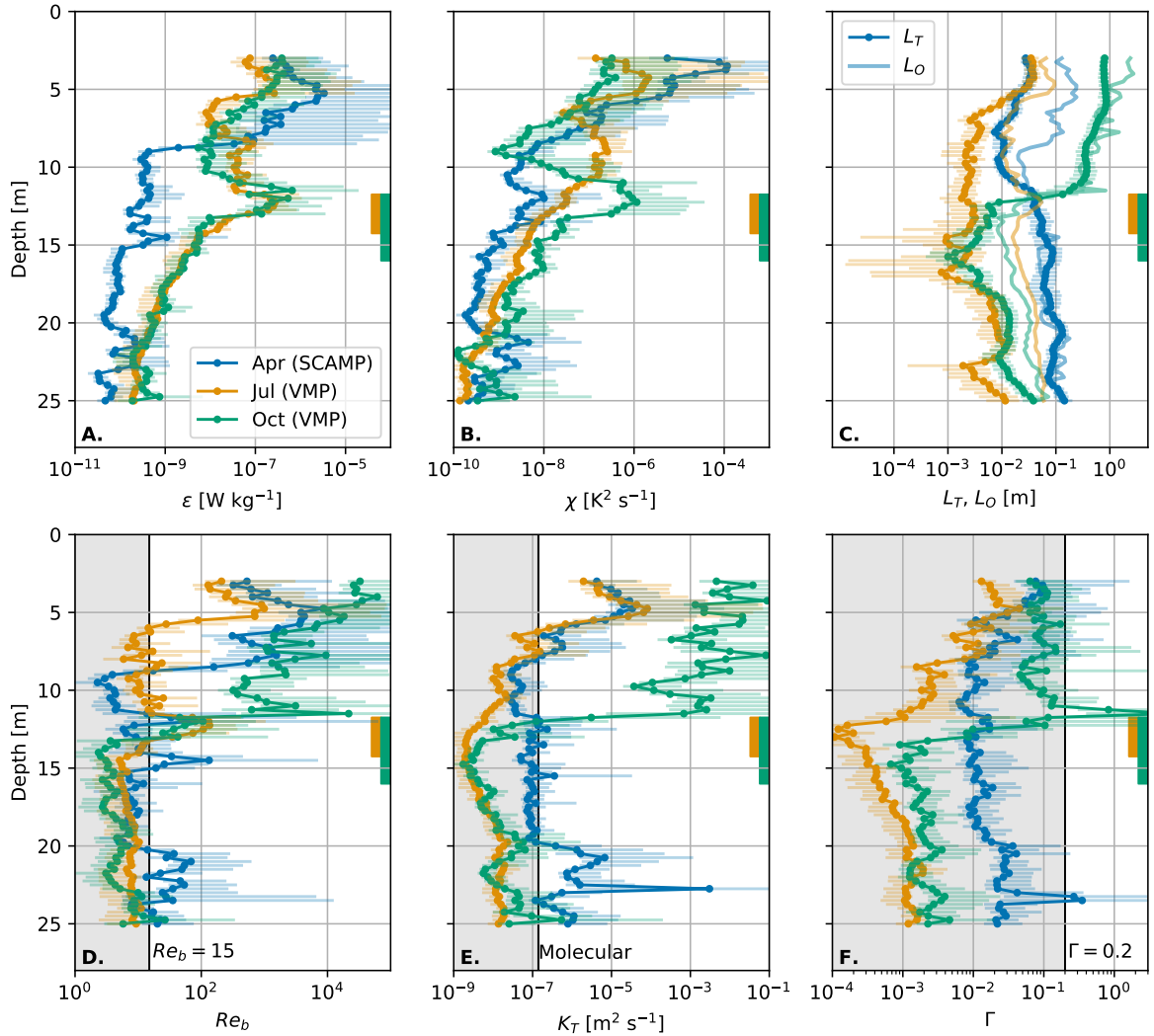

Figure 4.5 – Mean (maximum likelihood estimate, MLE) profiles of turbulence-related variables derived from the microstructure profiles during 24–26 April 2018 (blue, SCAMP profiler), 17–19 July 2018 (orange, VMP profiler) and 2–4 October 2018 (green, VMP profiler) in st1. **A.** TKE dissipation rate (ε), **B.** thermal variance dissipation rate (χ), **C.** Thorpe (L_T, dotted lines) and Ozmidov (L_O, semi-transparent lines) length-scales, **D.** buoyancy Reynolds number (Re_b), **E.** heat diffusivity (K_T), and **F.** mixing efficiency (Γ). The 90% confidence intervals are also represented. The depth range of the *P. rubescens* thin layer, defined as the range where chl-a > max(chl-a)/e, is indicated by filled rectangles for July (orange) and October (green).

In October, ε and χ where maximal (10^{-7} W kg^{-1}, and 10^{-7} K^2 s^{-1}) in the upper SML (2–5 m), minimal (10^{-8} W kg^{-1}, and 10^{-9} K^2 s^{-1}) in the lower SML (5–10 m; Figure 4.5). Both quantities showed a local maximum in the main thermocline (10^{-7} W kg^{-1}, and 10^{-6} K^2 s^{-1}), and decreased below, as for July. The other turbulent quantities showed a sharp transition close to 11 m depth, at the base of the SML. In the SML, $Re_b > 1000$ indicated energetic turbulence, L_T and L_O were larger (20–100 cm) and similar, K_T was also large (10^{-3} m^2 s^{-1}),

and $\Gamma \approx 0.1$, close to the canonical value. Below the mixed layer, the conditions were similar to those found in July.

Small-scale turbulence in the thin plankton layer

The probability distribution and mean values of the turbulence-related quantities derived from the microstructure profiles within the chl-a maximum are described here, for July and October 2018 (Figure 4.6 and Table 4.3). The vertical extent of the layer was defined as the depth range where chl-$a > \max($chl-$a)/e$ ($e \approx 2.718$).

In July, energy dissipation rates were distributed over three orders of magnitude (ε from 10^{-9} to 10^{-6} W kg^{-1}) within the depth range of the thin layer (11.75–14.25 m, Table 4.3; Figure 4.6A). The distribution was approximately lognormal, but somewhat skewed, with a longer queue of high values. As a consequence, the ε maximum likelihood estimate (MLE) of the mean (assuming a log-normal distribution) was $7.7\,[6.4-26.4] \times 10^{-8}$ W kg^{-1} (90% confidence intervals in brackets), larger than the median (2.2×10^{-8} W kg^{-1}). It is worth to note that only about 43% of the fits to the Batchelor spectrum passed the quality criterion, which indicates that the shape of the temperature gradient spectra was strongly influenced by finestruture in such strongly stratified environment (Gregg, 1977; Luketina and Imberger, 2001). A similar distribution, but slightly sharper and containing more outliers, was found for χ, with median and MLE values of 0.78×10^{-8} K^2 s^{-1} and $1.5\,[1.3-24] \times 10^{-8}$ K^2 s^{-1}, respectively (Figure 4.6B).
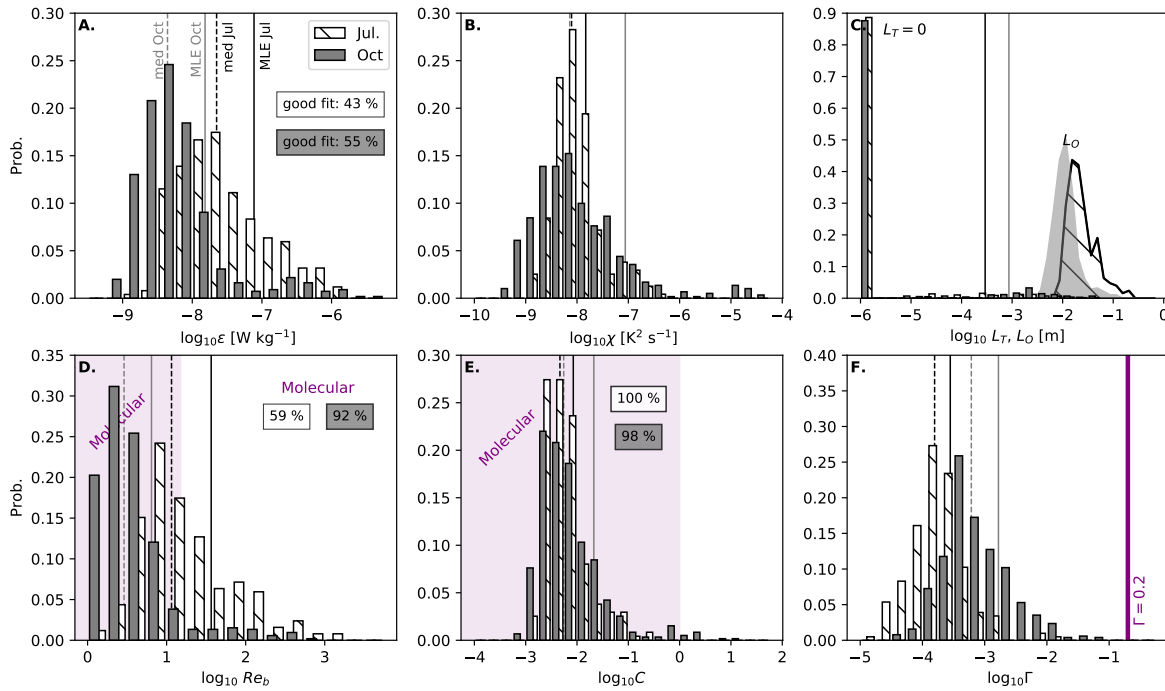
Figure 4.6 – Probability distribution within the *P. rubescens* layer, defined as the depth range where chl-$a > \max($chl-$a)/e$ of turbulence-related quantities derived from the microstructure profiles during 17–19 July 2018 (white) and 2–4 October 2018 (gray) at st1. **A.** TKE dissipation rate (ε), **B.** thermal variance dissipation rate (χ), **C.** Thorpe (L_T, bars) and Ozmidov (L_O, filled lines) length-scales, **D.** buoyancy Reynolds number (Re_b), **E.** Cox number (C), and **F.** mixing efficiency (Γ). MLE logarithmic mean (arithmetic mean for L_T) and median values are represented by solid and dashed vertical lines, respectively (see values in Table 4.3). Black lines are for July and gray lines for October, respectively. The probability of occurrence of molecular conditions according to the criteria $Re_b < 15$ and $C \le 1$ is indicated in panels **D.** and **E.**, respectively.

While L_O was distributed around 2.2 cm, with MLE $2.5\,[1.5-2.5]$ cm, L_T was 0 almost 90% of the time,

indicating that overturning motions were actually mostly undetectable, and when detectable, generally $L_T < L_O$ (Figure 4.6C). Within the layer, Re_b fell below 15 for 56% of the values where ε could be detected, with a median of 11.5 and MLE of 36.6 [30.5 − 104.5] (Figure 4.6D). Assuming that the badly-shaped spectra are non-turbulent, this indicates that non-turbulent conditions were found 80% of the time. Despite this small but regular occurrence of $Re_b > 15$ (overall ~20% probability), the distribution of the Cox number (median: $C = 0.0047$, MLE: $C = 0.0085 [0.007 − 0.0122]$), indicated that turbulent mixing did not enhance molecular heat fluxes –which would imply $C > 1$– at any time (Figure 4.6E). Even for relatively elevated ε, no turbulent mixing was observed, which resulted in Γ being always much smaller than 0.2 (median: $\Gamma/0.2 = 0.008$, MLE: $\Gamma/0.2 = 0.0014$) (Figure 4.6F).

In October, ε exhibited a bi-modal distribution (Figure 4.6A), due likely to the sharp vertical variations around the ε maximum (Figure 4.5A). The median (0.4×10^{-8} W kg^{-1}) of the distribution was centered at the smaller mode. The peak of larger dissipation, corresponding to the ε vertical maximum, had a much smaller number of occurrences due to the large amount of discarded fits in this range of very strong stratification. The ε MLE mean was $1.5 [1.3 − 5.2] \times 10^{-8}$ W kg^{-1}. Similar situation was found for χ, with median and MLE mean, 0.72×10^{-8} K^2 s^{-1} and $8.7 [6.2 − 132.0] \times 10^{-8}$ K^2 s^{-1}, respectively (Figure 4.6B). Vertical overturns were again undetectable 90% of the time, and C and Re_b suggest that molecular fluxes were dominant over turbulent in a similar proportion (Figure 4.6B). Again, mixing efficiency was always << 0.2 (Figure 4.6C).

Table 4.3 – Median and maximum likelihood estimate (MLE) mean (or arithmetic mean* for L_T) values and 90%-confidence intervals (ci, in brackets) for the turbulence parameters in the *P. rubescens* thin layer during the July 2018 and October 2018 samplings based on the data collected with the microstructure profiler (VMP) and the HR-mooring.

	July 2018				October 2018			
	VMP		Mooring		VMP		Mooring	
	median	MLE [ci] (mean*)	median	MLE [ci] (mean*)	median	MLE [ci] (mean*)	median	MLE [ci] (mean*)
Depth range [m]		$11.75 − 14.25$		$10.84 − 12.90$		$11.75 − 16$		$10.13 − 12.19$, $T \le 18\,^{\circ}$C
N [s^{-1}]	0.041	0.041 [0.026 − 0.042]	0.042	0.043 [0.014 − 0.043]	0.042	0.052 [0.050 − 0.055]	0.072	0.071 [0.068 − 0.139]
ε [10^{-8} W kg^{-1}]	2.2	7.7 [6.4 − 26.4]	3.6	6.27 [6.26 − 8.81]	0.4	1.5 [1.3 − 5.2]	24	44 [43 − 56]
Re_b	11.5	36.6 [30.5 − 104.5]	15.7	27.4 [27.3 − 38.5]	2.9	6.4 [5.6 − 12.8]	44	79.1 [79.0 − 102.4]
q [mm s^{-1}]	0.75	1.1 [0.7 − 1.12]	0.92	1.1 [0.6 − 1.1]	0.35	0.48 [0.27 − 0.51]	1.8	2.2 [1.1 − 2.2]
q_h [mm s^{-1}]			0.90	1.0 [0.6 − 1.0]			1.7	2.1 [1.1 − 2.1]
q_v [mm s^{-1}]			0.19	0.22 [0.12 − 0.22]			0.58	0.68 [0.46 − 0.68]
L_O [cm]	2.0	2.8 [1.7 − 3.1]	2.2	2.5 [1.4 − 2.5]	1.1	1.3 [0.7 − 1.4]	2.7	3.1 [1.7 − 3.1]
L_T [cm]	0	0.27* [0.21 − 0.33]			0	0.48* [0.42 − 0.54]		
χ [10^{-8} K^2 s^{-1}]	0.78	1.5 [1.3 − 2.4]			0.72	8.7 [6.2 − 132.0]		
C	0.0047	0.0085 [0.007 − 0.0122]			0.0055	0.0213 [0.0176 − 0.0778]		
$\Gamma/0.2$	0.0008	0.0014 [0.0012 − 0.0027]			0.0031	0.008 [0.007 − 0.0019]		

4.3.3 High-resolution velocity measurements in the thermocline

The high-resolution current velocity and temperature measurements collected on 18 July and 5 October 2018 in the upper thermocline are shown in Figure 4.7A-C. During both periods, some internal wave activity was observed at high (a few minutes) and relatively low frequencies (hours), with vertical displacements of the isotherms of some cm and velocities of a few cm s^{-1}. In July, the sampling range (10.84–12.9 m depth) spanned a region included in the main thermocline, with relatively uniform and strong temperature gradient (roughly 3.5 °C over 2.5 m; Figure 4.7A,B). The amplitude of the fluctuations of current velocities and the isothermal displacements was generally uniform during the eight deployment hours. In October, the sampling range (10.13–12.19 m depth) included part of the mixed layer at the beginning of the deployment. For the first two

hours, background currents were relatively weak with no fluctuations of the isotherms but, after 10h30, a progressive enhancement of the background flow was observed, and high-frequency fluctuations were also triggered. The increase of the background flow (up to a maximum of 5 cm s^{-1} at about 13h00) was coincident with an uplift of the pycnocline, which occupied the whole sampling range by the end of the deployment. This event was probably a manifestation of the lake response to increasing wind speed at this time of the day (Figure 4.4C).
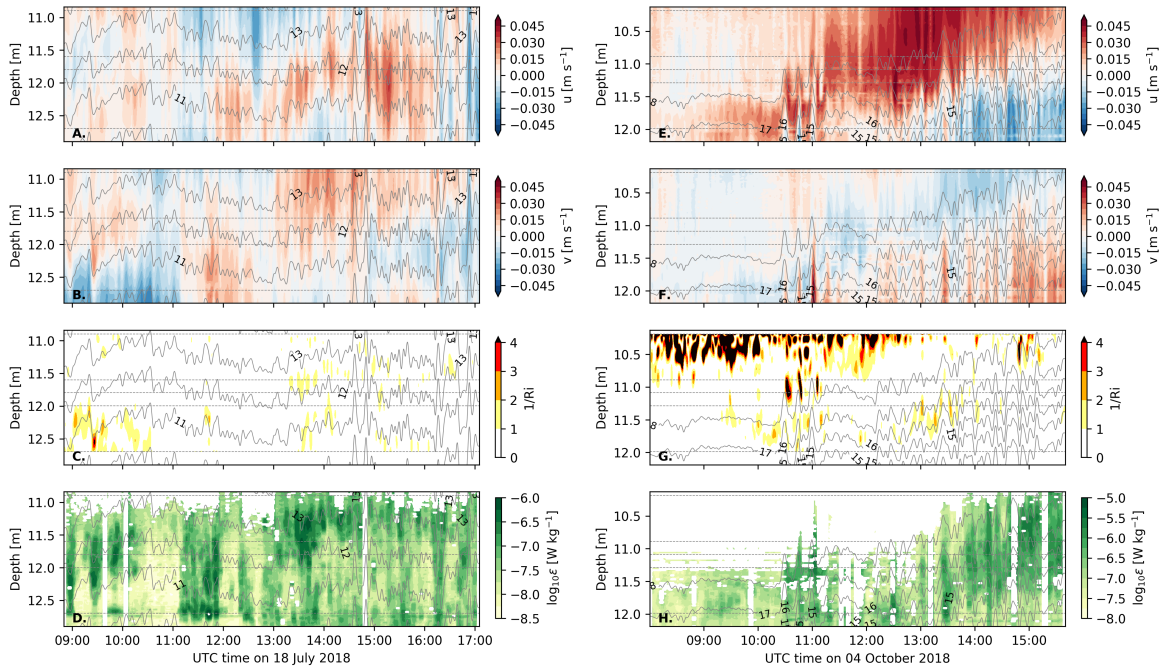
Figure 4.7 – Measurements of horizontal eastward (u) and northward (v) velocities (blue-red filled contours in panels **A., B., E., F.**), temperature (gray lines in all panels), inverse Richardson number ($1/Ri = S^2/N^2$, **C., G.**), and TKE dissipation rate (ε, **D., H.**) obtained with the HR-mooring at st1 in July and October 2018. The position of the thermistors is indicated by horizontal dashed lines. Data on **A-D.** were collected on 18 July 2018, and data on **E-H.** correspond to 4 October 2018. The displayed temperature and velocity signals were smoothed with a low-pass Butterworth filter with a 5-minutes period. Data in blank areas in panels **D, H.** were excluded due to poor (< 50%) beam correlation.

The horizontal flow velocities evidenced vertical structure during both deployments, even within the narrow sampling range of a few m. This shear ($S^2 = (\partial u/\partial z)^2 + (\partial v/\partial z)^2$) in the mean flow has the potential to trigger shear instabilities driving turbulence and mixing if it overcomes the stabilizing effect of stratification. This situation occurs when the gradient Richardson number ($Ri = N^2/S^2$) drops below the critical value of $1/4$ (Miles, 1961) (or, equivalently, $1/Ri > 4$). The high-resolution measurements show that, despite the existence of background shear, unstable values of Ri were very infrequent, due to the strong stratification, with 93% occurrence of stable conditions ($Ri > 1$) in July and 80% in October (Figure 4.7C,G). Furthermore, in October, most of the unstable values were found in the weakly-stratified mixed layer, but had little effect on the thermocline.

Energy dissipation rates derived from turbulent velocity fluctuations ranged between 10^{-8} W kg^{-1} and 10^{-6} W kg^{-1} in July, and 10^{-5} W kg^{-1} in October (Figure 4.7D,H). In July, ε showed a patchy, intermittent structure, with an alternation of calm and more dissipative conditions in different areas, with little visual correlation with Ri (Figure 4.7C). In October, ε was weaker during the first 2 and 1/2 hours, when the internal

wave activity was weak, and was enhanced later on. The MLE mean was $6.27\,[6.26 - 8.84] \times 10^{-8}$ W kg^{-1} (median: 3.6×10^{-8} W kg^{-1}) and $44\,[43 - 56] \times 10^{-8}$ W kg^{-1} (median: 24×10^{-8} W kg^{-1}), for July and October, respectively (Table 4.3). Those values agreed well with the microstructure-derived ε for the same depth range (Figure 4.5A) and, thus, the derived L_O and Re_b values were also similar (Table 4.3).
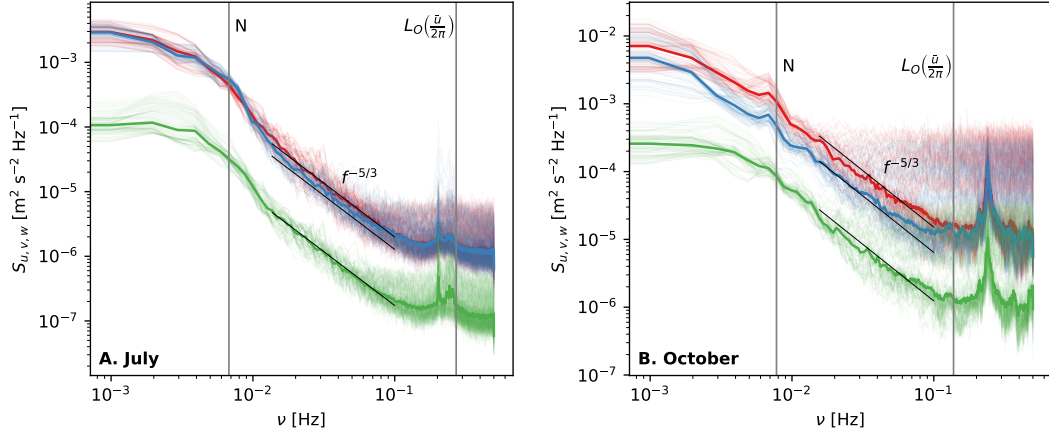
Figure 4.8 – Power spectra of zonal (red), meridional (blue) and vertical (green) velocities for the mooring measurements collected on **A.** 18 July 2018 and **B.** 8 October 2018. The spectra for individual depths are represented by the thin semi-transparent lines, and the median spectra are represented by thicker lines. The slope of the turbulence spectrum in the inertial sub-range, mean buoyancy frequency (N), and the frequency-equivalent of the mean Ozmidov scale (L_O) are shown in both panels. The Taylor frozen flow hypothesis was used to convert L_O to frequency units by multiplying by $\bar{u}/2\pi$, where $\bar{u}$ is a representative velocity of the mean flow, calculated as the mean of the magnitude of the low-passed flow velocities (July: 0.015 m s^{-1}, October 0.022 m s^{-1}).

The velocity fluctuations (u') during the summer and fall deployments showed a spectral decay of energy density for frequencies (ν) higher than the buoyancy frequency, up to a maximum of 0.1 Hz, where instrument noise and contamination by surface waves became dominant (Figure 4.8). Over this range, the spectral slope was compatible with the theoretical slope for the inertial sub-range (-5/3) for the three velocity components. However, a strong anisotropy was found for this spectral range, as the vertical component was ten times less energetic than the horizontal components. Consequently, the turbulent horizontal velocity scale ($q_h = 1.1$ mm s^{-1} for July, $q_h = 2.2$ mm s^{-1} for October), was 3-5 times larger compared to the vertical ($q_v = 0.22$ mm s^{-1} for July, $q_v = 0.68$ mm s^{-1} for October), indicating a suppression of the vertical turbulent velocities by stratification.

An illustration of the anisotropic character of turbulent fluctuations can be achieved by placing our measurements in the Lumley diagram (Lumley and Newman, 1977). For both deployments, the values of the second and third invariants of the anisotropy tensor were distributed along a line linking the limits of disk-like axisymmetric and one-dimensional turbulence, and always far from isotropic conditions (Figure 4.9). In the disk-like axisymmetric limit, one of the components of the turbulent velocity fluctuations is smaller compared to the other two, which are similar, while in the one-dimensional limit, turbulent fluctuations occur mainly along one preferential axis. The turbulent velocity field in our observations evolved between these two limiting regimes. This indicates that there was always a strong suppression of one of the velocity components (i.e. the vertical), but also that one of the other two components was generally preferential, and contained more energy than the other. In any case, these results show clearly the anisotropic character of turbulence in the thermocline of Lake Zurich, with a strong suppression of the vertical fluctuations, which is consistent with the

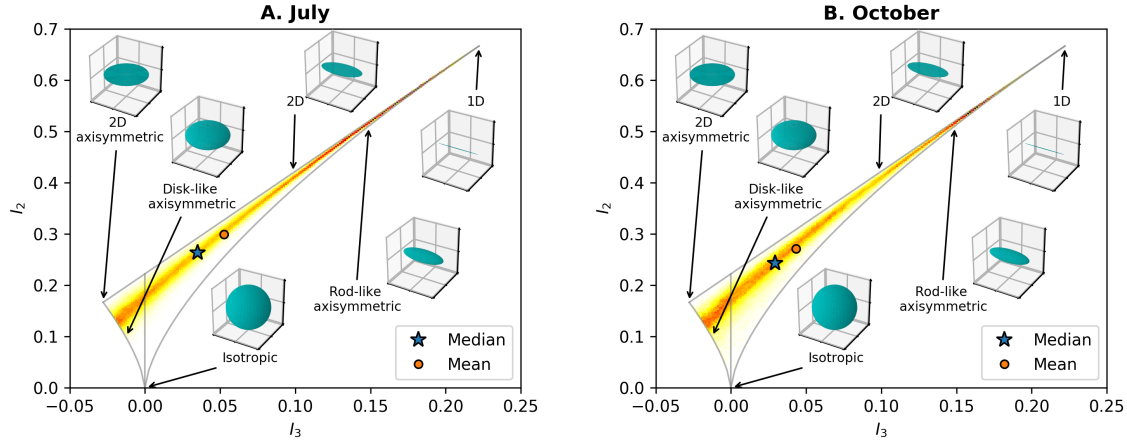reduced vertical turbulent fluxes inferred from microstructure measurements.

Figure 4.9 – Characterization of anisotropy of turbulent velocity fluctuations with the Lumley triangle using the second (I_2) and third (I_3) invariants of the anisotropy tensor (Lumley and Newman, 1977). The lower corner of the triangle is the limit of isotropic turbulence, the upper-left corner, is the limit of two dimensional axisymmetric turbulence (turbulence motions are inhibited in one axis), and the upper-right corner is the limit of one-dimensional turbulence, where turbulent motions have a single component. The background color gradient (white to red) represents an histogram of I_2 and I_3 for the velocity fluctuations registered with the Aquadopp HR in July (**A.**) and October (**B.**). Median and mean values for I_2 and I_3 are shown as a blue star and red circle, respectively.

4.4   Discussion

4.4.1   On the nature of suppressed thermocline mixing

Independent estimates of TKE dissipation rate with microstructure and high-resolution current measurements in the highly stratified seasonal thermocline of Lake Zurich revealed moderate levels of turbulent kinetic energy (TKE) dissipation, $\varepsilon \approx 10^{-8}$ W kg^{-1}, with a high degree of intermittency spanning three orders of magnitude. However, the Cox number (C), representing ratio of turbulent to molecular diffusion, was permanently $C << 1$, which means that turbulent fluxes across the thermocline were negligible compared to molecular diffusion. The mixing efficiency (Γ), i.e. the ratio of the turbulent buoyancy flux to energy dissipation, was correspondingly small. In other words, $C = 3\langle \partial T'/\partial z\rangle^2/(\partial \overline{T}/\partial z)^2 << 1$ means that turbulent stirring does not produce sufficient variance at small scales to enhance the action of molecular diffusion on the background gradient.

We also showed that unstable Richardson number values ($Ri < 1/4$) and detectable vertical turbulent overturns were very infrequent (< 10% occurrence) and, when observed, $L_T \leq L_O \approx 2$ cm, which is much smaller than typical values for the ocean thermocline (Gregg, 1987), and in the lower-end of previous observations in weakly stratified deep-waters of lakes (Etemad-Shahidi and Imberger, 2001; Lorke and Wüest, 2002). The vertical turbulent overturns temporally store potential energy, $0.5L_T^2 N^2$ (Dillon and Park, 1987), which is transferred to the mean density profile when the overturns collapse. The scarcity of overturns and its small size is thus a strong indicator of very weak turbulent mixing in the thermocline. Finally, high-resolution current measurements showed that turbulent motions were highly anisotropic and, occasionally close to one-dimensional, with a strong suppression of the vertical velocity component ($q_v \approx 0.1$ mm s^{-1}), which

strongly constrains the magnitude of vertical fluxes. The vertical turbulent diffusivity can be seen as the product of the vertical velocity and length-scales, $K \approx q_v l$ (Tennekes and Lumley, 1972), if $l \approx L_T \approx 1$ mm, then $K \approx 10^{-7}$ m^2 s^{-1}, not larger than molecular.

There is an on-going vivid debate on the magnitude of mixing efficiency in the ocean and lakes and on the factors driving its variability (Ivey and Imberger, 1991; Shih et al., 2005; Bouffard and Boegman, 2013; Maffioli et al., 2016; Gregg et al., 2017; Monismith et al., 2018). Different sources of evidence, including observations, laboratory experiments and simulations, indicate that turbulent fluxes become negligible when the buoyancy Reynolds number ($Re_b = (L_O/L_K)^{4/3}$), which is a measure of the size of the inertial subrange ($L_O > l > L_K$), falls below $\mathcal{O}(15)$ (Ivey and Imberger, 1991; Gibson, 1999; Shih et al., 2005). Our thermocline observations fall mostly in this range.

Another relevant parameter for the mixing efficiency of turbulence is the turbulent Froude number, $Fr_T = (L_O/L_T)^{2/3}$. This number is a ratio between the turbulent eddy size for which the interplay between inertial and buoyancy forces becomes relevant (L_O) and the observed vertical eddy size (L_T). When Fr_T is close or below 1, the interaction between turbulent eddies and background stratification takes place, and the potential to generate turbulent mixing and, hence, Γ are expected to be maximal (Mashayek et al., 2017). Because L_T was overall much smaller than L_O in our dataset for Lake Zurich thermocline, Fr_T was large, which means that the turbulent eddies were too small to disturb the background stratification significantly (Ivey and Imberger, 1991; Smyth et al., 2001; Ijichi and Hibiya, 2018). In such situation, the expected mixing efficiencies are low, consistent with observations.

In this study, we used a wide-spread technique and inferred turbulent mixing rates indirectly, from measured rates of dissipation of TKE and thermal variance, assuming that local balance is achieved between production, dissipation and mixing (Osborn and Cox, 1972). Measuring turbulent fluxes directly is technically challenging. However, a few studies reported direct measurements of turbulent fluxes of heat or dissolved substances in the thermocline of lakes using the eddy correlation technique (Saggio and Imberger, 2001; Etemad-Shahidi and Imberger, 2001; Weck and Lorke, 2017), whereby the flux is determined from the correlation between vertical velocity and temperature (concentration) fluctuations, $F = \langle w'T' \rangle$. Those studies found generally small or negligible turbulent fluxes, often below what could be expected from the Osborn formula with a canonical mixing efficiency of 0.2 (Oakey, 1982). In particular, Etemad-Shahidi and Imberger (2001) describe a similar situation for the thermocline of two stratified lakes, where relatively high dissipation rates ($\varepsilon \approx 10^{-7}$ W kg^{-1}) developed simultaneously with fine-grained small overturns and negligible vertical fluxes. The authors argued that, in such situation, turbulent dissipation is driven by wave-wave interactions, resulting in high-intermittency and weak vertical fluxes, rather than formation of overturning billows due to shear instabilities (Itsweire et al., 1993; Teoh et al., 1997). These results are consistent with our indirect observations.

Overall, the picture presented here is consistent with previous microstructure and tracer release studies in small and medium size lakes, which showed that turbulent fluxes in the interior are generally weak, and that mixing at the basin-scale is dominated by processes occurring at the boundaries (Goudsmit et al., 1997; Wüest et al., 2000; MacIntyre et al., 1999). Basin-scale estimates of vertical diffusivity using the heat budget method were indeed 10–100 times larger than molecular diffusion in the meta- and hypolimnion, respectively. The relevance of boundary *vs* interior mixing, typically decreases with lake size (Ravens et al., 2000; Bouffard et al., 2012), as larger lakes exhibit Kelvin and Poincarré waves, which can drive overturning instabilities in the interior metalimnion (Preusse et al., 2010; Bouffard et al., 2012). Although Lake Zurich is relatively long, it seems to behave like smaller lakes in this respect, with the bigger share of the net mixing occurring at the boundaries (Wüest et al., 2000). This situation is probably due to the weak wind forcing, and also to the lake narrowness, which limits the influence of the Earth's rotation in the basin-scale response to wind forcing (Horn et al., 1986).

Finally, the observation of strongly anisotropic nature of turbulence and the scarcity and small size of turbulent overturns in the thermocline might compromise the assumptions underlying ε estimates, both from microstructure and current measurements (Dillon and Caldwell, 1980; Smyth and Moum, 2000; Bluteau et al., 2011), and the relatively large ε must be regarded carefully. In fact, about half of the temperature-gradient spectral fits had to be discarded because the observational spectra did not follow the Batchelor shape. This indicates that conditions were probably not at all turbulent in those cases, and the spectra were influenced by finescale structures (Gregg, 1977). However, as previously mentioned, high levels of dissipation in the absence of vertical fluxes are not an uncommon feature in lakes (Etemad-Shahidi and Imberger, 2001; MacIntyre et al., 2009). Our results can also be compared with a bulk estimate of ε from the background potential energy budget (Eq. 4.7). The buoyancy flux for a representative rate of summer-time wind work ($P_{10} \approx 0.05$ W m^{-2}), is $B = \delta P_{10} \approx 0.225$ mW m^{-2}. Assuming a basin-scale mixing efficiency of $B/\varepsilon = 0.16$ (Wüest et al., 2000) and a mean-water column depth of 49 m, this corresponds to basin-scale interior dissipation of $\varepsilon = 2.9 \times 10^{-8}$ W kg^{-1}, which increases the confidence in our results.

4.4.2 Implications for thin layer persistence

In addition to its well known seasonal persistence, our high-resolution measurements revealed an outstanding stability of the *P. rubescens* thin layer at daily scales. The individual chl-*a* profiles during the microstructure sampling were barely unchanged during each survey (Figure 4.4), at least when projected on isothermal coordinates, which isolates the effect of irreversible diapycnal mixing from reversible deformation by internal waves (Cuypers et al., 2011). To achieve such stability, *P. rubescens* filaments must overcome the dispersive effect of turbulent mixing. To do so, *P. rubescens* regulate their vertical position by adjusting their buoyancy by means of gas vacuoles and changes in the concentration of carbohydrates within the cells, as a result from the photosynthesis-respiration balance (Walsby, 2005). *P. rubescens* filaments become neutrally buoyant at a depth where they receive a daily solar radiation of 0.28 mol photon m^{-2} d^{-1}. It is at that depth where the thin layer is often observed (Walsby et al., 2004). When a *P. rubescens* filament is displaced from the neutral buoyancy depth, i.e. by a mixing event, it will experience a restoring force proportional to the density difference with the ambient water.

Here we quantify the seasonal variations in the competition between turbulent mixing and buoyancy regulation. For that, we compared the vertical restoring velocities that the *P. rubescens* filaments can develop when displaced from their depth of neutral buoyancy (w_{buoy}), with the velocities that would be required to compensate the dispersive effect of turbulent mixing (w_{eq}), for each microstructure sampling in 2018 (Figure 4.10). This equilibrium velocity can be calculated by integrating the advection-diffusion equation, with the assumption of steady state and zero net growth (Stacey et al., 2007; Steinbuck et al., 2009), and it is given by

$$w_{eq}(z) = K_z(z) \frac{\partial}{\partial z} \left[\ln \left(\frac{C(z)}{C_{max}} \right) \right], \tag{4.8}$$

where C represents the concentration, in this case of chl-*a*, and K_z is vertical diffusivity, both derived from the mean observed profiles. The restoring velocity is set by the balance between buoyancy and drag and calculated as

$$w_{buoy}(z) = \frac{g d_e^2 (1 - \rho_{fil}/\rho(z))}{18\nu} \tag{4.9}$$

where d_e is the equivalent spherical diameter of a filament (~ 40 μm, Walsby, 2005), and ρ_{fill} is the density of the filaments. We assumed that, for short term perturbations, the density of the filaments is equivalent to the density of water at the chl-*a* peak. However, if the filaments are exposed to higher (lower) light levels for sufficiently long (several hours, days), they will gain ballast (buoyancy) to a maximum (minimum) anomaly of

+27 kg m^{-3} (-30 kg m^{-3}), and the restoring velocities will be maximal (w_{buoy}^{max}). Here, we will refer to the latter as long-term response.
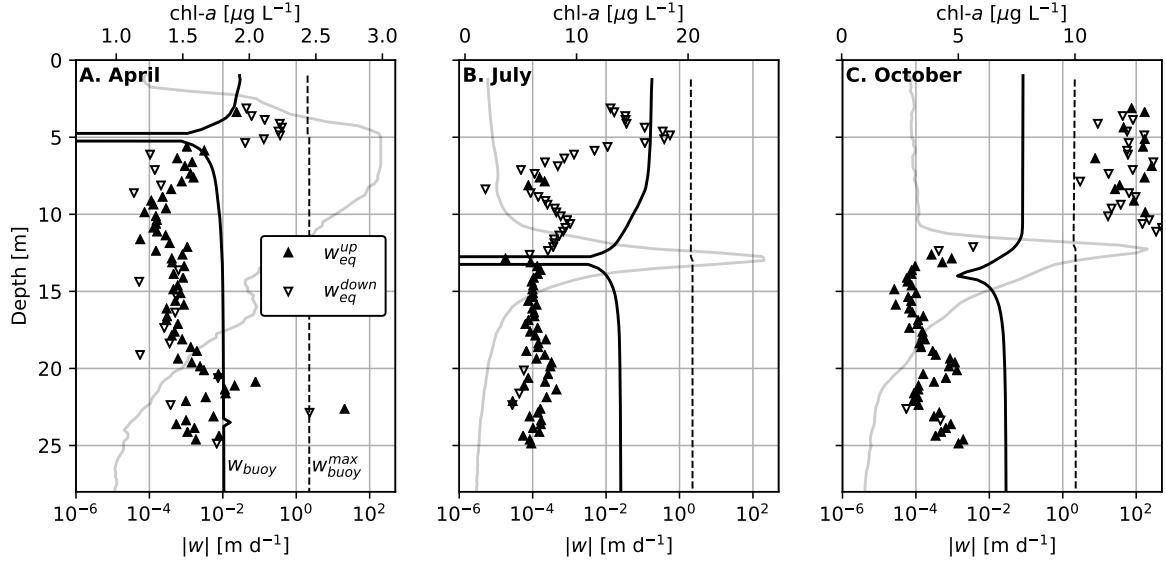

Figure 4.10 – Vertical velocity (w_{eq}, triangles) required for *P. rubescens* to overcome turbulent diffusion, as derived from the advection-diffusion balance (Eq. 4.8). Upward (downward) velocities are shown as filled upward-pointing (empty downward-pointing) triangles. Stokes velocities (w_{buoy}) for *P. rubescens* filaments having their neutral density at the chl-*a* peak are shown as black solid lines (i.e. short-term response). Maximum *P. rubescens* Stokes velocities (i.e. long-term response) for maximum/minimum density anomalies (+27/-30 kg m^{-3}) observed for *P. rubescens* in lab cultures are shown as dashed lines, positive (negative) anomalies are used above and below the chl-*a* maximum. The mean chl-*a* profile is shown in gray for each period.

In April, short-term response buoyancy velocities ($w_{buoy} \approx 0.01$ m d^{-1}, black line) were lower than w_{eq} above the chl-*a* maximum (upper 5 m), but higher below (Figure 4.10A). For the long-term response (dashed line), maximum restoring velocities ($w_{buoy}^{max} \approx 2$ m d^{-1}) were 2–3 orders of magnitude larger than w_{eq}. This indicates that conditions were favorable for the *P. rubescens* filaments, which had been entrained into the deeper part of the lake, to rise and form the layer. In fact, the layer was already detected by the regular monitoring one week after this survey (Figure 4.2C). The time scale for the accumulation by buoyancy alone, $\tau \approx (|z_{mean}|/2)/w_{buoy}^{max}$, could be as low as ~12 days, which is consistent with the observations and suggests that vertical migration is a primary driver for the early onset of the layer.

In July, the short-term restoring velocities increased with respect to April, reaching $w_{buoy} > 0.1$ m d^{-1}, due to the large density gradient in the thermocline, and $w_{buoy} > w_{eq}$ everywhere except in a narrow band close to the chl-*a* peak (Figure 4.10B). In October, $w_{buoy} > w_{eq}$ below the *P. rubescens* layer, but w_{buoy} reduced slightly (due to reduced density differences) and w_{eq} increased sharply in the surface mixed-layer to > 10 m d^{-1}, just above the upper limit of the plankton layer (Figure 4.10C). There, both w_{buoy} and w_{buoy}^{max} were smaller than w_{eq}, indicating that any filament eventually entrained into the mixed layer will not be able to overcome turbulent mixing and return to the layer.

This shows that mixing in the lake's interior thermocline during the stratified season, which is mainly driven by wind stirring, is too weak to significantly disturb the *P. rubescens* thin layer, and that buoyancy regulation of the filaments was sufficient to overcome turbulent dispersion. Although some of the microstructure profiles

were carried out under above-average wind forcing, the representativeness of our short-duration surveys might be questionable due to the transient nature of turbulent events. This lack of representativeness can be circumvented by considering the basin-scale diffusivity (Figure 4.3C), which integrates both episodic mixing in the lake's interior as well as mixing at the boundaries. In the main thermocline, where the *P. rubescens* layer is located, basin-scale $K_T^{BS} \approx 10^{-6}$ m^2 s^{-1}. With buoyancy restoring velocities in the range $w_{buoy} = 0.01 - 1.0$ m d^{-1}, and considering a layer characteristic length of $l \approx 1$ m, the Péclet number would be $Pe = w_{buoy}l/K = 0.1 - 10$, indicating a tighter interplay between turbulent dispersion and restoring by buoyancy. However, the persistence of the layer suggests that, overall, restoring forces dominate.
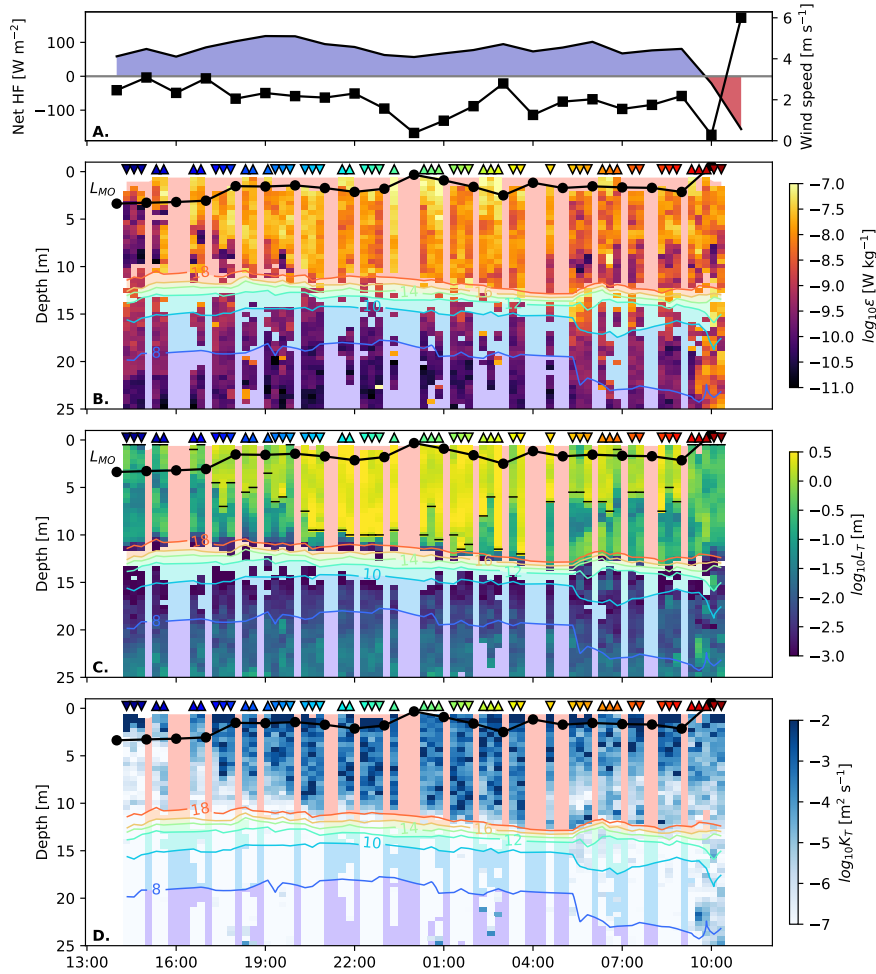
Figure 4.11 – Microstructure measurements collected with a microCTD profiler during the dedicated nighttime sampling on 24–25 September 2019 at st0. **A.** surface heat flux (colors) and wind speed (black) derived from COSMO model, **B.** TKE dissipation rate (ε), **C.** Thorpe scale (L_T), and **D.** heat diffusivity (K_T). Temperature contours every 2°C and Monin-Obukhov length-scale (L_{MO}, black line with dots) are plotted in panels **B-D.**. Upward and downward looking triangles indicate ascending and descending profiling, respectively. The color scale of the triangles represents the sampling time. Surface mixing-layer depth (defined as $L_T > 1$ m) is indicated with horizontal black markers in panel **C.** Time in the x-axis UTC time (local time was UTC+2).

4.4.3 Layer breakdown: the role of nighttime convection

The previous analysis showed that, after the onset of nighttime convection in late summer, the turbulence parameters in the surface mixed-layer change radically, with large turbulent overturns, while vertical mixing in the thermocline remains negligible. The seasonal monitoring showed some signs of entrainment of *P. rubescens* cells into the mixed layer from mid-October on, when the mixed layer approached the location of the thin layer (Figure 4.2). At that time, lake number, L_N, was still overall large, showing no indication of significant wind-driven mixing affecting the metalimnion (Figure 4.3). Further, the chl-*a* profile remained barely unchanged throughout our day-time microstructure surveys in early October, but the strong asymmetry in the shape of the peak could indicate that it had been previously disturbed by convection during nighttime.These evidences suggest that nighttime convection is more important than wind driven metalimnetic mixing for the dissolution of the *P. rubescens* layer in fall.
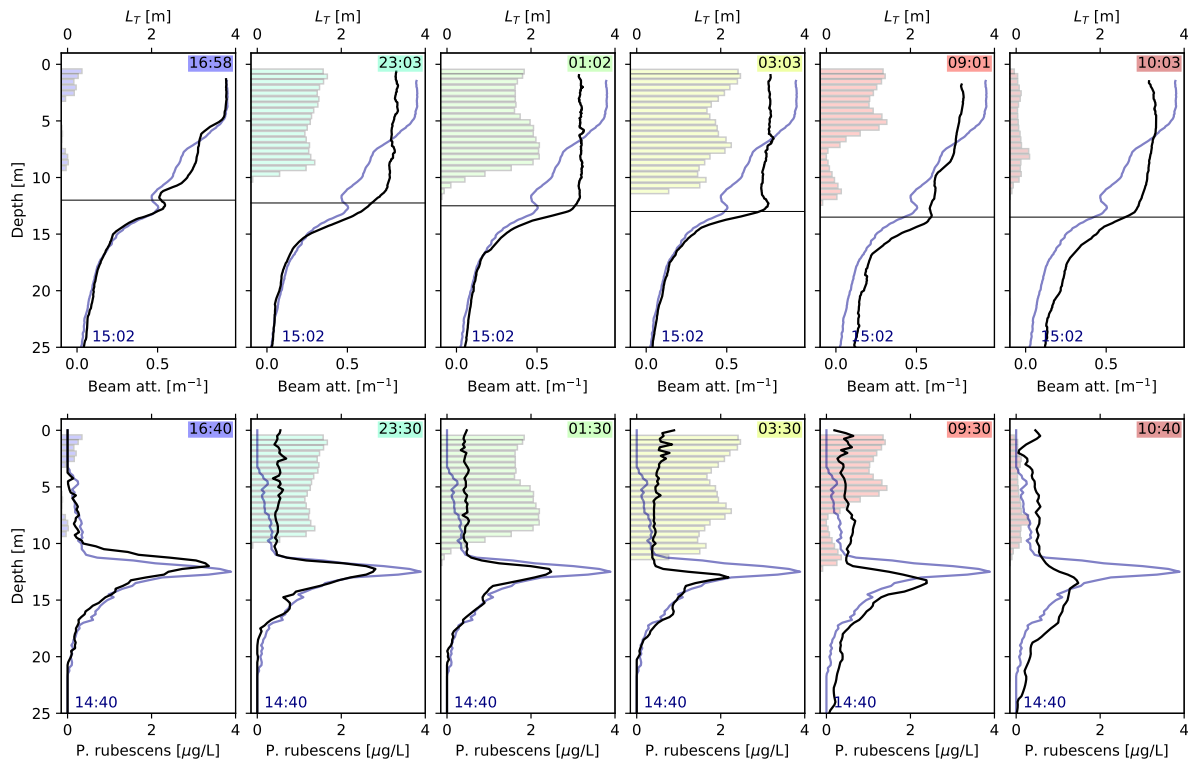
Figure 4.12 – Profiles of beam attenuation (upper row) and *P. rubescens* chl-*a* concentration (lower row) collected during the the dedicated nighttime sampling on 24-25 September 2019 at st0 with a SeaBird CTD and a fluoroprobe, respectively. The profile at the indicated sampling time (color rectangle) is shown as a black line, and initial reference profile is shown as a light blue line. The bar plots represent mean profiles of Thorpe scale (L_T) between the previous and current fluoroprobe profile. The color code indicates the sampling time in relation to Figure 4.11.

To confirm this hypothesis, a nighttime survey was conducted with a microstructure profiler, a CTD and a fluoroprobe between 14:40 UTC (16:40 local) on the 24th of September 2019 and 10:40 UTC on the following 25th (Figure 4.11). During the survey, wind over the lake was weak (2 m s^{-1}) and a moderate heat loss was observed throughout (Figure 4.11A). A SML of 10 m with $T = 18\,°$C and a sharp pycnocline between 10 and 15 m depth were found (Figure 4.11B). Consistent with the previous results, ε was hardly determined at the thermocline by Batchelor fitting (empty bins represent bad fits in Figure 4.11B), turbulent overturns were rare (empty bins represent $L_T = 0$ in Figure 4.11C), and vertical diffusivity was close or below molec-

ular levels (Figure 4.11D). In the SML, below the Monin-Obukhov depth ($L_{MO} = u_*^3/(\kappa B_0)$), ε was initially small (10^{-10} W kg^{-1}), $L_T < 1$ m and K_T close to molecular. After 5pm, a mixing layer with enhanced ε (2×10^{-8} W kg^{-1}), L_T (1–3 m) and K_T ($> 10^{-4}$ m^2 s^{-1}), penetrated below L_{MO} and, at about 9pm, it reached the thermocline, which also deepened slightly overnight. The intensity and depth reach of the convective mixing declined after 4am, and completely shut down after sunrise, when the heat flux became negative (into the lake).

The effect of convective mixing is illustrated by the temporal evolution of beam attenuation (representing the concentration of particles in water) and *P. rubescens* concentration, determined with the CTD and fluoroprobe, respectively (Figure 4.12). The initial profiles in the early afternoon (15:02 and 14:40, respectively) are plotted in light blue in every panel for clarity, and bars representing the L_T are added to illustrate the vertical extent and intensity of mixing. Beam attenuation was not uniform in the SML in the early afternoon, but it was vigorously homogenized during the night, when convection was active. In the morning, the vertical distribution became slightly non-uniform again. *P. rubescens* was found in a well defined peak in the afternoon, and its concentration in the SML was small. Overnight, convection reached the top of the thin layer, maximum *P. rubescens* concentration at the layer progressively declined and their concentration in the SML increased, as a result of filament entrainment by convective plumes eroding the layer from above. These results clearly show that nighttime convection in early-fall has a much stronger disruptive effect over the *P. rubescens* layer compared to wind-driven metalimnetic mixing. It is therefore very likely that convection plays a major role in the seasonal breakdown of the thin layer, as net cooling results in deepening of the thermocline during fall (Figure 4.2).

4.5   Conclusions

The interplay between vertical turbulent mixing and the seasonal persistence (May–October) of an annually recurrent thin layer of toxic cyanobacteria (*Planktothrix rubescens*) in Lake Zurich was investigated by means of four microstructure surveys and high-resolution mooring deployments. Our measurements revealed that the strong metalimnetic stratification induces anisotropic turbulence and inhibits vertical overturns. This results in negligible turbulent vertical fluxes, which provides a very stable environment for the *P. rubescens* thin layer to form and persist. Moreover, even when considering the overall basin-scale diffusivity, derived from the heat-budget method, the intensity of mixing was still not strong enough to overcome the buoyancy restoring forces of *P. rubescens* filaments, which explains the seasonal persistence of the layer. Finally, we also showed that the planktonic layer decline in fall is not caused by wind-driven stratified turbulence in the thermocline, but rather by nighttime convective mixing eroding the layer from above.

As a consequence of increasing air temperatures and sky brightening, the thermal budget of lake Zurich has been altered over the past decades, resulting in net warming (Schmid and Köster, 2016), and a deepening, strengthening, and prolongation of the metalimnetic stratification (Livingstone, 2003; Posch et al., 2012), and a reduction in the occurrence of holomixis during winter (Yankova et al., 2017). Although relatively large, Lake Zurich is exposed to weak winds and the internal motions are weakly influenced by the Earth's rotation, which is probably a key factor to understand why metalimnetic turbulent fluxes are so small in the lake's interior (Bouffard et al., 2012). Our results show that, in such a situation, nighttime convective mixing plays a crucial role not only for the seasonal evolution of stratification, but also for the dynamics of the phytoplanktonic communities. This is critical, as nighttime convection is particularly sensitive to the ongoing climatic changes (Livingstone, 2003). These changes are altering the mixing regimes of lakes worldwide (Woolway and Merchant, 2019), and this alteration goes along with changes in the nutrient regime following restoration measures. The interplay of both can favor or undermine the proliferation of certain planktonic

species, such as *P. rubescens* (Posch et al., 2012; Jacquet et al., 2014). Because the dynamics of Lake Zurich are considered as representative for medium-sized lakes in temperate climates (Schmid and Köster, 2016), our results are valuable to understand how these systems may evolve in the future, from a physical and ecological viewpoint.

Acknowledgements

References

Abbott, M. R., Denman, K. L., Powell, T. M., Richerson, P. J., Richards, R. C., and Goldman, C. R. (1984). Mixing and the dynamics of the deep chlorophyll maximum in Lake Tahoe. *Limnology and Oceanography*, 29(4):862–878. doi:10.4319/lo.1984.29.4.0862.

Banerjee, S., Krahl, R., Durst, F., and Zenger, C. (2007). Presentation of anisotropy properties of turbulence, invariants versus eigenvalue approaches. *Journal of Turbulence*, 8:1–27. doi:10.1080/14685240701506896.

Batchelor, G. K., Howells, I. D., and Townsend, A. A. (1959). Small-scale variation of convected quantities like temperature in turbulent fluid: Part 1. General discussion and the case of small conductivity. *Journal of Fluid Mechanics*, 5(1):113–133. doi:10.1017/S002211205900009.

Benoit-Bird, K. J., Cowles, T. J., and Wingard, C. E. (2009). Edge gradients provide evidence of ecological interactions in planktonic thin layers. *Limnology and Oceanography*, 54(4):1382–1392. doi:10.4319/lo.2009.54.4.1382.

Bluteau, C. E., Jones, N. L., and Ivey, G. N. (2011). Estimating turbulent kinetic energy dissipation using the inertial subrange method in environmental flows. *Limnology and Oceanography: Methods*, 9:302–321. doi:10.4319/lom.2011.9.302.

Boegman, L., Imberger, J., Ivey, G. N., and Antenucci, J. P. (2003). High-frequency internal waves in large stratified lakes. *Limnology and Oceanography*, 48(2):895–919. doi:10.4319/lo.2003.48.2.0895.

Boehrer, B. and Schultze, M. (2008). Stratification of lakes. *Reviews in Geophysics*, 46:RG000205. doi:8755-1209/08/2006RG000210.

References

Bossard, P., Gammeter, S., Lehmann, C., Schanz, F., Bachofen, R., Bürgi, H. R., Steiner, D., and Zimmermann, U. (2001). Limnological description of the Lakes Zürich, Lucerne, and Cadagno. *Aquatic Sciences*, 63(3):225–249. doi:10.1007/PL00001353.

Bouffard, D. and Boegman, L. (2013). A diapycnal diffusivity model for stratified environmental flows. *Dynamics of Atmospheres and Oceans*, 61-62:14–34. doi:10.1016/j.dynatmoce.2013.02.002.

Bouffard, D., Boegman, L., and Rao, Y. R. (2012). Poincaré wave–induced mixing in a large lake. *Limnology and Oceanography*, 57(4):1201–1216. doi:10.4319/lo.2012.57.4.1201.

Broullón, E., López-Mozos, M., Reguera, B., Chouciño, P., Doval, M. D., Fernández-Castro, B., Gilcoto, M., Nogueira, E., Souto, C., and Mouriño-Carballido, B. (2020). Thin layers of phytoplankton and harmful algae events in a coastal upwelling system. *Progress in Oceanography*, page Submitted.

Cheriton, O. M., McManus, M. A., Stacey, M. T., and Steinbuck, J. V. (2009). Physical and biological controls on the maintenance and dissipation of a thin phytoplankton layer. *Marine Ecology Progress Series*, 378(2003):55–69. doi:10.3354/meps07847.

Csanady, G. T. (1975). Hydrodynamics of large lakes. *Annu Rev Fluid Mech*, 7(1):357–386. doi:10.1146/annurev.fl.07.010175.002041.

Cullen, J. J. (2015). Subsurface chlorophyll maximum layers: enduring enigma or mystery solved? *Annual Review of Marine Science*, 7(1):207–239. doi:10.1146/annurev-marine-010213-135111.

Cuypers, Y., Vinçon-Leite, B., Groleau, A., Tassin, B., and Humbert, J. F. (2011). Impact of internal waves on the spatial distribution of Planktothrix rubescens (cyanobacteria) in an alpine lake. *ISME Journal*, 5(4):580–589. doi:10.1038/ismej.2010.154.

Dekshenieks, M. M., Donaghay, P. L., Sullivan, J. M., Rines, J. E., Osborn, T. R., and Twardowski, M. S. (2001). Temporal and spatial occurrence of thin phytoplankton layers in relation to physical processes. *Marine Ecology Progress Series*, 223:61–71. doi:10.3354/meps223061.

Dillon, T. M. and Caldwell, D. R. (1980). The Batchelor spectrum and dissipation in the upper ocean. *Journal of Geophysical Research*, 85(C4):1910–1916. doi:10.1029/JC085iC04p01910.

Dillon, T. M. and Park, M. M. (1987). The available potential energy of overturns as an indicator of mixing in the seasonal thermocline. *Journal of Geophysical Research*, 92(C5):5345–5353. doi:10.1029/JC092iC05p05345.

Durham, W. M. and Stocker, R. (2012). Thin phytoplankton layers: characteristics, mechanisms, and consequences. *Annual Review of Marine Science*, 4(1):177–207. doi:10.1146/annurev-marine-120710-100957.

Etemad-Shahidi, A. and Imberger, J. (2001). Anatomy of turbulence in thermally stratified lakes. *Limnology and Oceanography*, 46(5):1158–1170. doi:10.4319/lo.2001.46.5.1158.

Fink, G., Schmid, M., Wahl, B., Wolf, T., and Wüest, A. (2014). Heat flux modifications related to climate-induced warming of large European lakes. *Water Resources Research*, 50:2072–2085. doi:10.1002/2013WR014448.

Gargett, A. E. (1999). Velcro measurement of turbulence kinetic energy dissipation rate ϵ. *Journal of Atmospheric and Oceanic Technology*, 16(12):1973–1993. doi:10.1175/1520-0426(1999)016<1973:VMOTKE>2.0.CO;2.

Gibson, C. H. (1999). Fossil turbulence revisited. *Journal of Marine Systems*, 21(1-4):147–167. doi:10.1016/S0924-7963(99)00024-X.

Goudsmit, G. H., Peeters, F., Gloor, M., and Wüest, A. (1997). Boundary versus internal diapycnal mixing in stratified natural waters. *Journal of Geophysical Research: Oceans*, 102(C13):27903–27914. doi:10.1029/97JC01861.

Gregg, M., D'Asaro, E., Riley, J., and Kunze, E. (2017). Mixing efficiency in the ocean. *Annual Review of Marine Science*, 10(1):443–473. doi:10.1146/annurev-marine-121916-063643.

Gregg, M. C. (1977). Variations in the intensity of small-scale mixing in the main thermocline. *Journal of Physical Oceanography*, 7(3):436–454. doi:10.1175/1520-0485(1977)007<0436:vitios>2.0.co;2.

Gregg, M. C. (1987). Diapycnal mixing in the thermocline: a review. *Journal of Geophical Research*, 92(C5):5249–5286. doi:10.1016/0198-0254(87)90591-7.

Horn, W., Mortimer, C. H., and Schwab, D. J. (1986). Wind-induced internal seiches in Lake Zurich observed and modeled. *Limnology and Oceanography*, 31(6):1232–1254. doi:10.4319/lo.1986.31.6.1232.

Huisman, J., Oostveen, P. V., Weissing, F. J., and Nov, N. (1999). Critical depth and critical turbulence: two different mechanisms for the development of phytoplankton blooms. *Limnology and Oceanography*, 44(7):1781–1787. doi:10.4319/lo.1999.44.7.1781.

Ijichi, T. and Hibiya, T. (2018). Observed variations in turbulent mixing efficiency in the deep ocean. *Journal of Physical Oceanography*, 48(8):1815–1830. doi:10.1175/JPO-D-17-0275.1.

Imberger, J. and Patterson, J. C. (1989). Physical Limnology. *Advances in Applied Mechanics*, 27:303–475. doi:10.1016/S0065-2156(08)70199-6.

Imboden, D. M. and Wüest, A. (1995). Mixing mechanisms in lakes. In Lerman, A., Imboden, D., and Gat, J., editors, *Physics and Chemistry of Lakes*, pages 83–138. Springer.

Itsweire, E. C., Koseff, J. R., Briggs, D. A., and Ferziger, J. H. (1993). Turbulence in stratified shear flows: implications for interpreting shear-induced mixing in the ocean. *Journal of Physical Oceanography*, 23:1508–1522. doi:10.1175/1520-0485(1993)023<1508:TISSFI>2.0.CO;2.

Ivey, G. N. and Imberger, J. (1991). On the nature of turbulence in a stratified fluid. Part I: the energetics of mixing. *Journal of Physical Oceanography*, 21(5):650–658. doi:10.1175/1520-0485(1991)021<0650:OTNOTI>2.0.CO;2.

Jacquet, S., Kerimoglu, O., Rimet, F., Paolini, G., and Anneville, O. (2014). Cyanobacterial bloom termination: The disappearance of Planktothrix rubescens from Lake Bourget (France) after restoration. *Freshwater Biology*, 59(12):2472–2487. doi:10.1111/fwb.12444.

Leach, T. H., Beisner, B. E., Carey, C. C., Pernica, P., Rose, K. C., Huot, Y., Brentrup, J. A., Domaizon, I., Grossart, H. P., Ibelings, B. W., Jacquet, S., Kelly, P. T., Rusak, J. A., Stockwell, J. D., Straile, D., and Verburg, P. (2018). Patterns and drivers of deep chlorophyll maxima structure in 100 lakes: The relative importance of light and thermal stratification. *Limnology and Oceanography*, 63(2):628–646. doi:10.1002/lno.10656.

Li, Y. H. (1973). Vertical eddy diffusion coefficient in Lake Zürich. *Schweizerische Zeitschrift für Hydrologie*, 35(1):1–7. doi:10.1007/BF02502061.

Livingstone, D. M. (2003). Impact of secular climate change on the thermal structure of a large temperate central European lake. *Climatic Change*, 57:205–225. doi:10.1023/A:1022119503144.

Lorke, A., Peeters, F., and Wüest, A. (2005). Shear-induced convective mixing in bottom boundary layers on slopes. *Limnol. Oceanogr*, 50(5):1612–1619. doi:10.4319/lo.2005.50.5.1612.

References

Lorke, A. and Wüest, A. (2002). Probability density of displacement and overturning length scales under diverse stratification. *Journal of Geophysical Research: Oceans*, 107(C12):3214. doi:10.1029/2001JC001154.

Luketina, D. A. and Imberger, J. (2001). Determining turbulent kinetic energy dissipation from Batchelor curve fitting. *Journal of Atmospheric and Oceanic Technology*, 18(1):100–113. doi:10.1175/1520-0426(2001)018<0100:DTKEDF>2.0.CO;2.

Lumley, J. L. and Newman, G. R. (1977). The return to isotropy of homogeneous turbulence. *Journal of Fluid Mechanics*, 82(1):161–178. doi:10.1017/S002211200100386X.

MacIntyre, S., Clark, J. F., Jellison, R., and Framb, J. P. (2009). Turbulent mixing induced by nonlinear internal waves in Mono Lake, California. *Limnology and Oceanography*, 54(6):2255–2272. doi:10.4319/lo.2009.54.6.2255.

MacIntyre, S., Flynn, K. M., Jellison, R., and Romero, J. R. (1999). Boundary mixing and nutrient fluxes in Mono Lake, California. *Limnology and Oceanography*, 44(3):512–529. doi:10.4319/lo.1999.44.3.0512.

MacIntyre, S., Sickman, J. O., Goldthwait, S. A., and Kling, G. W. (2006). Physical pathways of nutrient supply in a small, ultraoligotrophic arctic lake during summer stratification. *Limnology and Oceanography*, 51(2):1107–1124. doi:10.4319/lo.2006.51.2.1107.

Maffioli, A., Brethouwer, G., and Lindborg, E. (2016). Mixing efficiency in stratified turbulence. *Journal of Fluid Mechanics*, 794:R3. doi:10.1017/jfm.2016.206.

Mashayek, A., Caulfield, C. P., and Peltier, W. R. (2017). Role of overturns in optimal mixing in stratified mixing layers. *Journal of Fluid Mechanics*, 826:522–552. doi:10.1017/jfm.2017.374.

McManus, M. A., Alldredge, A. L., Barnard, A. H., Boss, E., Case, J. F., Cowles, T. J., Donaghay, P. L., Eisner, L. B., Gifford, D. J., Greenlaw, C. F., Herren, C. M., Holliday, D. V., Johnson, D., MacIntyre, S., McGehee, D. M., Osborn, T. R., Perry, M. J., Pieper, R. E., Rines, J. E., Smith, D. C., Sullivan, J. M., Talbot, M. K., Twardowski, M. S., Weidemann, A., and Zaneveld, J. R. (2003). Characteristics, distribution and persistence of thin layers over a 48 hour period. *Marine Ecology Progress Series*, 261:1–19. doi:10.3354/meps261001.

Miles, J. W. (1961). On the stability of heterogeneous shear flows. *Journal of Fluid Mechanics*, 10:496–508. doi:10.1143/JJAP.8.821.

Monismith, S. G., Koseff, J. R., and White, B. L. (2018). Mixing efficiency in the presence of stratification: when is it constant? *Geophysical Research Letters*, 45(11):5627–5634. doi:10.1029/2018GL077229.

Nielsen, T., Kiorboe, T., and Bjørnsen, P. (1990). Effects of a Chrysochromulina polylepis subsurface bloom on the planktonic community. *Marine Ecology Progress Series*, 62:21–35. doi:10.3354/meps062021.

Oakey, N. S. (1982). Determination of the rate of dissipation of turbulent energy from simultaneous temperature and velocity shear microstructure measurements. *Journal of Physical Oceanography*, 12(3):256–271. doi:10.1175/1520-0485(1982)012<0256:DOTROD>2.0.CO;2.

Osborn, T. R. (1980). Estimates of the local rate of vertical diffusion from dissipation measurements. *Journal of Physical Oceanography*, 10:83–89. doi:10.1175/1520-0485(1980)010<0083:EOTLRO>2.0.CO;2.

Osborn, T. R. and Cox, C. S. (1972). Oceanic fine structure. *Geophysical Fluid Dynamics*, 3(1):321–345. doi:10.1080/03091927208236085.

Piccolroaz, S., Toffolon, M., and Majone, B. (2013). A simple lumped model to convert air temperature into surface water temperature in lakes. *Hydrology and Earth System Sciences*, 17(8):3323–3338. doi:10.5194/hess-17-3323-2013.

Posch, T., Köster, O., Salcher, M. M., and Pernthaler, J. (2012). Harmful filamentous cyanobacteria favoured by reduced water turnover with lake warming. *Nature Climate Change*, 2(11):809–813. doi:10.1038/nclimate1581.

Powell, T. and Jassby, A. (1974). The estimation of vertical eddy diffusivities below the thermocline in lakes. *Water Resources Research*, 10(2):191–198. doi:10.1029/WR010i002p00191.

Preusse, M., Peeters, F., and Lorke, A. (2010). Internal waves and the generation of turbulence in the thermocline of a large lake. *Limnology and Oceanography*, 55(6):2353–2365. doi:10.4319/lo.2010.55.6.2353.

Ravens, T. M., Kocsis, O., Wüest, A., and Granin, N. (2000). Small-scale turbulence and vertical mixing in Lake Baikal. *Limnology and Oceanography*, 45(1):159–173. doi:10.4319/lo.2000.45.1.0159.

Rippeth, T. P., Wiles, P. J., Palmer, M. R., Sharples, J., and Tweddle, J. (2009). The diapycnal nutrient flux and shear-induced diapycnal mixing in the seasonally stratified western Irish Sea. *Continental Shelf Research*, 29(13):1580–1587. doi:10.1016/j.csr.2009.04.009.

Robertson, D. M. and Imberger, J. (1994). Lake Number, a quantitative indicator of mixing used to estimate changes in dissolved oxygen. *Internationale Revue der gesamten Hydrobiologie und Hydrographie*, 79(2):159–176. doi:10.1002/iroh.19940790202.

Ruddick, B., Anis, A., and Thompson, K. (2000). Maximum likelihood spectral fitting: The Batchelor spectrum. *Journal of Atmospheric and Oceanic Technology*, 17(11):1541–1555. doi:10.1175/1520-0426(2000)017<1541:MLSFTB>2.0.CO;2.

Saggio, A. and Imberger, J. (2001). Mixing and turbulent fluxes in the metalimnion of a stratified lake. *Limnology and Oceanography*, 46(2):392–409. doi:10.4319/lo.2001.46.2.0392.

Sanford, L. P. (1997). Turbulent mixing in experimental ecosystem studies. *Marine Ecology Progress Series*, 161:265–293. doi:10.3354/meps161265.

Schmid, M. and Köster, O. (2016). Excess warming of a Central European lake driven by solar brightening. *Water Resources Research*, 52:8103–8116. doi:10.1111/j.1752-1688.1969.tb04897.x.

Sharples, J., Moore, C. M., Rippeth, T. P., Holligan, P. M., Hydes, D. J., Fisher, N. R., and Simpson, J. H. (2001). Phytoplankton distribution and survival in the thermocline. *Limnology and Oceanography*, 46(3):486–496. doi:10.4319/lo.2001.46.3.0486.

Shih, L. H., Koseff, J. R., Ivey, G. N., and Ferziger, J. H. (2005). Parameterization of turbulent fluxes and scales using homogeneous sheared stably stratified turbulence simulations. *Journal of Fluid Mechanics*, 525:193–214. doi:10.1017/S0022112004002587.

Shroyer, E. L., Benoit-Bird, K. J., Nash, J. D., and Moum, J. N. (2014). Stratification and mixing regimes in biological thin layers over the Mid-Atlantic Bight. *Limnology and Oceanography*, 59(4):1349–1363. doi:10.4319/lo.2014.59.4.1349.

Simpson, J. H. and Sharples, J. (2012). *Introduction to the Physical and Biological Oceanography of Shelf Seas*. Cambridge University Press, Cambridge, United Kingdom.

Smyth, W. D. and Moum, J. N. (2000). Anisotropy of turbulence in stably stratified mixing layers. *Physics of Fluids*, 12(6):1343–1362. doi:10.1063/1.870386.

Smyth, W. D., Moum, J. N., and Caldwell, D. R. (2001). The efficiency of mixing in turbulent patches: Inferences from direct simulations and microstructure observations. *Journal of Physical Oceanography*, 31(8):1969–1992. doi:10.1175/1520-0485(2001)031<1969:teomit>2.0.co;2.

References

Sommer, T., Carpenter, J. R., Schmid, M., Lueck, R. G., and Wüest, A. (2013). Revisiting microstructure sensor responses with implications for double-diffusive fluxes. *Journal of Atmospheric and Oceanic Technology*, 30(8):1907–1923. doi:10.1175/JTECH-D-12-00272.1.

Spigel, R. H. and Imberger, J. (1987). Mixing processes relevant to phytoplankton dynamics in lakes. *New Zealand Journal of Marine and Freshwater Research*, 21(3):361–377. doi:10.1080/00288330.1987.9516233.

Stacey, M. T., McManus, M. A., and Steinbuck, J. V. (2007). Convergences and divergences and thin layer formation and maintenance. *Limnology and Oceanography*, 52(4):1523–1532. doi:10.4319/lo.2007.52.4.1523.

Steinbuck, J. V., Stacey, M. T., McManus, M. A., Cheriton, O. M., and Ryan, J. P. (2009). Observations of turbulent mixing in a phytoplankton thin layer: Implications for formation, maintenance, and breakdown. *Limnology and Oceanography*, 54(4):1353–1368. doi:10.4319/lo.2009.54.4.1353.

Stevens, C. and Imberger, J. (1996). The initial response of a stratified lake to a surface shear stress. *Journal of Fluid Mechanics*, 312:39–66. doi:10.1017/S0022112096001917.

Strickland, J. (1968). A comparison of profiles of nutrient and chlorophyll concentrations taken from discrete depths and by continuous recording. *Limnology and Oceanography*, 13:388–391.

Tennekes, H. and Lumley, J. (1972). *A first course in turbulence*. MIT Press.

Teoh, S. G., Ivey, G. N., and Imberger, J. (1997). Laboratory study of the interaction between two internal wave rays. *Journal of Fluid Mechanics*, 336:91–122. doi:10.1017/S0022112096004508.

Thorpe, S. A. (1977). Turbulence and Mixing in a Scottish Loch. *Phil. Trans. R. Soc. Lond. A*, 286(1334):125–181. doi:10.1098/rsta.1977.0112.

Toffolon, M., Piccolroaz, S., Majone, B., Soja, A. M., Peeters, F., Schmid, M., and Wüest, A. (2014). Prediction of surface temperature in lakes with different morphology using air temperature. *Limnology and Oceanography*, 59(6):2185–2202. doi:10.4319/lo.2014.59.6.2185.

Walsby, A. E. (2005). Stratification by cyanobacteria in lakes: A dynamic buoyancy model indicates size limitations met by Planktothrix rubescens filaments. *New Phytologist*, 168(2):365–376. doi:10.1111/j.1469-8137.2005.01508.x.

Walsby, A. E., Ng, G., Dunn, C., and Davis, P. A. (2004). Comparison of the depth where Planktothrix rubescens stratifies and the depth where the daily insolation supports its neutral buoyancy. *New Phytologist*, 162(1):133–145. doi:10.1111/j.1469-8137.2004.01020.x.

Walsby, A. E. and Schanz, F. (2002). Light-dependent growth rate determines changes in the population of Planktothrix rubescens over the annual cycle in lake Zürich, Switzerland. *New Phytologist*, 154(3):671–687. doi:10.1046/j.1469-8137.2002.00401.x.

Weck, J. and Lorke, A. (2017). Mixing efficiency in the thermocline of lakes observed from eddy correlation flux measurements. *Journal of Geophysical Research: Oceans*, 122(1):291–305. doi:10.1002/2016JC012188.

Woolway, R. I. and Merchant, C. J. (2019). Worldwide alteration of lake mixing regimes in response to climate change. *Nature Geoscience*, 12(4):271–276. doi:10.1038/s41561-019-0322-x.

Woolway, R. I., Simpson, J. H., Spiby, D., Feuchtmayr, H., Powell, B., and Maberly, S. C. (2018). Physical and chemical impacts of a major storm on a temperate lake: a taste of things to come? *Climatic Change*, 151(2):333–347. doi:10.1007/s10584-018-2302-3.

Wüest, A. and Lorke, A. (2003). Small scale hydrodynamics in lakes. *Annual Review of Fluid Mechanics*, 35(1):373–412. doi:10.1146/annurev.fluid.35.101101.161220.

Wüest, A., Piepke, G., and Halfman, J. (1996). Combined effects of dissolved solids and temperature on the density stratification of Lake Malawi. In Johnson, T. C. and Odada, E. O., editors, *The Limnology, Climatology and Paleoclimatology of the East African Lakes*, pages 183–202. Gordon and Breach, Toronto.

Wüest, A., Piepke, G., and Van Senden, D. C. (2000). Turbulent kinetic energy balance as a tool for estimating vertical diffusivity in wind-forced stratified waters. *Limnology and Oceanography*, 45(6):1388–1400. doi:10.4319/lo.2000.45.6.1388.

Yankova, Y., Neuenschwander, S., Köster, O., and Posch, T. (2017). Abrupt stop of deep water turnover with lake warming: Drastic consequences for algal primary producers. *Scientific Reports*, 7(1):1–9. doi:10.1038/s41598-017-13159-9.

Yankova, Y., Villiger, J., Pernthaler, J., Schanz, F., and Posch, T. (2016). Prolongation, deepening and warming of the metalimnion change habitat conditions of the harmful filamentous cyanobacterium Planktothrix rubescens in a prealpine lake. *Hydrobiologia*, 776(1):125–138. doi:10.1007/s10750-016-2745-3.

5 Towards the assessment of lateral variability in lakes: Turbulent mixing from an underwater glider in Lake Geneva

Oscar Sepúlveda Steiner[1], **Alexander Forrest**[2], **Jasmin McInerney**[2], **Sébastien Lavanchy**[1], **Bieito Fernández-Castro**[1], **Damien Bouffard**[3], and **Alfred Wüest**[1,3]

[1]Physics of Aquatic Systems Laboratory, Margaretha Kamprad Chair, Institute of Environmental Engineering, École Polytechnique Fédérale de Lausanne, Lausanne, Switzerland.

[2]Civil & Environmental Engineering, University of California – Davis, Davis, CA, USA.

[3]Department of Surface Waters – Research and Management, Eawag, Swiss Federal Institute of Aquatic Science and Technology, Kastanienbaum, Switzerland.

Abstract

Vertical representation in lakes, resulting from stratification-imposed conditions, has led to fundamental advances in the understanding of seasonal and long-term development. Yet, the spatial extent of basin-scale dynamics such as internal-waves and upwelling events cannot be represented with this framework. Numerical models combined with in-situ measurements have provided valuable insight on the spatio-temporal evolution of this processes. In addition, remote sensing has demonstrated the surface waters response. However, we still lack a comprehensive in-situ characterization of the spatial variability of water properties induced by basin-scale processes. During the summer of 2018, we explored the connection between lateral variability of physical properties, namely turbulence, and the distribution of bio-optical properties in Lake Geneva using an underwater glider equipped with a turbulence package. Main efforts went into the validation of glider-based turbulence estimates from temperature microstructure as proven for the open ocean. We confirmed its applicability in a strongly stratified, weakly energetic environment by analyzing spectral shape characteristics and confirming the expected vertical structure of turbulent quantities. Based on our turbulence results, we show that mixing in the interior was extremely weak at the thermocline (mixing efficiency $Ri_f << 0.17$). We attribute this to the strong stratification in this region, which exhibited Cox numbers ≤ 1. As encountered in other systems, the inhibited mixing may explain the presence of a spatially-persistent chlorophyll-a fluorescence maxima in the thermocline. We explored spatio-temporal heterogeneity in the spatial distribution of this algae-related feature using a set of repeated cross-shore and along-shore transects. Analyzing anomalies with respect to a composite mean-transect, we attempt to demonstrate that our large-scale measurements captured algal patches variability.

5.1   Introduction

Almost all standing waters are characterized by vertical structures resulting from some types of density stratification. Specifically, in deep lakes, one-dimensional (1D) vertical representation perform well to explain seasonal and long-term changes of the ecosystem (e.g. Peeters et al., 2007; Schwefel et al., 2016). Even in the most elongated lakes, such as Baikal and Tanganyika, the limited lateral extend justifies the 1D representation for most of the annual cycle.

Despite the vertical structure dominance, several basin-scale processes develop over the spatial extent of lakes, which drive stirring and spatial variability of water constituents. In stratified lakes, flow-bathymetry interactions, induced by wind surface shear, drive several basin-scale processes. A primary response to wind forcing is the generation of internal seiches (Mortimer, 1952), which are standing waves that cause constant thermocline dislocations and therefore lateral variability. Dislocations can even cause rise of intermediate or bottom waters when strong winds blow steadily for a long period, process known as upwelling (Monismith, 1986; Schladow et al., 2004). In large lakes, the interaction of wind with the earth rotation affects baroclinic motions and leads to complex basin-scale internal wave dynamics (Csanady, 1975). The most common are Kelvin waves (Antenucci et al., 2000; Appt et al., 2004; Preusse et al., 2010; Bouffard and Lemmin, 2013) and Poincaré waves (Bouffard et al., 2012; Choi et al., 2012). Internal waves are important features driving vertical mass transport (Saggio and Imberger, 2001; Bouffard et al., 2014) and horizontal dispersion (Woods, 1968; Steinbuck et al., 2011), particularly in the thermocline. Another feature in lakes affected by earth rotation occurs when wind stress curl interacts with the bathymetry inducing meso-scale rotational circulation patterns known as gyres (Csanady, 1975; Rueda et al., 2005; Shimizu et al., 2007; Akitomo et al., 2009), which also induce lateral variability.

The aforementioned basin-scale processes are all suspected to locally affect biogeochemical processes. Such spatial variability potentially challenges classical 1D monitoring programs. Therefore, it is important to evaluate the representativeness of typical sampling locations at the deepest sites of lakes. Indications may come from three dimensional (3D) model simulations (e.g. Leon et al., 2011; Soulignac et al., 2018) and remote sensing observations (Odermatt et al., 2012; Matthews, 2011). Recent remote sensing applications have greatly demonstrated the spatial heterogeneity in water bodies (Steissberg et al., 2005; Ng et al., 2011; Kiefer et al., 2015; Bouffard et al., 2018; Nouchi et al., 2019). However, they still provide limited temporal resolution and are restricted to the surface layer (Nouchi et al., 2018). Hydrodynamic 3D models validated against time series of vertical measurements (e.g. Hodges et al., 2000; Laval et al., 2003; Vidal et al., 2013; Valipour et al., 2015) have provided great insight on the underlying mechanisms and spatio-temporal evolution of basin-scale processes. However, the small- to meso-scale structures of hydrodynamic 3D model simulations usually suffer from deficits of calibration and accurate forcing.

The stirring induced by basin-scale physical processes generates turbulent mixing. Tracer release experiments (Peeters et al., 1996; Goudsmit et al., 1997; Choi et al., 2020) have demonstrated the horizontal extent of mixing and dispersion. In particular, these experiments have shown the difference in mixing intensity between the weak interior and the more vigorous bottom boundary layer. Characterizing the in-situ lateral variability that spans from basin-scale processes to small-scale turbulence may allow better constrain models, as well as to understand the role of turbulence in the physical exchange between the various lakes ecosystems (littoral, pelagic [interior] and benthic; MacIntyre and Melack, 1995).

Spatially-distributed measurements are required to characterize the lateral heterogeneity of physical and biogeochemical processes, and advance in their understanding. Manual observations of lateral variability such as CTD (measuring conductivity, temperature and depth) transects (MacIntyre et al., 2002, 2014; Alexander and Imberger, 2013) and piloted-submarine-based measurements (Gargett et al., 1984; Osborn and Lueck,

1985; Thorpe et al., 1999; Fer et al., 2002) have successfully being applied. Yet, they are logistically prohibitive and/or expensive. Novel autonomous measuring platforms such as self-propelled Autonomous Underwater Vehicles (AUVs; Laval et al., 2000; Forrest et al., 2008) and underwater gliders (Rudnick, 2016) enable the coupled scanning of vertical and horizontal gradients of water properties with less restrictions. The variety of sensors that can be integrated into underwater vehicles, including CTDs and water quality sensors (e.g. chlorophyll-a [Chl-a] and dissolved oxygen), makes them a suitable platform for the study of lateral variability.

The utilization of AUVs has demonstrated a remarkable applicability to assess a description in space and time of hydrodynamic processes in the ocean (Tippenhauer et al., 2015; Fisher et al., 2018) as well as to monitor and follow spatially-localized features, such as a harmful algal bloom (HAB; Robbins et al., 2006). In lakes, AUVs have been used to track density currents triggered by surface convection (Forrest et al., 2008) and a cyclonic gyre in an ice-covered lake (Forrest et al., 2013), and to estimate dispersion from a dye experiment in a small reservoir (Rogowski et al., 2019). Turbulence measurements are however complex to perform using this type of platform due to propeller-induced vibrations (Goodman et al., 2006).

Gliders are buoyancy-controlled autonomous underwater vehicles that follow a smooth (low levels of vibration and mechanical noise) sawtooth pattern through the water (Davis et al., 2002). This feature makes them an interesting platform for turbulence measurements, which require extremely low vibrations. Microstructure-based turbulence estimates using glider has been tested in deep oceanic environments featuring energetic (Fer et al., 2014; Peterson and Fer, 2014) and weak (Scheifele et al., 2018) regimes as well as in the upper ocean (Lucas et al., 2019) and in a shallow shelf sea (Schultze et al., 2017). Although the potential for underwater glider deployments in lakes has been previously identified (Austin, 2013), their application remains reduced (Austin, 2012, 2019). To the best of our knowledge, intensive glider-based turbulence estimates in lakes have not yet been published.

Our initial target was to shed light on the spatial variability associated with gyre circulation as often observed in Lake Geneva (Baracchini et al., 2020). However, the chosen location for the study, the western main basin (Figure 5.1), presented only weak gyre signature during our glider deployments. Despite this misfortune, we collected a large volume of data exhibiting lateral variability. The first goal of this study was to assess the possibility to estimate turbulence with a glider under the highly stratified and weakly turbulent conditions typically observed in the deep-water of lakes. With this technical barrier solved, the second goal was to evaluate the cause of the lateral variability in the turbulence observations collected with the glider. Finally, our last objective was to evaluate the effect of the lateral variability in stratification and turbulence on Chl-a distribution. Using glider-based turbulent dissipation estimates we explore the interplay between turbulence regimes and stratification driving algae abundance and patchiness below the thermocline of Lake Geneva.

5.2 Study site

This study was conducted on Lake Geneva (Lac Léman; Figure 5.1), a deep (309 m max. depth), large (582 km^2 of surface) and perialpine lake, located between Switzerland and France. Lake Geneva is the largest natural freshwater body of western Europe and is qualified as a warm-monomictic lake with rarely occurring complete winter mixing Schwefel et al. (2016). The lake has a eutrophic past and restoration has brought it back to a meso-to-eutrophic level (~18 mg m^3 of Phosphorus). Accordingly, the actual Chl-a concentration has a typical maximum in the range of 1 to 20 μg L^{-1} (Nouchi et al., 2018). During the seasonal stratification, the thermocline locates at ~5 to ~10 m depth in May and gradually deepens during summer and autumn before deep convective mixing sets in during winter. Wind stress is the driving force for lateral water mass movements (Bohle-Carbonell, 1986), exhibiting two dominant winds: North-East (La Bise) and South-West (Le Vent) (Lemmin and D'Adamo, 1996). However, it is well-known that the wind field is remarkably variable.

Previous studies confirmed that the Coriolis effect is important in Lake Geneva (Bauer et al., 1981; Lemmin et al., 2005; Bouffard and Lemmin, 2013), as the maximum width of the lake (~14 km) is more than three times larger than the internal Rossby radius (~4 km; Bouffard and Lemmin, 2013), which modifies the circulation and stirring in the lake.
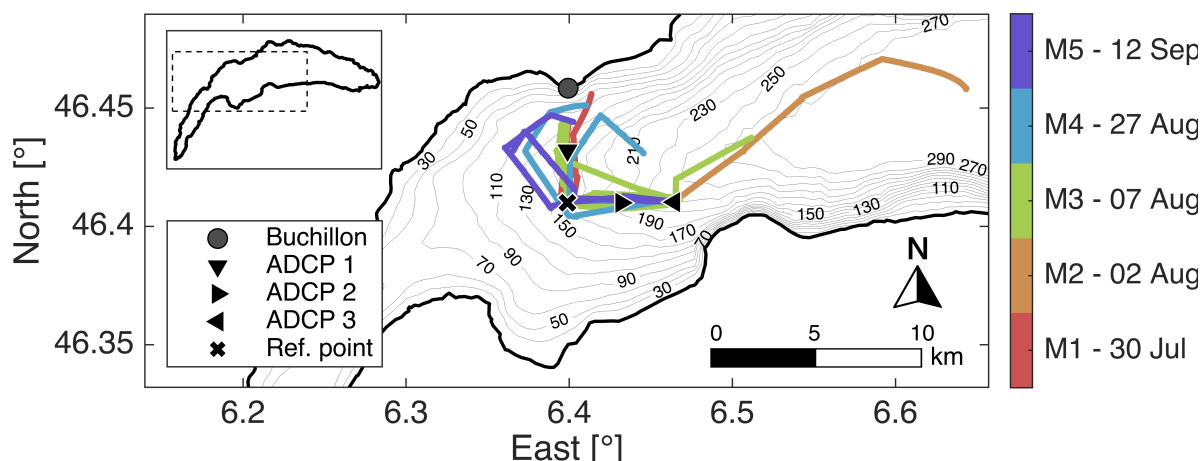

Figure 5.1 – Study site location. Bathymetry of Lake Geneva with location of the Buchillon station, moorings (ADCP 1 to 3) and a reference point for transects position. Glider missions M1 to M5 are depicted by color-coded lines. Dates correspond to the year 2018.

5.3 Materials and methods

5.3.1 Slocum glider and turbulence package

Spatially distributed measurements in Lake Geneva were performed with the UC Davis glider *Storm Petrel*, a G2 Slocum underwater glider (1000 m depth; Teledyne Webb Research). During our sampling campaigns, the glider payload included a SeaBird pumped CTD, SeaBird Eco Puck measuring Chl-a and an Aanderaa Optode dissolved oxygen (DO) sensor. Additional microstructure measurements were obtained with the turbulence package MicroRider-1000 (Rockland Scientific Canada) mounted on top of the glider (Fer et al., 2014). This customized instrument included two shear and two temperature microstructure channels as well as an inclinometer and an accurate pressure sensor sampling at 512 Hz. The glider with the mounted MicroRider was ballasted in a freshwater pool with water density comparable to lake water.

5.3.2 Measurements

Glider transects – Due to high passenger boat traffic in the center of the lake, which is likely to interfere with glider missions, it was decided to carry out the measurements in the western part of the lake's main basin. The sampling strategy consisted mainly of repeated L-shaped trajectories keeping the glider away from the littoral region for navigation safety (Figure 5.1). The glider was programmed to perform continuous dives and climbs (downcast and upcast profiles, respectively) between 3 and 100 m depth and to reach the surface every 4 h for communication and GPS position update. For this mission design, the glider performs 9 to 10 yo-yo's (dive and climb) in a period of 4 h. The glider was programmed to reach 100 m depth for navigation-safety and data quality purposes. Although a deep glider (1000 m depth) is slow at turns, the sampling strategy enables a

smooth passage through a significant portion of the water column representing a great range of variability and ensures that the deep hovering and weight distribution adjustments of the glider occurs far away from the main zone of interest - the thermocline. We programmed the glider to perform flights with fixed pitch angle, which allows for battery position adjustments throughout the missions. However, during each dive and climb the battery position remained basically constant, therefore not interfering with the flight behavior.

Shear microstructure was not always available due to accidental fishing line encounters and lack of spare probes. However, temperature microstructure show better performance to characterize weak turbulence, as typical in the stratified hypolimnion of lakes (Kocsis et al., 1999) and occasionally in strongly stratified zones of the ocean (Scheifele et al., 2018). We therefore focus on temperature microstructure in this study.

Current measurements – To complement the glider observations with background hydrodynamic information, we used current measurements performed with Acoustic Doppler Current Profilers (ADCPs). Three upward looking ADCPs where installed in the open water region (Figure 5.1), in addition to a long-term deployment of a bottom-moored ADCP at Buchillon Station (Figure 5.1). The installation of ADCP moorings 1 to 3 was performed by means of bottom moored lines equipped with subsurface floaters at their uppermost end (~50 m depth). Each ADCP was installed within a frame assembled to the line, 5 m below the floater. A releaser system was also installed at the bottom to retrieve the instruments. This was the sole installation possible, allowing ~1 m bin resolution, as the top 50 m of the water column in Lake Geneva are restricted for fishing. Although designed to fulfill this restriction, the final installations resulted above the intended depths. Table 5.1 lists instruments information and deployment depths.

Table 5.1 – Details of instruments deployed on each station (Figure 5.1). ADCPs 1 to 3 were installed from 25 July to 10 October 2018.

Station	Instrument	Frequency [kHz]	Ensemble interval [min]	Installation depth [m]	Bin size [m]
Buchillon		600	15	38	0.75
ADCP 1	Teledyne RD Instrument*	600	10	50	1
ADCP 2	Workhorse Sentinel	600	10	42	1
ADCP 3		300	5	46	1

*Same type of instrument installed in each station

5.3.3 Flight model

To perform appropriate turbulence estimations, it is necessary to account for glider along-path speeds (U). This is required for the analysis of microstructure data, which have to be treated with the Taylor frozen-flow hypothesis (section 5.3.4). Unfortunately, the vehicle's speed through water cannot directly be obtained from instrumentation commonly mounted on gliders and *Storm Petrel* is no exception. Flight models can serve to address this lack of data (Merckelbach et al., 2010; Frajka-Williams et al., 2011).

Here we used the dynamic flight model of Merckelbach et al. (2019). This methodology builds on the steady-state flight model of Merckelbach et al. (2010), where glider buoyancy, drag and lift forces are balanced out neglecting accelerations. Following this framework, U and angle of attack are calculated using measured pitch angle and changes in buoyancy accounted by the oil bladder volume. The dynamic model considers momentum variations induced by accelerations of the submerged body and flow changes around it. This results in an initial value problem and therefore a numerical solution needs to be implemented (e.g. Runge-Kutta methods). Estimations of parameters such as drag coefficients (parasite and motion-induced), glider

volume and lift-angle are obtained by coupling the numerical solution to a cost function which is then minimized.

The implementation was carried out by using the open-source codes provided by Merckelbach (2018). Ambient freshwater density was calculated from CTD data using TEOS 2010 (McDougall and Barker, 2011). The model initialization requires an initial guess of the parameters to be calibrated. We considered parasite and motion-induced drag, $C_{D_o} = 0.15$ and $C_{D_1} = 10.5$, respectively, following Merckelbach et al. (2010, 2019). The mass of glider *Storm Petrel* with the mounted MicroRider was $m_g = 63.6$ kg. With this value, the glider volume was obtained from $V_g = m_g \rho_o^{-1}$, where $\rho_o = 1000$ kg m^{-3} is the freshwater reference density. The lift-angle coefficient was initialized as $a_h = 3.8$ rad^{-1} (Merckelbach et al., 2019). The dynamic flight model was launched for each mission using the first 10'000 values between 10 and 100 m depth, for calibration purposes. Using the calibrated parameters, we obtained full-mission estimates of U and angle of attack for each mission.
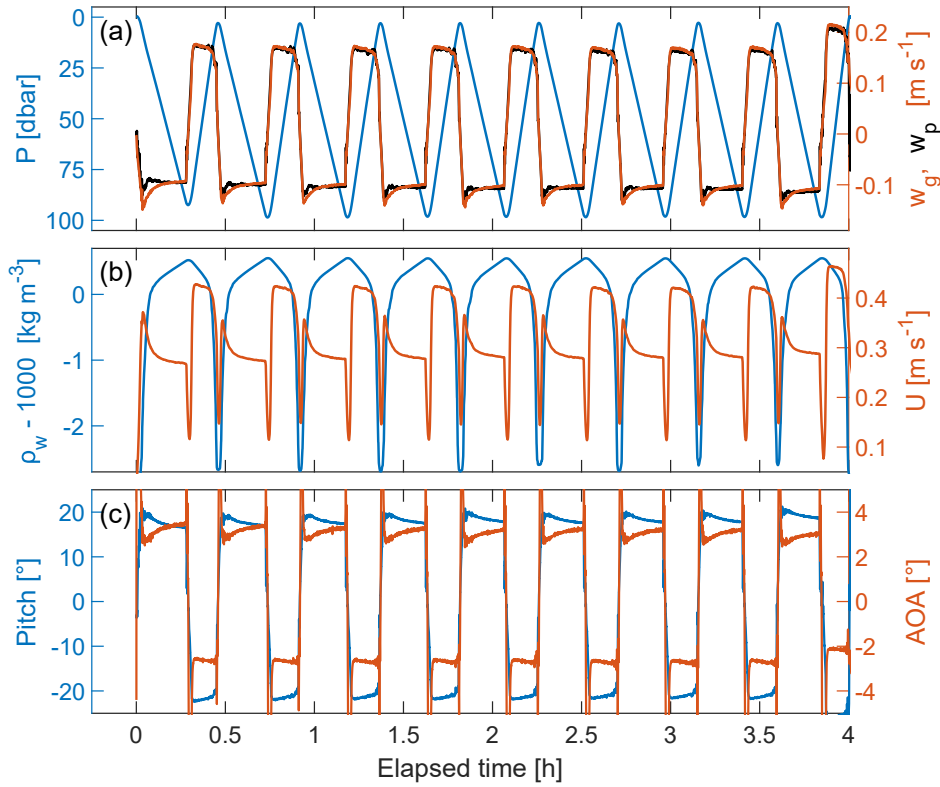
Figure 5.2 – Example of flight model results for mission M1. Time series as elapsed time from the start of M1 on 30 Jul 2018 at ~10:50 am. Results are presented as in Fer et al. (2014). Model inputs and outputs are depicted by blue and red lines, respectively. (a) Measured pressure (P; blue) accompanied by the glider vertical sinking speed deducted from the flight model (w_g; red). The black line corresponds to the vertical speed w_p inferred from P change. (b) Density (blue) and along path speed (U; red). (c) Pitch angle (blue) and angle of attack (AOA; red). AOA is presented with sign to distinguish dives from climbs.

Figure 5.2 shows an example of flight model results. Except for dive/climbs performed during horizontal turns (e.g. change heading from W to N), the data presented corresponds well with the flight behavior for all our missions. Pitch angles were approximately 19° and −21° for dives and climbs, respectively (without

considering hovering). This difference is presumably due to differences in battery angle during dives and climbs (Fer et al., 2014). The angle of attack was relatively constant, yet more stable for dives ($3° \pm 0.3°$) than for climbs ($3° \pm 1°$). Along-path speeds for dives (0.3 m s^{-1}) were slower than for climbs (0.4 m s^{-1}). Resulting U values fall within the speed range validated by Merckelbach et al. (2019) using a glider equipped with an electromagnetic current sensor. Flight model results are therefore considered of sufficient quality to be integrated into the turbulence estimation procedure.

5.3.4 Turbulence estimations

Turbulent dissipation from temperature microstructure – The estimation of turbulent parameters using temperature microstructure sensors mounted on gliders has already been successfully demonstrated (Peterson and Fer, 2014; Scheifele et al., 2018). Temperature microstructure measurements are used to estimate rates of turbulent kinetic energy dissipation ε (W kg^{-1}) by adjusting the theoretical Batchelor (1959) spectrum (S_B) to the spectra of measured temperature gradient fluctuations (S_{obs}).

In this study, we use the maximum likelihood spectral fitting method (Ruddick et al., 2000) to estimate ε complemented with the Steinbuck et al. (2009) correction to calculate the smoothing rate of temperature variance χ_θ (° C^2 s^{-1}). The spectral fitting allows us to infer the Batchelor cutoff wavenumber k_B (cpm) from S_{obs}. Since k_B is theoretically defined as a function of ε by:

$$k_B = \frac{1}{2\pi}\left(\frac{\varepsilon}{\nu D_T^2}\right)^{\frac{1}{4}}$$
(5.1)

where $\nu \approx 1.5 \times 10^{-6}$ m^2 s^{-1} is the kinematic viscosity and $D_T = 1.4 \times 10^{-7}$ m^2 s^{-1} is the molecular diffusion coefficient. This procedure yields ε estimates.

To obtain S_{obs}, the fast thermistors data are first treated with a frequency response correction following Sommer et al. (2013). Afterwards, the data processing closely follow the methodology exposed by Scheifele et al. (2018). However, we use half-overlapping microstructure temperature segments of 10 s to calculate frequency spectra. Subsequently, these spectra are transformed to wavenumber space using the Taylor frozen-flow hypothesis considering the along-path speed U directly obtained from the flight model. This data treatment allows us to maximize the amount of S_{obs} for turbulence analysis without compromising data quality (see *Method evaluation* in section 5.4.2).

The procedure then requires obtaining χ_θ to estimate k_B. Here we take advantage of the Steinbuck et al. (2009) correction to also filter-out the fine-scales (Gregg, 1977) and possible low frequency vehicle-induced contamination by modifying some commonly used parameters (namely k_{lw} and k_{uw}, see below). The calculation of χ_θ is performed by the following approach:

$$\chi_\theta = \chi_l + \chi_{obs} + \chi_u = 6D_T\left(\int_o^l S_B\,dk + \int_l^u (S_{obs} - S_n)\,dk + \int_u^\infty S_B\,dk\right)$$
(5.2)

the factor 6 comes from assuming isotropy. The lower (l) wavenumber end of the measured spectra is obtained by considering $l = \max\{\text{first } k_{obs} > 0; 3k_*\}$ where $k_* = 0.04 k_B (D_T/\nu)^{1/2}$ is the so-called transitional wavenumber (from inertial to viscous-convective subrange; Dillon and Caldwell, 1980). Whereas the upper (u) wavenumber end is the intersection of S_{obs} with the noise spectra S_n. Outside the range defined by l and u, given the lack of reliability of S_{obs}, Steinbuck et al. (2009) proposes to use the theoretical expression of S_B to obtain χ_l and χ_u.

By coupling the estimation of χ_θ and S_{obs} and solving iteratively for k_B, we finally obtain ε. Turbulence analyses exclude data collected 5 m close to turn points as these present diminished data quality from vibrations and may not satisfy the Taylor Hypothesis. Dissipation estimates obtained from poorly resolved spectra, which do not comply with the Bachelor fitting, are discarded following the likelihood and mean absolute deviation criteria proposed by Ruddick et al. (2000).

Turbulent quantities often exhibit lognormal character. Statistical analyses therefore uses the maximum likelihood estimator (mle) for lognormal distributions (Baker and Gibson, 1987). This approach reduces the influence of rare extreme values and provides ad-hoc estimates of statistical variability through the intermittency factor $\langle \sigma^2_{mle} \rangle$.

Diffusivity and mixing characteristics – Mixing is derived using χ_θ by following the diapycnal diffusivity model given in Osborn and Cox (1972), defined as:

$$K_T = \frac{\chi_\theta}{2\left(\frac{\partial \overline{T}}{\partial z}\right)^2} \quad (5.3)$$

where $\partial \overline{T}/\partial z$ is the background temperature gradient.

We use the isotropic version of the Cox number to quantify for the ratio of turbulent to molecular vertical mixing, defined as (Thorpe, 2007):

$$C_x = 3\frac{\left(\frac{\partial T'}{\partial z}\right)^2}{\left(\frac{\partial \overline{T}}{\partial z}\right)^2} = \frac{K_T}{D_T} \quad (5.4)$$

where $\partial T'/\partial z$ is the temperature fluctuation (T') gradient. This also accounts for the strength of turbulent fluctuations compared to the background temperature gradient. We use directly K_T obtained from Eq. (5.3) to compute Cox numbers.

The Richardson flux number, Ri_f, was used to account for mixing efficiency (Monismith et al., 2018). Assuming steady and homogeneous turbulence, the local shear production (P) balances with the sum of buoyancy flux and dissipation (i.e. $P = B + \varepsilon$; Ivey and Imberger, 1991). Hence, Ri_f can be represented as:

$$Ri_f = \frac{B}{B + \varepsilon} \quad (5.5)$$

where $B = K_T N^2$ is the buoyancy flux and $N^2 = g\rho_o^{-1}\partial\rho/\partial z$ is the water column stability, $g = 9.81$ m s^{-2} and z is the depth coordinate (positive downwards).

To characterize the intensity of turbulence with respect to stratification, we use the buoyancy Reynolds number (Gibson, 1980):

$$Re_b = \frac{\varepsilon}{\nu N^2} \quad (5.6)$$

Re_b defines three energy regimes (Ivey et al., 2008): molecular ($Re_b < 7$), transitional ($7 < Re_b < 100$) and turbulent ($Re_b > 100$).

5.3.5 Data processing and analysis

Transects as function of position – The goal of performing L-shaped trajectories was to compare water properties from transects approximately perpendicular (S-N) and parallel (W-E) to the shore (Figure 5.1). These are obtained by analyzing time-series of vehicle heading to determine alignments with S-N or W-

E trajectories, and ∼ 90° turns. For analysis and comparison, the data measured in each transect is then interpolated to a regular grid. We achieve this by performing 2D position-weighted averages using a Gaussian window, applying:

$$\Theta(x,z) = \frac{\sum_i \Theta_i \exp\left(-\frac{(x_i-x)^2}{\sigma_x^2}\right) \exp\left(-\frac{(z_i-z)^2}{\sigma_z^2}\right)}{\sum_i \exp\left(-\frac{(x_i-x)^2}{\sigma_x^2}\right) \exp\left(-\frac{(z_i-z)^2}{\sigma_z^2}\right)} \tag{5.7}$$

where Θ is a measured variable. Let $\mathscr{I}$ be the data subset defined by a transect, this method considers each element Θ_i performed at the position (x_i, z_i), such that $i \in \mathscr{I}$. The position (x, z) is a specific point of the grid (X, Z), where x represents a horizontal coordinate (either E or N) and z is depth. The grid was constructed using horizontal and vertical spacing of $\Delta x = 200$ m and $\Delta z = 1$ m, respectively. Factors σ_x and σ_z are spatial standard deviations in the x and z coordinates that determine the spatial extent of the weighted average procedure. We considered $\sigma_x = 2\Delta x$ and $\sigma_z = 2\Delta z$.

DO correction – Aanderaa optode DO sensors record significant differences between dives and climbs, presumably due to a lag in temperature measurements. We treated DO profiles with the Bishop (2008) correction method for temperature lag. This procedure replaces the sensor-measured temperature by the CTD temperature to recalculate in-situ DO.

Horizontal kinetic energy – We use the ADCP current data to determine the depth-integrated horizontal kinetic energy (HKE), as follows:

$$HKE = \frac{1}{2} \int_0^{z_{ADCP}} (u^2 + v^2) \; dz \;\; (\text{m}^3 \, \text{s}^{-2}) \tag{5.8}$$

where u and v are the are the East and North current components, respectively. The vertical integration range is defined from the surface ($z = 0$ m) to $z_{ADCP} = 40$ m depth. The characteristic radius resulting from current-induced circulation at a specific frequency band (f^* [Hz]), can then be approximated as:

$$R^* = \frac{\sqrt{2\overline{HKE}z_{ADCP}^{-1}}}{2\pi f^*} \tag{5.9}$$

where $\overline{HKE^*}$ is the mean of the f^*-band-pass filtered HKE.

5.4 Results

5.4.1 Overview of glider and current measurements

This research is sought to explore the capabilities of underwater gliders for studying lateral variability in a large lake. Glider *Storm Petrel* was deployed in Lake Geneva in summer 2018 with the goal to connect spatio-temporal water biogeochemical properties to turbulence activity. Throughout the five missions considered in this study, we measured 248 yo-yo's sets equivalent to 147 h of sampling, covering a lake surface distance of 148 km. In the following, we present an overview of the data collected by the glider and three moored ADCPs. Turbulence characteristics are evaluated in section 5.4.2.
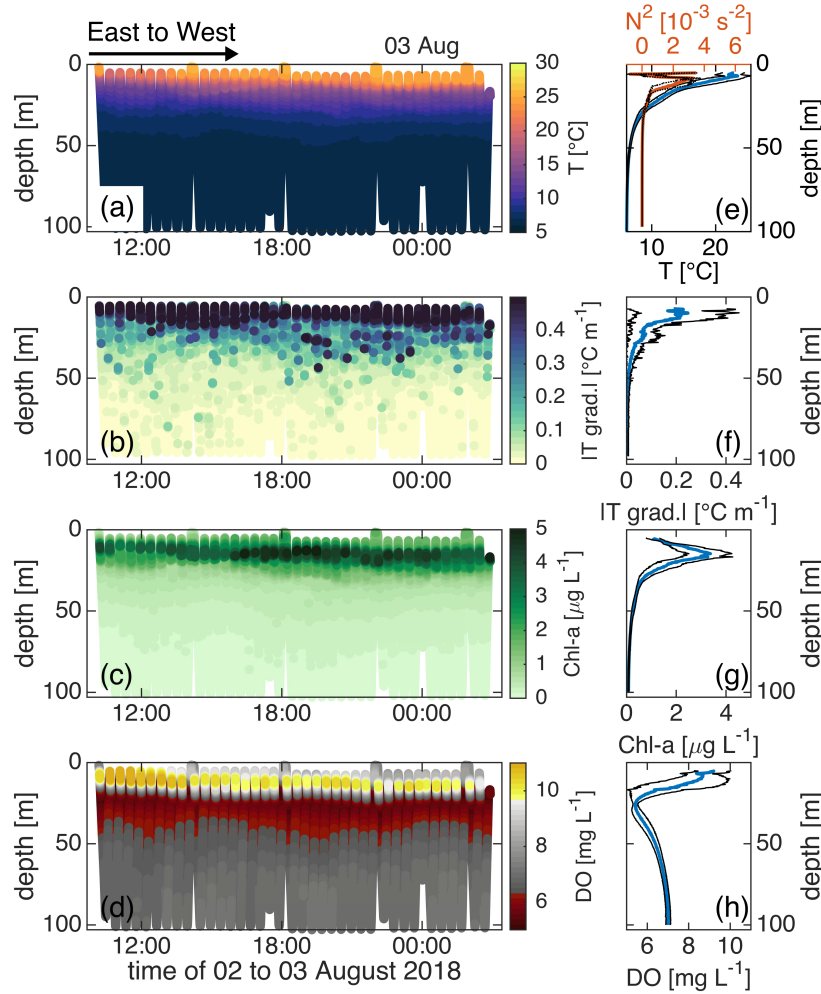
Figure 5.3 – Example of glider data collected on 2/3 August 2018. (a) Temperature (T). (b) Absolute value of the temperature gradient measured with the MicroRider, sub-sampled at 4 Hz for visualization. (c) Chlorophyll-a (Chl-a). (d) Dissolved oxygen (DO). Data presented corresponds to mission M2. Time increase corresponds to E-W direction (Figure 5.1). The tilted DO vertical structure in (d) shows that differences between dives and climbs were unfortunately not properly corrected. (e-h) Time-averaged profiles (blue lines) of measurements presented in (a-b), accompanied by their respective standard deviations (black line envelopes). Additionally, (e) shows the depth-averaged stability (N^2) profile for this mission (red line) with its standard deviation (black dotted envelope).

We show here a time-series example of collected data during mission M2 (Figures 5.3a-d), consisting of a long transect through the middle of the lake (Figure 5.1). When analyzing horizontally- averaged profiles (Figures 5.3e-h), the data shows a marked vertical structure. Temperature data shows a strong vertical stratification (Figure 5.3e). The Chl-a structure (Figure 5.3g) presents an overall persistent, yet weak, maxima of about 4 μg L^{-1} at ~15 m depth. DO follows the Chl-a maxima with maximal DO in the proximity of the same zone (Figures 5.3d,h). However, a more careful analysis of the transect reveals lateral heterogeneity in the top 50 m with varying thermocline (~ 15°C) depths (Figure 5.3a,b). The first 4 h of this mission presented colder temperatures close to the surface, with a Chl-a maxima (Figures 5.3c) also closer to the surface, suggesting a thermocline uplift. Overall Figure 5.3 shows lateral variability with a consistent patch of Chl-a below the

thermocline. This coupling and similar spatial variability were also observed during other missions.

The observed lateral variability must be analyzed with respect to basin-scale dynamics as potential driving mechanisms. We complement glider measurements with observations of horizontal current profiles at four different locations. Time series of current measurements from the four stations (Figure 5.1) are presented in Figure S5.1 (Supporting Information). Currents at Buchillon coastal station (shallow waters) were more energetic than those measured in the interior, with dominant low-frequency periodicities (Figures 5.4a,b).

In the lake interior, the spectra of currents (Figures 5.4a,b) were remarkably similar in the three monitored locations (ADCPs 1 to 3). Energized frequencies close to the inertial frequency (period of ~16.6 h for L. Geneva), indicate the presence of Poincaré internal waves. This phenomenon can generate turbulence and mixing in the lake interior (Bouffard et al., 2012). Times-series of HKE contained in a near-inertial frequency band (Figure 5.4c) were highly variable during the glider missions. While the level of energy in the Poincaré wave was high during M3, it was minimal during M1 and M5.

The inertial currents radius (Figure 5.4c) was 0.3 to 0.5 km for periods with noticeable Poincaré wave activity. A vector plot diagram for currents recorded in the thermocline during M3 confirms this observation (Figure 5.5), yet also indicates the presence of a basin-scale counterclockwise circulation.
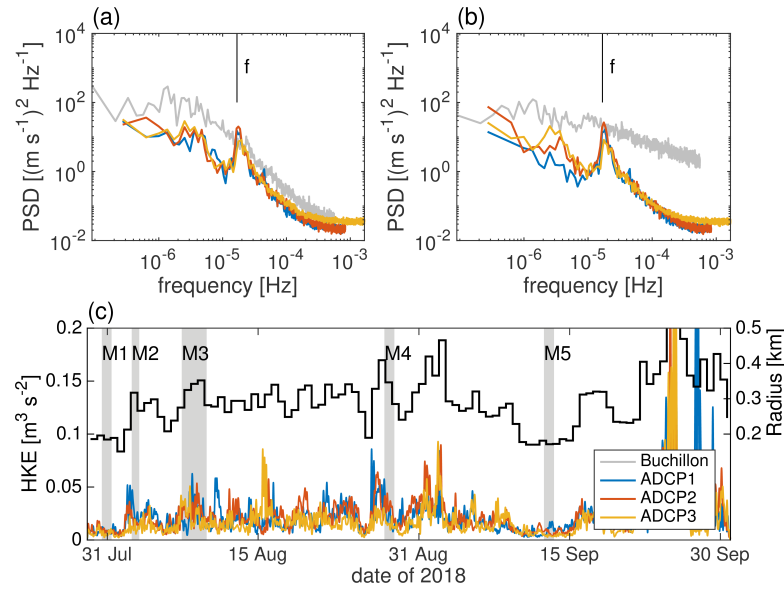
Figure 5.4 – Current measurements analysis. (a,b) Median PSDs for East and North current component, respectively. Curves are obtained by considering the PSD of each sampled bin through the whole water column. The inertial frequency is indicated by f and corresponds to a period of 16.6 h. (c) Left y-axis: horizontal kinetic energy (HKE) of the inertial range of velocities for ADCP1 to ADCP3. A band-pass filter around the inertial frequency range (from 1×10^{-5} to 5×10^{-5} Hz) was applied to the currents prior to calculation. Right y-axis: mean radius of inertial currents (black line) obtained from the three inertial HKE estimations (left y-axis). A 16 h window-average was applied to the time series. Gray areas in (c) denote the time-window of each mission.
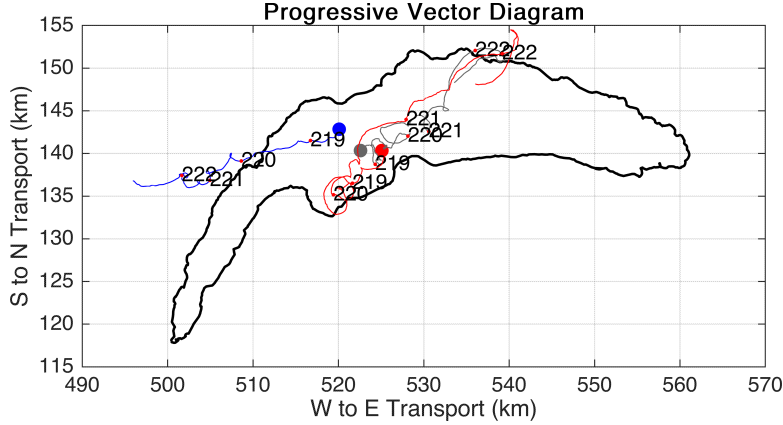
Figure 5.5 – Progressive vector diagram of currents in the thermocline (15 m) for the three ADCP stations during mission M3. Numbers inside the figure correspond to day of the year (219: 7 Aug 2018). Map in Swiss coordinates CH1903.

5.4.2   Turbulence and mixing

Considering the whole dataset (M1 to M5), we evaluate turbulence characteristics as obtained with a glider in the deep and strongly stratified Lake Geneva. First we assess the proposed methodology. Then, turbulence results are presented statistically and as vertical profiles. Finally mixing parameters are evaluated.

Method evaluation

To evaluate the microstructure analysis methodology for ε estimates, we performed a statistical assessment of the non-dimensional spectral shape following Dillon and Caldwell (1980). Both dives and climbs are considered. Figure 5.6 shows ensemble-averages of microstructure temperature gradient spectra that meet the Ruddick et al. (2000) method criteria and compare them with S_B for different ranges of Cox numbers (C_x). For small C_x, i.e. when the background temperature gradients are more prominent than those imposed by turbulent fluctuations, spectra present a shape seemingly in disagreement with the Batchelor form in the lower-end range. Above the characteristic roll-off, temperature fluctuations spectra show in general a remarkable similitude to S_B. This is evident for a wide range of C_x, namely $C_x > 0.1$.

The specific evaluation of our procedure to calculate χ_θ (Eq. 5.2), requires a careful analysis of the S_{obs} ensembles (Figure 5.6) at their wavenumber extremes. In the upper wavenumber end, the cutoff defined by the intersection between S_{obs} with S_n and the maximum likelihood method (Ruddick et al., 2000) prevents an overestimation of χ_θ . In low wavenumbers, the ensemble-averages are detached from the theoretical form S_B, possibly due to vehicle-induced vibrations and/or fine-scale structures of the stratification. This becomes more evident at the lower wavenumber end of the spectra for $C_x < 10$. However, the variance-preserving spectra (circles in Figure 5.6) show that the statistical variability introduced by S_{obs} not complying with the theoretical S_B shape, only affects wavenumers below $3\alpha_*$ (where α_* is the non-dimensional form of k_*) for $C_x < 0.1$ and therefore it is filtered out. Figure 5.6 thus shows that our procedure yields an overall salient performance.
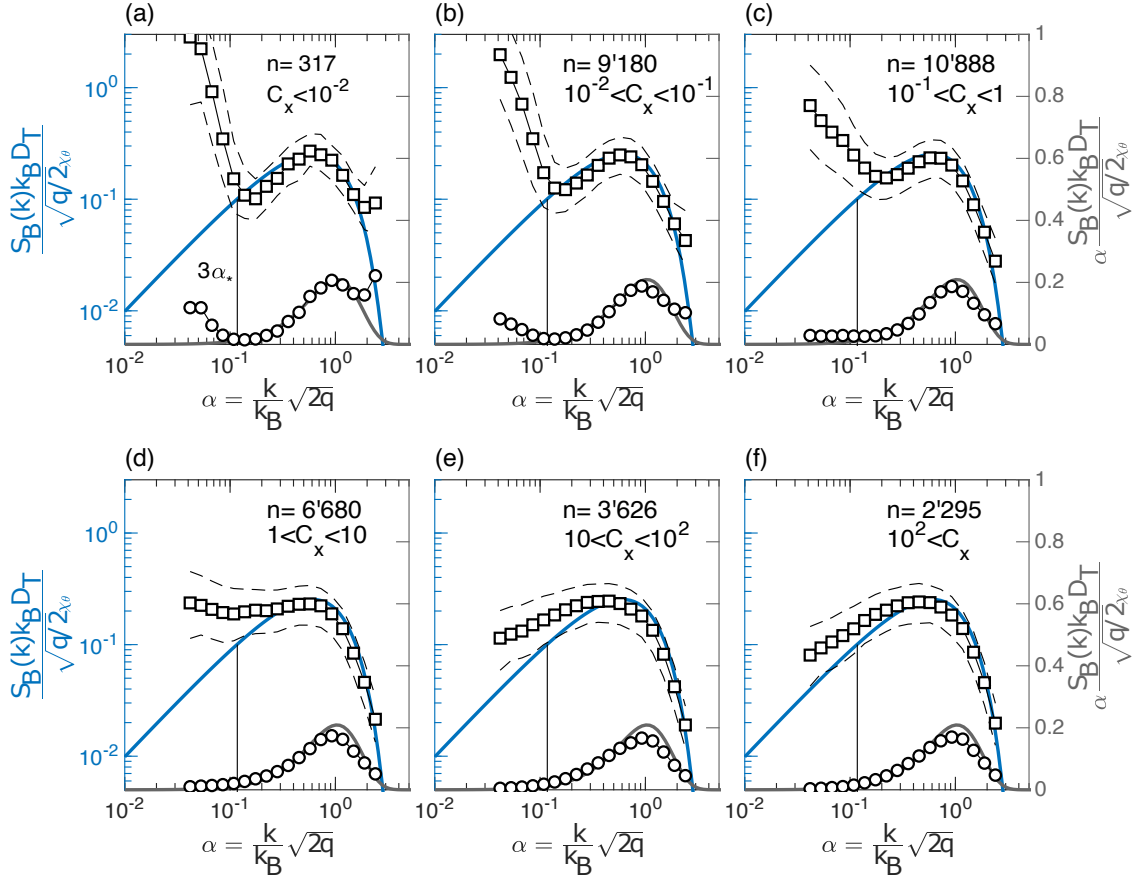
Figure 5.6 – Spectral statistics following Dillon and Caldwell (1980). (a-f) Left y-axis corresponds to ensemble-averaged non-dimensional spectrum (squares) for Cox numbers (C_x) specified in the top right corner of each panel. The amount of spectra considered for obtaining the ensemble-averaged is indicated by n. Dashed envelope represent 25th and 75th percentile confidence interval, respectively. The blue line is the non-dimensional Batchelor spectrum $\frac{S_B(k)k_B D_T}{\sqrt{(q/2)}\chi_\theta}$, where $q = 3.4$ is the universal spectral constant. The value $\alpha_* = 0.04\sqrt{\frac{D_T 2q}{\nu}} \approx 0.03$ (vertical black lines) corresponds to the non-dimensional form of the transitional wavenumber k_*. (a-f) Right y-axis corresponds to the variance-preserving plot of ensemble-averaged non-dimensional spectrum (circles) presented in the left y-axis. Gray line is the variance-preserving non-dimensional Batchelor spectrum $\alpha \frac{S_B(k)k_B D_T}{\sqrt{(q/2)}\chi_\theta}$. Only spectra that meet the Ruddick et al. (2000) criteria only, are considered for this analysis.

Statistical and vertical distribution of turbulent quantities

Turbulent dissipation and temperature smoothing rates were obtained using the methods described above for the whole set of glider missions. Glider-based temperature microstructure observations in strongly stratified waters by Scheifele et al. (2018) reported no difference ε estimations between dives and climbs. Therefore, our analysis considers both dives and climbs. Figures 5.7a,c show histograms of ε and χ_θ for the whole dataset, color-coded for stability (N^2). Distributions of these quantities (22'762 samples) appear lognormal however their log-data kurtosis was 2.3 for ε and 3.6 for χ_θ, distant from the expected value of 3 (lognormal distribution kurtosis). The mle-mean and median for ε were 2.0×10^{-8} W kg^{-1} ⟨9.8⟩ and 9.8×10^{-11} W kg^{-1}, respectively.

Whereas for χ_θ the mle-mean and median were $5.7 \times 10^{-8}\,°C^2\,s^{-1}\,\langle 10.7 \rangle$ and $1.8 \times 10^{-10}\,°C^2\,s^{-1}$, respectively. This indicate a generally weak to moderate turbulent regime, which is confirmed below in Figure 5.8d.

Vertical distributions (Figures 5.7b,d) show an overall decay of ε and χ_θ with depth. The N^2 color-code reveals maximal values of ε in the zone of sharper gradients (i.e. maximal N^2). Moreover Results also show an increase of ε when approaching 100 m depth. We attribute this to glider flight maneuvers close to its mission maximal depth (100 m) and to measurements performed closer to the littoral zone, which is expected to present enhanced mixing due to its proximity to the bottom.
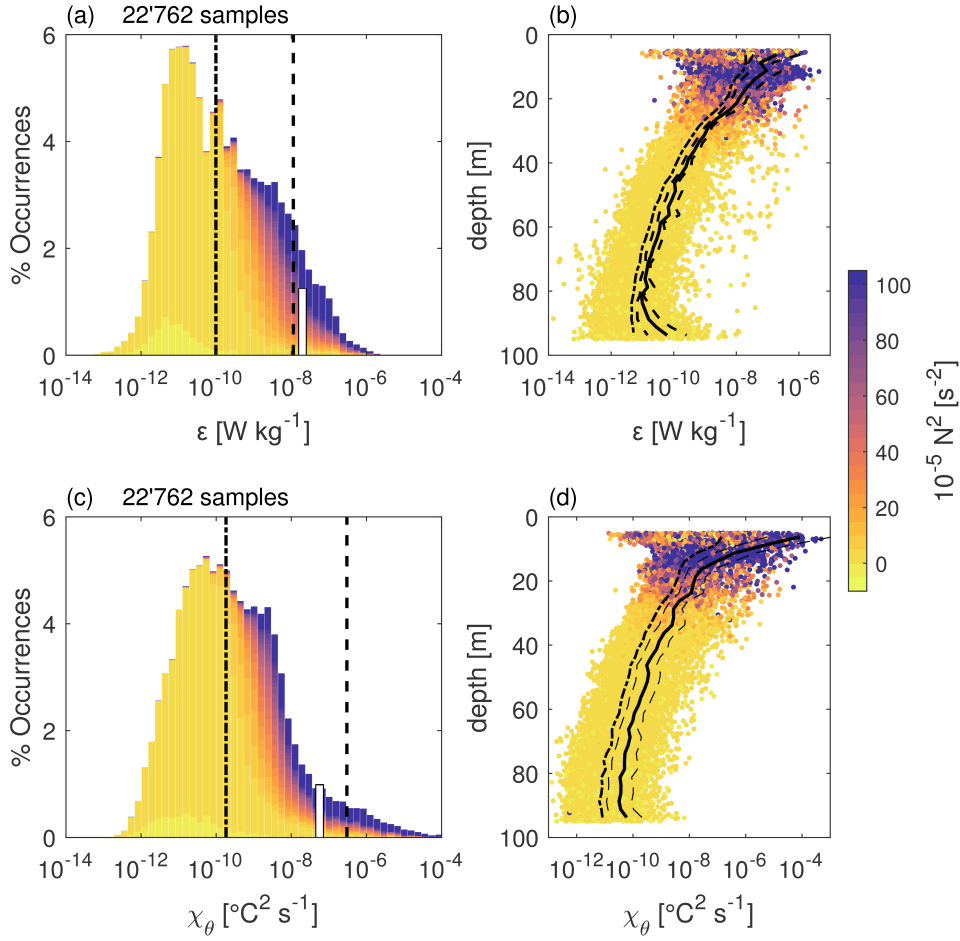
Figure 5.7 – Statistical and vertical distribution of measured turbulent characteristics. (a, c) Histograms of turbulent dissipation ε and smoothing rate of temperature variance χ_θ, respectively. White vertical bar corresponds to the mle-mean for a log-normal distribution (Baker and Gibson, 1987). Dashed and dot-dashed lines represent arithmetic mean and median, respectively. (b, d) Vertical distribution of ε and χ_θ, respectively. Thick black line and dashed envelope correspond to the mle-mean and statistical variability given by the intermittency factor, respectively. The dot-dashed line represents the median. Only estimations that meet the Ruddick et al. (2000) criteria were considered for this analysis. Data displayed were obtained by averaging the resulting estimates from the profile as sampled by the two fast thermistors mounted on the MicroRider (data segments with only one sample meeting the criteria were also considered).

Mixing

We analyze mixing to identify predominant features controlling vertical fluxes in the water column, particularly in the thermocline region that host abundant Chl-a concentrations.

There is a long-standing debate on whether mixing efficiency can be assumed constant (i.e. $Ri_f = 0.17$; Osborn, 1980) or if is a function of turbulence characteristics, as indicated by substantial research (Ivey et al., 2008; Bouffard and Boegman, 2013; Monismith et al., 2018). The glider-based turbulence dataset presented above allows us to analyze the sensitivity of Ri_f to different turbulent parameters, such as C_x and Re_b (Figure 5.8).
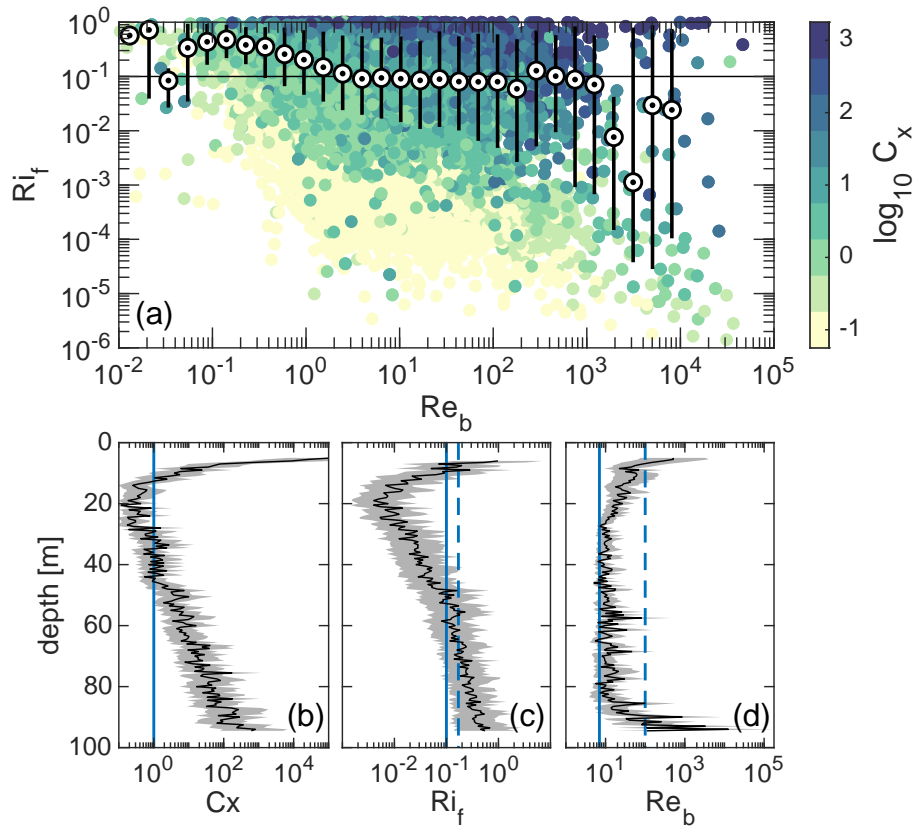
Figure 5.8 – Mixing estimations. (a) Richardson flux number (Ri_f) as a function of buoyancy Reynolds number (Re_b) color-coded for Cox numbers (C_x). Dotted white circles represent the median of Ri_f in each bin for data points with $C_x > 1$. Error bars show 10th and 90th percentiles of the same subset. The horizontal black line corresponds to $Ri_f = 0.1$. (b-c) mle-mean profiles (black lines) of C_x, Ri_f and Re_b, respectively. Gray areas in (b-c) represent statistical variability given by the intermittency factor $\langle \sigma^2_{mle} \rangle$. Blue line in (b) is $C_x = K_T D_T^{-1} = 1$. Continuous and dashed lines in (b) represent $Ri_f = 0.1$ (this research) and $Ri_f = 0.17$ (Osborn, 1980), respectively. In (d), continues and dashed blue lines depict lower and upper limits of the transitional regime ($7 < Re_b < 100$; Ivey et al., 2008).

The $Ri_f(Re_b)$ relation (Figure 5.8a) shows a large scatter with values spanning more than 5 decades. Binning data points with $C_x > 1$ only (i.e. temperature turbulent fluctuations overcome the background gradient), and averaging within the domain $1 < Re_b < 1000$, yields $Ri_f \approx 0.1$. For a compilation of similar datasets, Monismith et al. (2018) found $Ri_f \approx 0.17$, when considering data below the thermocline of the ocean. Since Lake Geneva is a less energetic environment (median $Re_b = 6$ for $C_x > 1$) than the ocean (median $Re_b = 26$; Monismith et al.,

2018), the $Ri_f \approx 0.1$ obtained herein appears as a reasonable result. Notwithstanding, Figure 5.8a clearly shows dependency of Ri_f to C_x and Re_b, supporting the need for more elaborated parameterizations of mixing efficiency.

More specific characteristics of mixing in the water column may be revealed by analyzing depth-averaged vertical profiles. All three mixing parameters show maximal values in the surface mixed layer (Figure 5.8b-d), a zone normally influenced by the wind. Vertical profiles of C_x and Ri_f (Figures 5.8b and 5.8c, respectively), present minimum values around 20 m depth. The vertical profile of Re_b (Figure 5.8d) shows that the water column lies almost completely within the transitional regime ($7 < Re_b < 100$). Besides ubiquitous Poincaré waves in the interior (Figure 5.4) and moderate turbulence (Figure 5.7b), Figures 5.8b-d show that stratification inhibits mixing between 10 and 40 m depth which comprises the thermocline region.

5.4.3   Spatial variability of temperature, turbulence and mixing

In the following, we attempt to relate glider-observations to large-scale processes. Mission M3, repeating the same path four times (performed from 07 to 10 Aug 2018), was considered to this end. Although only one fast thermistor recorded during M3, this was the most sampling-intensive mission. Only transects within the L-shaped path from ADCP1 to ADCP3 were considered. For good spatial representation, S-N and W-E transects were interpolated using a Gaussian window to regular grids with a common spatial origin (see reference point in Figure 5.1).

Figure 5.9 shows the resulting transects of temperature, dissipation rate (ε) and diffusivity (K_T). Temperature transects show variable vertical displacements with a heterogeneous lateral structure. The S-N and W-E transects exhibit difference in the near surface temperature. For instance, we notice a systematic colder temperature in the cross-shore S-N profile compared to the more offshore W-E transects (Figures 5.9a.1, 5.9a.3 and 5.9a.2, 5.9a.4). We also observe large temperature displacement at the borders of the transects, where the origin is at the center of the lake (for S-N and W-E transects), and the right end is at ~ 2 and ~ 4 km from the shore for N-S and W-E transects, respectively. This could be signaling dynamic processes such as gyres or Kelvin waves (Figure 5.5; Bouffard and Lemmin, 2013).

Turbulent dissipation (ε; Figures 5.9b,e) transects, although patchy, show a structure rather controlled by vertical gradients (see Figure 5.7b). Diffusivity (K_T) transects (Figure 5.9c,f) show episodic enhancement of mixing in the surface layer and distinct inhibited mixing in the thermocline region (below $\sim 15°C$ isothermal). Despite this, several high diffusivity patches were identified in the top 50 m of the water column with horizontal length scales of ~ 0.5 to 1 km, with values up to 3 orders of magnitude compared to the background. When approaching perpendicular to the north shore of the lake (N-S transect at 4 km), it would be expected an increase in ε and K_T for the whole water column, yet the transect only shows enhancement in the surface. This result indicates that turbulence conditions in the interior are quite uniform, with no striking structures, however the encountered hot-spots show the intermittent nature of turbulent processes.
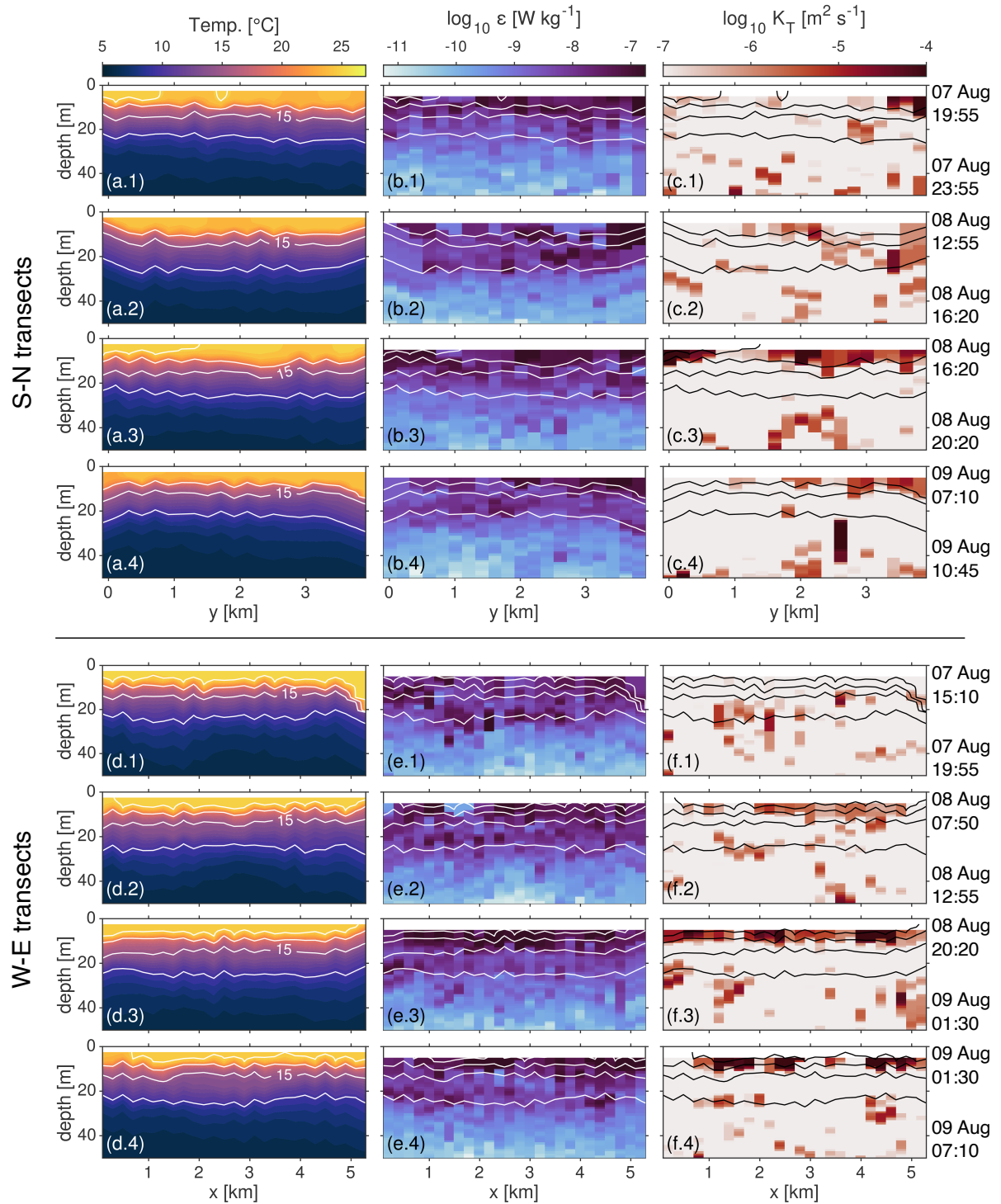
Figure 5.9 – Mission M3 repeated transects. (a,d) Temperature. (b,e) Turbulent dissipation ε. (c,f) Diffusivity (K_T). Contours in each plot correspond to 10°, 15°, 20° and 25° C isotherms. Transect positions are presented relative to the reference point (×) defined in Figure 5.1. Local start- and end-time of each transect indicated at top and bottom of each row, respectively.

5.4.4 Implications for Chl-a lateral variability

Understanding the role or physical processes for the development of Chl-a patches was one of the main objectives of this study. In general, the Chl-a aggregated in a layer located at ∼15 m which exhibited values of 4 to 5 μg L^{-1} (Figure 5.10a). However, mission M5 presented a more superficial peak of ∼7 μg L^{-1}. Throughout the missions, Chl-a closely followed temperature, specifically, the peak was located below the thermocline (15°C isotherm) and was seemingly coupled to temperature vertical displacements (see Figure 5.3). The region where the Chl-a maxima developed presented strong stratification and weak mixing (Figure 5.8). When analyzing turbulence characteristics at the depths of the Chl-a maxima (Figure 5.10b), we found that it occurred mainly in molecular-to-transitional regimes. This suggests that the strong stratification provides stable conditions for the development of algae in the thermocline (e.g. Fernandez-Castro et al. submitted; Chapter 4).
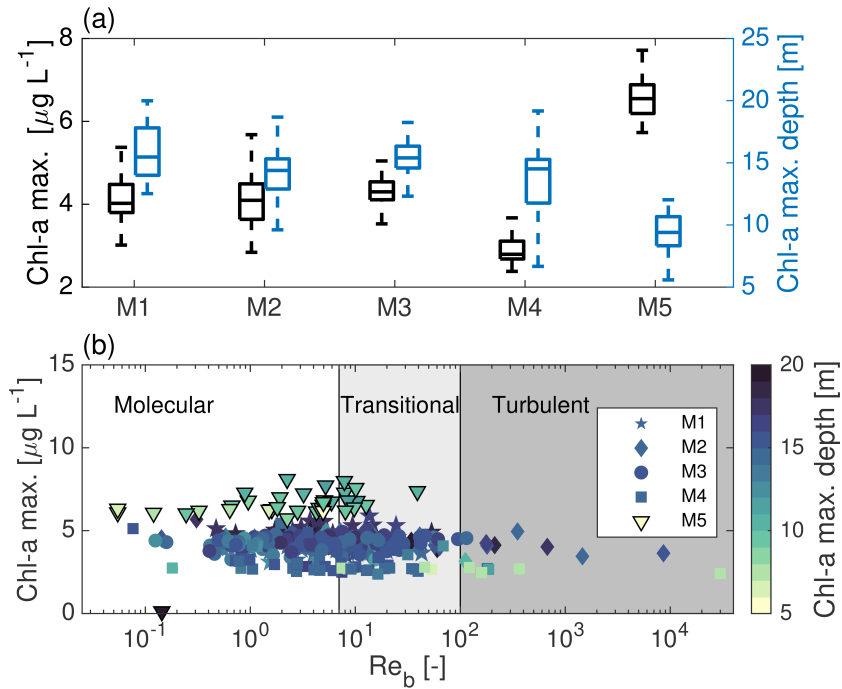
Figure 5.10 – Chl-a layer characteristics. (a) Box plot of Chl-a maximum (black) and its respective depth (blue). The central mark of each box indicates the median, whereas the bottom and top box edges indicate the 25th and 75th percentiles, respectively. Whiskers depict the extent of data not considered outlier. (b) Chl-a maximum as a function of the buoyancy Reynolds number (Re_b) for all missions. The three areas corresponds to the different regimes defined by Re_b (Ivey et al., 2008; see *Materials and methods*).

As the initial goal was to explore algae patchiness, we intend to perform a spatial analysis of Chl-a variability considering also the repeated transects from M3. To determine whether temperature vertical dislocations accounts for changes in Chl-a, we analyze their variations in terms of anomalies with respect to a mission composite-average of S-N/W-E transects (Figure 5.11). This is performed first, in a depth structured domain (vertical anomaly) and then in a temperature domain (isothermal anomaly; Δ_{iso-T}). Isothermal anomalies are computed with the aim to filter out temperature displacements.

Vertical anomalies of temperature and Chl-a (ΔTemp. and ΔChl-a in Figure 5.11) show a general positive correlation (correlation coefficient $r_{10-20} \approx 0.3$) at depths between 10 and 20 m for S-N and W-E transects. This provides further proof of the coupling between Chl-a peak and thermocline positions.
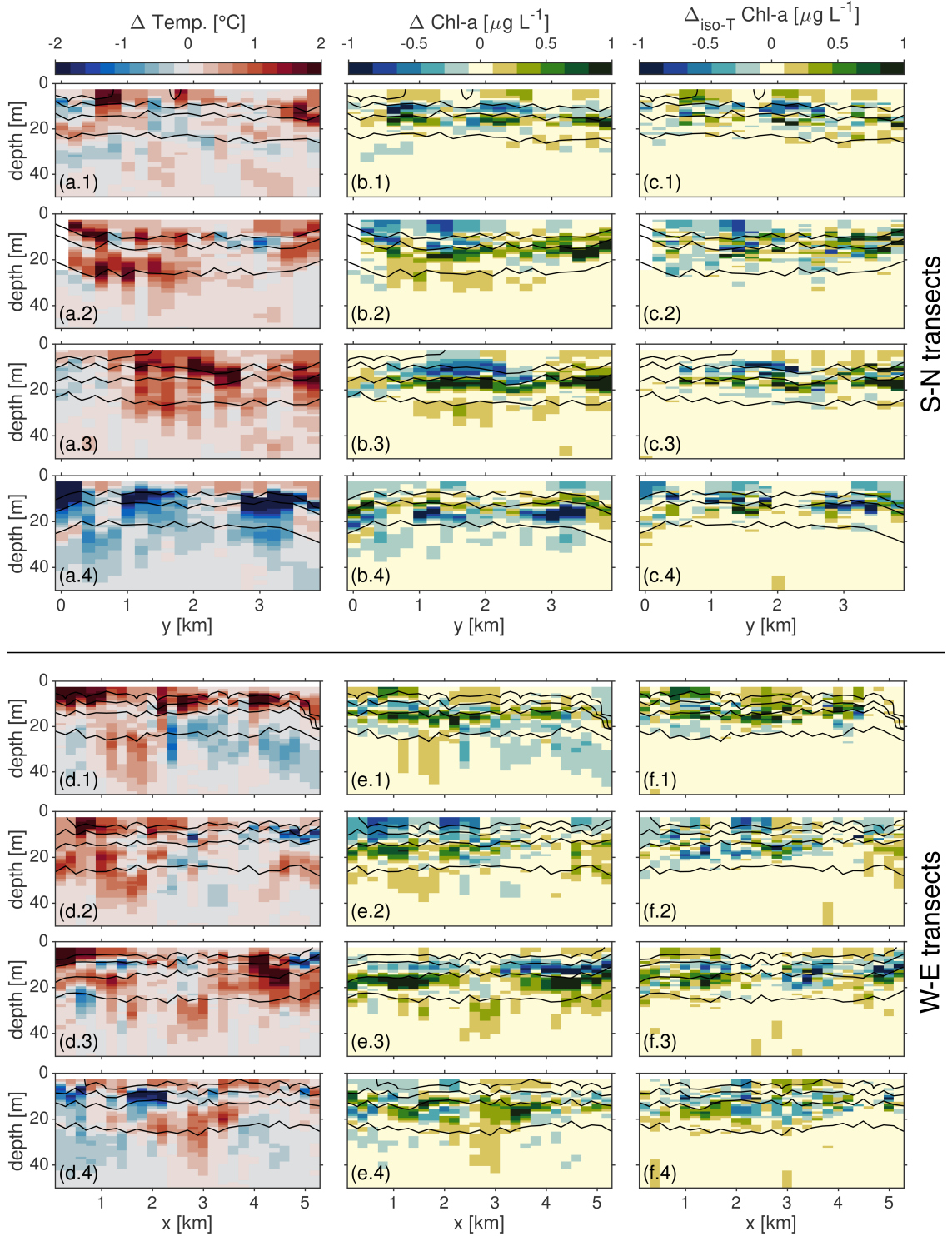
Figure 5.11 – Temperature and Chl-a anomalies from repeated transects of mission M3. (a,d) Temperature vertical anomaly. (b,e) Chl-a vertical anomaly. (c,f) Chl-a isothermal (Δ_{iso-T}) anomaly. The anomalies correspond to the difference between each transect and the bin-average S-N /W-E transect, considering every transect of the mission. Contours in each plot correspond to 10°, 15°, 20° and 25° C isotherms. Transect positions are presented relative to the reference point (×) defined in Figure 5.1 . Transect times are the same as in Figure 5.9.

Both type of Chl-a anomalies reveal several patches with length scale of ~1 km. For consecutive transects (e.g. Figures 5.11c2 and c3, and Figures 5.11f3 and f4), measured Chl-a patches change considerably. As the passage of the glider occur in a time-scale of hours, this suggest the presence of a horizontal transport mechanisms.

Comparing the variance of depth and isothermal anomalies can provide a simple quantitative indication of the variability that is not induced by vertical displacements. For the depth range of 10 to 20 m, the ratio of isothermal- to depth-anomaly variances is ≈ 0.6 for both S-N and W-E transects. This result suggests that 40% of Chl-a variability is induced by processes other than vertical displacements.

In-situ growth/mortality, mixing and currents are mechanisms that could explain the changes in Chl-a. The repeated transects during M3 indicate that the changes occur at the scales of hours both at day and at night, thus algae growth seems an unlikely explanation for these anomalies. Poincaré waves (Figure 5.4), instead, can induce mixing and currents. Yet, mixing was largely inhibited in the thermocline zone by the strong stratification (Figures 5.7 and 5.8). Therefore, given the unsteady patchiness depicted in Figure 5.11, we hypothesize that near-inertial (Poincaré wave) currents may induce advection of algae patches, explaining the encountered lateral variability of Chl-a.

5.5 Discussion and conclusions

This study is a first attempt to understand spatio-temporal heterogeneities of water properties in lakes using a glider. Further analyses of the collected data are needed to decipher the effects of turbulence and stratification on algal patch variability. However, several results, particularly the glider-based turbulence estimates, are valuable contributions toward the assessment of lateral variability in lakes.

On glider deployments in lakes
Gliders enable the scanning of lateral variability of water constituents and offer an outstanding sampling endurance. However, there are restrictions on the spatial resolution that can be achieved with gliders. For instance, immersions as designed in this study, until 100 m depth, implies that along 1 km only two complete yo-yo's can be performed. Practically, manual CTD transects can outcompete this spatial resolution. Consequently, prior knowledge on the characteristic lengths of the process to be studied is important to evaluate whether gliders are the correct sampling platform. Gliders perform at best for large scale scanning. The target processes to study in lakes with gliders, should hence exhibit characteristic length-scales of several kilometers such as gyres (Shimizu et al., 2007) and upwelling events (Schladow et al., 2004). Yet, during bad weather conditions, gliders enable measurements that cannot be obtained through ship-based operations and therefore represent a qualitative breakthrough in data acquisition.

Turbulence and mixing
Glider-based turbulence measurements have been mainly reported for energetic ocean environments (Fer et al., 2014; Schultze et al., 2017). Since Lake Geneva summer conditions exhibit a strongly stratified and weakly energized water column, our first focus was the validation of turbulence estimates. Performing an analysis similar to Dillon and Caldwell (1980), we binned temperature microstructure spectra in different ranges of Cox number and calculated their ensemble-average (Figure 5.6). The analysis demonstrated that spectra meeting the Batchelor fitting conditions capture the variance and the roll-off as expected characteristics of the theoretical shape.

Turbulence estimates in the interior presented a strong vertical structure with maximal values close to the surface ($\sim 10^{-7}$ W kg^{-1}) that weakened with depth ($\sim 10^{-11}$ W kg^{-1}). The expected enhancement of ε close to the bottom of the deep interior was not measured as glider mission were designed to reach 100 m depth, yet

some profiles closer to the shore showed enhanced ε estimates of up to 10^{-9} W kg^{-1} below 90 m depth.

A considerable amount of studies (e.g. Kocsis et al., 1999; Saggio and Imberger, 2001; Etemad-Shahidi and Imberger, 2001; Bouffard and Boegman, 2013) have evaluated turbulence using temperature microstructure in lakes. These studies also detected a similar vertical structure exhibiting a turbulence profile that decrease with depth. However, they were performed in shallow zones or shallow lakes, and the reported ε values were 2 orders of magnitude higher than our estimates. Perhaps a comparable study site is Lake Baikal (similar vertical wind energy fluxes of 100 to 200 mW m^{-2}), where values ε of 10^{-10} W kg^{-1} have been reported for the interior (Ravens et al., 2000). Further glider deployments may help mitigate the lack of turbulence measurements in deep, large lakes. The data presented herein can be considered as a starting point.

Based on the validated turbulence parameters, we encountered inhibited mixing in the thermocline ($R_f \sim 0.01$) and a mixing efficiency in the deep interior below the canonical mixing efficiency reported for the ocean ($Ri_f \approx 0.1 < Ri_f^{ocean} = 0.17$). The extremely low mixing efficiency in the thermocline is in line with several studies using microstructure and other indirect methods (e.g. Wüest et al., 2000; Etemad-Shahidi and Imberger, 2001) The apparent dependence between Cox numbers, buoyancy Reynolds number and Richardson flux number (Figures 5.8b,c) remains to be investigated.
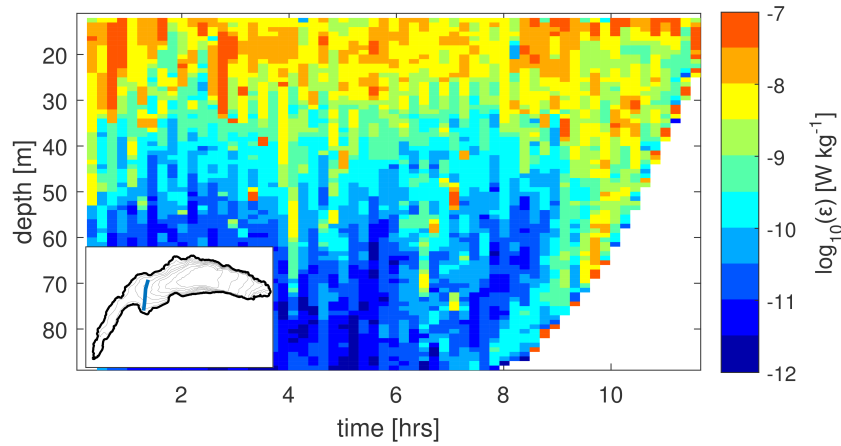
Figure 5.12 – Glider transect showing cross-shore lateral variability of turbulent dissipation (ε). Mission was performed on 26 Jul 2018, starting at 10:50 am local time. Inset shows the approximate trajectory. The collection of these data was only possible due to the gentle slope of the mapped area.

Spatial variability of turbulence
Unfortunately, none of our glider missions was carried out during strong gyre activity but rather during periods dominated by near-inertial (Poincaré) waves activity. Besides some intermittent patches, presumably induced by such internal waves, turbulence and mixing in the interior was rather steady. In fact, not even N-S transects (Mission M3) captured an enhancement in the thermocline when approaching the shore. This indicates that our missions were designed too far from the shore to detect the transition between interior and bottom boundary layer, where variability is expected (e.g. Figure 1 in Wüest and Lorke, 2003).

Because of the initial interest in gyres as well as for navigation safety we measured mainly in the interior. Yet, we did perform one opportunistic mission in the littoral region. Figure 5.12 shows a transect towards the shore, which captured striking lateral variability of turbulent dissipation. Our measurements reveal a more intense mixing at the boundaries as also concluded from tracer release experiments (e.g. Goudsmit et al., 1997). The only comparable measurements in Lake Geneva are those from microstructure sensors mounted on a submarine, reported by Fer et al. (2002). Despite their measurements were performed during winter,

when stratification is weaker, our turbulent dissipation estimates near the slopes (10^{-9} – 10^{-7} W kg^{-1}; Figure 5.12) are in agreement with those reported by Fer et al. (2002) during windy conditions. While the interior of lakes seems a much more challenging environment for the assessment of lateral variability, Figure 5.12 suggests that glider deployment efforts should focus on the littoral zone.

Algae distribution

The vertical profile of chlorophyll-a (Chl-a) presented in general a maxima of 4 to 5 μg L^{-1} located in the thermocline. This was a spatially persistent characteristic found in several different locations and was basically present in every yo-yo performed with the glider. Encountering the Chl-a maxima in the thermocline may have an explanation related to the low turbulence properties of this region (Figure 5.10b). As the strong stratification inhibited mixing in the thermocline (Figure 5.8b,c) , this appears to be a favorable environment that provides stable conditions for the development of algae (Fernandez-Castro et al. submitted; Chapter 4).

Regarding lateral variability, the small concentrations and the lack of a prominent spatial feature, made the analysis extremely difficult. The calculated anomalies show the presence of patches with differing concentrations and length-scales of ~1 km (Figure 5.11). This result is almost twice the radius of near-inertial currents, so we hypothesize that advection induced by Poincaré waves may drive the encountered patchiness. However, our analysis cannot provide a time dependency between anomalies and circulation. Complementing our results with particle tracking resulting from 3D modeling could help us test this hypothesis. Undoubtedly, the anomalies procedure presented here requires further validation, yet it may have potential for the analysis of glider measurements exhibiting a more pronounced lateral variability.

Acknowledgements

References

Akitomo, K., Tanaka, K., Kumagai, M., and Jiao, C. (2009). Annual cycle of circulations in Lake Biwa, part 2: Mechanisms. *Limnology*, 10(2):119–129. doi:10.1007/s10201-009-0267-7.

Alexander, R. and Imberger, J. (2013). Phytoplankton patchiness in Winam Gulf, Lake Victoria: a study using principal component analysis of in situ fluorescent excitation spectra. *Freshwater Biology*, 58(2):275–291. doi:10.1111/fwb.12057.

Antenucci, J. P., Imberger, J., and Saggio, A. (2000). Seasonal evolution of the basin-scale internal wave field in a large stratified lake. *Limnology and Oceanography*, 45(7):1621–1638. doi:10.4319/lo.2000.45.7.1621.

Appt, J., Imberger, J., and Kobus, H. (2004). Basin-scale motion in stratified Upper Lake Constance. *Limnology and Oceanography*, 49(4):919–933. doi:10.4319/lo.2004.49.4.0919.

Austin, J. (2012). Resolving a persistent offshore surface temperature maximum in Lake Superior using an autonomous underwater glider. *Aquatic Ecosystem Health and Management*, 15(3):316–321. doi:10.1080/14634988.2012.711212.

Austin, J. (2013). The potential for autonomous underwater gliders in large lake research. *Journal of Great Lakes Research*, 39(S1):8–13. doi:10.1016/j.jglr.2013.01.004.

Austin, J. A. (2019). Observations of radiatively driven convection in a deep lake. *Limnology and Oceanography*, 64(5):2152–2160. doi:10.1002/lno.11175.

Baker, M. A. and Gibson, C. H. (1987). Sampling turbulence in the stratified ocean: Statistical consequences of strong intermittency. *Journal of Physical Oceanography*, 17(10):1817–1836. doi:10.1175/1520-0485(1987)017<1817:STITSO>2.0.CO;2.

Baracchini, T., Wüest, A., and Bouffard, D. (2020). Meteolakes: An operational online three-dimensional forecasting platform for lake hydrodynamics. *Water Research*, 172:115529. doi:10.1016/j.watres.2020.115529.

Batchelor, G. K. (1959). Small-scale variation of convected quantities like temperature in turbulent fluid Part 1. General discussion and the case of small conductivity. *Journal of Fluid Mechanics*, 5(1):113–133. doi:10.1017/S002211205900009X.

Bauer, S. W., Graf, W. H., Mortimer, C. H., and Perrinjaquet, C. (1981). Inertial motion in Lake Geneva (Le Léman). *Archives for Meteorology, Geophysics, and Bioclimatology Series A*, 30(3):289–312. doi:10.1007/BF02257850.

Bishop, C. M. (2008). Sensor dynamics of autonomous underwater gliders, Master Thesis, Memorial University of Newfoundland, Canada.

Bohle-Carbonell, M. (1986). Currents in Lake Geneva. *Limnology and Oceanography*, 31(6):1255–1266. doi:10.4319/lo.1986.31.6.1255.

Bouffard, D. and Boegman, L. (2013). A diapycnal diffusivity model for stratified environmental flows. *Dynamics of Atmospheres and Oceans*, 61-62:14–34. doi:10.1016/j.dynatmoce.2013.02.002.

Bouffard, D., Boegman, L., Ackerman, J. D., Valipour, R., and Rao, Y. R. (2014). Near-inertial wave driven dissolved oxygen transfer through the thermocline of a large lake. *Journal of Great Lakes Research*, 40(2):300–307. doi:10.1016/j.jglr.2014.03.014.

Bouffard, D., Boegman, L., and Rao, Y. R. (2012). Poincaré wave–induced mixing in a large lake. *Limnology and Oceanography*, 57(4):1201–1216. doi:10.4319/lo.2012.57.4.1201.

Bouffard, D., Kiefer, I., Wüest, A., Wunderle, S., and Odermatt, D. (2018). Are surface temperature and chlorophyll in a large deep lake related? An analysis based on satellite observations in synergy with hydrodynamic modelling and in-situ data. *Remote Sensing of Environment*, 209:510–523. doi:10.1016/j.rse.2018.02.056.

Bouffard, D. and Lemmin, U. (2013). Kelvin waves in Lake Geneva. *Journal of Great Lakes Research*, 39(4):637–645. doi:10.1016/j.jglr.2013.09.005.

Choi, J., Troy, C., Hawley, N., McCormick, M., and Wells, M. (2020). Lateral dispersion of dye and drifters in the center of a very large lake. *Limnology and Oceanography*, 65(2):336–348. doi:10.1002/lno.11302.

Choi, J., Troy, C. D., Hsieh, T.-C., Hawley, N., and McCormick, M. J. (2012). A year of internal Poincaré waves in southern Lake Michigan. *Journal of Geophysical Research: Oceans*, 117:C07014. doi:10.1029/2012JC007984.

References

Csanady, G. T. (1975). Hydrodynamics of Large Lakes. *Annual Review of Fluid Mechanics*, 7(1):357–386. doi:10.1146/annurev.fl.07.010175.002041.

Davis, R. E., Eriksen, C. C., and Jones, C. (2002). Autonomous buoyancy-driven underwater gliders. In Griffiths, G., editor, *Technology and Applications of Autonomous Underwater Vehicles*, pages 37–58. Taylor & Francis.

Dillon, T. M. and Caldwell, D. R. (1980). The Batchelor spectrum and dissipation in the upper ocean. *Journal of Geophysical Research*, 85(C4):1910–1916. doi:10.1029/JC085iC04p01910.

Etemad-Shahidi, A. and Imberger, J. (2001). Anatomy of turbulence in thermally stratified lakes. *Limnology and Oceanography*, 46(5):1158–1170. doi:10.4319/lo.2001.46.5.1158.

Fer, I., Lemmin, U., and Thorpe, S. A. (2002). Observations of mixing near the sides of a deep lake in winter. *Limnology and Oceanography*, 47(2):535–544. doi:10.4319/lo.2002.47.2.0535.

Fer, I., Peterson, A. K., and Ullgren, J. E. (2014). Microstructure measurements from an underwater glider in the turbulent Faroe Bank Channel overflow. *Journal of Atmospheric and Oceanic Technology*, 31(5):1128–1150. doi:10.1175/JTECH-D-13-00221.1.

Fisher, A. W., Nidzieko, N. J., Scully, M. E., Chant, R. J., Hunter, E. J., and Mazzini, P. L. F. (2018). Turbulent mixing in a far-field plume during the transition to upwelling conditions: Microstructure observations from an AUV. *Geophysical Research Letters*, 45(18):9765–9773. doi:10.1029/2018GL078543.

Forrest, A. L., Laval, B. E., Pieters, R., and Lim, D. S. (2013). A cyclonic gyre in an ice-covered lake. *Limnology and Oceanography*, 58(1):363–375. doi:10.4319/lo.2013.58.1.0363.

Forrest, A. L., Laval, B. E., Pieters, R., and Lim, D. S. S. (2008). Convectively driven transport in temperate lakes. *Limnology and Oceanography*, 53(5):2321–2332. doi:10.4319/lo.2008.53.5_part_2.2321.

Frajka-Williams, E., Eriksen, C. C., Rhines, P. B., and Harcourt, R. R. (2011). Determining vertical water velocities from Seaglider. *Journal of Atmospheric and Oceanic Technology*, 28(12):1641–1656. doi:10.1175/2011JTECHO830.1.

Gargett, A. E., Osborn, T. R., and Nasmyth, P. W. (1984). Local isotropy and the decay of turbulence in a stratified fluid. *Journal of Fluid Mechanics*, 144:231–280. doi:10.1017/S0022112084001592.

Gibson, C. H. (1980). Fossil temperature, salinity, and vorticity turbulence in the ocean. In J. C. Nihoul, editor, *Marine Turbulence Proceedings of the 11th International Liege Colloquium on Ocean Hydrodynamics, Elsevier Oceanography Series*, pages Vol. 28, pp. 221–257, New York NY. Elsevier/North-Holland Inc.

Goodman, L., Levine, E. R., and Lueck, R. G. (2006). On measuring the terms of the turbulent kinetic energy budget from an AUV. *Journal of Atmospheric and Oceanic Technology*, 23(7):977–990. doi:10.1175/JTECH1889.1.

Goudsmit, G.-H., Peeters, F., Gloor, M., and Wüest, A. (1997). Boundary versus internal diapycnal mixing in stratified natural waters. *Journal of Geophysical Research*, 102(C13):27903–27914. doi:10.1029/97JC01861.

Gregg, M. C. (1977). Variations in the intensity of small-scale mixing in the main thermocline. *Journal of Physical Oceanography*, 7(3):436–454. doi:10.1175/1520-0485(1977)007<0436:VITIOS>2.0.CO;2.

Hodges, B. R., Imberger, J., Saggio, A., and Winters, K. B. (2000). Modeling basin-scale internal waves in a stratified lake. *Limnology and Oceanography*, 45(7):1603–1620. doi:10.4319/lo.2000.45.7.1603.

Ivey, G., Winters, K., and Koseff, J. (2008). Density stratification, turbulence, but how much mixing? *Annual Review of Fluid Mechanics*, 40(1):169–184. doi:10.1146/annurev.fluid.39.050905.110314.

Ivey, G. N. and Imberger, J. (1991). On the nature of turbulence in a stratified fluid. Part I: The energetics of mixing. *Journal of Physical Oceanography*, 21(5):650–658. doi:10.1175/1520-0485(1991)021<0650:OTNOTI>2.0.CO;2.

Kiefer, I., Odermatt, D., Anneville, O., Wüest, A., and Bouffard, D. (2015). Application of remote sensing for the optimization of in-situ sampling for monitoring of phytoplankton abundance in a large lake. *Science of The Total Environment*, 527-528:493–506. doi:10.1016/j.scitotenv.2015.05.011.

Kocsis, O., Prandke, H., Stips, A., Simon, A., and Wüest, A. (1999). Comparison of dissipation of turbulent kinetic energy determined from shear and temperature microstructure. *Journal of Marine Systems*, 21(1-4):67–84. doi:10.1016/S0924-7963(99)00006-8.

Laval, B., Bird, J. S., and Helland, P. D. (2000). An autonomous underwater vehicle for the study of small lakes. *Journal of Atmospheric and Oceanic Technology*, 17(1):69–76. doi:10.1175/1520-0426(2000)017<0069:AAUVFT>2.0.CO;2.

Laval, B., Imberger, J., Hodges, B. R., and Stocker, R. (2003). Modeling circulation in lakes: Spatial and temporal variations. *Limnology and Oceanography*, 48(3):983–994. doi:10.4319/lo.2003.48.3.0983.

Lemmin, U. and D'Adamo, N. (1996). Summertime winds and direct cyclonic circulation: observations from Lake Geneva. *Annales Geophysicae*, 14(11):1207–1220. doi:10.1007/s00585-996-1207-z.

Lemmin, U., Mortimer, C. H., and Bäuerle, E. (2005). Internal seiche dynamics in Lake Geneva. *Limnology and Oceanography*, 50(1):207–216. doi:10.4319/lo.2005.50.1.0207.

Leon, L. F., Smith, R. E., Hipsey, M. R., Bocaniov, S. A., Higgins, S. N., Hecky, R. E., Antenucci, J. P., Imberger, J. A., and Guildford, S. J. (2011). Application of a 3D hydrodynamic–biological model for seasonal and spatial dynamics of water quality and phytoplankton in Lake Erie. *Journal of Great Lakes Research*, 37(1):41–53. doi:10.1016/j.jglr.2010.12.007.

Lucas, N. S., Grant, A. L. M., Rippeth, T. P., Polton, J. A., Palmer, M. R., Brannigan, L., and Belcher, S. E. (2019). Evolution of oceanic near-surface stratification in response to an autumn storm. *Journal of Physical Oceanography*, 49(11):2961–2978. doi:10.1175/JPO-D-19-0007.1.

MacIntyre, S. and Melack, J. M. (1995). Vertical and horizontal transport in lakes: linking littoral, benthic, and pelagic habitats. *Journal of the North American Benthological Society*, 14(4):599–615. doi:10.2307/1467544.

MacIntyre, S., Romero, J. R., and Kling, G. W. (2002). Spatial-temporal variability in surface layer deepening and lateral advection in an embayment of Lake Victoria, East Africa. *Limnology and Oceanography*, 47(3):656–671. doi:10.4319/lo.2002.47.3.0656.

MacIntyre, S., Romero, J. R., Silsbe, G. M., and Emery, B. M. (2014). Stratification and horizontal exchange in Lake Victoria, East Africa. *Limnology and Oceanography*, 59(6):1805–1838. doi:10.4319/lo.2014.59.6.1805.

Matthews, M. W. (2011). A current review of empirical procedures of remote sensing in Inland and near-coastal transitional waters. *International Journal of Remote Sensing*, 32(21):6855–6899. doi:10.1080/01431161.2010.512947.

McDougall, T. J. and Barker, P. (2011). Getting started with TEOS-10 and the Gibbs Seawater (GSW) oceanographic toolbox. *SCOR/IAPSO WG.*, 127:1–28.

Merckelbach, L. (2018). Initial realse of Glider flight model. Version 1.0.1. *Zenodo*. doi:10.5281/zenodo.2222694.
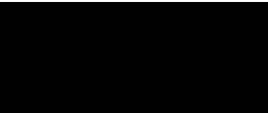
References

Merckelbach, L., Berger, A., Krahmann, G., Dengler, M., and Carpenter, J. R. (2019). A dynamic flight model for Slocum gliders and implications for turbulence microstructure measurements. *Journal of Atmospheric and Oceanic Technology*, 36(2):281–296. doi:10.1175/JTECH-D-18-0168.1.

Merckelbach, L., Smeed, D., and Griffiths, G. (2010). Vertical water velocities from underwater gliders. *Journal of Atmospheric and Oceanic Technology*, 27(3):547–563. doi:10.1175/2009JTECHO710.1.

Monismith, S. (1986). An experimental study of the upwelling response of stratified reservoirs to surface shear stress. *Journal of Fluid Mechanics*, 171:407–439. doi:10.1017/S0022112086001507.

Monismith, S. G., Koseff, J. R., and White, B. L. (2018). Mixing efficiency in the presence of stratification: When is it constant? *Geophysical Research Letters*, 45(11):5627–5634. doi:10.1029/2018GL077229.

Mortimer, C. H. (1952). Water movements in lakes during summer stratification; evidence from the distribution of temperature in Windermere. *Philosophical Transactions of the Royal Society of London. Series B, Biological Sciences*, 236(635):355–398. doi:10.1098/rstb.1952.0005.

Ng, S. M. Y., Antenucci, J. P., Hipsey, M. R., Tibor, G., and Zohary, T. (2011). Physical controls on the spatial evolution of a dinoflagellate bloom in a large lake. *Limnology and Oceanography*, 56(6):2265–2281. doi:10.4319/lo.2011.56.6.2265.

Nouchi, V., Kutser, T., Wüest, A., Müller, B., Odermatt, D., Baracchini, T., and Bouffard, D. (2019). Resolving biogeochemical processes in lakes using remote sensing. *Aquatic Sciences*, 81(2):27. doi:10.1007/s00027-019-0626-3.

Nouchi, V., Odermatt, D., Wüest, A., and Bouffard, D. (2018). Effects of non-uniform vertical constituent profiles on remote sensing reflectance of oligo- to mesotrophic lakes. *European Journal of Remote Sensing*, 51(1):808–821. doi:10.1080/22797254.2018.1493360.

Odermatt, D., Gitelson, A., Brando, V. E., and Schaepman, M. (2012). Review of constituent retrieval in optically deep and complex waters from satellite imagery. *Remote Sensing of Environment*, 118:116–126. doi:10.1016/j.rse.2011.11.013.

Osborn, T. R. (1980). Estimates of the local rate of vertical diffusion from dissipation measurements. *Journal of Physical Oceanography*, 10(1):83–89. doi:10.1175/1520-0485(1980)010<0083:EOTLRO>2.0.CO;2.

Osborn, T. R. and Cox, C. S. (1972). Oceanic fine structure. *Geophysical Fluid Dynamics*, 3(1):321–345. doi:10.1080/03091927208236085.

Osborn, T. R. and Lueck, R. G. (1985). Turbulence measurements with a submarine. *Journal of Physical Oceanography*, 15(11):1502–1520. doi:10.1175/1520-0485(1985)015<1502:TMWAS>2.0.CO;2.

Peeters, F., Straile, D., Lorke, A., and Ollinger, D. (2007). Turbulent mixing and phytoplankton spring bloom development in a deep lake. *Limnology and Oceanography*, 52(1):286–298. doi:10.4319/lo.2007.52.1.0286.

Peeters, F., Wüest, A., Piepke, G., and Imboden, D. M. (1996). Horizontal mixing in lakes. *Journal of Geophysical Research: Oceans*, 101(C8):18361–18375. doi:10.1029/96JC01145.

Peterson, A. K. and Fer, I. (2014). Dissipation measurements using temperature microstructure from an underwater glider. *Methods in Oceanography*, 10:44–69. doi:10.1016/j.mio.2014.05.002.

Preusse, M., Peeters, F., and Lorke, A. (2010). Internal waves and the generation of turbulence in the thermocline of a large lake. *Limnology and Oceanography*, 55(6):2353–2365. doi:10.4319/lo.2010.55.6.2353.

Ravens, T. M., Kocsis, O., Wüest, A., and Granin, N. (2000). Small-scale turbulence and vertical mixing in Lake Baikal. *Limnology and Oceanography*, 45(1):159–173.

Robbins, I. C., Kirkpatrick, G. J., Blackwell, S. M., Hillier, J., Knight, C. A., and Moline, M. A. (2006). Improved monitoring of HABs using autonomous underwater vehicles (AUV). *Harmful Algae*, 5(6):749–761. doi:10.1016/j.hal.2006.03.005.

Rogowski, P., Merrifield, S., Ding, L., Terrill, E., and Gesiriech, G. (2019). Robotic mapping of mixing and dispersion of augmented surface water in a drought frequent reservoir. *Limnology and Oceanography: Methods*, 17(9):475–489. doi:10.1002/lom3.10326.

Ruddick, B., Anis, A., and Thompson, K. (2000). Maximum likelihood spectral fitting: The Batchelor spectrum. *Journal of Atmospheric and Oceanic Technology*, 17(11):1541–1555. doi:10.1175/1520-0426(2000)017<1541:MLSFTB>2.0.CO;2.

Rudnick, D. L. (2016). Ocean research enabled by underwater gliders. *Annual Review of Marine Science*, 8(1):519–541. doi:10.1146/annurev-marine-122414-033913.

Rueda, F. J., Schladow, S. G., Monismith, S. G., and Stacey, M. T. (2005). On the effects of topography on wind and the generation of currents in a large multi-basin lake. *Hydrobiologia*, 532(1-3):139–151. doi:10.1007/s10750-004-9522-4.

Saggio, A. and Imberger, J. (2001). Mixing and turbulent fluxes in the metalimnion of a stratified lake. *Limnology and Oceanography*, 46(2):392–409. doi:10.4319/lo.2001.46.2.0392.

Scheifele, B., Waterman, S., Merckelbach, L., and Carpenter, J. R. (2018). Measuring the dissipation rate of turbulent kinetic energy in strongly stratified, low-energy environments: A case study from the Arctic Ocean. *Journal of Geophysical Research: Oceans*, 123(8):5459–5480. doi:10.1029/2017JC013731.

Schladow, S. G., Pálmarsson, S. Ó., Steissberg, T. E., Hook, S. J., and Prata, F. E. (2004). An extraordinary upwelling event in a deep thermally stratified lake. *Geophysical Research Letters*, 31(15):L15504. doi:10.1029/2004GL020392.

Schultze, L. K. P., Merckelbach, L. M., and Carpenter, J. R. (2017). Turbulence and mixing in a shallow shelf sea from underwater gliders. *Journal of Geophysical Research: Oceans*, 122(11):9092–9109. doi:10.1002/2017JC012872.

Schwefel, R., Gaudard, A., Wüest, A., and Bouffard, D. (2016). Effects of climate change on deepwater oxygen and winter mixing in a deep lake (Lake Geneva): Comparing observational findings and modeling. *Water Resources Research*, 52(11):8811–8826. doi:10.1002/2016WR019194.

Shimizu, K., Imberger, J., and Kumagai, M. (2007). Horizontal structure and excitation of primary motions in a strongly stratified lake. *Limnology and Oceanography*, 52(6):2641–2655. doi:10.4319/lo.2007.52.6.2641.

Sommer, T., Carpenter, J. R., Schmid, M., Lueck, R. G., and Wüest, A. (2013). Revisiting microstructure sensor responses with implications for double-diffusive fluxes. *Journal of Atmospheric and Oceanic Technology*, 30(8):1907–1923. doi:10.1175/JTECH-D-12-00272.1.

Soulignac, F., Danis, P.-a., Bouffard, D., Chanudet, V., Dambrine, E., Guénand, Y., Harmel, T., Ibelings, B. W., Trevisan, D., Uittenbogaard, R., and Anneville, O. (2018). Using 3D modeling and remote sensing capabilities for a better understanding of spatio-temporal heterogeneities of phytoplankton abundance in large lakes. *Journal of Great Lakes Research*, 44(4):756–764. doi:10.1016/j.jglr.2018.05.008.

References

Steinbuck, J. V., Koseff, J. R., Genin, A., Stacey, M. T., and Monismith, S. G. (2011). Horizontal dispersion of ocean tracers in internal wave shear. *Journal of Geophysical Research*, 116(C11):C11031. doi:10.1029/2011JC007213.

Steinbuck, J. V., Stacey, M. T., and Monismith, S. G. (2009). An Evaluation of χT estimation techniques: Implications for Batchelor fitting and ϵ. *Journal of Atmospheric and Oceanic Technology*, 26(8):1652–1662. doi:10.1175/2009JTECHO611.1.

Steissberg, T. E., Hook, S. J., and Schladow, S. G. (2005). Characterizing partial upwellings and surface circulation at Lake Tahoe, California–Nevada, USA with thermal infrared images. *Remote Sensing of Environment*, 99(1-2):2–15. doi:10.1016/j.rse.2005.06.011.

Thorpe, S. A. (2007). *An introduction to ocean turbulence*. Cambridge University Press, Cambridge.

Thorpe, S. A., Lemmin, U., Perrinjaquet, C., and Fer, I. (1999). Observations of the thermal structure of a lake using a submarine. *Limnology and Oceanography*, 44(6):1575–1582. doi:10.4319/lo.1999.44.6.1575.

Tippenhauer, S., Dengler, M., Fischer, T., and Kanzow, T. (2015). Turbulence and finestructure in a deep ocean channel with sill overflow on the mid-Atlantic ridge. *Deep Sea Research Part I: Oceanographic Research Papers*, 99:10–22. doi:10.1016/j.dsr.2015.01.001.

Valipour, R., Bouffard, D., Boegman, L., and Rao, Y. R. (2015). Near-inertial waves in Lake Erie. *Limnology and Oceanography*, 60(5):1522–1535. doi:10.1002/lno.10114.

Vidal, J., MacIntyre, S., McPhee-Shaw, E. E., Shaw, W. J., and Monismith, S. G. (2013). Temporal and spatial variability of the internal wave field in a lake with complex morphometry. *Limnology and Oceanography*, 58(5):1557–1580. doi:10.4319/lo.2013.58.5.1557.

Woods, J. D. (1968). Wave-induced shear instability in the summer thermocline. *Journal of Fluid Mechanics*, 32(4):791–800. doi:10.1017/S0022112068001035.

Wüest, A. and Lorke, A. (2003). Small-scale hydrodynamics in lakes. *Annual Review of Fluid Mechanics*, 35(1):373–412. doi:10.1146/annurev.fluid.35.101101.161220.

Wüest, A., Piepke, G., and Van Senden, D. C. (2000). Turbulent kinetic energy balance as a tool for estimating vertical diffusivity in wind-forced stratified waters. *Limnology and Oceanograhy*, 45(6):1388–1400. doi:10.4319/lo.2000.45.6.1388.

Supporting information for Chapter 5
Towards the assessment of lateral variability in lakes: Turbulent mixing from an underwater glider in Lake Geneva

Oscar Sepúlveda Steiner[1], Alexander Forrest[2], Jasmin McInerney[2], Sébastien Lavanchy[1], Bieito Fernández-Castro[1], Damien Bouffard[3], and Alfred Wüest[1,3]

[1]Physics of Aquatic Systems Laboratory, Margaretha Kamprad Chair, Institute of Environmental Engineering, École Polytechnique Fédérale de Lausanne, Lausanne, Switzerland.

[2]Civil & Environmental Engineering, University of California – Davis, Davis, CA, USA.

[3]Department of Surface Waters – Research and Management, Eawag, Swiss Federal Institute of Aquatic Science and Technology, Kastanienbaum, Switzerland.

Figure S5.1 – Time series of ADCP measurements. The location of each station is indicated in Figure 5.1

6 Conclusions and outlook

6.1 Summary

The goal of this work was to examine turbulence characteristics of bio-physical interactions within aquatic environments. We studied in detail the formation and persistence of three characteristic spatial structures in three lakes of different levels of external forcing: (i) bioconvection-induced mixed layer (Chapters 2 and 3), (ii) cyanobacterial thin layer (Chapter 4), and, (iii) heterogeneities within algae patches (Chapter 5). These interactions were investigated using vertical and/or lateral sampling strategies. Turbulent mixing within the biological structure and its surroundings was assessed by means of temperature microstructure measurements. The bioconvective mixed layer and thin phytoplankton layer were characterized vertically with conventional profilers. We provide a better understanding of the interaction of these layers with vertical turbulent processes in lakes. For the last application, we invested great effort into the validation and analysis of lateral variability of turbulence and mixing acquired with an underwater glider. The measurements performed are a first step and provide a solid base for future in-situ turbulence of phytoplankton patches affected by turbulence and transport processes.

Bioconvection observed in the alpine, meromictic Lake Cadagno offered a unique environment to analyze the role of biological activity in influencing the vertical structure of the water column they inhabit. A highly concentrated layer of heavy, motile and photoautotrophic bacteria *Chromatium okenii* forms a convective mixing layer (ML) at the depth of the oxic-anoxic interface. Microstructure measurements from six summer field campaigns, spanning three summer periods, were combined with an analytical diffusive-shape model, to evaluate the effects of turbulent diffusion adjacent to the bioconvective MLs (Chapter 2). Numerous forms of the well-defined ML were detected in the field data, which also revealed their persistence during the entire day-night cycle. The average mixed layer thickness h_{mix} was 0.61 ± 0.30 m associated with a mean convective time scale of $\tau^* \approx 20$ min. The surrounding turbulent diffusivity of the ML affected the transitional boundaries between ML and background stratification, by an adjustment distance of $\delta \approx 0.15 \pm 0.09$ m. Microstructure measurements yielded diffusivity results in good agreement with estimates from previous dye release experiments in Lake Cadagno (1.6×10^{-6} m^2 s^{-1}; Wüest, 1994). Altogether, these observations combine into a time scale of ≈ 2.5 h to smooth an inactive ML of average characteristics. Considering ML shapes, as obtained from the model (h_{mix} and δ) and turbulence estimates from microstructure profiles, we derived a scaling based on the Péclet number, which compares convection and diffusion. The generalization of this scheme, showed good agreement with double-diffusive and radiatively-driven under-ice convection in other convectively-mixed aquatic settings. This constitutes further proof of the convective nature of the exceptional subsurface bacteria-induced ML in Lake Cadagno.

Since *C. okenii* are photoautotrophic bacteria that seek light at the oxic-anoxic interface for anoxygenic photosynthesis, the encountered nighttime ML is an unexpected result. Moreover, the average smoothing time scale turned out much shorter than the duration of one night (Chapter 2). These results suggest that bacteria must remain active during nights or else diffusivity would completely erode the ML. Therefore, in Chapter 3, we focused on the persistence of the ML induced by bioconvection over the entire daily cycle. ML shape and turbulent characteristics were evaluated with an intensive 48-hours survey combining vertical microstructure and high-resolution current measurements. Additionally, turbidity profiles informed on the bacterial layer position and shape. These observations revealed more intense turbulent dissipation by a factor of five during daytime than nighttime. However, ML shape and turbid layer shape remained virtually unchanged through the diel cycle. Furthermore, the nighttime ML presented convective activity that remained above the level of decay for a sudden cessation of convective turbulence (Caldwell et al., 1997). This provides evidence that the ML does not form every day at dawn but rather is actively maintained by bacterial migration occurring also during nights. These observations raise questions on whether bioconvection is also an ecological strategy. The physical analysis performed cannot provide an answer, but may shed light on the advantages of upward migration during dark periods without photosynthesis. Further conceptual and data analysis resulted in ML formation time scales of about a daytime, and favorable conditions for high concentration of *C. okenii* to drive convective plumes. The latter suggests that overnight maintenance of the ML may be an energy-efficient strategy.

In Chapter 4 we analyzed the seasonal persistence (May to October) of a cyanobacterial thin layer (*Planktothrix rubescens*) forming every year in Lake Zurich. The thin layer develops in the thermocline, close to where the mean daily insolation supports neutral buoyancy for this species. We characterized turbulence, mixing and stratification in this zone by means of vertical microstructure profiles as well as high-resolution current measurements. The data revealed an strongly stratified thermocline where vertical turbulent overturns were very rare and small. As a result, turbulent vertical fluxes were negligible and the stratification provided a very stable environment for the *P. rubescens* thin layer. The weak vertical exchange explains the seasonal persistence of the layer. We also showed that the layer decline in fall is not caused by wind-driven stratified turbulence in the thermocline, but rather by nighttime convective mixing eroding the layer from above. Convective vertical motions entrain *P. rubescens* filaments to the surface mixed layer, where larger eddies, not constrained by stratification, prevent them to form their characteristic filamentous layering.

In Chapter 5, we explored the connection between lateral variability of physical properties, namely turbulence, and the distribution of bio-optical properties in Lake Geneva using a glider equipped with a turbulence package. To the best of our knowledge, this is the first study using temperature microstructure from a glider to estimate turbulence parameters in a lake. For this reason, our first focus was the validation of glider-based turbulence estimations. Performing an analysis similar to Dillon and Caldwell (1980), we binned 30'000 temperature microstructure spectra in different ranges of Cox number and calculated their ensemble-average. The analysis demonstrated that spectra meeting the Batchelor fitting conditions capture the variance and the roll-off as expected characteristics of the theoretical shape. Yet, spectra obtained from segments of data with low Cox numbers deviate from the Batchelor shape at low wavenumbers. Based on the validated turbulence parameters, we encountered inhibited mixing in the thermocline ($R_f < 0.01$) and a mixing efficiency in the deep interior below the canonical efficiency reported for the ocean ($Ri_f \approx 0.1 < Ri_f^{ocean} = 0.17$). The former appears as a favorable condition for algae to develop in the thermocline (similar as in Chapter 4). The spatio-temporal heterogeneity in the distribution of algal communities was investigated using fluorescence measurements collected during a set of cross-shore and along-shore repeated glider transects. Fluorescence anomalies with respect to a composite mean-transect captured algal patches with a characteristic horizontal size of ~1 km. This is comparable to twice the radius of near-inertial Poincaré oscillations recorded with three moored acoustic current profilers. We hypothesize that currents induced by large-scale dynamics,

such as internal Poincaré waves, drive advection of algae patches, explaining the encountered variability. However, further analysis of our measurements and 3D modeling is needed to address this. The anomalies methodology could be applied in future glider deployments with repeated trajectories to assess the spatio-temporal variability of water properties.

6.2 Future development

This thesis is far from closing a topic. We investigated turbulence and mixing processes in lakes and tried to apply them to biophysical interactions. Most interesting advances were summarized in the previous section. Yet, these studies and a big volume of data gathered through these four years, not reported here, also open new research questions.

Bioconvection

At the beginning of this thesis, besides the proof of concept presented by Sommer et al. (2017), little was known about bioconvection in a natural system. The interaction of the convective ML with the surrounding waters presented in Chapter 2 is a first step towards a systematic evaluation of the process. There is still much research needed to understand the onset, time evolution, and break down of the bioconvective mixed layer, which is annually formed in Lake Cadagno. How the bacterial community reacts and adapts to storms or several days of photosynthesis-inhibiting bad weather conditions, and the effect those conditions impose on the ML remain still unknown. Chapter 3 presents a first time-dependent analysis, regarding the diel cycle. The next step should include the analysis of the seasonal evolution, such as the response to changing meteorological forcing and seasonal deepening of the thermocline. Field measurements such as the seasonal CTD profile monitoring presented in Chapter 3 (Figure 3.11) are a great starting point. However, research would best benefit from complementary modeling. A simplified model incorporating production of convection by bacteria, background stratification and diffusivity smoothing would allow to evaluate short developments under varying conditions. Coupling this model with a 1D model capturing the seasonal evolution of the lake vertical structure would provide further understanding of the bioconvective layer response to the external drivers.

The intensive sampling undertaken to characterize the evolution of the bioconvective ML unveiled also unexpected physical features in the interior of Lake Cadagno. We recorded a persistent vertical oscillation with a period of ≈40 min, 4 times faster than the fundamental internal seiche (e.g. Figure 3.5, Chapter 3). This suggest the presence of nonlinear internal waves (Boehrer and Stevens, 2005; Henderson and Deemer, 2012). More important than the underlying mechanisms is that internal baroclinic motions may contract and stretch the bacterial layer, likely having an impact on bio-convection dynamics. Particularly, contraction of density profiles that are already unstable due to bacteria accumulation at the top of the oxic-anoxic interface (Figure 3.3) may intensify the generation of convection. The examination of these interactions requires long-term, high temporal (30 s) and vertical resolution (20-30 cm) measurements of temperature and turbidity in the ML and its surroundings. This would allow to account for temperature fluctuations, the effective strain rate (e.g. Alford and Pinkel, 2000) induced by dislocations as well as ML position and a proxy for bacteria concentration. Numerical modeling combined with stability analysis could yield a detailed critical condition for the generation of convection. Complementing observations and modeling may elucidate whether vertical dislocation intensify the generation of bioconvection.

Factors controlling mixing in the thermocline of deep lakes

Our microstructure measurements in Lakes Zurich and Geneva revealed that turbulent mixing in the thermocline was inhibited in the lakes' interior. A possible mechanism explaining this interplay is a positive feedback between the weak forcing and the strong stratification, which further inhibits the vertical turbulent exchange and thereby makes the stratification even stronger, intensifying the inhibition of turbulence. This seems sound for Lake Zurich that is exposed to weak winds and the internal motions are only weakly influenced by Earth rotation. However, this observation is more surprising in Lake Geneva, where more than 2-fold wind energy is available for mixing compared to lake Zurich and where the larger size of the lake allows for more complex rotational internal waves to develop, with dominant Poincaré waves in the interior (Chapter 5). Although they conducted their study in a shallow lake (~20 m), Bouffard et al. (2012) demonstrated that internal Poincaré waves can become unstable and can induce mixing away from the lake boundaries. This raises the question of what the factors are that determine the generation of mixing in the interior of large lakes affected by Earth's rotation, and why these interactions seem to be absent in some large, deep lakes, like Lake Geneva. There is still a lack of fundamental understanding about the factors controlling the mixing dynamics in lakes of varying sizes, depths and external forcing. Further research, including high-resolution temperature, current and turbulence measurements in Lake Geneva and other systems are required to address these questions.

Exploring lateral variability with novel technology

Gliders – Underwater gliders are expected to break new ground in the study of basin-scale processes in large lakes (Austin, 2013). Recently, Austin (2019) pioneered this path and reported convective chimneys (Wadhams et al., 2002) measured with a glider in Lake Superior. Our glider-based research was initially designed to shed light on the spatial variability associated with gyre circulation as often observed in Lake Geneva (Baracchini et al., 2020). For logistic reasons related to passenger boats traffic, we decided to perform most of our measurements in the western side of the main basin, where there is less traffic activity. As reported in Chapter 5, the signature of the gyre was barely undetectable in our glider measurements. An additional opportunistic mission, motivated by three-dimensional model forecasts (Figure 6.1a; meteolakes.ch), was performed to characterize the center of the main basin in Lake Geneva. These measurements were not further considered in this thesis because (i) the turbulence package did not work and (ii) the lack of background moored measurements (currents and temperature) in this area. However, the glider-based CTD measurements were of great quality (Figures 6.1b,c), showing a doming structure, as expected for a baroclinic gyre. Moreover, the chlorophyll-a signal was coupled with the thermocline upwelling. These field observations highlight the potential of gliders in revealing large-scale features. Much advancement could be achieved in Lake Geneva, which develops persistent basin-scale gyres. Yet, the top 50 m are reserved for fishing activities, therefore glider navigation is risky and temporal characterization of the background stratification cannot be resolved. Despite the difficulties associated with glider navigation and logistic, I would strongly recommend to continue efforts with using gliders. Knowledge about gyres (Shimizu et al., 2007) and upwelling events (Schladow et al., 2004; Roberts, 2019) as well as the spatial variability they induce in water properties and their ecological implications may greatly benefit from further glider deployments in large lakes.

AUVs – Intended for resolving small to fine scales of cm in the vertical to dm in the horizontal, Autonomous Underwater Vehicles (AUVs) can close the gap between basin-scale horizontal measurements (glider) and vertically well resolved structures (microstructure profilers). The role of turbulence and mixing in the hydrodynamic connectivity between littoral, benthic and pelagic habitats (MacIntyre and Melack, 1995) is a challenging biophysical interaction in lakes that would greatly benefit from this approach.
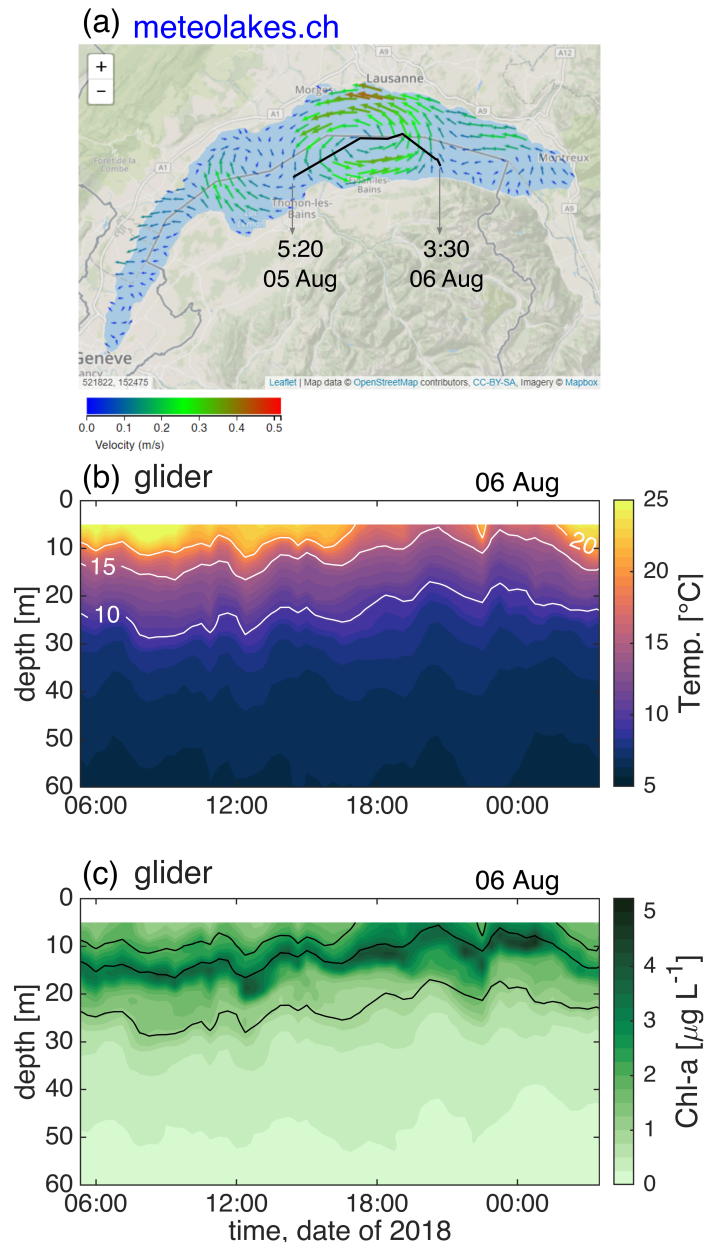
Figure 6.1 – Gyre in the center of the main basin of Lake Geneva. (a) Surface currents predicted by the operational forecast model meteolakes.ch (Baracchini et al., 2020) for 05 August 2018 21:00. (b,c) Temperature and chlorophyll-a measured with the glider along the trajectory marked with a black line in (a). Contours are constructed using a Gaussian window weighted average (see Chapter 5 – Methods). The sampling was designed upon results of the model.

Bibliography

Abbott, M. R., Denman, K. L., Powell, T. M., Richerson, P. J., Richards, R. C., and Goldman, C. R. (1984). Mixing and the dynamics of the deep chlorophyll maximum in Lake Tahoe. *Limnology and Oceanography*, 29(4):862–878. doi:10.4319/lo.1984.29.4.0862.

Abraham, E. R. (1998). The generation of plankton patchiness by turbulent stirring. *Nature*, 391(6667):577–580. doi:10.1038/35361.

Adrian, R., O'Reilly, C. M., Zagarese, H., Baines, S. B., Hessen, D. O., Keller, W., Livingstone, D. M., Sommaruga, R., Straile, D., Van Donk, E., Weyhenmeyer, G. A., and Winder, M. (2009). Lakes as sentinels of climate change. *Limnology and Oceanography*, 54(6part2):2283–2297. doi:10.4319/lo.2009.54.6_part_2.2283.

Akitomo, K., Tanaka, K., Kumagai, M., and Jiao, C. (2009). Annual cycle of circulations in Lake Biwa, part 2: Mechanisms. *Limnology*, 10(2):119–129. doi:10.1007/s10201-009-0267-7.

Alexander, R. and Imberger, J. (2013). Phytoplankton patchiness in Winam Gulf, Lake Victoria: a study using principal component analysis of in situ fluorescent excitation spectra. *Freshwater Biology*, 58(2):275–291. doi:10.1111/fwb.12057.

Alford, M. H. and Pinkel, R. (2000). Observations of Overturning in the Thermocline: The Context of Ocean Mixing. *Journal of Physical Oceanography*, 30(5):805–832. doi:10.1175/1520-0485(2000)030<0805:OOOITT>2.0.CO;2.

Anneville, O., Souissi, S., Ibanez, F., Ginot, V., Druart, J. C., and Angeli, N. (2002). Temporal mapping of phytoplankton assemblages in Lake Geneva: Annual and interannual changes in their patterns of succession. *Limnology and Oceanography*, 47(5):1355–1366. doi:10.4319/lo.2002.47.5.1355.

Antenucci, J. P., Imberger, J., and Saggio, A. (2000). Seasonal evolution of the basin-scale internal wave field in a large stratified lake. *Limnology and Oceanography*, 45(7):1621–1638. doi:10.4319/lo.2000.45.7.1621.

Appt, J., Imberger, J., and Kobus, H. (2004). Basin-scale motion in stratified Upper Lake Constance. *Limnology and Oceanography*, 49(4):919–933. doi:10.4319/lo.2004.49.4.0919.

Austin, J. (2012). Resolving a persistent offshore surface temperature maximum in Lake Superior using an autonomous underwater glider. *Aquatic Ecosystem Health and Management*, 15(3):316–321. doi:10.1080/14634988.2012.711212.

Austin, J. (2013). The potential for autonomous underwater gliders in large lake research. *Journal of Great Lakes Research*, 39(S1):8–13. doi:10.1016/j.jglr.2013.01.004.

Austin, J. A. (2019). Observations of radiatively driven convection in a deep lake. *Limnology and Oceanography*, 64(5):2152–2160. doi:10.1002/lno.11175.

Bibliography

Baker, M. A. and Gibson, C. H. (1987). Sampling turbulence in the stratified ocean: Statistical consequences of strong intermittency. *Journal of Physical Oceanography*, 17(10):1817–1836. doi:10.1175/1520-0485(1987)017<1817:STITSO>2.0.CO;2.

Banerjee, S., Krahl, R., Durst, F., and Zenger, C. (2007). Presentation of anisotropy properties of turbulence, invariants versus eigenvalue approaches. *Journal of Turbulence*, 8:1–27. doi:10.1080/14685240701506896.

Baracchini, T., Wüest, A., and Bouffard, D. (2020). Meteolakes: An operational online three-dimensional forecasting platform for lake hydrodynamics. *Water Research*, 172:115529. doi:10.1016/j.watres.2020.115529.

Barton, A. D., Ward, B. A., Williams, R. G., and Follows, M. J. (2014). The impact of fine-scale turbulence on phytoplankton community structure. *Limnology and Oceanography: Fluids and Environments*, 4(1):34–49. doi:10.1215/21573689-2651533.

Batchelor, G. K. (1959). Small-scale variation of convected quantities like temperature in turbulent fluid Part 1. General discussion and the case of small conductivity. *Journal of Fluid Mechanics*, 5(1):113–133. doi:10.1017/S002211205900009X.

Bauer, S. W., Graf, W. H., Mortimer, C. H., and Perrinjaquet, C. (1981). Inertial motion in Lake Geneva (Le Léman). *Archives for Meteorology, Geophysics, and Bioclimatology Series A*, 30(3):289–312. doi:10.1007/BF02257850.

Bearon, R. N. and Grünbaum, D. (2006). Bioconvection in a stratified environment: Experiments and theory. *Physics of Fluids*, 18(12):127102. doi:10.1063/1.2402490.

Bees, M. A. (2020). Advances in bioconvection. *Annual Review of Fluid Mechanics*, 52(1):449–476. doi:10.1146/annurev-fluid-010518-040558.

Bees, M. A. and Hill, N. A. (1997). Wavelengths of bioconvection patterns. *Journal of Experimental Biology*, 200(10):1515–1526.

Benoit-Bird, K. J., Cowles, T. J., and Wingard, C. E. (2009). Edge gradients provide evidence of ecological interactions in planktonic thin layers. *Limnology and Oceanography*, 54(4):1382–1392. doi:10.4319/lo.2009.54.4.1382.

Berg, J. S., Pjevac, P., Sommer, T., Buckner, C. R., Philippi, M., Hach, P. F., Liebeke, M., Holtappels, M., Danza, F., Tonolla, M., Sengupta, A., Schubert, C. J., Milucka, J., and Kuypers, M. M. (2019). Dark aerobic sulfide oxidation by anoxygenic phototrophs in anoxic waters. *Environmental Microbiology*, 21(5):1611–1626. doi:10.1111/1462-2920.14543.

Bishop, C. M. (2008). Sensor dynamics of autonomous underwater gliders, Master Thesis, Memorial University of Newfoundland, Canada.

Bluteau, C. E., Jones, N. L., and Ivey, G. N. (2011). Estimating turbulent kinetic energy dissipation using the inertial subrange method in environmental flows. *Limnology and Oceanography: Methods*, 9:302–321. doi:10.4319/lom.2011.9.302.

Boegman, L., Imberger, J., Ivey, G. N., and Antenucci, J. P. (2003). High-frequency internal waves in large stratified lakes. *Limnology and Oceanography*, 48(2):895–919. doi:10.4319/lo.2003.48.2.0895.

Boehrer, B. and Schultze, M. (2008). Stratification of lakes. *Reviews of Geophysics*, 46(2):RG2005. doi:10.1029/2006RG000210.

Boehrer, B. and Stevens, C. (2005). Ray waves in a pit lake. *Geophysical Research Letters*, 32(24):L24608. doi:10.1029/2005GL024678.

Bohle-Carbonell, M. (1986). Currents in Lake Geneva. *Limnology and Oceanography*, 31(6):1255–1266. doi:10.4319/lo.1986.31.6.1255.

Bossard, P., Gammeter, S., Lehmann, C., Schanz, F., Bachofen, R., Bürgi, H. R., Steiner, D., and Zimmermann, U. (2001). Limnological description of the Lakes Zürich, Lucerne, and Cadagno. *Aquatic Sciences*, 63(3):225–249. doi:10.1007/PL00001353.

Bouffard, D. and Boegman, L. (2013). A diapycnal diffusivity model for stratified environmental flows. *Dynamics of Atmospheres and Oceans*, 61-62:14–34. doi:10.1016/j.dynatmoce.2013.02.002.

Bouffard, D., Boegman, L., Ackerman, J. D., Valipour, R., and Rao, Y. R. (2014). Near-inertial wave driven dissolved oxygen transfer through the thermocline of a large lake. *Journal of Great Lakes Research*, 40(2):300–307. doi:10.1016/j.jglr.2014.03.014.

Bouffard, D., Boegman, L., and Rao, Y. R. (2012). Poincaré wave–induced mixing in a large lake. *Limnology and Oceanography*, 57(4):1201–1216. doi:10.4319/lo.2012.57.4.1201.

Bouffard, D., Kiefer, I., Wüest, A., Wunderle, S., and Odermatt, D. (2018). Are surface temperature and chlorophyll in a large deep lake related? An analysis based on satellite observations in synergy with hydrodynamic modelling and in-situ data. *Remote Sensing of Environment*, 209:510–523. doi:10.1016/j.rse.2018.02.056.

Bouffard, D. and Lemmin, U. (2013). Kelvin waves in Lake Geneva. *Journal of Great Lakes Research*, 39(4):637–645. doi:10.1016/j.jglr.2013.09.005.

Bouffard, D. and Wüest, A. (2019). Convection in lakes. *Annual Review of Fluid Mechanics*, 51(1):189–215. doi:10.1146/annurev-fluid-010518-040506.

Bouffard, D., Zdorovennov, R. E., Zdorovennova, G. E., Pasche, N., Wüest, A., and Terzhevik, A. Y. (2016). Ice-covered Lake Onega: effects of radiation on convection and internal waves. *Hydrobiologia*, 780(1):21–36. doi:10.1007/s10750-016-2915-3.

Bouffard, D., Zdorovennova, G., Bogdanov, S., Efremova, T., Lavanchy, S., Palshin, N., Terzhevik, A., Vinnå, L. R., Volkov, S., Wüest, A., Zdorovennov, R., and Ulloa, H. N. (2019). Under-ice convection dynamics in a boreal lake. *Inland Waters*, 9(2):142–161. doi:10.1080/20442041.2018.1533356.

Broullón, E., López-Mozos, M., Reguera, B., Chouciño, P., Doval, M. D., Fernández-Castro, B., Gilcoto, M., Nogueira, E., Souto, C., and Mouriño-Carballido, B. (2020). Thin layers of phytoplankton and harmful algae events in a coastal upwelling system. *Progress in Oceanography*, page Submitted.

Cadier, M., Gorgues, T., LHelguen, S., Sourisseau, M., and Memery, L. (2017). Tidal cycle control of biogeochemical and ecological properties of a macrotidal ecosystem. *Geophysical Research Letters*, 44(16):8453–8462. doi:10.1002/2017GL074173.

Caldwell, D. R., Lien, R.-C., Moum, J. N., and Gregg, M. C. (1997). Turbulence decay and restratification in the equatorial ocean surface layer following nighttime convection. *Journal of Physical Oceanography*, 27(6):1120–1132. doi:10.1175/1520-0485(1997)027<1120:TDARIT>2.0.CO;2.

Cheriton, O. M., McManus, M. A., Stacey, M. T., and Steinbuck, J. V. (2009). Physical and biological controls on the maintenance and dissipation of a thin phytoplankton layer. *Marine Ecology Progress Series*, 378(2003):55–69. doi:10.3354/meps07847.

Bibliography

Choi, J., Troy, C., Hawley, N., McCormick, M., and Wells, M. (2020). Lateral dispersion of dye and drifters in the center of a very large lake. *Limnology and Oceanography*, 65(2):336–348. doi:10.1002/lno.11302.

Choi, J., Troy, C. D., Hsieh, T.-C., Hawley, N., and McCormick, M. J. (2012). A year of internal Poincaré waves in southern Lake Michigan. *Journal of Geophysical Research: Oceans*, 117:C07014. doi:10.1029/2012JC007984.

Codd, G. A., Morrison, L. F., and Metcalf, J. S. (2005). Cyanobacterial toxins: Risk management for health protection. *Toxicology and Applied Pharmacology*, 203(3 SPEC. ISS.):264–272. doi:10.1016/j.taap.2004.02.016.

Crawford, G. B. and Collier, R. W. (1997). Observations of a deep-mixing event in Crater Lake, Oregon. *Limnology and Oceanography*, 42(2):299–306. doi:10.4319/lo.1997.42.2.0299.

Csanady, G. T. (1975). Hydrodynamics of large lakes. *Annu Rev Fluid Mech*, 7(1):357–386. doi:10.1146/annurev.fl.07.010175.002041.

Cullen, J. J. (2015). Subsurface chlorophyll maximum layers: enduring enigma or mystery solved? *Annual Review of Marine Science*, 7(1):207–239. doi:10.1146/annurev-marine-010213-135111.

Culver, D. A. (1977). Biogenic meromixis and stability in a soft-water lake. *Limnology and Oceanography*, 22(4):667–686. doi:10.4319/lo.1977.22.4.0667.

Cuypers, Y., Vinçon-Leite, B., Groleau, A., Tassin, B., and Humbert, J. F. (2011). Impact of internal waves on the spatial distribution of Planktothrix rubescens (cyanobacteria) in an alpine lake. *ISME Journal*, 5(4):580–589. doi:10.1038/ismej.2010.154.

Danza, F., Storelli, N., Roman, S., Lüdin, S., and Tonolla, M. (2017). Dynamic cellular complexity of anoxygenic phototrophic sulfur bacteria in the chemocline of meromictic Lake Cadagno. *PLoS ONE*, 12(12):e0189510. doi:10.1371/journal.pone.0189510.

Davis, R. E., Eriksen, C. C., and Jones, C. (2002). Autonomous buoyancy-driven underwater gliders. In Griffiths, G., editor, *Technology and Applications of Autonomous Underwater Vehicles*, pages 37–58. Taylor & Francis.

Deardorff, J. W. (1970). Convective velocity and temperature scales for the unstable planetary boundary layer and for Rayleigh convection. *Journal of the Atmospheric Sciences*, 27(8):1211–1213. doi:10.1175/1520-0469(1970)027<1211:CVATSF>2.0.CO;2.

Dekshenieks, M. M., Donaghay, P. L., Sullivan, J. M., Rines, J. E., Osborn, T. R., and Twardowski, M. S. (2001). Temporal and spatial occurrence of thin phytoplankton layers in relation to physical processes. *Marine Ecology Progress Series*, 223:61–71. doi:10.3354/meps223061.

Del Don, C., Hanselmann, K. W., Peduzzi, R., and Bachofen, R. (2001). The meromictic alpine Lake Cadagno: Orographical and biogeochemical description. *Aquatic Sciences*, 63(1):70–90. doi:10.1007/PL00001345.

Dillon, T. M. (1982). Vertical overturns: A comparison of Thorpe and Ozmidov length scales. *Journal of Geophysical Research*, 87(C12):9601–9613. doi:10.1029/JC087iC12p09601.

Dillon, T. M. and Caldwell, D. R. (1980). The Batchelor spectrum and dissipation in the upper ocean. *Journal of Geophysical Research*, 85(C4):1910–1916. doi:10.1029/JC085iC04p01910.

Dillon, T. M. and Park, M. M. (1987). The available potential energy of overturns as an indicator of mixing in the seasonal thermocline. *Journal of Geophysical Research*, 92(C5):5345–5353. doi:10.1029/JC092iC05p05345.

Dufois, F., Hardman-Mountford, N. J., Greenwood, J., Richardson, A. J., Feng, M., and Matear, R. J. (2016). Anticyclonic eddies are more productive than cyclonic eddies in subtropical gyres because of winter mixing. *Science Advances*, 2(5):e1600282. doi:10.1126/sciadv.1600282.

Durham, W. M. and Stocker, R. (2012). Thin phytoplankton layers: Characteristics, mechanisms, and consequences. *Annual Review of Marine Science*, 4(1):177–207. doi:10.1146/annurev-marine-120710-100957.

Egli, K., Wiggli, M., Fritz, M., Klug, J., Gerss, J., and Bachofen, R. (2004). Spatial and temporal dynamics of a plume of phototrophic microorganisms in a meromictic alpine lake using turbidity as a measure of cell density. *Aquatic Microbial Ecology*, 35(2):105–113. doi:10.3354/ame035105.

Etemad-Shahidi, A. and Imberger, J. (2001). Anatomy of turbulence in thermally stratified lakes. *Limnology and Oceanography*, 46(5):1158–1170. doi:10.4319/lo.2001.46.5.1158.

Fer, I., Lemmin, U., and Thorpe, S. A. (2002). Observations of mixing near the sides of a deep lake in winter. *Limnology and Oceanography*, 47(2):535–544. doi:10.4319/lo.2002.47.2.0535.

Fer, I., Peterson, A. K., and Ullgren, J. E. (2014). Microstructure measurements from an underwater glider in the turbulent Faroe Bank Channel overflow. *Journal of Atmospheric and Oceanic Technology*, 31(5):1128–1150. doi:10.1175/JTECH-D-13-00221.1.

Fink, G., Schmid, M., Wahl, B., Wolf, T., and Wüest, A. (2014). Heat flux modifications related to climate-induced warming of large European lakes. *Water Resources Research*, 50:2072–2085. doi:10.1002/2013WR014448.

Fisher, A. W., Nidzieko, N. J., Scully, M. E., Chant, R. J., Hunter, E. J., and Mazzini, P. L. F. (2018). Turbulent mixing in a far-field plume during the transition to upwelling conditions: Microstructure observations from an AUV. *Geophysical Research Letters*, 45(18):9765–9773. doi:10.1029/2018GL078543.

Forrest, A. L., Laval, B. E., Pieters, R., and Lim, D. S. (2013). A cyclonic gyre in an ice-covered lake. *Limnology and Oceanography*, 58(1):363–375. doi:10.4319/lo.2013.58.1.0363.

Forrest, A. L., Laval, B. E., Pieters, R., and Lim, D. S. S. (2008). Convectively driven transport in temperate lakes. *Limnology and Oceanography*, 53(5):2321–2332. doi:10.4319/lo.2008.53.5_part_2.2321.

Frajka-Williams, E., Eriksen, C. C., Rhines, P. B., and Harcourt, R. R. (2011). Determining vertical water velocities from Seaglider. *Journal of Atmospheric and Oceanic Technology*, 28(12):1641–1656. doi:10.1175/2011JTECHO830.1.

Gargett, A. E. (1999). Velcro measurement of turbulence kinetic energy dissipation rate ϵ. *Journal of Atmospheric and Oceanic Technology*, 16(12):1973–1993. doi:10.1175/1520-0426(1999)016<1973:VMOTKE>2.0.CO;2.

Gargett, A. E., Osborn, T. R., and Nasmyth, P. W. (1984). Local isotropy and the decay of turbulence in a stratified fluid. *Journal of Fluid Mechanics*, 144:231–280. doi:10.1017/S0022112084001592.

Garneau, M.-È., Posch, T., Hitz, G., Pomerleau, F., Pradalier, C., Siegwart, R., and Pernthaler, J. (2013). Short-term displacement of Planktothrix rubescens (cyanobacteria) in a pre-alpine lake observed using an autonomous sampling platform. *Limnology and Oceanography*, 58(5):1892–1906. doi:10.4319/lo.2013.58.5.1892.

Gibson, C. H. (1980). Fossil temperature, salinity, and vorticity turbulence in the ocean. In J. C. Nihoul, editor, *Marine Turbulence Proceedings of the 11th International Liege Colloquium on Ocean Hydrodynamics, Elsevier Oceanography Series*, pages Vol. 28, pp. 221–257, New York NY. Elsevier/North-Holland Inc.

Gibson, C. H. (1999). Fossil turbulence revisited. *Journal of Marine Systems*, 21(1-4):147–167. doi:10.1016/S0924-7963(99)00024-X.

Bibliography

Goodman, L., Levine, E. R., and Lueck, R. G. (2006). On measuring the terms of the turbulent kinetic energy budget from an AUV. *Journal of Atmospheric and Oceanic Technology*, 23(7):977–990. doi:10.1175/JTECH1889.1.

Goudsmit, G. H., Peeters, F., Gloor, M., and Wüest, A. (1997). Boundary versus internal diapycnal mixing in stratified natural waters. *Journal of Geophysical Research: Oceans*, 102(C13):27903–27914. doi:10.1029/97JC01861.

Gregg, M., D'Asaro, E., Riley, J., and Kunze, E. (2017). Mixing efficiency in the ocean. *Annual Review of Marine Science*, 10(1):443–473. doi:10.1146/annurev-marine-121916-063643.

Gregg, M. C. (1977). Variations in the intensity of small-scale mixing in the main thermocline. *Journal of Physical Oceanography*, 7(3):436–454. doi:10.1175/1520-0485(1977)007<0436:vitios>2.0.co;2.

Gregg, M. C. (1987). Diapycnal mixing in the thermocline: a review. *Journal of Geophical Research*, 92(C5):5249–5286. doi:10.1016/0198-0254(87)90591-7.

Guazzelli, E. and Morris, J. F. (2011). *A Physical Introduction to Suspension Dynamics*. Cambridge University Press, Cambridge.

Henderson, S. M. and Deemer, B. R. (2012). Vertical propagation of lakewide internal waves. *Geophysical Research Letters*, 39(6):L06405. doi:10.1029/2011GL050534.

Hill, N. A. and Pedley, T. J. (2005). Bioconvection. *Fluid Dynamics Research*, 37(1-2):1–20. doi:10.1016/j.fluiddyn.2005.03.002.

Hodges, B. R., Imberger, J., Saggio, A., and Winters, K. B. (2000). Modeling basin-scale internal waves in a stratified lake. *Limnology and Oceanography*, 45(7):1603–1620. doi:10.4319/lo.2000.45.7.1603.

Horn, W., Mortimer, C. H., and Schwab, D. J. (1986). Wind-induced internal seiches in Lake Zurich observed and modeled. *Limnology and Oceanography*, 31(6):1232–1254. doi:10.4319/lo.1986.31.6.1232.

Houghton, I. A., Koseff, J. R., Monismith, S. G., and Dabiri, J. O. (2018). Vertically migrating swimmers generate aggregation-scale eddies in a stratified column. *Nature*, 556(7702):497–500. doi:10.1038/s41586-018-0044-z.

Huisman, J., Oostveen, P. V., Weissing, F. J., and Nov, N. (1999). Critical depth and critical turbulence: two different mechanisms for the development of phytoplankton blooms. *Limnology and Oceanography*, 44(7):1781–1787. doi:10.4319/lo.1999.44.7.1781.

Huppert, H. E. and Turner, J. S. (1972). Double-diffusive convection and its implications for the temperature and salinity structure of the ocean and Lake Vanda. *Journal of Physical Oceanography*, 2(4):456–461. doi:10.1175/1520-0485(1972)002<0456:DDCAII>2.0.CO;2.

Hutchinson, G. E. (1961). The paradox of the plankton. *The American Naturalist*, 95(882):137–145. doi:10.1086/282171.

Ijichi, T. and Hibiya, T. (2018). Observed variations in turbulent mixing efficiency in the deep ocean. *Journal of Physical Oceanography*, 48(8):1815–1830. doi:10.1175/JPO-D-17-0275.1.

Imberger, J. (1985). The diurnal mixed layer. *Limnology and Oceanography*, 30(4):737–770. doi:10.4319/lo.1985.30.4.0737.

Imberger, J. (1998). Flux paths in a stratified lake: A review. In Imberger, J., editor, *Physical Processes in lakes and oceans*, volume 54, pages 1–17. American Geophysical Union.

Imberger, J. and Patterson, J. C. (1989). Physical Limnology. *Advances in Applied Mechanics*, 27:303–475. doi:10.1016/S0065-2156(08)70199-6.

Imboden, D. M. and Wüest, A. (1995). Mixing mechanisms in lakes. In Lerman, A., Imboden, D., and Gat, J., editors, *Physics and Chemistry of Lakes*, pages 83–138. Springer.

Imhoff, J. F. (2015). Chromatium. In *Bergey's Manual of Systematics of Archaea and Bacteria*, pages 1–8. John Wiley & Sons, Ltd, Chichester, UK.

Ishikawa, K., Kumagai, M., Vincent, W. F., Tsujimura, S., and Nakahara, H. (2002). Transport and accumulation of bloom-forming cyanobacteria in a large, mid-latitude lake: The gyre-Microcystis hypothesis. *Limnology*, 3(2):87–96. doi:10.1007/s102010200010.

Itsweire, E. C., Koseff, J. R., Briggs, D. A., and Ferziger, J. H. (1993). Turbulence in stratified shear flows: implications for interpreting shear-induced mixing in the ocean. *Journal of Physical Oceanography*, 23:1508–1522. doi:10.1175/1520-0485(1993)023<1508:TISSFI>2.0.CO;2.

Ivey, G., Winters, K., and Koseff, J. (2008). Density Stratification, Turbulence, but How Much Mixing? *Annual Review of Fluid Mechanics*, 40(1):169–184. doi:10.1146/annurev.fluid.39.050905.110314.

Ivey, G. N. and Imberger, J. (1991). On the nature of turbulence in a stratified fluid. Part I: the energetics of mixing. *Journal of Physical Oceanography*, 21(5):650–658. doi:10.1175/1520-0485(1991)021<0650:OTNOTI>2.0.CO;2.

Jacquet, S., Briand, J. F., Leboulanger, C., Avois-Jacquet, C., Oberhaus, L., Tassin, B., Vinçon-Leite, B., Paolini, G., Druart, J. C., Anneville, O., and Humbert, J. F. (2005). The proliferation of the toxic cyanobacterium Planktothrix rubescens following restoration of the largest natural French lake (Lac du Bourget). *Harmful Algae*, 4(4):651–672. doi:10.1016/j.hal.2003.12.006.

Jacquet, S., Kerimoglu, O., Rimet, F., Paolini, G., and Anneville, O. (2014). Cyanobacterial bloom termination: The disappearance of Planktothrix rubescens from Lake Bourget (France) after restoration. *Freshwater Biology*, 59(12):2472–2487. doi:10.1111/fwb.12444.

Jánosi, I. M., Kessler, J. O., and Horváth, V. K. (1998). Onset of bioconvection in suspensions of Bacillus subtilis. *Physical Review E*, 58(4):4793–4800. doi:10.1103/PhysRevE.58.4793.

Jonas, T., Stips, A., Eugster, W., and Wüest, A. (2003). Observations of a quasi shear-free lacustrine convective boundary layer: Stratification and its implications on turbulence. *Journal of Geophysical Research*, 108(C10):3328. doi:10.1029/2002JC001440.

Kiefer, I., Odermatt, D., Anneville, O., Wüest, A., and Bouffard, D. (2015). Application of remote sensing for the optimization of in-situ sampling for monitoring of phytoplankton abundance in a large lake. *Science of The Total Environment*, 527-528:493–506. doi:10.1016/j.scitotenv.2015.05.011.

Kirillin, G., Leppäranta, M., Terzhevik, A., Granin, N., Bernhardt, J., Engelhardt, C., Efremova, T., Golosov, S., Palshin, N., Sherstyankin, P., Zdorovennova, G., and Zdorovennov, R. (2012). Physics of seasonally ice-covered lakes: a review. *Aquatic Sciences*, 74(4):659–682. doi:10.1007/s00027-012-0279-y.

Kocsis, O., Prandke, H., Stips, A., Simon, A., and Wüest, A. (1999). Comparison of dissipation of turbulent kinetic energy determined from shear and temperature microstructure. *Journal of Marine Systems*, 21(1-4):67–84. doi:10.1016/S0924-7963(99)00006-8.

Kunze, E. (2019). Biologically generated mixing in the ocean. *Annual Review of Marine Science*, 11(1):215–226. doi:10.1146/annurev-marine-010318-095047.

Bibliography

Kunze, E., Dower, J. F., Beveridge, I., Dewey, R., and Bartlett, K. P. (2006). Observations of biologically generated turbulence in a coastal inlet. *Science.*, 313(5794):1768–1770. doi:10.1126/science.1129378.

Laval, B., Bird, J. S., and Helland, P. D. (2000). An autonomous underwater vehicle for the study of small lakes. *Journal of Atmospheric and Oceanic Technology*, 17(1):69–76. doi:10.1175/1520-0426(2000)017<0069:AAUVFT>2.0.CO;2.

Laval, B., Imberger, J., Hodges, B. R., and Stocker, R. (2003). Modeling circulation in lakes: Spatial and temporal variations. *Limnology and Oceanography*, 48(3):983–994. doi:10.4319/lo.2003.48.3.0983.

Leach, T. H., Beisner, B. E., Carey, C. C., Pernica, P., Rose, K. C., Huot, Y., Brentrup, J. A., Domaizon, I., Grossart, H. P., Ibelings, B. W., Jacquet, S., Kelly, P. T., Rusak, J. A., Stockwell, J. D., Straile, D., and Verburg, P. (2018). Patterns and drivers of deep chlorophyll maxima structure in 100 lakes: The relative importance of light and thermal stratification. *Limnology and Oceanography*, 63(2):628–646. doi:10.1002/lno.10656.

Legendre, L. (1981). Hydrodynamic control of marine phytoplankton production: The paradox of stability. *Elsevier Oceanography Series*, 32:191–207. doi:10.1016/S0422-9894(08)70410-0.

Lemmin, U. and D'Adamo, N. (1996). Summertime winds and direct cyclonic circulation: observations from Lake Geneva. *Annales Geophysicae*, 14(11):1207–1220. doi:10.1007/s00585-996-1207-z.

Lemmin, U., Mortimer, C. H., and Bäuerle, E. (2005). Internal seiche dynamics in Lake Geneva. *Limnology and Oceanography*, 50(1):207–216. doi:10.4319/lo.2005.50.1.0207.

Leon, L. F., Smith, R. E., Hipsey, M. R., Bocaniov, S. A., Higgins, S. N., Hecky, R. E., Antenucci, J. P., Imberger, J. A., and Guildford, S. J. (2011). Application of a 3D hydrodynamic–biological model for seasonal and spatial dynamics of water quality and phytoplankton in Lake Erie. *Journal of Great Lakes Research*, 37(1):41–53. doi:10.1016/j.jglr.2010.12.007.

Lévy, M., Franks, P. J. S., and Smith, K. S. (2018). The role of submesoscale currents in structuring marine ecosystems. *Nature Communications*, 9(1):4758. doi:10.1038/s41467-018-07059-3.

Li, Y. H. (1973). Vertical eddy diffusion coefficient in Lake Zürich. *Schweizerische Zeitschrift für Hydrologie*, 35(1):1–7. doi:10.1007/BF02502061.

Livingstone, D. M. (2003). Impact of secular climate change on the thermal structure of a large temperate central European lake. *Climatic Change*, 57:205–225. doi:10.1023/A:1022119503144.

Lombardo, C. P. and Gregg, M. C. (1989). Similarity scaling of viscous and thermal dissipation in a convecting surface boundary layer. *Journal of Geophysical Research*, 94(C5):6273–6284. doi:10.1029/JC094iC05p06273.

Lorenzen, C. J. (1972). Extinction of light in the ocean by phytoplankton. *ICES Journal of Marine Science*, 34(2):262–267. doi:10.1093/icesjms/34.2.262.

Lorke, A., Peeters, F., and Wüest, A. (2005). Shear-induced convective mixing in bottom boundary layers on slopes. *Limnology and Oceanography*, 50(5):1612–1619. doi:10.4319/lo.2005.50.5.1612.

Lorke, A. and Probsta, W. N. (2010). In situ measurements of turbulence in fish shoals. *Limnology and Oceanography*, 55(1):354–364. doi:10.4319/lo.2010.55.1.0354.

Lorke, A. and Wüest, A. (2002). Probability density of displacement and overturning length scales under diverse stratification. *Journal of Geophysical Research: Oceans*, 107(C12):3214. doi:10.1029/2001JC001154.

Lucas, N. S., Grant, A. L. M., Rippeth, T. P., Polton, J. A., Palmer, M. R., Brannigan, L., and Belcher, S. E. (2019). Evolution of oceanic near-surface stratification in response to an autumn storm. *Journal of Physical Oceanography*, 49(11):2961–2978. doi:10.1175/JPO-D-19-0007.1.

Lueck, R. G., Hertzman, O., and Osborn, T. R. (1977). The spectral response of thermistors. *Deep Sea Research*, 24(10):951–970. doi:10.1016/0146-6291(77)90565-3.

Lueck, R. G., Wolk, F., and Yamazaki, H. (2002). Oceanic microstructure measurements in the 20th century. *Journal of Oceanography*, 58(1):153–174. doi:10.1023/A:1015837020019.

Luedin, S. M., Liechti, N., Cox, R. P., Danza, F., Frigaard, N.-U., Posth, N. R., Pothier, J. F., Roman, S., Storelli, N., Wittwer, M., and Tonolla, M. (2019). Draft genome sequence of Chromatium okenii isolated from the stratified alpine Lake Cadagno. *Scientific Reports*, 9(1):1936. doi:10.1038/s41598-018-38202-1.

Luketina, D. A. and Imberger, J. (2001). Determining turbulent kinetic energy dissipation from Batchelor curve fitting. *Journal of Atmospheric and Oceanic Technology*, 18(1):100–113. doi:10.1175/1520-0426(2001)018<0100:DTKEDF>2.0.CO;2.

Lumley, J. L. and Newman, G. R. (1977). The return to isotropy of homogeneous turbulence. *Journal of Fluid Mechanics*, 82(1):161–178. doi:10.1017/S002211200100386X.

MacIntyre, S. (1998). Turbulent mixing and resource supply to phytoplankton. In Imberger, J., editor, *Physical Processes in Lakes and Oceans, Coastal Estuarine Studies*, volume 54, pages 561–590.

MacIntyre, S., Clark, J. F., Jellison, R., and Framb, J. P. (2009). Turbulent mixing induced by non-linear internal waves in Mono Lake, California. *Limnology and Oceanography*, 54(6):2255–2272. doi:10.4319/lo.2009.54.6.2255.

MacIntyre, S., Flynn, K. M., Jellison, R., and Romero, J. R. (1999). Boundary mixing and nutrient fluxes in Mono Lake, California. *Limnology and Oceanography*, 44(3):512–529. doi:10.4319/lo.1999.44.3.0512.

MacIntyre, S. and Melack, J. M. (1995). Vertical and horizontal transport in lakes: linking littoral, benthic, and pelagic habitats. *Journal of the North American Benthological Society*, 14(4):599–615. doi:10.2307/1467544.

MacIntyre, S., Romero, J. R., and Kling, G. W. (2002). Spatial-temporal variability in surface layer deepening and lateral advection in an embayment of Lake Victoria, East Africa. *Limnology and Oceanography*, 47(3):656–671. doi:10.4319/lo.2002.47.3.0656.

MacIntyre, S., Romero, J. R., Silsbe, G. M., and Emery, B. M. (2014). Stratification and horizontal exchange in Lake Victoria, East Africa. *Limnology and Oceanography*, 59(6):1805–1838. doi:10.4319/lo.2014.59.6.1805.

MacIntyre, S., Sickman, J. O., Goldthwait, S. A., and Kling, G. W. (2006). Physical pathways of nutrient supply in a small, ultraoligotrophic arctic lake during summer stratification. *Limnology and Oceanography*, 51(2):1107–1124. doi:10.4319/lo.2006.51.2.1107.

Maffioli, A., Brethouwer, G., and Lindborg, E. (2016). Mixing efficiency in stratified turbulence. *Journal of Fluid Mechanics*, 794:R3. doi:10.1017/jfm.2016.206.

Margalef, R. (1997). Turbulence and marine life. *Scientia Marina*, 61(SUPPL.1):109–123.

Mashayek, A., Caulfield, C. P., and Peltier, W. R. (2017). Role of overturns in optimal mixing in stratified mixing layers. *Journal of Fluid Mechanics*, 826:522–552. doi:10.1017/jfm.2017.374.

Bibliography

Matthews, M. W. (2011). A current review of empirical procedures of remote sensing in Inland and near-coastal transitional waters. *International Journal of Remote Sensing*, 32(21):6855–6899. doi:10.1080/01431161.2010.512947.

McDougall, T. J. and Barker, P. (2011). Getting started with TEOS-10 and the Gibbs Seawater (GSW) oceanographic toolbox. *SCOR/IAPSO WG.*, 127:1–28.

McGillicuddy, D. J., Anderson, L. A., Doney, S. C., and Maltrud, M. E. (2003). Eddy-driven sources and sinks of nutrients in the upper ocean: Results from a 0.1° resolution model of the North Atlantic. *Global Biogeochemical Cycles*, 17(2):1035. doi:10.1029/2002GB001987.

McManus, M. A., Alldredge, A. L., Barnard, A. H., Boss, E., Case, J. F., Cowles, T. J., Donaghay, P. L., Eisner, L. B., Gifford, D. J., Greenlaw, C. F., Herren, C. M., Holliday, D. V., Johnson, D., MacIntyre, S., McGehee, D. M., Osborn, T. R., Perry, M. J., Pieper, R. E., Rines, J. E., Smith, D. C., Sullivan, J. M., Talbot, M. K., Twardowski, M. S., Weidemann, A., and Zaneveld, J. R. (2003). Characteristics, distribution and persistence of thin layers over a 48 hour period. *Marine Ecology Progress Series*, 261:1–19. doi:10.3354/meps261001.

Merckelbach, L. (2018). Initial realse of Glider flight model. Version 1.0.1. *Zenodo.* doi:10.5281/zenodo.2222694.

Merckelbach, L., Berger, A., Krahmann, G., Dengler, M., and Carpenter, J. R. (2019). A dynamic flight model for Slocum gliders and implications for turbulence microstructure measurements. *Journal of Atmospheric and Oceanic Technology*, 36(2):281–296. doi:10.1175/JTECH-D-18-0168.1.

Merckelbach, L., Smeed, D., and Griffiths, G. (2010). Vertical water velocities from underwater gliders. *Journal of Atmospheric and Oceanic Technology*, 27(3):547–563. doi:10.1175/2009JTECHO710.1.

Miles, J. W. (1961). On the stability of heterogeneous shear flows. *Journal of Fluid Mechanics*, 10:496–508. doi:10.1143/JJAP.8.821.

Monbet, Y. (1992). Control of phytoplankton biomass in estuaries: A comparative analysis of microtidal and macrotidal estuaries. *Estuaries*, 15(4):563. doi:10.2307/1352398.

Monismith, S. (1986). An experimental study of the upwelling response of stratified reservoirs to surface shear stress. *Journal of Fluid Mechanics*, 171:407–439. doi:10.1017/S0022112086001507.

Monismith, S. G., Koseff, J. R., and White, B. L. (2018). Mixing efficiency in the presence of stratification: When is it constant? *Geophysical Research Letters*, 45(11):5627–5634. doi:10.1029/2018GL077229.

Mortimer, C. H. (1952). Water movements in lakes during summer stratification; evidence from the distribution of temperature in Windermere. *Philosophical Transactions of the Royal Society of London. Series B, Biological Sciences*, 236(635):355–398. doi:10.1098/rstb.1952.0005.

Moum, J. N., Perlin, A., Klymak, J. M., Levine, M. D., Boyd, T., and Kosro, P. M. (2004). Convectively driven mixing in the bottom boundary layer. *Journal of Physical Oceanography*, 34(10):2189–2202. doi:10.1175/1520-0485(2004)034<2189:CDMITB>2.0.CO;2.

Ng, S. M. Y., Antenucci, J. P., Hipsey, M. R., Tibor, G., and Zohary, T. (2011). Physical controls on the spatial evolution of a dinoflagellate bloom in a large lake. *Limnology and Oceanography*, 56(6):2265–2281. doi:10.4319/lo.2011.56.6.2265.

Nielsen, T., Kiorboe, T., and Bjørnsen, P. (1990). Effects of a Chrysochromulina polylepis subsurface bloom on the planktonic community. *Marine Ecology Progress Series*, 62:21–35. doi:10.3354/meps062021.

Noss, C. and Lorke, A. (2014). Direct observation of biomixing by vertically migrating zooplankton. *Limnology and Oceanography*, 59(3):724–732. doi:10.4319/lo.2014.59.3.0724.

Nouchi, V., Kutser, T., Wüest, A., Müller, B., Odermatt, D., Baracchini, T., and Bouffard, D. (2019). Resolving biogeochemical processes in lakes using remote sensing. *Aquatic Sciences*, 81(2):27. doi:10.1007/s00027-019-0626-3.

Nouchi, V., Odermatt, D., Wüest, A., and Bouffard, D. (2018). Effects of non-uniform vertical constituent profiles on remote sensing reflectance of oligo- to mesotrophic lakes. *European Journal of Remote Sensing*, 51(1):808–821. doi:10.1080/22797254.2018.1493360.

Oakey, N. S. (1982). Determination of the rate of dissipation of turbulent energy from simultaneous temperature and velocity shear microstructure measurements. *Journal of Physical Oceanography*, 12(3):256–271. doi:10.1175/1520-0485(1982)012<0256:DOTROD>2.0.CO;2.

Odermatt, D., Gitelson, A., Brando, V. E., and Schaepman, M. (2012). Review of constituent retrieval in optically deep and complex waters from satellite imagery. *Remote Sensing of Environment*, 118:116–126. doi:10.1016/j.rse.2011.11.013.

Osborn, T. R. (1980). Estimates of the local rate of vertical diffusion from dissipation measurements. *Journal of Physical Oceanography*, 10(1):83–89. doi:10.1175/1520-0485(1980)010<0083:EOTLRO>2.0.CO;2.

Osborn, T. R. and Cox, C. S. (1972). Oceanic fine structure. *Geophysical Fluid Dynamics*, 3(1):321–345. doi:10.1080/03091927208236085.

Osborn, T. R. and Crawford, W. R. (1980). An airfoil probe for measuring turbulent velocity fluctuations in water. In *Air-Sea Interaction*, pages 369–386. Springer US, Boston, MA.

Osborn, T. R. and Lueck, R. G. (1985). Turbulence measurements with a submarine. *Journal of Physical Oceanography*, 15(11):1502–1520. doi:10.1175/1520-0485(1985)015<1502:TMWAS>2.0.CO;2.

Oschlies, A. and Garçon, V. (1998). Eddy-induced enhancement of primary production in a model of the North Atlantic Ocean. *Nature*, 394(6690):266–269. doi:10.1038/28373.

Paerl, H. W. and Paul, V. J. (2012). Climate change: Links to global expansion of harmful cyanobacteria. *Water Research*, 46(5):1349–1363. doi:10.1016/j.watres.2011.08.002.

Peeters, F., Straile, D., Lorke, A., and Ollinger, D. (2007). Turbulent mixing and phytoplankton spring bloom development in a deep lake. *Limnology and Oceanography*, 52(1):286–298. doi:10.4319/lo.2007.52.1.0286.

Peeters, F., Wüest, A., Piepke, G., and Imboden, D. M. (1996). Horizontal mixing in lakes. *Journal of Geophysical Research: Oceans*, 101(C8):18361–18375. doi:10.1029/96JC01145.

Peterson, A. K. and Fer, I. (2014). Dissipation measurements using temperature microstructure from an underwater glider. *Methods in Oceanography*, 10:44–69. doi:10.1016/j.mio.2014.05.002.

Peterson, B. J. (2001). Control of Nitrogen Export from Watersheds by Headwater Streams. *Science.*, 292(5514):86–90. doi:10.1126/science.1056874.

Piccolroaz, S., Toffolon, M., and Majone, B. (2013). A simple lumped model to convert air temperature into surface water temperature in lakes. *Hydrology and Earth System Sciences*, 17(8):3323–3338. doi:10.5194/hess-17-3323-2013.

Bibliography

Posch, T., Köster, O., Salcher, M. M., and Pernthaler, J. (2012). Harmful filamentous cyanobacteria favoured by reduced water turnover with lake warming. *Nature Climate Change*, 2(11):809–813. doi:10.1038/nclimate1581.

Powell, T. and Jassby, A. (1974). The estimation of vertical eddy diffusivities below the thermocline in lakes. *Water Resources Research*, 10(2):191–198. doi:10.1029/WR010i002p00191.

Prairie, J. C., Sutherland, K. R., Nickols, K. J., and Kaltenberg, A. M. (2012). Biophysical interactions in the plankton: A cross-scale review. *Limnology and Oceanography: Fluids and Environments*, 2(1):121–145. doi:10.1215/21573689-1964713.

Preusse, M., Peeters, F., and Lorke, A. (2010). Internal waves and the generation of turbulence in the thermocline of a large lake. *Limnology and Oceanography*, 55(6):2353–2365. doi:10.4319/lo.2010.55.6.2353.

Quraishi, A., Bahr, A., Schill, F., and Martinoli, A. (2018). Autonomous feature tracing and adaptive sampling in real-world underwater environments. In *2018 IEEE International Conference on Robotics and Automation (ICRA)*, pages 5699–5704. IEEE.

Ravens, T. M., Kocsis, O., Wüest, A., and Granin, N. (2000). Small-scale turbulence and vertical mixing in Lake Baikal. *Limnology and Oceanography*, 45(1):159–173. doi:10.4319/lo.2000.45.1.0159.

Raymond, P. A., Saiers, J. E., and Sobczak, W. V. (2016). Hydrological and biogeochemical controls on watershed dissolved organic matter transport: Pulse- shunt concept. *Ecology*, 97(1):5–16. doi:10.1890/14-1684.1.

Rippeth, T. P., Wiles, P. J., Palmer, M. R., Sharples, J., and Tweddle, J. (2009). The diapycnal nutrient flux and shear-induced diapycnal mixing in the seasonally stratified western Irish Sea. *Continental Shelf Research*, 29(13):1580–1587. doi:10.1016/j.csr.2009.04.009.

Robbins, I. C., Kirkpatrick, G. J., Blackwell, S. M., Hillier, J., Knight, C. A., and Moline, M. A. (2006). Improved monitoring of HABs using autonomous underwater vehicles (AUV). *Harmful Algae*, 5(6):749–761. doi:10.1016/j.hal.2006.03.005.

Roberts, D. C. (2019). *Physical processes in the littoral zone of a large lake and the implications for water quality*. PhD thesis, University of California, Davis.

Robertson, D. M. and Imberger, J. (1994). Lake Number, a quantitative indicator of mixing used to estimate changes in dissolved oxygen. *Internationale Revue der gesamten Hydrobiologie und Hydrographie*, 79(2):159–176. doi:10.1002/iroh.19940790202.

Rogowski, P., Merrifield, S., Ding, L., Terrill, E., and Gesiriech, G. (2019). Robotic mapping of mixing and dispersion of augmented surface water in a drought frequent reservoir. *Limnology and Oceanography: Methods*, 17(9):475–489. doi:10.1002/lom3.10326.

Rothschild, B. and Osborn, T. (1988). Small-scale turbulence and plankton contact rates. *Journal of Plankton Research*, 10(3):465–474. doi:10.1093/plankt/10.3.465.

Ruddick, B., Anis, A., and Thompson, K. (2000). Maximum likelihood spectral fitting: The batchelor spectrum. *Journal of Atmospheric and Oceanic Technology*, 17(11):1541–1555. doi:10.1175/1520-0426(2000)017<1541:MLSFTB>2.0.CO;2.

Rudnick, D. L. (2016). Ocean research enabled by underwater gliders. *Annual Review of Marine Science*, 8(1):519–541. doi:10.1146/annurev-marine-122414-033913.

Rueda, F. J., Schladow, S. G., Monismith, S. G., and Stacey, M. T. (2005). On the effects of topography on wind and the generation of currents in a large multi-basin lake. *Hydrobiologia*, 532(1-3):139–151. doi:10.1007/s10750-004-9522-4.

Saggio, A. and Imberger, J. (2001). Mixing and turbulent fluxes in the metalimnion of a stratified lake. *Limnology and Oceanography*, 46(2):392–409. doi:10.4319/lo.2001.46.2.0392.

Sánchez, X. and Roget, E. (2007). Microstructure measurements and heat flux calculations of a triple-diffusive process in a lake within the diffusive layer convection regime. *Journal of Geophysical Research*, 112(C2):C02012. doi:10.1029/2006JC003750.

Sanford, L. P. (1997). Turbulent mixing in experimental ecosystem studies. *Marine Ecology Progress Series*, 161:265–293. doi:10.3354/meps161265.

Sarmiento, J. L., Slater, R., Barber, R., Bopp, L., Doney, S. C., Hirst, A. C., Kleypas, J., Matear, R., Mikolajewicz, U., Monfray, P., Soldatov, V., Spall, S. A., and Stouffer, R. (2004). Response of ocean ecosystems to climate warming. *Global Biogeochemical Cycles*, 18(3):GB3003. doi:10.1029/2003GB002134.

Sathyendranath, S., Gouveia, A. D., Shetye, S. R., Ravindran, P., and Platt, T. (1991). Biological control of surface temperature in the Arabian Sea. *Nature*, 349(6304):54–56. doi:10.1038/349054a0.

Schanz, F. (1985). Vertical light attenuation and phytoplankton development in Lake Zürich. *Limnology and Oceanography*, 30(2):299–310. doi:10.4319/lo.1985.30.2.0299.

Schanz, F., Fischer-Romero, C., and Bachofen, R. (1998). Photosynthetic production and photoadaptation of phototrophic sulfur bacteria in Lake Cadagno (Switzerland). *Limnology and Oceanography*, 43(6):1262–1269. doi:10.4319/lo.1998.43.6.1262.

Scheifele, B., Waterman, S., Merckelbach, L., and Carpenter, J. R. (2018). Measuring the dissipation rate of turbulent kinetic energy in strongly stratified, low-energy environments: A case study from the Arctic Ocean. *Journal of Geophysical Research: Oceans*, 123(8):5459–5480. doi:10.1029/2017JC013731.

Schill, F., Bahr, A., and Martinoli, A. (2018). Vertex: A new distributed underwater robotic platform for environmental monitoring. In Groß, R., Kolling, A., Berman, S., Frazzoli, E., Martinoli, A., Matsuno, F., and Melvin, G., editors, *Distributed Autonomous Robotic Systems. Springer Proceedings in Advanced Robotics, vol 6*, pages 679–693. Springer, Cham.

Schladow, S. G., Pálmarsson, S. Ó., Steissberg, T. E., Hook, S. J., and Prata, F. E. (2004). An extraordinary upwelling event in a deep thermally stratified lake. *Geophysical Research Letters*, 31(15):L15504. doi:10.1029/2004GL020392.

Schmid, M., Budnev, N. M., Granin, N. G., Sturm, M., Schurter, M., and Wüest, A. (2008). Lake Baikal deepwater renewal mystery solved. *Geophysical Research Letters*, 35(9):L09605. doi:10.1029/2008GL033223.

Schmid, M. and Köster, O. (2016). Excess warming of a Central European lake driven by solar brightening. *Water Resources Research*, 52:8103–8116. doi:10.1111/j.1752-1688.1969.tb04897.x.

Schultze, L. K. P., Merckelbach, L. M., and Carpenter, J. R. (2017). Turbulence and mixing in a shallow shelf sea from underwater gliders. *Journal of Geophysical Research: Oceans*, 122(11):9092–9109. doi:10.1002/2017JC012872.

Schwefel, R., Gaudard, A., Wüest, A., and Bouffard, D. (2016). Effects of climate change on deepwater oxygen and winter mixing in a deep lake (Lake Geneva): Comparing observational findings and modeling. *Water Resources Research*, 52(11):8811–8826. doi:10.1002/2016WR019194.

Bibliography

Sengupta, A., Carrara, F., and Stocker, R. (2017). Phytoplankton can actively diversify their migration strategy in response to turbulent cues. *Nature*, 543(7646):555–558. doi:10.1038/nature21415.

Sepúlveda Steiner, O., Bouffard, D., and Wüest, A. (2019). Convection-diffusion competition within mixed layers of stratified natural waters. *Geophysical Research Letters*, 46(22):13199–13208. doi:10.1029/2019GL085361.

Sharples, J., Moore, C. M., Rippeth, T. P., Holligan, P. M., Hydes, D. J., Fisher, N. R., and Simpson, J. H. (2001). Phytoplankton distribution and survival in the thermocline. *Limnology and Oceanography*, 46(3):486–496. doi:10.4319/lo.2001.46.3.0486.

Shay, T. J. and Gregg, M. C. (1986). Convectively driven turbulent mixing in the upper ocean. *Journal of Physical Oceanography*, 16(11):1777–1798. doi:10.1175/1520-0485(1986)016<1777:CDTMIT>2.0.CO;2.

Shih, L. H., Koseff, J. R., Ivey, G. N., and Ferziger, J. H. (2005). Parameterization of turbulent fluxes and scales using homogeneous sheared stably stratified turbulence simulations. *Journal of Fluid Mechanics*, 525:193–214. doi:10.1017/S0022112004002587.

Shimizu, K., Imberger, J., and Kumagai, M. (2007). Horizontal structure and excitation of primary motions in a strongly stratified lake. *Limnology and Oceanography*, 52(6):2641–2655. doi:10.4319/lo.2007.52.6.2641.

Shroyer, E. L., Benoit-Bird, K. J., Nash, J. D., and Moum, J. N. (2014). Stratification and mixing regimes in biological thin layers over the Mid-Atlantic Bight. *Limnology and Oceanography*, 59(4):1349–1363. doi:10.4319/lo.2014.59.4.1349.

Simoncelli, S., Thackeray, S. J., and Wain, D. J. (2018). On biogenic turbulence production and mixing from vertically migrating zooplankton in lakes. *Aquatic Sciences*, 80(4):35. doi:10.1007/s00027-018-0586-z.

Simpson, J. H. and Sharples, J. (2012). *Introduction to the Physical and Biological Oceanography of Shelf Seas.* Cambridge University Press, Cambridge, United Kingdom.

Smyth, W. D. and Moum, J. N. (2000). Anisotropy of turbulence in stably stratified mixing layers. *Physics of Fluids*, 12(6):1343–1362. doi:10.1063/1.870386.

Smyth, W. D., Moum, J. N., and Caldwell, D. R. (2001). The efficiency of mixing in turbulent patches: Inferences from direct simulations and microstructure observations. *Journal of Physical Oceanography*, 31(8):1969–1992. doi:10.1175/1520-0485(2001)031<1969:teomit>2.0.co;2.

Sommer, T., Carpenter, J. R., Schmid, M., Lueck, R. G., Schurter, M., and Wüest, A. (2013a). Interface structure and flux laws in a natural double-diffusive layering. *Journal of Geophysical Research: Oceans*, 118(11):6092–6106. doi:10.1002/2013JC009166.

Sommer, T., Carpenter, J. R., Schmid, M., Lueck, R. G., and Wüest, A. (2013b). Revisiting microstructure sensor responses with implications for double-diffusive fluxes. *Journal of Atmospheric and Oceanic Technology*, 30(8):1907–1923. doi:10.1175/JTECH-D-12-00272.1.

Sommer, T., Danza, F., Berg, J., Sengupta, A., Constantinescu, G., Tokyay, T., Bürgmann, H., Dressler, Y., Sepúlveda Steiner, O., Schubert, C. J., Tonolla, M., and Wüest, A. (2017). Bacteria-induced mixing in natural waters. *Geophysical Research Letters*, 44(18):9424–9432. doi:10.1002/2017GL074868.

Sommer, T., Schmid, M., and Wüest, A. (2019). The role of double diffusion for the heat and salt balance in Lake Kivu. *Limnology and Oceanography*, 64(2):650–660. doi:10.1002/lno.11066.

Soulignac, F., Danis, P.-a., Bouffard, D., Chanudet, V., Dambrine, E., Guénand, Y., Harmel, T., Ibelings, B. W., Trevisan, D., Uittenbogaard, R., and Anneville, O. (2018). Using 3D modeling and remote sensing capabilities for a better understanding of spatio-temporal heterogeneities of phytoplankton abundance in large lakes. *Journal of Great Lakes Research*, 44(4):756–764. doi:10.1016/j.jglr.2018.05.008.

Spigel, R. H. and Imberger, J. (1987). Mixing processes relevant to phytoplankton dynamics in lakes. *New Zealand Journal of Marine and Freshwater Research*, 21(3):361–377. doi:10.1080/00288330.1987.9516233.

Stacey, M. T., McManus, M. A., and Steinbuck, J. V. (2007). Convergences and divergences and thin layer formation and maintenance. *Limnology and Oceanography*, 52(4):1523–1532. doi:10.4319/lo.2007.52.4.1523.

Steinbuck, J. V., Koseff, J. R., Genin, A., Stacey, M. T., and Monismith, S. G. (2011). Horizontal dispersion of ocean tracers in internal wave shear. *Journal of Geophysical Research*, 116(C11):C11031. doi:10.1029/2011JC007213.

Steinbuck, J. V., Stacey, M. T., McManus, M. A., Cheriton, O. M., and Ryan, J. P. (2009a). Observations of turbulent mixing in a phytoplankton thin layer: Implications for formation, maintenance, and breakdown. *Limnology and Oceanography*, 54(4):1353–1368. doi:10.4319/lo.2009.54.4.1353.

Steinbuck, J. V., Stacey, M. T., and Monismith, S. G. (2009b). An Evaluation of χT estimation techniques: Implications for Batchelor fitting and ϵ. *Journal of Atmospheric and Oceanic Technology*, 26(8):1652–1662. doi:10.1175/2009JTECHO611.1.

Steissberg, T. E., Hook, S. J., and Schladow, S. G. (2005). Characterizing partial upwellings and surface circulation at Lake Tahoe, California–Nevada, USA with thermal infrared images. *Remote Sensing of Environment*, 99(1-2):2–15. doi:10.1016/j.rse.2005.06.011.

Stevens, C. and Imberger, J. (1996). The initial response of a stratified lake to a surface shear stress. *Journal of Fluid Mechanics*, 312:39–66. doi:10.1017/S0022112096001917.

Stocker, R. (2012). Marine Microbes See a Sea of Gradients. *Science.*, 338(6107):628–633. doi:10.1126/science.1208929.

Stöckli, A. (2012). Das Plankton zeigt die Gesundung des Hallwilersees. *Umwelt Aargau*, (58):13–20.

Strickland, J. (1968). A comparison of profiles of nutrient and chlorophyll concentrations taken from discrete depths and by continuous recording. *Limnology and Oceanography*, 13:388–391.

Strutton, P. G. and Chavez, F. P. (2004). Biological heating in the equatorial Pacific: Observed variability and potential for real-time calculation. *Journal of Climate*, 17(5):1097–1109. doi:10.1175/1520-0442(2004)017<1097:BHITEP>2.0.CO;2.

Talling, J. F. (1966). The annual cycle of stratification and phytoplankton growth in Lake Victoria (East Africa). *Internationale Revue der gesamten Hydrobiologie und Hydrographie*, 51(4):545–621. doi:10.1002/iroh.19660510402.

Tedford, E. W., MacIntyre, S., Miller, S. D., and Czikowsky, M. J. (2014). Similarity scaling of turbulence in a temperate lake during fall cooling. *Journal of Geophysical Research: Oceans*, 119(8):4689–4713. doi:10.1002/2014JC010135.

Tennekes, H. and Lumley, J. (1972). *A first course in turbulence*. MIT Press.

Teoh, S. G., Ivey, G. N., and Imberger, J. (1997). Laboratory study of the interaction between two internal wave rays. *Journal of Fluid Mechanics*, 336:91–122. doi:10.1017/S0022112096004508.

Bibliography

Thorpe, S. A. (1977). Turbulence and mixing in a Scottish Loch. *Philosophical Transactions of the Royal Society A: Mathematical, Physical and Engineering Sciences*, 286(1334):125–181. doi:10.1098/rsta.1977.0112.

Thorpe, S. A. (2007). *An introduction to ocean turbulence*. Cambridge University Press, Cambridge.

Thorpe, S. A., Lemmin, U., Perrinjaquet, C., and Fer, I. (1999). Observations of the thermal structure of a lake using a submarine. *Limnology and Oceanography*, 44(6):1575–1582. doi:10.4319/lo.1999.44.6.1575.

Tippenhauer, S., Dengler, M., Fischer, T., and Kanzow, T. (2015). Turbulence and finestructure in a deep ocean channel with sill overflow on the mid-Atlantic ridge. *Deep Sea Research Part I: Oceanographic Research Papers*, 99:10–22. doi:10.1016/j.dsr.2015.01.001.

Toffolon, M., Piccolroaz, S., Majone, B., Soja, A. M., Peeters, F., Schmid, M., and Wüest, A. (2014). Prediction of surface temperature in lakes with different morphology using air temperature. *Limnology and Oceanography*, 59(6):2185–2202. doi:10.4319/lo.2014.59.6.2185.

Tonolla, M., Demarta, A., Peduzzi, R., and Hahn, D. (1999). In situ analysis of phototrophic sulfur bacteria in the chemocline of meromictic Lake Cadagno (Switzerland). *Applied and Environmental Microbiology*, 65(3):1325–1330.

Turner, J. S. (1973). *Buoyancy effects in fluids*. Cambridge University Press.

Uhde, M. (1992). Mischungsprozesse im Hypolimnion des meromiktischen lago Cadagno: Eine Untersuchung mit Hilfe natürlicher und künstlicher Tracer. Master Thesis, University of Freiburg, Germany.

Ulloa, H. N., Winters, K. B., de la Fuente, A., and Niño, Y. (2015). Degeneration of internal Kelvin waves in a continuous two-layer stratification. *Journal of Fluid Mechanics*, 777:68–96. doi:10.1017/jfm.2015.311.

Ulloa, H. N., Wüest, A., and Bouffard, D. (2018). Mechanical energy budget and mixing efficiency for a radiatively heated ice-covered waterbody. *Journal of Fluid Mechanics*, 852:R1. doi:10.1017/jfm.2018.587.

Valipour, R., Bouffard, D., Boegman, L., and Rao, Y. R. (2015). Near-inertial waves in Lake Erie. *Limnology and Oceanography*, 60(5):1522–1535. doi:10.1002/lno.10114.

Viaroli, P., Azzoni, R., Bartoli, M., Iacumin, P., Longhi, D., Mosello, R., Rogora, M., Rossetti, G., Salmaso, N., and Nizzoli, D. (2018). Persistence of meromixis and its effects on redox conditions and trophic status in Lake Idro (Southern Alps, Italy). *Hydrobiologia*, 824(1):51–69. doi:10.1007/s10750-018-3767-9.

Vidal, J., MacIntyre, S., McPhee-Shaw, E. E., Shaw, W. J., and Monismith, S. G. (2013). Temporal and spatial variability of the internal wave field in a lake with complex morphometry. *Limnology and Oceanography*, 58(5):1557–1580. doi:10.4319/lo.2013.58.5.1557.

Visser, A. W. and Kiørboe, T. (2006). Plankton motility patterns and encounter rates. *Oecologia*, 148(3):538–546. doi:10.1007/s00442-006-0385-4.

Wadhams, P., Holfort, J., Hansen, E., and Wilkinson, J. P. (2002). A deep convective chimney in the winter greenland sea. *Geophysical Research Letters*, 29(10):76–1–76–4. doi:10.1029/2001GL014306.

Walsby, A. E. (2001). Determining the photosynthetic productivity of a stratified phytoplankton population. *Aquatic Sciences*, 63(4):18–43. doi:https://doi.org/10.1007/PL00022510.

Walsby, A. E. (2005). Stratification by cyanobacteria in lakes: A dynamic buoyancy model indicates size limitations met by Planktothrix rubescens filaments. *New Phytologist*, 168(2):365–376. doi:10.1111/j.1469-8137.2005.01508.x.

Walsby, A. E., Ng, G., Dunn, C., and Davis, P. A. (2004). Comparison of the depth where Planktothrix rubescens stratifies and the depth where the daily insolation supports its neutral buoyancy. *New Phytologist*, 162(1):133–145. doi:10.1111/j.1469-8137.2004.01020.x.

Walsby, A. E. and Schanz, F. (2002). Light-dependent growth rate determines changes in the population of Planktothrix rubescens over the annual cycle in lake Zürich, Switzerland. *New Phytologist*, 154(3):671–687. doi:10.1046/j.1469-8137.2002.00401.x.

Waterhouse, A. F., MacKinnon, J. A., Nash, J. D., Alford, M. H., Kunze, E., Simmons, H. L., Polzin, K. L., St. Laurent, L. C., Sun, O. M., Pinkel, R., Talley, L. D., Whalen, C. B., Huussen, T. N., Carter, G. S., Fer, I., Waterman, S., Naveira Garabato, A. C., Sanford, T. B., and Lee, C. M. (2014). Global patterns of diapycnal mixing from measurements of the turbulent dissipation rate. *Journal of Physical Oceanography*, 44(7):1854–1872. doi:10.1175/JPO-D-13-0104.1.

Weck, J. and Lorke, A. (2017). Mixing efficiency in the thermocline of lakes observed from eddy correlation flux measurements. *Journal of Geophysical Research: Oceans*, 122(1):291–305. doi:10.1002/2016JC012188.

Weimer, W. C. and Lee, F. F. (1973). Some considerations of the chemical limnology of meromictic Lake Mary. *Limnology and Oceanography*, 18(3):414–425. doi:10.4319/lo.1973.18.3.0414.

Weiss, R. F., Carmack Carmack, E. C., and Koropalov, V. M. (1991). Deep-water renewal and biological production in Lake Baikal. *Nature*, 349(6311):665–669. doi:10.1038/349665a0.

Woods, J. D. (1968). Wave-induced shear instability in the summer thermocline. *Journal of Fluid Mechanics*, 32(4):791–800. doi:10.1017/S0022112068001035.

Woolway, R. I. and Merchant, C. J. (2019). Worldwide alteration of lake mixing regimes in response to climate change. *Nature Geoscience*, 12(4):271–276. doi:10.1038/s41561-019-0322-x.

Woolway, R. I., Simpson, J. H., Spiby, D., Feuchtmayr, H., Powell, B., and Maberly, S. C. (2018). Physical and chemical impacts of a major storm on a temperate lake: a taste of things to come? *Climatic Change*, 151(2):333–347. doi:10.1007/s10584-018-2302-3.

Wüest, A. (1994). Interactions in lakes: Biology as source of dominant physical forces. *Limnologica*, 24(2):93–104.

Wüest, A. and Lorke, A. (2003). Small scale hydrodynamics in lakes. *Annual Review of Fluid Mechanics*, 35(1):373–412. doi:10.1146/annurev.fluid.35.101101.161220.

Wüest, A., Piepke, G., and Halfman, J. (1996). Combined effects of dissolved solids and temperature on the density stratification of Lake Malawi (East Africa). In Johnson, T. C. and Odada, E. O., editors, *The Limnology, Climatology and Paleoclimatology of the East African Lakes*, pages 183–202. Gordon and Breach Scientific Publishers, New York.

Wüest, A., Piepke, G., and Van Senden, D. C. (2000). Turbulent kinetic energy balance as a tool for estimating vertical diffusivity in wind-forced stratified waters. *Limnology and Oceanograhy*, 45(6):1388–1400. doi:10.4319/lo.2000.45.6.1388.

Yang, B., Young, J., Brown, L., and Wells, M. (2017). High-frequency observations of temperature and dissolved oxygen reveal under-ice convection in a large lake. *Geophysical Research Letters*, 44(24):12,218–12,226. doi:10.1002/2017GL075373.

Bibliography

Yankova, Y., Neuenschwander, S., Köster, O., and Posch, T. (2017). Abrupt stop of deep water turnover with lake warming: Drastic consequences for algal primary producers. *Scientific Reports*, 7(1):1–9. doi:10.1038/s41598-017-13159-9.

Yankova, Y., Villiger, J., Pernthaler, J., Schanz, F., and Posch, T. (2016). Prolongation, deepening and warming of the metalimnion change habitat conditions of the harmful filamentous cyanobacterium Planktothrix rubescens in a prealpine lake. *Hydrobiologia*, 776(1):125–138. doi:10.1007/s10750-016-2745-3.

Oscar
SEPÚLVEDA STEINER

Av. Louis-Ruchonnet 2B
1003 Lausanne, Switzerland
🕿 (+41) 78 652 10 76
✉ oscar.sepulvedasteiner@epfl.ch
oscarsepulveda32@gmail.com
🆂 osepulve32

Abstract

I am an engineer passionate about science, with a great interest in the environment and its preservation. My main research interest is physical limnology; aiming to understand aquatic physical processes entailing ecological implications using novel field measurement techniques and modeling. I have experience working with a variety of field equipment including microstructure profilers and acoustic current profilers (ADCPs). I also have experience performing outdoor activities under diverse (and unfavourable) conditions.

Personal Information

Nationality	Chilean	Date of Birth	May 28th, 1989
Marital Status	Single, without children	Driving Licence	Car: category B / Boat: category A
Swiss permit	B		

Education

2016-2020 **Ph.D. in Environmental Sciences**, *École Polytechnique Fédérale de Lausanne (EPFL)*, Switzerland.
Supervisors: Prof. A. Wüest. and Dr. D. Bouffard

2013-2015 **M.Sc. in Water Resources and Environment**, *University of Chile*, Santiago, Chile.
Supervisor: Prof. A. de la Fuente.

2011-2012 **Civil Engineer Diploma with major in Water Resources**, *University of Chile*, Santiago, Chile.

2007-2010 **B.Sc. in Civil Engineering**, *University of Chile*, Santiago, Chile.

Scholarships awarded

2013-2014 **National Master scholarship** (∼15% selection rate), *granted by the National Commission for Scientific and Technological Research - CONICYT*, Chile.

2014 **Scholarship for international research internship**, *granted by University of Chile*.
destination: APHYS Laboratory, EPFL, Switzerland.

Publications

Published

[1] Sommer, T., Danza, F., Berg, J., Sengupta, A., Constantinescu, G., Tokyay, T., Bürgmann, H., Dressler, Y., Sepúlveda Steiner, O., Schubert, C. J., Tonolla, M., & Wüest, A. (2017). Bacteria-induced mixing in natural waters. *Geophysical Research Letters*.

[2] Ulloa, H. N., Constantinescu, G., Chang, K., Horna-Munoz, D., Sepúlveda Steiner, O., Bouffard, D., & Wüest, A. (2019). Hydrodynamics of a periodically wind-forced small and narrow stratified basin: A large-eddy simulation experiment. *Environmental Fluid Mechanics*.

[3] Sepúlveda Steiner, O., Bouffard, D., & Wüest, A. (2019). Convection-diffusion competition within mixed layers of stratified natural waters. *Geophysical Research Letters*.

Submitted & in preparation

[1] Sepúlveda Steiner, O., Bouffard, D., & Wüest, A. Persistence of bioconvection-induced mixed layers in a stratified lake. Submitted to *Limnology and Oceanography*.

[2] Fernández-Castro, B., Sepúlveda Steiner, O., Knapp, D., Posch, T., Bouffard, D., & Wüest, A. Inhibited vertical mixing and seasonal persistence of a cyanobacterial thin layer in a stratified lake. Submitted to *Limnology and Oceanography*.

[3] Bartosiewicz, M., Venetz, J., Sepúlveda Steiner, O., Bouffard, D., Zopfi, J. & Lehmann, M. F. Planktonic detritus fuels the methane paradox in a meromictic alpine lake. In preparation for submission to *Ecological Applications* .

[4] Sepúlveda Steiner, O., Forrest, A. L., McInerney, J. B. T.,Fernández-Castro, B., Lavanchy, S., Bouffard, D., & Wüest, A. Turbulent mixing and algae patches from an underwater glider in Lake Geneva. In preparation.

Experience

2016-2019 **Teaching assistant, EPFL**.
Limnology (3 times), Hydrological risks and structures (2 times).

2012-2014 **Teaching assistant, University of Chile**.
Numerical modeling for hydraulic and environmental applications, Environmental hydrodynamics, Transport processes in aquatic systems, Newtonian Systems ($\sim$Physics II), Hydraulics (grader), Fluid mechanics (grader).

2013 **Professional Internship**, *Centro de Ecología Aplicada ltda.*, Santiago, Chile.
Design of a telemetric monitoring system of meteorological, hydrodynamic and water quality parameters for fjords and lakes. Supervisor: Dr. C. Meruane.

2012 **Research Assistant**, *Civil engineering department*, University of Chile.
Perform fieldworks and meteorological data analysis for research project on oxygen transport through the sediment-water interface in shallow salty lagoons. Supervisor: Prof. A. de la Fuente.

2011 **Professional Internship**, *Endesa S.A.*, Santiago, Chile.
2D modeling of hydraulic structures using `Iber` software.

Languages

Spanish	Mother tongue	French	Good fluency
English	Professional proficiency		

Computer skills

Operative Systems	Windows, Linux	Typography	LaTeX,Microsoft Word
Scientific programming	MATLAB, Python, Fortran 90		

Service

2016-2019 **Treasurer** for the Association of Chilean Researchers in Switzerland - **ICES**.

Other activities

Mountaineering and sport climbing

Craft Beer Brewing